Conference Proceedings of the Society for Experimental Mechanics Series

Jay Carroll · Shuman Xia · Allison M. Beese · Ryan B. Berke
Garrett J. Pataky *Editors*

Fracture, Fatigue, Failure and Damage Evolution, Volume 6

Proceedings of the 2018 Annual Conference on Experimental and Applied Mechanics

SEM

Springer

Conference Proceedings of the Society for Experimental Mechanics Series

Series Editor

Kristin B. Zimmerman, Ph.D.
Society for Experimental Mechanics, Inc.,
Bethel, CT, USA

More information about this series at http://www.springer.com/series/8922

Jay Carroll • Shuman Xia • Allison M. Beese • Ryan B. Berke
Garrett J. Pataky
Editors

Fracture, Fatigue, Failure and Damage Evolution, Volume 6

Proceedings of the 2018 Annual Conference on Experimental and Applied Mechanics

Springer

Editors
Jay Carroll
Sandia National Lab, MS 0889
Albuquerque, NM, USA

Allison M. Beese
Pennsylvania State University
State College, PA, USA

Garrett J. Pataky
Fluor Daniel Innovation Bldg 245
Clemson University
Clemson, SC, USA

Shuman Xia
Mechanical Engineering Georgia Tech, MRDC 4103
Georgia Institute of Technology
Atlanta, GA, USA

Ryan B. Berke
Department of Mechanical and Aerospace Engineering
Utah State University
Logan, UT, USA

ISSN 2191-5644 ISSN 2191-5652 (electronic)
Conference Proceedings of the Society for Experimental Mechanics Series
ISBN 978-3-319-95878-1 ISBN 978-3-319-95879-8 (eBook)
https://doi.org/10.1007/978-3-319-95879-8

Library of Congress Control Number: 2018955468

This Springer imprint is published by the registered company Springer Nature Switzerland AG
The registered company address is: Gewerbestrasse 11, 6330 Cham, Switzerland

Preface

Fracture, Fatigue, Failure and Damage Evolution represents one of the eight volumes of technical papers presented at the 2018 SEM Annual Conference & Exposition on Experimental and Applied Mechanics organized by the Society for Experimental Mechanics and held in Greenville, SC, June 4–7, 2018. The complete Proceedings also includes volumes on *Dynamic Behavior of Materials*; *Challenges in Mechanics of Time-Dependent Materials*; *Advancement of Optical Methods & Digital Image Correlation in Experimental Mechanics*; *Mechanics of Biological Systems & Micro-and Nanomechanics*; *Mechanics of Composite, Hybrid & Multifunctional Materials*; *Residual Stress, Thermomechanics & Infrared Imaging, Hybrid Techniques and Inverse Problems*; and *Mechanics of Additive and Advanced Manufacturing*.

Each collection presents early findings from experimental and computational investigations on an important area within experimental mechanics, fracture and fatigue being one of these areas.

Fatigue and fracture are two of the most critical considerations in engineering design. Understanding and characterizing fatigue and fracture has remained as one of the primary focus areas of experimental mechanics for several decades. Advances in experimental techniques, such as digital image correlation, acoustic emissions, and electron microscopy, have allowed for deeper study of phenomena related to fatigue and fracture. This volume contains the results of investigations of several aspects of fatigue and fracture such as microstructural effects, the behavior of interfaces, the behavior of different and/or complex materials such as composites, and environmental and loading effects. The collection of experimental mechanics research included here represents another step toward solving the long-term challenges associated with fatigue and fracture.

Albuquerque, NM, USA — Jay Carroll
Atlanta, GA, USA — Shuman Xia
State College, PA, USA — Allison M. Beese
Logan, UT, USA — Ryan B. Berke
Clemson, SC, USA — Garrett J. Pataky

Contents

Chapter 1
In Situ Strain Measurement in Solid-State Li-Ion Batteries

B. Koohbor, L. Sang, Ö. Ö. Çapraz, A. A. Gewirth, R. G. Nuzzo, S. R. White, and N. R. Sottos

Abstract Volumetric changes due to repeated lithiation and delithiation are a significant source of electrode degradation and capacity fade in rechargeable batteries. Measurement of such volumetric changes and their resultant electro-chemo-mechanical strains and stresses have previously been investigated in conventional liquid-electrolyte Li-ion batteries. In the present study, we propose to extend the current knowledge and measurement techniques into the area of all-solid-state Li-ion batteries. Due to the presence of inherent property mismatch as well as confinements imposed at the interfaces between the electrodes and solid electrolyte, solid-state battery components are more prone to interfacial damage and. In this work, novel experimental approaches are designed to facilitate in-situ strain measurements on solid electrolytes (SE), electrodes and SE/electrode interface. Digital image correlation (DIC) is utilized to enable full-field strain measurements.

Keywords Solid-state battery · *In situ* strain measurement · DIC · Electrode mechanics

Solid-state Li-ion batteries have attracted tremendous attention in the past decade as a substitute for conventional liquid-electrolyte batteries. Inherently safer nature, prevention of Li dendrite formation, and significantly reduced active material dissolution are among the main advantages of using solid electrolytes (SE) in place of a liquid [1]. One of the drawbacks limiting the application of solid-state batteries is their propensity to crack due to non-uniform volumetric expansions across the SE/electrode interface. Such volumetric expansions result from lithium insertion and removal in battery electrodes [2].

Our objective in the present study is to evaluate the chemo-electromechanical response of electrodes and solid electrolytes in all-solid-state lithium-ion batteries. In particular, we measure *in situ* strain evolution in electrodes and the electrode/electrolyte interface vicinity using Digital Image Correlation (DIC). A previously-designed custom-cell [2] is modified to provide optical access to the working electrodes and solid electrolyte cross-section while the cell is charged/discharged. A garnet type solid electrolyte fabricated from $Li_{1.5}Al_{0.5}Ge_{1.5}(PO_4)_3$ (LAGP) investigated. Electrode surface measurements are conducted on a Au thin film working electrode coated on the LAGP SE via e-beam technique. Through-thickness measurements are performed on symmetric cells that use Li foil as both anode and cathode.

In both measurement scenarios, the custom-cell is assembled inside an Ar-filled glove box. The assembled custom-cell is mounted vertically in front of a 5 MP camera equipped with high magnification zoom lens to facilitate time-lapse acquisition of images from a sub-millimeter area of interest. Figure 1.1 shows the experimental setup developed in this study.

Results obtained from the Au electrode surface measurement indicate that mechanical strain generation initiates during the first lithiation cycle. Strain build up continues during the successive lithiation/delithiation cycles, giving rise to the formation of areas with highly localized deformations. SE through-thickness measurements also indicate highly localized strain regions

B. Koohbor (✉) · Ö. Ö. Çapraz
Department of Materials Science and Engineering, University of Illinois at Urbana-Champaign, Urbana, IL, USA
e-mail: koohbor@email.sc.edu

L. Sang · A. A. Gewirth · R. G. Nuzzo
Department of Chemistry, University of Illinois at Urbana-Champaign, Urbana, IL, USA

S. R. White
Department of Aerospace Engineering, University of Illinois at Urbana-Champaign, Urbana, IL, USA

Beckman Institute for Advanced Science, University of Illinois at Urbana-Champaign, Urbana, IL, USA

N. R. Sottos
Department of Materials Science and Engineering, University of Illinois at Urbana-Champaign, Urbana, IL, USA

Beckman Institute for Advanced Science, University of Illinois at Urbana-Champaign, Urbana, IL, USA

J. Carroll et al. (eds.), *Fracture, Fatigue, Failure and Damage Evolution, Volume 6*, Conference Proceedings of the Society for Experimental Mechanics Series, https://doi.org/10.1007/978-3-319-95879-8_1

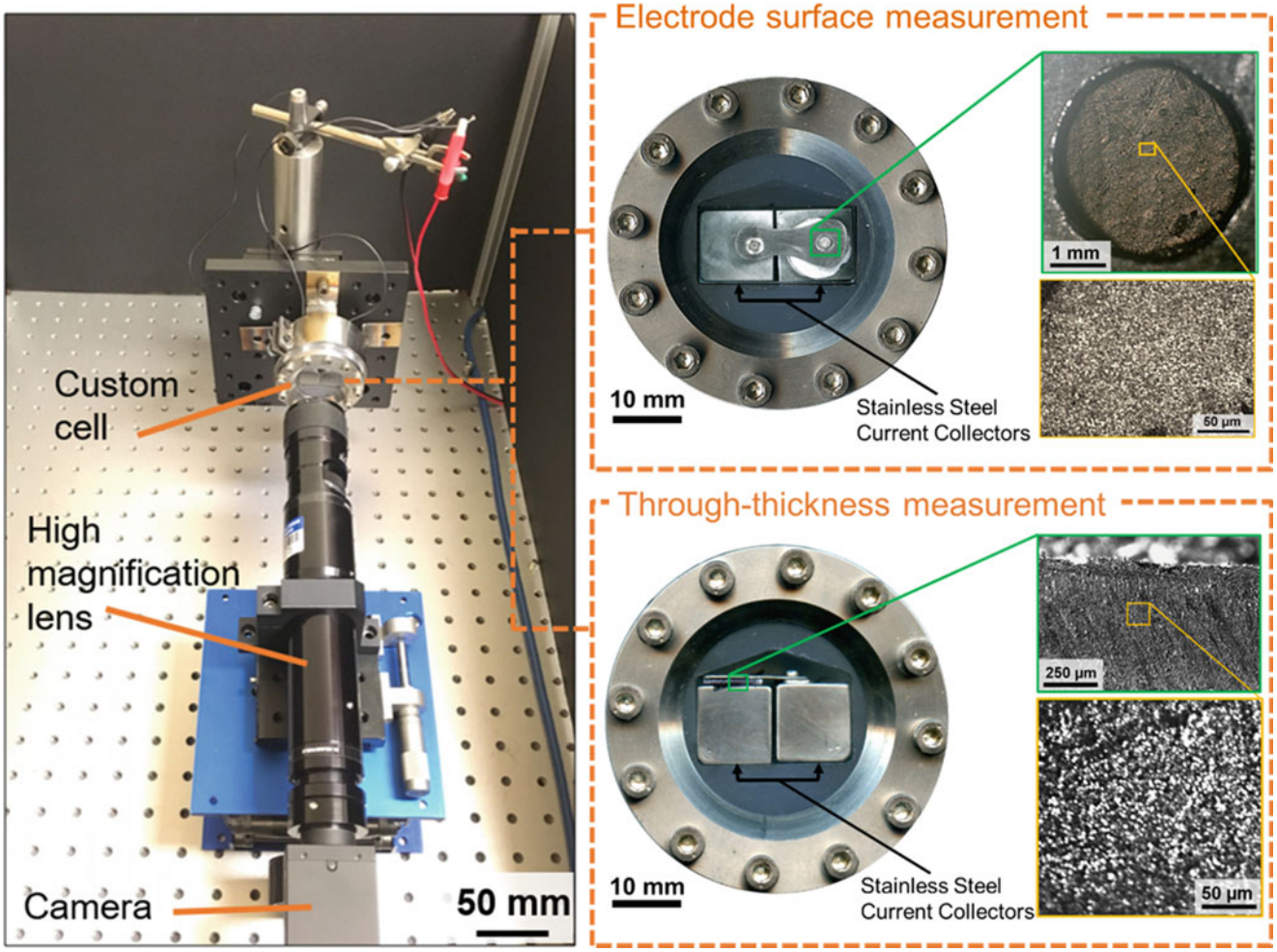

Fig. 1.1 Experimental setup used for *in situ* measurement of strains on working electrode surface and SE thickness

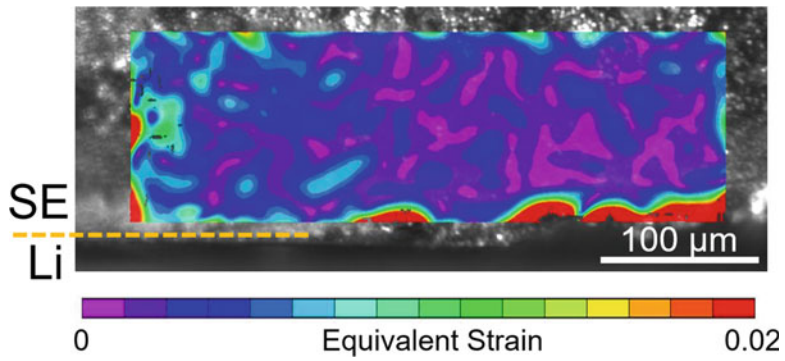

Fig. 1.2 Distribution of equivalent strain within a narrow region near the SE/electrode interface

near the SE/electrode interface. An example of such behavior is shown in Fig. 1.2. Ex-situ high magnification SEM images prove the presence of a narrow damage zone near the SE/electrode interface vicinity.

Acknowledgement This work was supported as part of the Center for Electrochemical Energy Science (CEES), an Energy Frontier Research Center funded by the U.S. Department of Energy, Office of Science, Basic Energy Sciences.

References

1. Kim, J.G., Son, B., Mukherjee, S., Schuppert, N., Bates, A., Kwon, O., Choi, M.J., Chung, H.Y., Park, S.: A review of lithium and non-lithium based solid state batteries. J. Power Sources. **282**, 299–322 (2015). https://doi.org/10.1016/j.jpowsour.2015.02.054
2. Jones, E.M.C., Silberstein, M.N., White, S.R., Sottos, N.R.: In situ measurements of strains in composite battery electrodes during electrochemical cycling. Exp. Mech. **54**(6), 971–985 (2014). https://doi.org/10.1007/s11340-014-9873-3

Chapter 2
Crack-Tip Plastic Zone Size and Shape via DIC

G. L. G. Gonzáles, J. A. O. González, V. E. L. Paiva, and J. L. F. Freire

Abstract In this paper Digital Image Correlation (DIC) is used to characterize the crack-tip plastic zone size and shape under plane stress and plane strain situations. For that, two disk-shaped tension DC(T) specimens made of 1020 steel with thicknesses 2 and 30 mm were used in fatigue crack growth tests to simulated plane stress and plane strain conditions, respectively. Fatigue cracks were grown under quasi-constant ΔK (stress intensity factor range) and stress ratio (R) respectively equal to 20 MPa$\sqrt{\text{m}}$ and 0.1. A single 100% overload was applied when the crack reached a crack length of 6 mm (i.e. total crack length/specimen width = 0.3). Experimental measurements of the monotonic plastic zone at different stages during overload application are compared with finite elements simulations to predict the size and shape of the crack-tip plastic zone. A detailed discussion is given based on the DIC measurements obtained from the current investigation, including the experimental observations of crack closure.

Keywords Plastic zone · Crack closure · Fatigue crack · Digital Image Correlation

2.1 Introduction

During fatigue crack propagation, plastic deformation occurs ahead of the crack tip as a result of the high stresses that concentrate on its tip. The region affected by plasticity is known as the plastic zone. It is recognized that, for most metallic materials, the crack-tip plastic zone plays an important role because it is related to the mechanisms which govern the fatigue crack growth. Indeed, it can be stated that fatigue cracks do not grow by cutting virgin material. They always propagate through a region that has already been damaged by their prior load history [1]. According to Elber [2], plasticity-induced crack closure is associated with the residual plastic wake left behind the crack caused by the monotonic plastic zone ahead of a growing fatigue crack. Moreover, delay effects in fatigue crack propagation observed after overloading are related to the interaction of the plastic zone hypertrophied by the overload with the current plastic zone [3–5].

In the literature, most of the reported work utilizes approaches based on Linear Elastic Fracture Mechanics (LEFM) to characterize the crack-tip plastic zone size and shape. The crack tip models developed by Dugdale and Irwin are commonly used to estimate the plastic zone size for a crack under mode I loading. These models give a good estimate of the radius of the monotonic plastic zone size in front of the crack tip. A more accurate estimate of its shape can be obtained by using a yield criterion, Tresca or von Mises equivalent stress, in conjunction with the material yielding strength S_Y [6]. In this way, the elastoplastic border around the crack tip is estimated using only the linear elastic stresses generated by the mode I stress intensity factor K_I. Similar analyses can be made for crack opening modes II and III.

In this paper, Digital Image Correlation [7] technique has been used to experimentally characterize the shape and size of crack tip plastic zone. For that, the von Mises yield criterion has been employed to delimit the border of the plastic zone, indicating whether or not plastic yielding is to be expected.

Various researchers have also studied the crack tip plastic zone using DIC technique [8–11]. It is well known that the DIC technique provides accurate and reliable measurements of displacements and strains. This information is used to obtain important fracture parameters from the region surrounding the crack, such as crack open displacement (COD), J-integral, and stress intensity factor (SIF).

The objective of the current work is to characterize the plastic zone at the tip of a given crack during FCG test in conditions of plane stress and plane strain. For that, fatigue crack growth (FCG) tests were performed in specimens with thicknesses of 2 mm and 30 mm in order to simulate plane stress and plane strain conditions, respectively. It is known that the specimen

G. L. G. Gonzáles (✉) · J. A. O. González · V. E. L. Paiva · J. L. F. Freire
Pontifical Catholic University of Rio de Janeiro, PUC-Rio, Rio de Janeiro, RJ, Brazil

J. Carroll et al. (eds.), *Fracture, Fatigue, Failure and Damage Evolution, Volume 6*, Conference Proceedings of the Society for Experimental Mechanics Series, https://doi.org/10.1007/978-3-319-95879-8_2

thickness largely affects the state of stress at the crack tip and, consequently, the shape of the plastic zone [6]. To determine the stress state ahead the crack tip, the maximum size of its plastic zone (pz_{max}) is compared with the specimen thickness (t). If $t >> pz_{max}$ the crack grows under predominantly plane strain (pl-ε) conditions. If $t \leq pz_{max}$, plane stress (pl-σ) develops. Moreover, if neither such conditions are satisfied, the crack grows under a mixed state.

2.2 Experimental Methods

The fatigue tests were performed in a servo-hydraulic testing machine using disk shaped tension DC(T) specimens made of steel 1020 shown in the Fig. 2.1. Two specimens were machined from the same 3″ steel round bar, one to a thickness of 2 mm (thin specimen) and one to a thickness of 30 mm (thick specimen). The specimen thickness determines pl-σ conditions (i.e $t \leq pz_{max}$) in the thin specimens and pl-ε conditions in the thicker ones, assuming that classical ASTM E399 pl-ε requirements can be used in fatigue as well (i.e. $t > 2.5(K_{max}/S_Y)^2$).

The FCG tests were performed under constant ΔK and loading conditions, following the traditional standard ASTM procedures. The thinner specimens were loaded under $\Delta K = 20$ MPa$\sqrt{\text{m}}$ and $R = 0.1$ and, to force the crack to grow under nominally pl-σ conditions, they had $t = 2$ mm $< pz_{max} = (1/\pi) \cdot (K_{max}/S_Y)^2 = (1/\pi) \cdot [20/(0.9 \cdot 262)]^2 = 2.29$ mm (using Irwin's estimate for the maximum plastic zone ahead of the crack tip). The thicker ones were loaded under $\Delta K = 20$ MPa$\sqrt{\text{m}}$ and $R = 0.1$, and to force the crack to grow under predominantly pl-ε conditions they had $t = 30$ mm $> 2.5 \cdot (K_{max}/S_Y)^2 = 2.5 \cdot [20/(0.9 \cdot 262)]^2 = 17.98$ mm, using the ASTM E399 criterion.

After crack initiation, the applied load was adjusted to maintain the SIF range (ΔK) approximately constant. Once the crack length reached approximately 6 mm, a single 100% overload cycle was applied to both specimens. Different images from each specimen were captured during the normal fatigue cycle, as well as during and after the overload event. The loading history is shown in Fig. 2.2. The image acquisition and analyses were performed using the VIC-3D system developed by Correlation Solutions Inc. [12]. The stereoscopic system consists of two Point Grey GRAS-50S5M cameras with high magnification lenses mounted on a rigid tripod located in front of the specimen. To enable the DIC measurement, a high-contrast random pattern was sprayed on the specimen surface.

The images were processed using the following DIC parameters: a subset size of 31 × 31 pixels, a step size of 7 pixels and a strain windows of 15 × 15 displacement points. The reference image used in the DIC analysis was captured when the crack had reached a length of about 4 mm and with the specimen in the unloaded state, it appears marked with a red square in Fig. 2.2. For the von Mises strain calculation, the VIC-3D software uses a principal plane strain formulation as follows:

$$\varepsilon_{vm} = \sqrt{\varepsilon_1^2 - \varepsilon_1 \cdot \varepsilon_2 + \varepsilon_2^2} \tag{2.1}$$

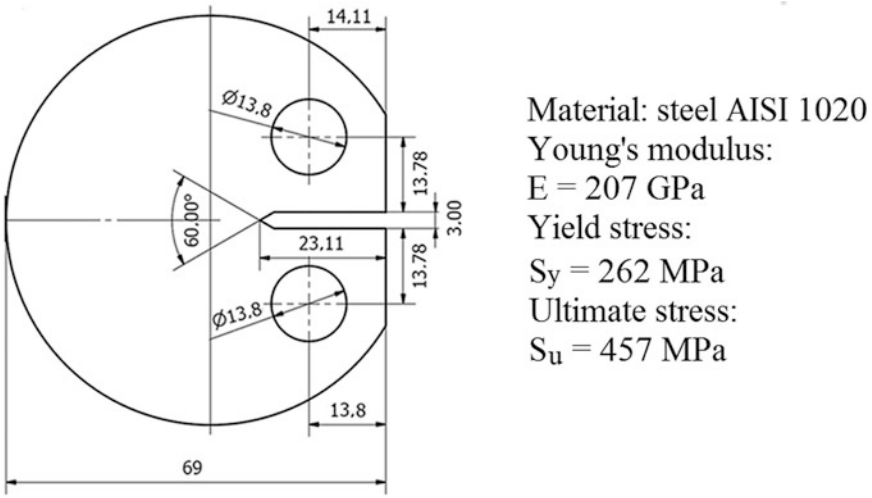

Fig. 2.1 Specimen dimensions and mechanical material properties

2.3 Results and Discussion

Figure 2.3 shows the values of strain measurements at a point located at 0.5 mm ahead of the crack tip during overloading, for a cycle just before and after the overload event. It can be observed the presence of crack closure at low load values in the pre-overload cycle. During overloading, significantly plastic deformation was induced in the region ahead of the crack tip, blunting its tip. Therefore, the crack tip remains open during the entire loading cycle even at zero loading, neglecting the crack closure effects as observed in the post-overload cycle.

The results given in Figs. 2.4 and 2.5 were obtained from the DIC analysis using the von Mises yield criterion to detect the presence of plastic deformation. For that, the equivalent von Mises stress is calculated from the von Mises strain map obtained from DIC analysis (Eq. 2.1). These values are compared with the material's yield stress, indicating whether or not plastic yielding is to be expected and therefore delimiting the plastic zone boundary. Fig. 2.4 corresponds to the 30 mm-thickness specimen (plane strain) and Fig. 2.5 to the 2 mm-thickness specimen (plane stress). These figures show the evolution of the crack tip plastic zone size at 25%, 50%, 75% and 100% overload cycle in which the plastic zone increases in size with the load level applied during the overload cycle.

The experimental results show that the plastic zone size is larger in plane stress than in plain strain. Furthermore, it is observed that the shape of the plastic zone differs significantly in the two cases. In the 30 mm-thickness specimen, the plastic zone is elongated and butterfly shaped, while in the 2 mm-thickness specimen is more extended and flattened. These observations are in good agreement with the residual wake of plastic deformation at the specimen's surfaces show in Fig. 2.6 and with experimental results reported in the literature [6].

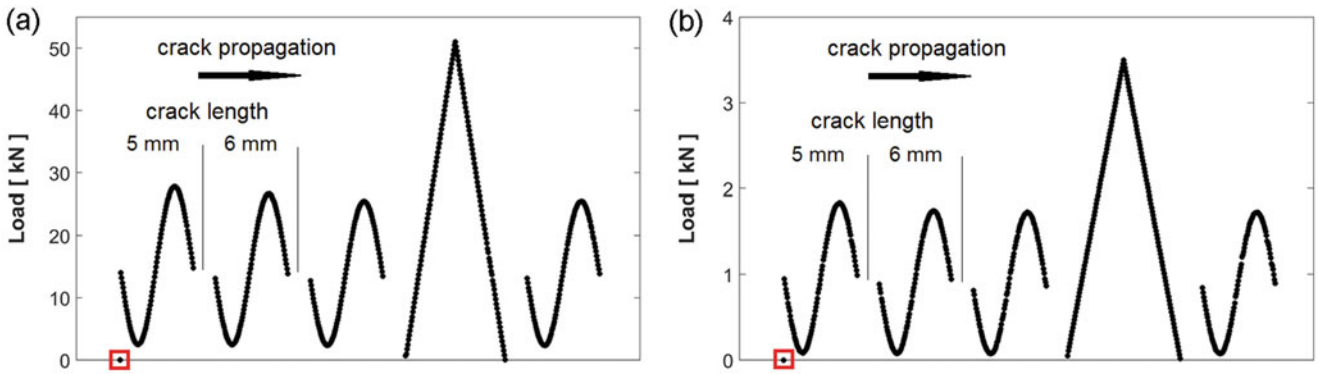

Fig. 2.2 Loading history for image acquisition. (**a**) 30 mm-thickness specimen and (**b**) 2 mm-thickness specimen

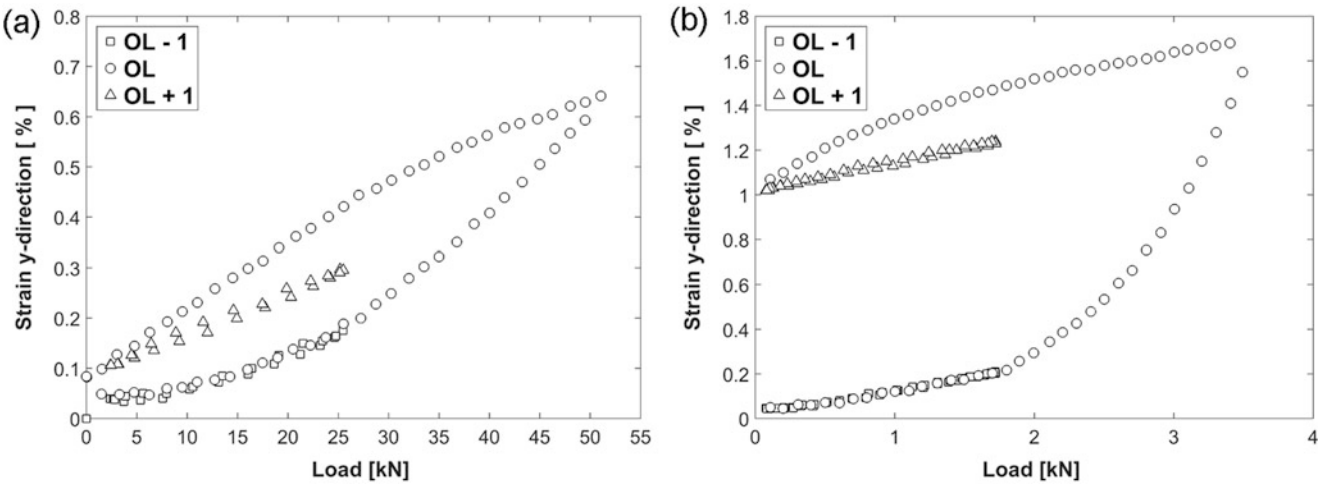

Fig. 2.3 (**a**) Strain behavior at 0.5 mm ahead the crack tip for the 30 mm-thickness specimen. (**b**) Strain behavior at 0.5 mm ahead the crack tip for the 2 mm-thickness specimen

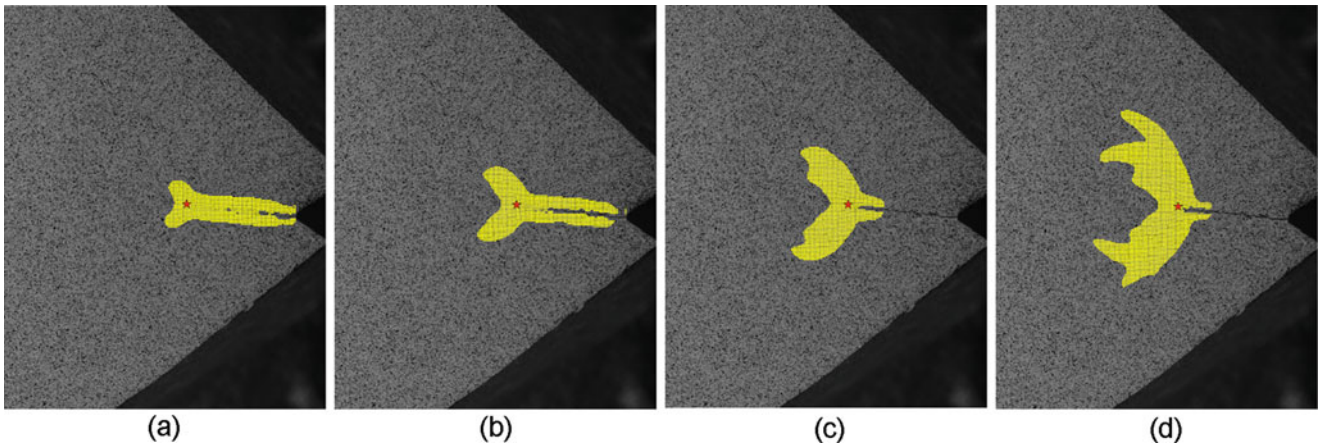

Fig. 2.4 Crack tip plastic zone from DIC analysis for the 30 mm-thickness specimen at (**a**) 25%, (**b**) 50%, (**c**) 75%, and (**d**) 100% overload

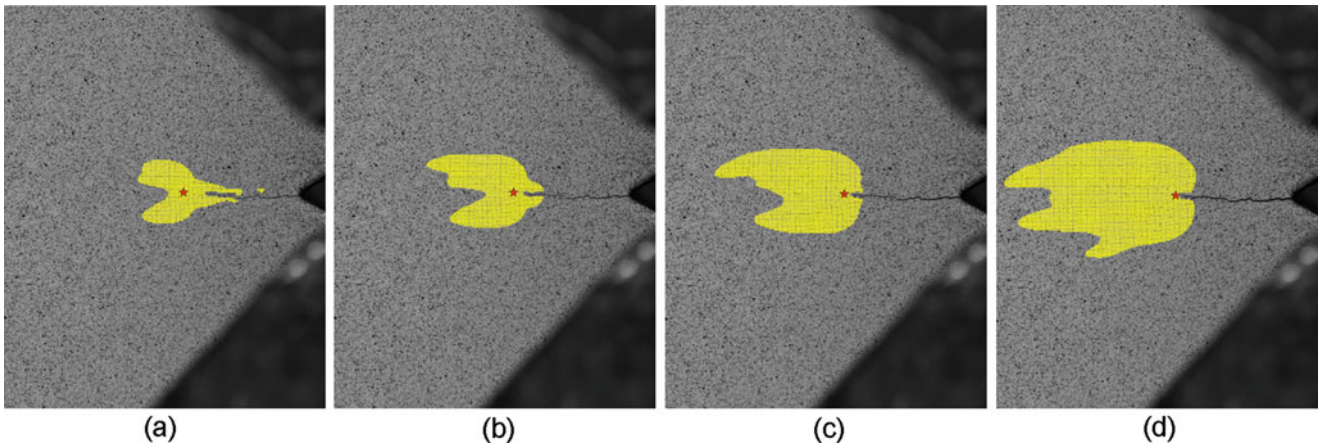

Fig. 2.5 Crack tip plastic zone from DIC analysis for the 2 mm-thickness specimen at (**a**) 25%, (**b**) 50%, (**c**) 75%, and (**d**) 100% overload

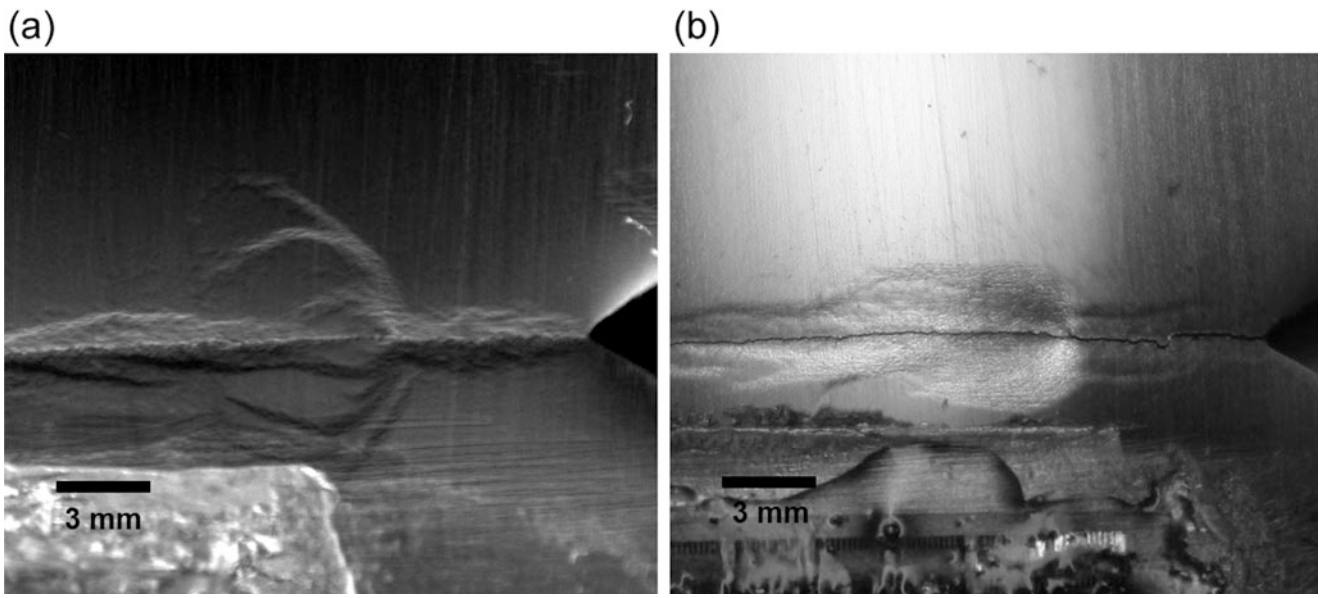

Fig. 2.6 Crack growth morphologies during FCG test for the (**a**) 30 mm-thickness specimen and the (**b**) 2 mm-thickness specimen

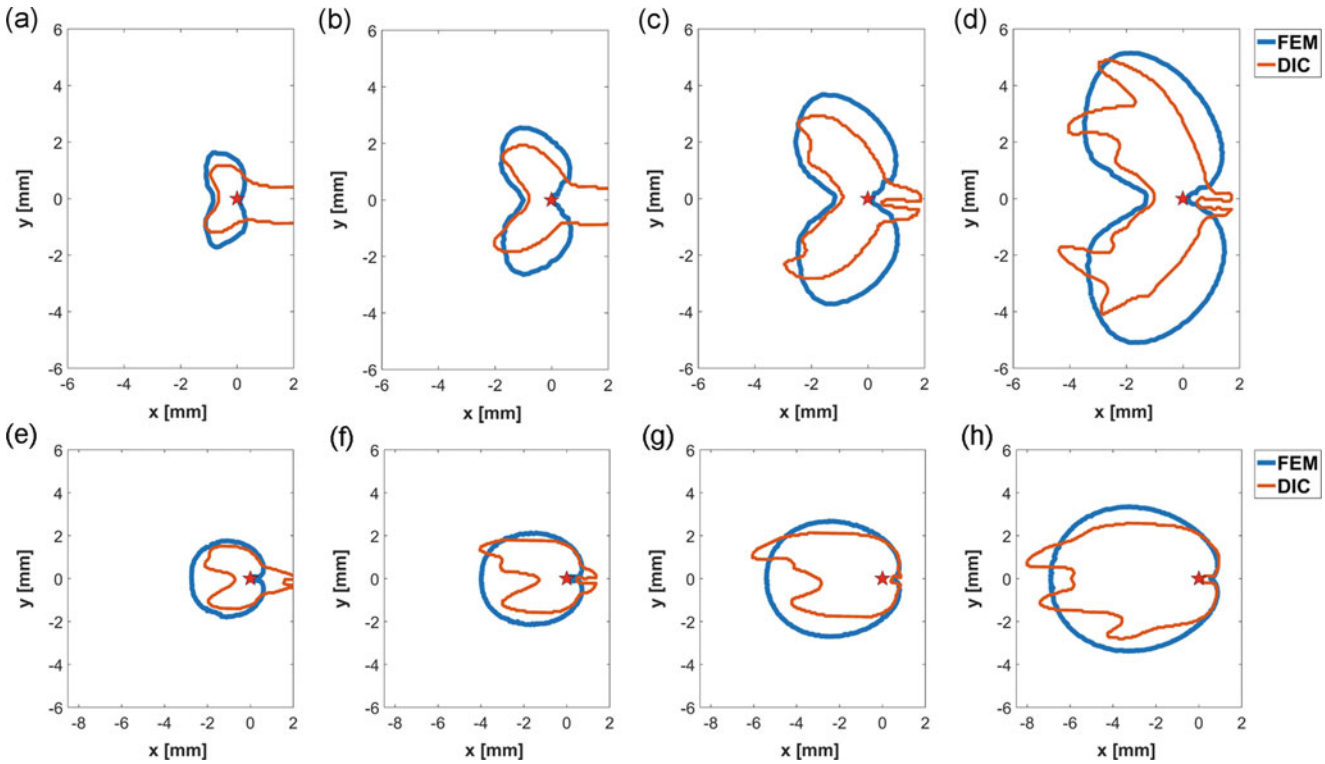

Fig. 2.7 Comparison of simulated and experimental data for the 30 mm-thickness specimen at (**a**) 25%, (**b**) 50%, (**c**) 75%, and (**d**) 100% overload, and the 2 mm-thickness specimen at (**e**) 25%, (**f**) 50%, (**g**) 75%, and (**h**) 100% overload

Moreover, Fig. 2.6 clearly show the plastic wake left behind the crack tip caused by the plastic zone or crack tip plasticity during fatigue cracking. It can be seen that the width of the plastic wake is uniform along the crack flanks, since the cracks were grown under conditions of constant stress intensity factor range.

In addition, this study compares the experimental data from surface DIC measurements with finite-element (FE) simulation results obtained by using the ANSYS Workbench 15.0 software. The FE analysis adopted an elastic-plastic material model with multilinear kinematic hardening. The 3D model was constructed with second order tetrahedral elements (SOLID 186), most of them concentrated near the crack tip. The information required to define the model was extracted from experimental tests carried out to determine specific properties of the material used here.

Figure 2.7 depicts the comparison of simulated and experimental data at different load intensities during the overload cycle. In general, the shape of the experimentally determined plastic zones was in agreement with Finite Element predictions. However, it seems to match much better in plane strain than in plain stress. It is important to note that in the FE analysis, the von Mises stress used to delimit the plastic zone boundary was calculated using all three major tensors of stress. Further, differences in size are observed in both specimens. In particular, it is expected that the experimentally determined plastic zone sizes were slightly smaller than the numerical predictions due to the presence of crack closure which causes an offset between the theoretical and the experimental SIF values as shown in Fig. 2.8. In this figure the mode I SIF at the crack tip during overloading was calculated using the J-integral approach proposed in [13]. The J-integral was computed directly from the DIC displacement data along a contour path placed around the crack tip outside the plastic zone, in which linear elastic conditions are valid. The theoretical SIF calculated from the ASTM equation agreed with the SIF obtained from FE simulations, which assume that the crack is fully opened during the entire loading cycle, neglecting crack closure observed at low loads.

2.4 Conclusions

Results presented in this paper show that DIC measurements combined with the von Mises yield criterion characterized accordingly the shape and size of the plastic zone around the crack tip. The methodology was successfully tested in two DC (T) specimens with thicknesses of 2 mm and 30 mm in order to assess plane stress and plane strain conditions, respectively.

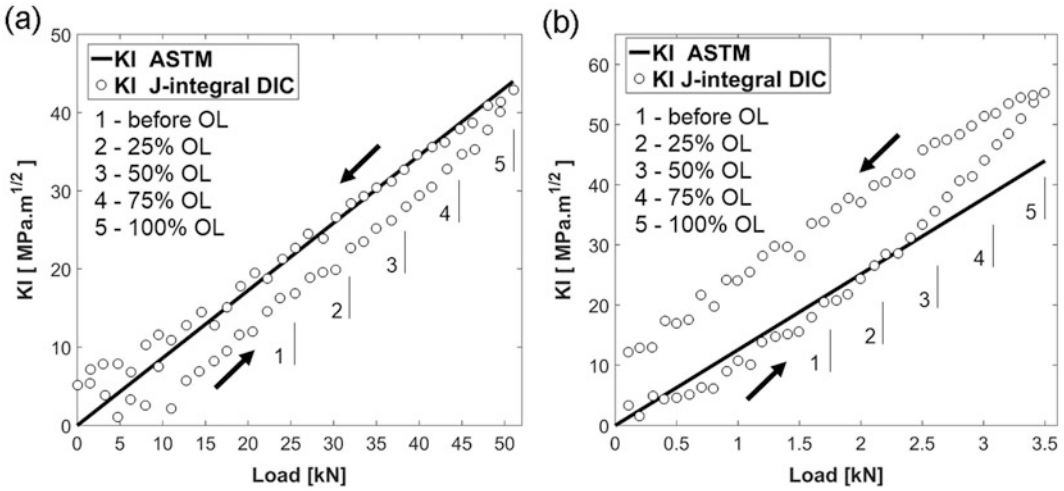

Fig. 2.8 SIF evaluation from J-integral approach for the (**a**) 30 mm-thickness specimen and (**b**) 2 mm-thickness specimen during overloading

However, it is important to note that the experimental data contains information on the nonlinearities induced by crack tip phenomena such as crack closure, crack tip plasticity, and crack tip blunting.

References

1. Castro, J., Meggiolaro, M.: Fatigue Design Techniques (in 3 volumes). CreateSpace, Scotts Valley (2016)
2. Wolf, E.: Fatigue crack closure under cyclic tension. Eng. Fract. Mech. **2**(1), 37–45 (1970)
3. Gonzáles, G., González, J., Castro, J., Freire, J.: Detecting fatigue crack closure and crack growth delays after an overload using DIC measurements. Fract. Fatigue Fail. Damage Evol. **7**, 57–65 (2018)
4. Nowell, D., De Matos, P.: Application of digital image correlation to the investigation of crack closure following overloads. Procedia Eng. **2**(1), 1035–1043 (2010)
5. Withers, P., Lopez-Crespo, P., Mostafavi, M., Steuwer, A., Kelleher, J., Buslaps, T.: 2D mapping of plane stress crack-tip fields following an overload. Frattura ed Integrità Strutturale. **9**(33), 151 (2015)
6. Sousa, R., Castro, J., Lopes, A., Martha, L.: On improved crack tip plastic zone estimates based on T-stress and on complete stress fields. Fatigue Fract. Eng. Mater. Struct. **36**(1), 25–38 (2013)
7. Sutton, M.A., Orteu, J.J., Schreier, H.: Image correlation for shape, motion and deformation measurements: basic concepts, theory and applications. Springer US, Boston, MA (2009)
8. Camas, D., Lopez-Crespo, P., Gonzalez-Herrera, A., Moreno, B.: Numerical and experimental study of the plastic zone in cracked specimens. Eng. Fract. Mech. **185**, 20–32 (2017)
9. Vasco-Olmo, J., James, M., Christopher, C., Patterson, E., Díaz, F.: Assessment of crack tip plastic zone size and shape and its influence on crack tip shielding. Fatigue Fract. Eng. Mater. Struct. **39**(8), 969–981 (2016)
10. Du, Y., Patki, A., Patterson, E.: Monitoring crack tip plastic zone size during fatigue loading. Exp. Appl. Mech. **6**, 569–573 (2011)
11. Rossi, M., Sasso, M., Chiappini, G., Mancini, E., Amodio, D.: Identification of the plastic zone using digital image correlation. Frattura ed Integrità Strutturale. **30**, 552 (2014)
12. VIC-3D, "®Software," Correlated Solutions Inc. http://www.correlatedsolutions.com/. (2010)
13. Gonzáles, G.L., González, J.A., Castro, J.T., Freire, J.L.: A J-integral approach using digital image correlation for evaluating stress intensity factors in fatigue cracks with closure effects. Theor. Appl. Fract. Mech. **90**, 14–21 (2017)

Chapter 3
Investigating Dynamic Fracture Parameters for Al7075-T651 Using Modified Hopkinson Pressure Bar (MHPB)

Sanjay Kumar, Anoop Kumar Pandouria, and Vikrant Tiwari

Abstract Dynamic fracture toughness of engineering materials is an important parameter in damage evaluation and safety assessment of the structures that are often subjected to impact loading. In the current work, dynamic initiation fracture toughness has been experimentally evaluated at different loading rates for a aluminium alloy Al7075-T651. It was observed that dynamic fracture toughness increases with the loading rates. The experimental set up used in this study is a Modified Hopkinson Pressure Bar consisting of the incident bar, a projectile, and a adjustable three-point bend fixture. Specimens used in the experiments are machined according to ASTM-E399 standard. Two different sets of experiments were conducted at projectile velocities of 12.7 m/s and 13.9 m/s with corresponding launch pressure of 1 bar and 1.5 bar respectively. Stress intensity factor was evaluated using a established load point displacement technique, while the time of initiation of fracture (t_f) was obtained using a stereo-configuration of high speed cameras in conjunction with 3D Digital Image Correlation. The dynamic initiation fracture toughness was evaluated and was found to be 18.48 MPa$\sqrt{m}$ and 21.68 MPa$\sqrt{m}$ for the given boundary conditions respectively.

Keywords Dynamic fracture toughness · Load point displacement · Modified Hopkinson Pressure Bar · Stress intensity factor

3.1 Introduction

Since the beginning of twentieth century, researchers and scientists have battled many problems related to selection of materials for design of mechanical and structural components. A high factor of safety was considered an easy option during design to prevent the failures [1]. Mechanical properties like yield strength, tensile strength were the main parameters on which engineering design was based. Since the advent of fracture mechanics after World War II focus of research was shifted towards parameters like crack size, crack growth and materials ability to resist crack propagation. One such parameter toughness is defined as energy absorbed by the material before fracture and it is estimated by finding the area under stress-strain curve up to rupture point. Fracture toughness measures the resistance of a material to crack extension [2]. Commonly used fracture toughness in design is of four types, G_{Ic},K_{Ic},J_{Ic}, and CMOD. Different types of fracture toughness are used for the different mechanical behaviour of materials and geometries of materials depending on the application. G_{Ic}, is generally used for a brittle materials, K_{Ic} is used for LEFM while J_{Ic}, CMOD are used for EPFM [1]. Aluminium alloys are commonly used as structural materials for vehicles and aircrafts etc., which often encounter severe crash and collisions [3] warranty the research towards the dynamic characterisation of the aluminium alloys.In this research article we have evaluated the effect of loading rates on the dynamic initiation fracture toughness for aluminium Al7075-T651 using Modified Hopkinson Pressure Bar (MHPB). However unlike the measurement of static fracture toughness, there is no standard technique available for measuring the fracture initiation toughness. In the present article higher loading rate has been used which are similar to the earlier research efforts [4, 5].

S. Kumar (✉)
Delhi Technological University, Delhi, India
e-mail: sanjaykumar@dtu.ac.in

A. K. Pandouria · V. Tiwari
Indian Institute of Technology Delhi, Hauz Khas, New Delhi, India

J. Carroll et al. (eds.), *Fracture, Fatigue, Failure and Damage Evolution, Volume 6*, Conference Proceedings of the Society for Experimental Mechanics Series, https://doi.org/10.1007/978-3-319-95879-8_3

3.2 Experimental Procedure

3.2.1 Experiment

Modified Hopkinson Pressure bar used in this study mainly consists of a gas gun, striker bar, input bar, data acquisition, system, three-point bend specimen support.The schematic of the experimental set up can be seen in Fig. 3.1. Both striker and incident bar were obtained from maraging steel rod of 20 mm diameter. There individual length was selected to be 300 mm and 1510 mm respectively. The one end of input bar toward striker side, is flat and another end was machined similar to the shape of the hammer of the conventional Charpy test. The striker bar was propelled using a compressed air gas gun. On contact a compressive pulse is induced in incident bar. This strain wave was observed using two strain gauges at a sampling rate of 1MHZ. Single Edge Notched Bend (SENB) specimen (Fig. 3.2) was placed between input bar and support in a manner such that three-point bend condition are maintained (Fig. 3.3). When a incident wave hits the specimen, some of its energy is absorbed by the specimen and remaining is returned back as the reflected wave. The incident and reflected strain pulses are recorded by same strain gauges glued at the middle of the incident bar. One dimensional wave theory was then used to evaluate force and displacements on the specimen in term of incident and reflected strain pulses.

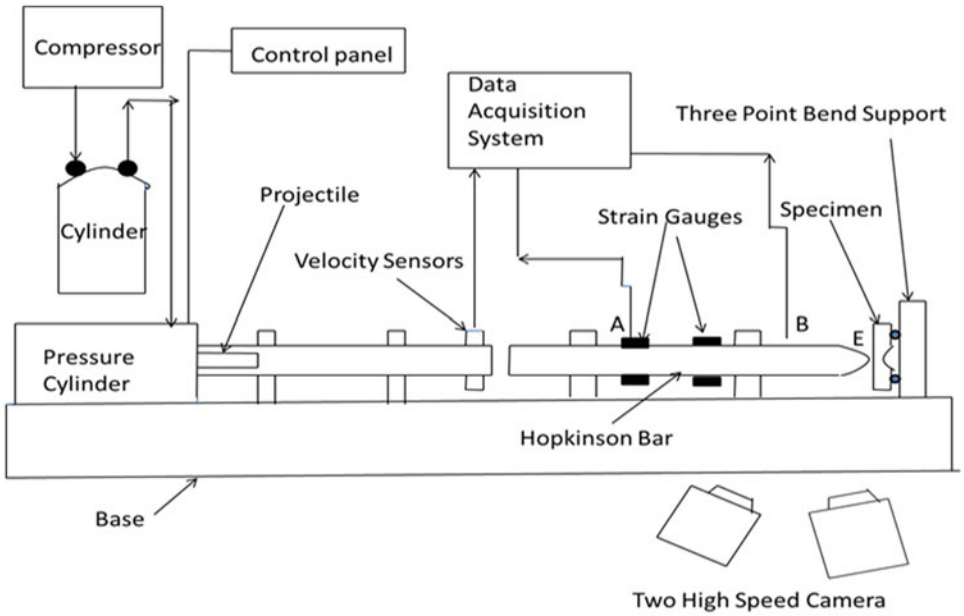

Fig. 3.1 Schematic of experimental set up (MHPB)

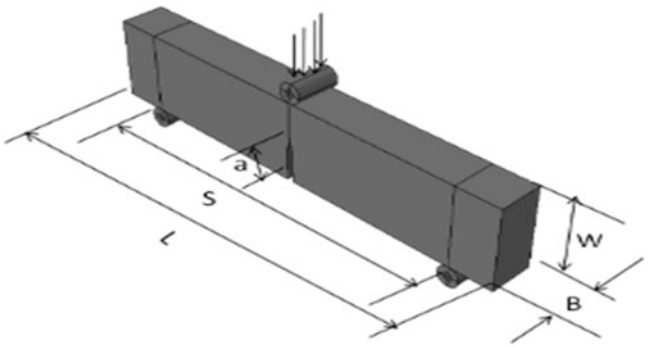

Fig. 3.2 Three-point bend specimen

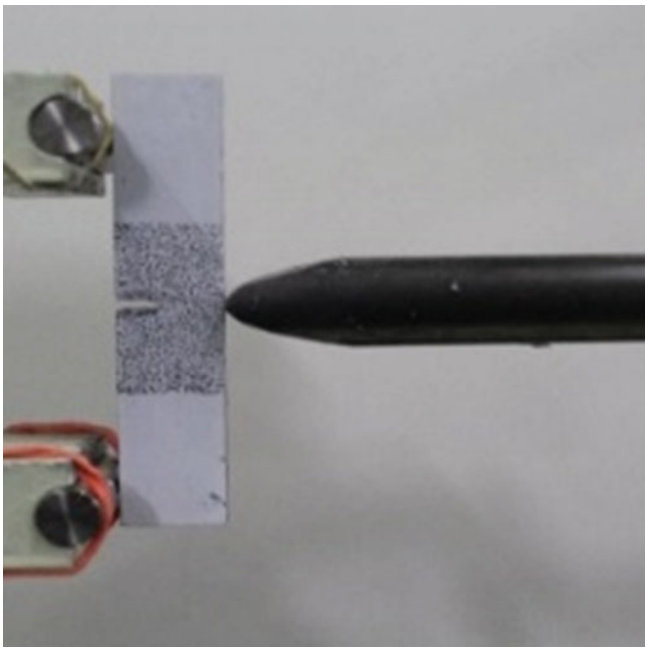

Fig. 3.3 Specimen with incident bar

Table 3.1 Chemeical composition of AL7075-T651

Elements	Al	Cr	Cu	Fe	Mg	Mn	Si	Ti	Zn	Sn
Present alloy (wt%)	90.28	0.231	1.373	0.117	2.335	0.032	0.0697	0.0607	5.473	0.001
Standard alloy (wt%)	87.1–91.4	0.18–0.28	1.2–2	Max 0.5	2.1–2.9	Max 0.3	Max 0.4	Max 0.2	5.1–6.1	–

3.2.2 Specimen

Three point bend specimens used in this study were fabricated from Al7075-T651, using ASTM (E-399) standard. The dimension of three-point bend specimen was 100 mm × 20 mm × 10 mm. While the span length of the specimen was 80 mm. A crack of uniform width 1.5 mm and length 7 mm was formed at the middle, subsequently, V-notch of length 1.5 mm at 30° inclined was generated and finally a fatigue crack length of 1.5 mm was generated on MTS machine of capacity 250kN. This three-point specimen was then used in the evaluation of dynamic initiation fracture toughness, (K_{1d}) [6]. The spectroscopy of this alloy was performed and chemical composition is listed in the Table 3.1.

This chemical composition of this specimen is compared with ASM material data sheet [7].

3.3 Theoretical Considerations

3.3.1 Dynamic Initiation Fracture Toughness, (K_{1d})

Transient strain data recorded during the experiment was utilized for determining dynamic initiation fracture toughness using one dimensional wave theory equation as given below.

$$P(t) = EA(\varepsilon_i(t) + \varepsilon_r(t)) \tag{3.1}$$

$$u_p(t) = c_o \int_0^\tau (\varepsilon_i(t) - \varepsilon_r(t))dt \tag{3.2}$$

Here, P represents the load and u represents load point displacement of input bar having Young's modulus E and cross sectional area A, and c_o represents the sound speed in the bar ($c_o = \sqrt{\frac{E}{\rho}}$, where ρ is mass density). Also $\varepsilon_i(t)$ and $\varepsilon_r(t)$ represents the incident and reflected strain pulse respectively.

As we know that stress intensity factor $K_I(t)$ is related to load point displacement ($u_p(t)$) of input bar as shown by Eq. (3.3) [8]. For present specimen $\left(\beta = \frac{S}{W} = 4, \alpha = \frac{a_o}{W}\right)$, where B and W represent thickness and width of the specimen. As shown in earlier literature [8] stress intensity factor related to the load point displacement $u_p(t)$ as shown below.

$$K_I(t) = \frac{3\beta u_p(t)}{2B\sqrt{W}C(\alpha)} k_\beta(\alpha) \tag{3.3}$$

$$Where \;\; k_\beta(\alpha) = \frac{\sqrt{a}}{(1-\alpha)^{3/2}(1+3\alpha)}\left(1.9 + 0.41\alpha + 0.51\alpha^2 - 0.17\alpha^3\right)$$

Here, $C(\alpha)$ represent the compliance of cracked specimen and details formulation to obtain is mentioned in the appendix of reference [8].

3.4 Experimental Results

Series of experiments were conducted to investigate the influence of loading rate on the dynamic fracture toughness of Al7075-T651. A typical result indicating variation of strain with respect to time in a incident bar is shown in Fig. 3.4. This indicates the variation of incident pulse $\varepsilon_i(t)$ and reflected pulse $\varepsilon_r(t)$ at point 'A' on the middle length of input bar. These strain signal for an incident and reflected pulse are compressive and tensile nature respectively. The young modulus of elasticity (205GPa) for steel and velocity (v) of the wave for the maraging steel was determined (5126 m/s) experimentally. The force at specimen and load point displacement are obtained from Eqs. (3.1) and (3.2). In present research load point displacement is used for determination of stress intensity factor, Fig. 3.5 shows the variation of load point displacement. Here, time in the microsecond is plotted on abscissa and load point displacement in mm on the ordinates. It represents variation of load point displacement at two different velocities (v = 12.7 m/s and 13.9 m/s) corresponding to two different launch pressures (1 bar and 1.5 bar). From this figure, it can be observed that displacement obtained at higher velocity are greater than displacement obtained at lower velocity.

Figure 3.6 represents the variation of stress intensity factor (SIF) with time. SIF is obtained from Eq. (3.3) in terms of load point displacement. Here, time in the microsecond is plotted on abscissa and stress intensity factor in MPa$\sqrt{m}$ on ordinates, for two different velocities (v = 12.7 m/s and 13.9 m/s) corresponding to two different launch pressures (1 bar and 1.5 bar). From

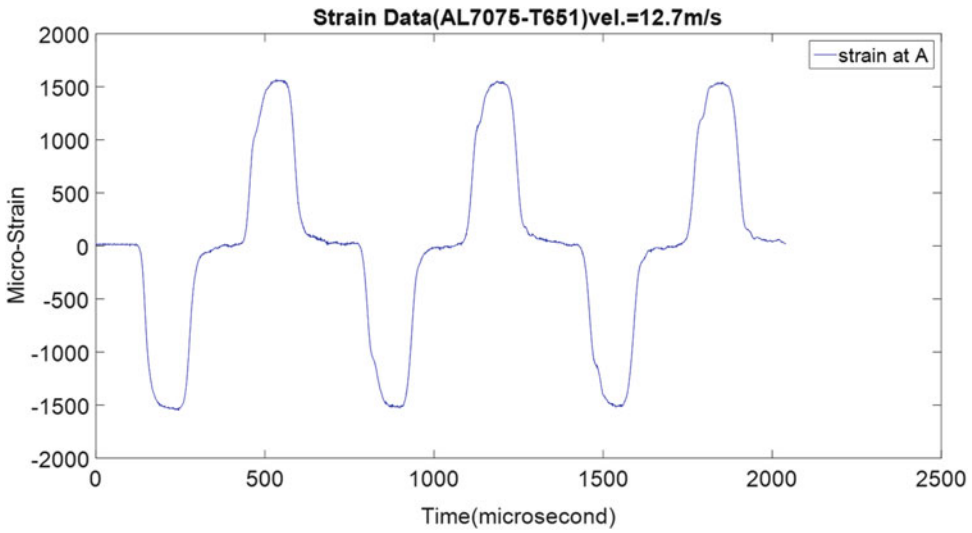

Fig. 3.4 Micro strain vs time at pressure 1 bar (v = 12.7 m/s)

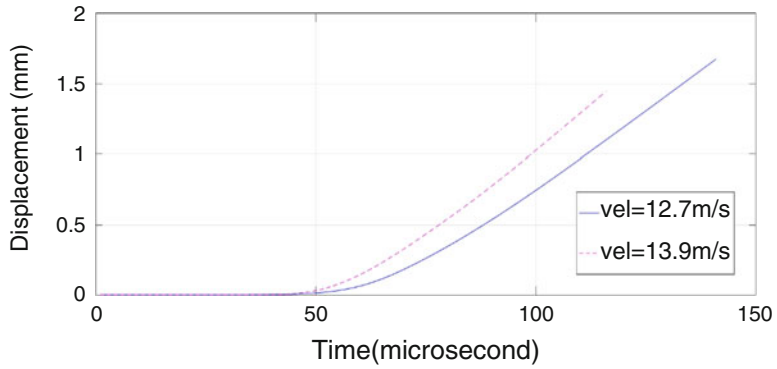

Fig. 3.5 Load point displacement vs time at different impact velocity (12.7 m/s and 13.9 m/s)

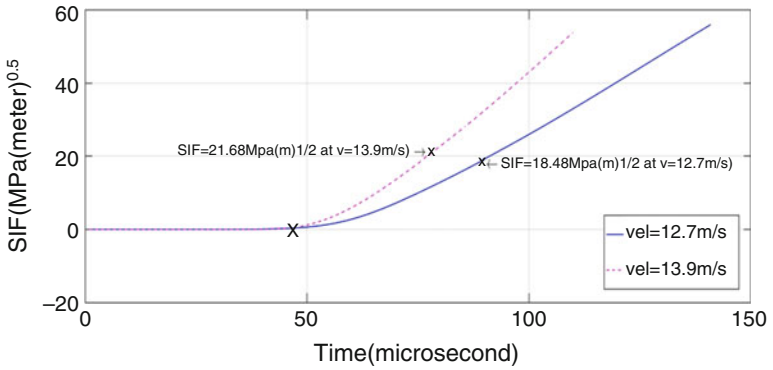

Fig. 3.6 Stress Intensity factor vs time at different impact velocity (12.7 m/s and13.9 m/s)

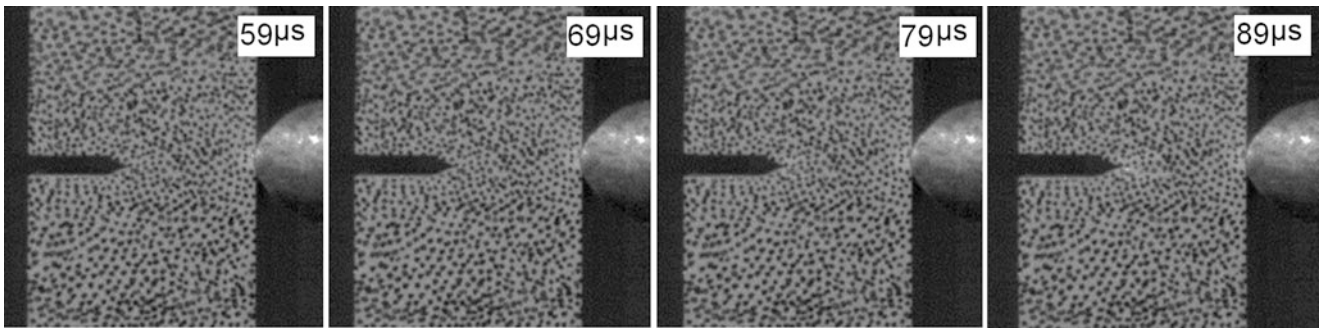

Fig. 3.7 Four images captured by high-speed camera at velocity 12.7 m/s (loading started to crack initiation)

this figure, it can be seen that SIF obtained at higher velocity is more than obtained at lower velocity. The trend of variation of load point displacement and SIF is same as SIF is directly proportional to load point displacement.

Figure 3.7 shows the different images captured from high-speed cameras at velocity 12.7 m/s, the frame rate of the camera was maintained (1,00,000 fps) during both experiments.

Here, four images are shown, which were captured during the experiment. Image (1) represents the start of loading. Image (2) and image (3) represents subsequent loading and crack initiation can be clearly seen in image (4). Time required for loading to crack initiation at velocity 12.7 m/s was found to be 40 μs. Similarly, the time required for loading to crack initiation at velocity 13.9 m/s was found to be 30 μs obtained from Fig. 3.8.

Variation of stress intensity factor with time at velocities 12.7 m/s and 13.9 m/s can be seen in Fig. 3.6. This figure shows that the loading on specimen has started at 49 μs because SIF increases from this point, which is shown by first cross mark 'x' in this figure at 49 μs. After 40 μs (crack initiation time) from this 'x' mark means (total time = 89 μs) the value of SIF becomes 18.48 MPa$\sqrt{m}$ at velocity 12.7 m/s. The fracture toughness at this loading rate is 18.48 MPa$\sqrt{m}$ is shown in Table 3.2. Similarly after 30 μs(crack initiation time) from this cross mark 'x' means (total time = 79μs) the value of SIF

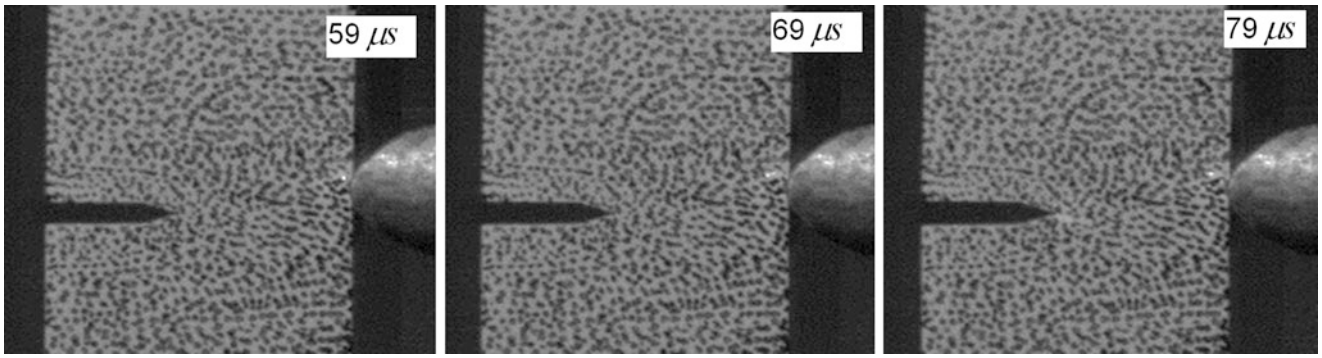

Fig. 3.8 Three images captured by high-speed camera at velocity 13.9 m/s (loading started to crack initiation)

Table 3.2 Experimental results

Specimen No.	Crack length (a_o) (mm)	Velocity (m/s)	Time of initiation (t_f) (microsecond)	Dynamic initiation fracture toughness MPa$\sqrt{m}$	Dynamic initiation fracture toughness [8] MPa$\sqrt{m}$
7	10.2	12.7	40	18.48	–
8	10.1	13.9	30	21.68	–
9	10.81	13.1	25	–	22
10	10.73	13.2	25	–	20

becomes 21.68 MPa$\sqrt{m}$ for the velocity of 13.9 m/s. These results are compared with value given in reference [8]. It can be seen that evaluated fracture toughness are closely matching with the value presented in reference [8].

It should be noted that, more experiments were performed on different launch pressures, in conjunction with high speed (DIC) methods, results of the analysis will be reported in the journal article.

3.5 Conclusions

1. Time of initiation of fracture (t_f) of three-point bend specimen as obtained by images analysis decreases from 40 μs to 30 μs with corresponding increase in velocity (from 12.7 m/s and 13.9 m/s).
2. The values of dynamic fracture toughness obtained in the study are 18.48 MPa$\sqrt{m}$ and 21.68 MPa$\sqrt{m}$ for velocities 12.7 m/s and 13.9 m/s respectively.
3. The dynamic fracture toughness increases from18.48 MPa$\sqrt{m}$ to 21.68 MPa$\sqrt{m}$, when velocity increases from 12.7 m/s and 13.9 m/s

References

1. Kumar, P.: Elments of Fracture Mechanics. Tata McGraw Hill, New Delhi (2004)
2. Anderson, T.L.: Fracture Mechanics: Fundamentals and Applications. CRC Press, Taylor & Francis Group, Boca, Raton, Florida (2005)
3. Kumar, S., Pandouria, A.K., Tiwari, V.: Evaluation of load and load point displacement through three point bend set up for dynamic loading. Int. J. Adv. Res. Innov. ISSN. **4**(1), 114–117 (2016)
4. Loya, J.A., Ferna, J.: Three-dimensional effects on the dynamic fracture determination of Al 7075-T651 using TPB specimens. Int. J. Solid Struct. **45**, 2203–2219 (2008)
5. Bacon, C., Farm, J., Latailade, J.L.: Dynamic Fracture Toughness Determined. (1), 217–223
6. Xing, M., Wang, Y., Jiang, Z.: Dynamic fracture behaviors of selected aluminum alloys under three-point bending. Def. Technol. **9**(4), 193–200 (2013)
7. ASM Material Data Sheet ASM Aerospace Specification Metal Inc.Aluminium7075-T651
8. Rubio, L., Fernández-Sáez, J., Navarro, C.: Determination of dynamic fracture-initiation toughness using three-point bending tests in a modified Hopkinson pressure bar. Exp. Mech. **43**(4), 379–386 (2003)

Chapter 4
Failure Testing Under In-Plane Biaxial Tension and Out-of-Plane Compression

Nathan Spulak, Robert Lowe, Jeremy Seidt, and Amos Gilat

Abstract The deformation and failure behavior of 2024 aluminum was investigated under combined in-plane equi-biaxial tension and out-of-plane compression. This loading configuration yields stress states of Lode parameter = −1 and triaxialities ranging from −0.67 to 0.17. Testing was performed using a variation of the standard ASTM quasi-static hemispherical punch test, with a reduced punch diameter and the addition of an annealed copper backing plate behind the specimen. The reported stress states at the failure point were then determined numerically using LS-DYNA.

Keywords Ductile failure · Lode parameter · Triaxiality · DIC · Failure strain

4.1 Introduction

Simulations of normal impact of ballistic projectiles onto flat plates have revealed that failure initiates in locations where the Lode parameter is equal to −1 [1]. A physical loading condition that results in such a Lode parameter is in-plane, equi-biaxial tension and out-of-plane compression [1]. By varying the ratio of out-of-plane compression to in-plane tension, different values for the triaxiality can be achieved [1]. Triaxiality, σ^*, and Lode parameter, μ, are defined by:

$$\sigma^* = \frac{p}{\sigma_{vm}}, \tag{4.1}$$

$$\mu = \frac{27}{2}\frac{J_3}{\sigma_{vm}^3}, \tag{4.2}$$

where $p = -\frac{1}{3}(\sigma_1 + \sigma_2 + \sigma_3)$ is the hydrostatic pressure and σ_1, σ_2, and σ_3 are the three principal stresses, σ_{vm} is the von Mises stress, and J_3 is the third invariant of the deviatoric stress tensor.

In order to achieve a state of in-plane, equi-biaxial tension, testing was done using several modifications of ASTM standard E643 for quasi-static punch testing of sheet metals [2]. First, a punch with a reduced diameter was used in order to minimize the effects of the boundary conditions on the deformation of the thin disk-shaped specimen and also to initiate failure as close to the center of the deformed specimen as possible, where equi-biaxial in-plane tension is actually experienced [1]. In addition, a backing plate of annealed copper was added behind the specimen to add out-of-plane compression for some tests [1]. Digital Image Correlation (DIC) was used to track the displacements and strains on the rear surface of the specimen and the copper backing plate.

4.2 Experimental Testing Setup

Testing under three different conditions was performed on 2024 aluminum specimens, as outlined in Table 4.1 below.

N. Spulak (✉) · J. Seidt · A. Gilat
Department of Mechanical and Aerospace Engineering, The Ohio State University, Columbus, OH, USA
e-mail: spulak.1@osu.edu

R. Lowe
Department of Mechanical and Aerospace Engineering, University of Dayton, Dayton, OH, USA

J. Carroll et al. (eds.), *Fracture, Fatigue, Failure and Damage Evolution, Volume 6*, Conference Proceedings of the Society for Experimental Mechanics Series, https://doi.org/10.1007/978-3-319-95879-8_4

Table 4.1 Overview of geometries and dimensions for small diameter punch tests

Case	Specimen Thickness (mm)	Backing Plate Thickness (mm)	Punch Diam. (mm)	Die Diam. (mm)
Unbacked	1.27	N/A	2.3	50.8
Backed thin	0.635	1.27	2.3	28.575
Backed thick	0.635	2.54	1.6	28.575

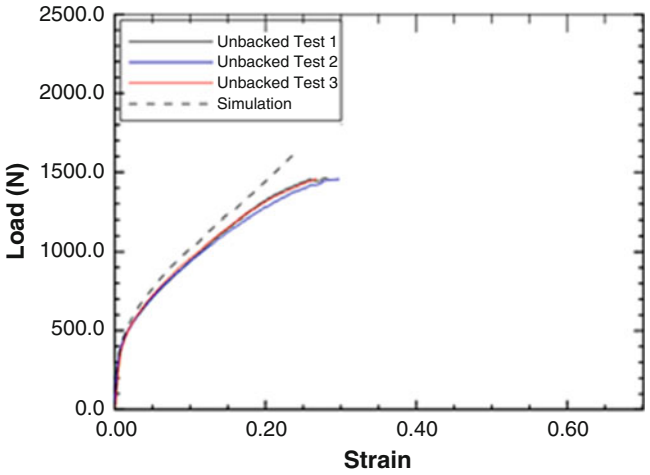

Fig. 4.1 Load vs maximum principal strain curves for the unbacked test case

For the unbacked tests, a speckle pattern was applied onto the rear surface of the specimen using black and white spray paint, and images for 3D-DIC analysis were taken as the loading was applied. For the backed tests, the copper backing plate did not allow a direct optical path to the specimen surface for the use of DIC on the actual specimen. However, DIC was still used on the copper backing plate, so that the displacement and strain of the backing plate could be compared to finite element simulations in LS-DYNA.

4.3 Results

The maximum principal strain measured by the DIC system at the point of maximum displacement and the corresponding load from the punch for the unbacked case are shown in Fig. 4.1, as well as the predicted curve from the finite element simulation. In addition, the load vs. punch stroke curves for each of the testing conditions and from the simulations are shown in Fig. 4.2. Each testing condition was simulated in LS-DYNA using a tabulated Johnson-Cook material model for 2024 aluminum [3, 4] and a piecewise linear-plasticity material model for the annealed copper, with the post yield portion of the stress-strain curve defined by uniaxial tension test data for the specific batch of annealed copper used during testing.

The simulations were able to predict the load and corresponding strain with reasonable accuracy for the unbacked test. The simulations were also able to predict the load vs. punch stroke for each of the testing conditions up until the point of element failure and erosion in the simulations. It is interesting to note that while the simulation correctly predicted the initial failure point in the unbacked case, the simulations prematurely predict the initiation of failure in the backed thick and backed thin cases. However, up until the point of element failure and erosion in the simulations, the simulation curves agree well with the test data. Therefore it can be expected that the calculated Lode parameter and triaxiality values from the simulations are accurate as well up until that point. The average Lode parameter was found to be -1 for all of the testing conditions and the average triaxiality was found to be -0.67, -0.20, and 0.17 for the unbacked, backed thin, and backed thick cases respectively.

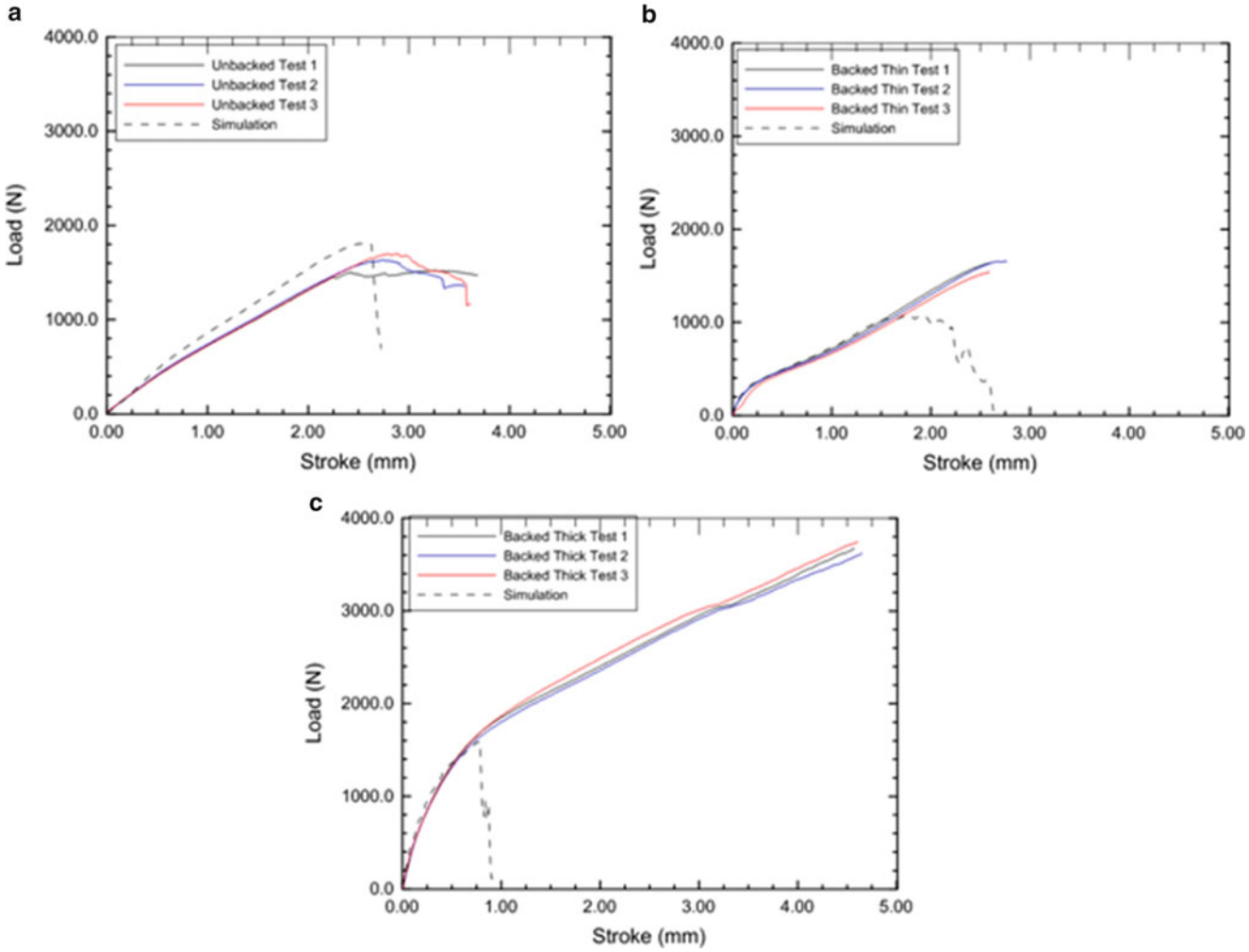

Fig. 4.2 Comparison of load vs. punch stroke curves from the tests and simulation for (**a**) unbacked, (**b**) backed thin, and (**c**) backed thick cases

4.4 Conclusions

The modifications of the ASTM quasi-static hemispherical punch test, by using a small diameter punch and the addition of a backing plate, were able to successfully achieve stress states with $\mu = -1$ and σ^* of -0.67, -0.20, and 0.17. The transition of σ^* from positive to negative indicates that the stress state transitioned from tension-dominated ($\sigma^* < 0$) in the unbacked and backed thin tests to compression-dominated ($\sigma^* > 0$) in the thickly backed tests.

References

1. Lowe, R.L., Seidt, J.D., Gilat, A.: Characterization of the Lode=−1 Meridian on the Al-2024 Failure Surface for *MAT_224 in LS-DYNA®. 14th International LS-DYNA Users Conference, 2016
2. ASTM E643-15 Standard Test Method for Ball Punch Deformation of Metallic Sheet Material, ASTM International, West Conshohocken, PA, 2015
3. Seidt, J.D.: Plastic Deformation and Ductile Fracture of 2024-T351 Aluminum under Various Loading Conditions, Ph.D. Thesis, The Ohio State University, 2010
4. Buyuk, M.: Development of a Tabulated Thermo-Viscoplastic Material Model with Regularized Failure for Dynamic Ductile Failure Prediction of Structures under Impact Loading, Ph.D. Thesis, The George Washington University, 2013

Chapter 5
An Experimental Method to Induce and Measure Crack Propagation in Brittle Polymers with Heterogeneities

Kimberley Mac Donald and Guruswami Ravichandran

Abstract Facture mechanics of heterogeneous brittle solids is a field of active research due to the recent developments in additive manufacturing to fabricate components with complex engineered microstructures. The majority of experimental work in crack propagation uses data from a single plane, usually on free surfaces, to measure the displacement field around the crack and the crack tip location. These measurements are used to determine the crack tip fields and fracture toughness which provides insights about the failure of a material. However, it is well known from three dimensional theory and experiments that the crack front shape and stress distribution is not constant through the thickness of a specimen. When toughening heterogeneities are added to a material, the theories and mechanics become significantly more complex. To better understand these stresses and shapes for both homogeneous and heterogeneous materials, an experimental method has been developed to induce steady-state crack propagation in thin, brittle hydrogel polymers. A microfilament needle inserted into the specimens allows for fluid to enter the crack and exert pressure on the crack surface, which effectively wedges the crack open. Distributed fluorescent microspheres serve as a speckle pattern for Digital Volume Correlation (DVC) of volumetric images captured using confocal microscopy. The DVC displacement field allows for determination of the 3D crack tip fields. This study seeks to provide an enhanced understanding of the three dimensional nature of crack interactions with heterogeneities and renucleation events, which can significantly improve our ability to design material toughness.

Keywords Confocal microscopy · Digital Volume Correlation (DVC) · Fracture mechanics · Heterogeneities · Soft polymers

5.1 Introduction

Image correlation methods such as Digital Image Correlation (DIC) and Digital Volume Correlation (DVC) have been widely used in solid mechanics experiments. Typically, a speckle pattern is painted on a flat, external surface, inherently limiting analysis to a single plane. Some studies have used a speckle pattern on an internal plane to better understand subsurface deformations in optically transparent materials [1]. In many continuum mechanics problems, planar data is useful because we can make assumptions of plane stress or plane strain. However, for more complex mechanics or geometries this limits experimental design to 2D approximations of 3D mechanisms. In fracture mechanics it is known that the crack length and stress distribution around the crack front vary over the specimen thickness which cannot be fully captured with analysis limited to a single plane [2, 3]. When heterogeneities are added to a material, crack fields and paths are significantly altered producing a toughening effect which has been demonstrated in many experiments including tape peeling 1D adhesion toughening, additively manufactured 2D toughening, and micro- and nanosphere 3D toughening effects [4–6]. Design of tougher materials with engineered heterogeneities requires a better understanding of the nucleation effects and stress fields around and between inclusions which has not been well demonstrated in experiments. DVC can be used to measure crack fields in 3D using a detectable 3D speckle pattern such as fluorescent microspheres distributed throughout a soft gel and imaged using confocal microscopy [7, 8]. Due to their brittleness, soft gels such as agarose have also been used to study fracture mechanics. A series of experiments on capillary fracture suggest that a crack may be driven in a soft gel by fluid pressure [9].

In this study, we develop an experimental method to induce steadily propagating cracks and measure their propagation and crack tip fields. First the specimens and experiments are described. Then a summary of preliminary results for a homogeneous gel specimen are presented. Specimens with heterogeneities such as spherical inclusions of softer or stiffer gels will be used to

K. Mac Donald (✉) · G. Ravichandran
Division of Engineering and Applied Science, California Institute of Technology, Pasadena, CA, USA
e-mail: kmacdonald@caltech.edu

J. Carroll et al. (eds.), *Fracture, Fatigue, Failure and Damage Evolution, Volume 6*, Conference Proceedings of the Society for Experimental Mechanics Series, https://doi.org/10.1007/978-3-319-95879-8_5

study the three dimensional nature of crack interactions with heterogeneities and renucleation events, which can significantly enhanced understanding of fracture mechanics while improving our ability to design material toughness.

5.2 Materials and Methods

5.2.1 Specimens

Thin polyacrylamide copolymer specimens are manufactured by casting several drops of monomer solution between two 25 mm diameter circular no. 1 glass coverslips. The monomer solution contains 0.263 ml ACRYL/BIS™ 19:1 40% solution (AMRESCO®), 0.010 ml ammonium persulfate 10% w/v solution (APS, AMRESCO®) as a source of free radicals, 0.727 ml deionized water, less the volume of fluorescent microsphere solution used to produce the volumetric speckle pattern, and 0.002 ml tetramethylethylenediamine (TEMED, Alfa-Aesar®) as a polymerization catalyst. In this study, 0.100 ml of a 2% solids aqueous solution of 2.0 µm carboxylate modified polystyrene FluoSpheres® (red, 580 nm peak excitation, 605 nm peak emission, Molecular Probes™) are used. The total volume of the monomer solution prior to adding the catalyst is 1.000 ml. An 18 gage luer stub is used to deposit 15 drops of the catalyzed monomer solution onto a glass coverslip and a second cover slip is carefully dropped on top to spread the solution and produce a sufficiently thin specimen for imaging. Once the disc has polymerized for at least 1 h it is submerged in deionized water and allowed to swell to equilibrium.

5.2.2 Experimental Design

An initial crack is introduced to the gel discs by carefully inserting a 28 gauge MicroFil needle (World Precision Instruments) into the side of the specimen and then pulling it slightly out. A successful crack is shown in Fig. 5.1a where the MicroFil outer diameter of 350 µm is approximately the same as the specimen thickness. Figure 5.1b shows a diagram of a specimen where glycerol is pumped into the crack through the MicroFil needle to drive the crack while confocal images are taken using a Zeiss LSM 800 laser scanning confocal microscope.

5.3 Preliminary Results

An initial study demonstrating our ability to induce and analyze a crack as it propagates uses 2D DIC confocal images of an internal plane of the gel disc is presented in what follows. Figure 5.2a shows a representative speckle pattern for a single frame as the crack propagates. The crack tip shape is approximately parabolic as shown by the green curve fitted to the crack edges. Further analysis of the crack shape will allow us to approximate fracture properties of the gel. DIC analysis is completed using an iterative code developed by Bar-Kochba, et al. [10]. The displacement results for an image pair are shown in Fig. 5.2b.

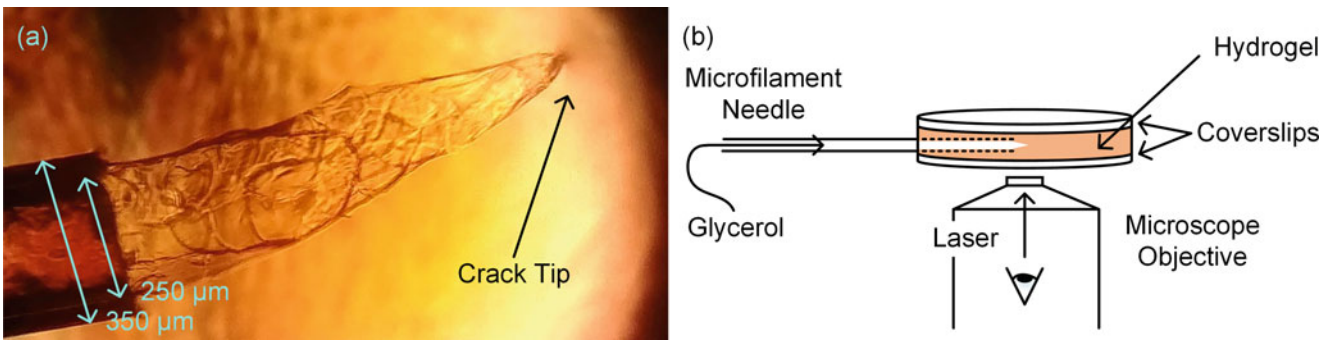

Fig. 5.1 Experimental design including (**a**) a wide-field microscopy image of a crack introduced to a hydrogel specimen using water injected through a 28 gauge MicroFil needle and (**b**) a diagram of a hydrogel specimen cast between two glass coverslips with a 28 gage microfilament needle used to inject glycerol into the crack and drive propagation

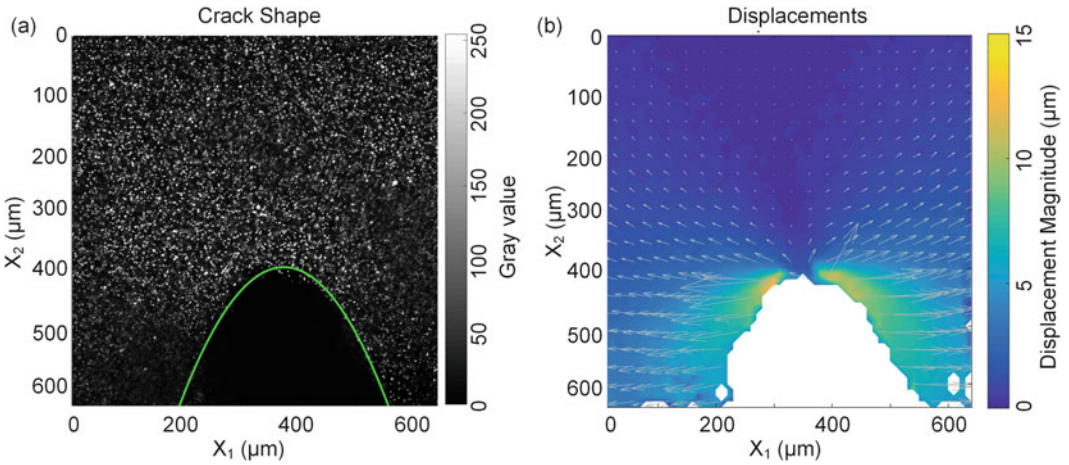

Fig. 5.2 (**a**) Confocal microscopy image of a propagating crack showing a fitted parabolic crack-tip shape (green) and (**b**) the displacement field for an image pair determined using DIC

As expected, there are significantly higher displacements behind the crack tip and near zero displacements ahead of it which indicates that we are able to detect concentrations near the crack tip.

Acknowledgements This material is based upon work supported by the National Science Foundation Graduate Research Fellowship Grant No. DGE-1144469 and Designing Materials to Revolutionize and Engineer our Future (DMREF) Award No. DMS-1535083. Imaging was performed in the Biological Imaging Facility, with the support of the Caltech Beckman Institute and the Arnold and Mabel Beckman Foundation.

References

1. Berfield, T., Patel, J., Shimmin, R., Braun, P., Lambros, J., Sottos, N.: Micro- and nanoscale deformation measurement of surface and internal planes via digital image correlation. Exp. Mech. **47**(1), 51–62 (2007)
2. Cooke, M., Pollard, D.: Fracture propagation paths under mixed mode loading within rectangular blocks of polymethyl methacrylate. J. Geophys. Res. Solid Earth. **101**(B2), 3387–3400 (1996)
3. Broek, D.: Elementary Engineering Fracture Mechanics, 1st edn. Springer, Dordrecht (1982)
4. Xia, S., Ponson, L., Ravichandran, G., Bhattacharya, K.: Toughening and asymmetry in peeling of heterogeneous adhesives. Phys. Rev. Lett. **108**, 196101 (2012)
5. Wang, N., Xia, S.: Cohesive fracture of elastically heterogeneous materials: an integrative modeling and experimental study. J. Mech. Phys. Solids. **98**, 87–105 (2017)
6. Hutchinson, J.: Mechanisms of toughening in ceramics. In: Germain, P., Piau, M., Caillerie, D. (eds.) Theoretical and Applied Mechanics, pp. 139–144. Elsevier, Amsterdam (1989)
7. Sutton, M., Orteu, J., Schreier, H.: Image correlation for shape, motion and deformation measurements: basic concepts, theory and applications, 1st edn. Springer US, New York (2009)
8. Franck, C., Hong, S., Maskarinec, S., Tirrell, D., Ravichandran, G.: Three-dimensional full-field measurements of large deformations in soft materials using confocal microscopy and digital volume correlation. Exp. Mech. **47**(3), 427–438 (2007)
9. Bostwick, J., Daniels, K.: Capillary fracture in soft gels. Physical Review Letters E. **88**(4), 042410 (2013)
10. Bar-Kochba, E., Toyjanova, J., Andrews, E., Kim, K., Franck, C.: A fast iterative digital volume correlation algorithm for large deformations. Exp. Mech. **55**(1), 261–274 (2015)

Chapter 6
The Sandia Fracture Challenge: How Ductile Failure Predictions Fare

Sharlotte Kramer, Brad Boyce, Amanda Jones, Jhana Gearhart, and Brad Salzbrenner

Abstract The Sandia Fracture Challenges provide the mechanics community a forum for assessing its ability to predict ductile fracture through a blind, round-robin format where computationalists are asked to predict the deformation and failure of an arbitrary geometry given experimental calibration data. This presentation will cover the three Sandia Fracture Challenges, with emphasis on the third. The third Challenge, issued in 2017, consisted of an additively manufactured 316L stainless steel tensile bar with through holes and internal cavities that could not have been conventionally machined. The volunteer prediction teams were provided extensive materials data from tensile tests of specimens printed on the same build tray to electron backscatter diffraction microstructural maps and micro-computed tomography scans of the Challenge geometry. The teams were asked a variety of questions, including predictions of variability in the resulting fracture response, as the basis for assessment of their predictive capabilities. This presentation will describe the Challenges and compare the experimental results to the predictions, identifying gaps in capabilities, both experimentally and computationally, to inform future investments. The Sandia Fracture Challenge has evolved into the Structural Reliability Partnership, where researchers will create several blind challenges covering a wider variety of topics in structural reliability. This presentation will also describe this new venture.

Keywords Ductile fracture · Blind prediction · Validation · Computational modeling

6.1 Introduction

Computational solid mechanics models are required to predict ever increasingly complex deformation and failure of structures in extreme environments. One way to build confidence in these predictions is to challenge the computational approaches with validation scenarios that can be experimentally tested for comparison. The Sandia Fracture Challenges provide the mechanics community a forum for assessing its ability to predict ductile fracture through a blind, round-robin format where computationalists are asked to predict the deformation and failure of an arbitrary geometry given experimental calibration data. These challenges were designed to (1) assess the whole prediction stream, from experiments and calibration methods to the constitutive models and numerical methods; (2) replicate real-world engineering constraints including limited calibration data and time to predict; (3) test a relatively simple, but unfamiliar "toy" problem that captures the salient features of real-world problems; (4) allow for blind participation from several computational groups with different approaches; (5) verify experimental outcomes in more than one laboratory to reduce experimental bias; and (6) use the post-blind assessment to inspire improvements. This paper overviews the three Sandia Fracture Challenges to date, with emphasis on the third, describing the Challenges, comparing the experimental results to the predictions, and identifying gaps in capabilities, both experimentally and computationally, to inform future investments. The Sandia Fracture Challenge has evolved into the Structural Reliability Partnership, where researchers will create several blind challenges covering a wider variety of topics in structural reliability. This presentation will also describe this new venture.

S. Kramer · B. Boyce · A. Jones (✉) · J. Gearhart · B. Salzbrenner
Sandia National Laboratories, Albuquerque, NM, USA
e-mail: ajones1@sandia.gov

J. Carroll et al. (eds.), *Fracture, Fatigue, Failure and Damage Evolution, Volume 6*, Conference Proceedings of the Society for Experimental Mechanics Series, https://doi.org/10.1007/978-3-319-95879-8_6

6.2 The First and Second Sandia Fracture Challenges

The first Sandia Fracture Challenge (SFC1) in 2012 was the first of its kind to provide a forum for candidly comparing different ductile failure prediction capabilities in the larger mechanics community. Here is a brief description of SFC1; a more detailed explanation can be found in a special issue of the *International Journal of Fracture* [1]. The thirteen participating teams predicted the initiation and propagation of a crack in a ductile structural stainless steel, 15-5 PH, under quasi-static room temperature test conditions. The SFC1 specimens were flat plates with a round root pre-cut slot and multiple holes influencing the crack-tip stress state. The participants were given tensile test data, sharp crack Mode-I fracture data, and some limited microstructural information. Three different experimental testing laboratories observed two different crack paths: a tensile-dominated or shear-dominated failure mode. The post-blind assessment of both experiments and computations revealed that variation in hole location led to the two different failure modes, where the out-of-tolerance geometry favored a shear-ligament crack path and the nominal geometry favored a tensile-ligament crack path. The teams expressed a desire for other calibration data in future challenges, in particular shear-dominated loading experimental data.

The second Sandia Fracture Challenge (SFC2) in 2014 focused on ductile fracture in different loading rate environments since many engineering scenarios with ductile fracture involve loading outside the quasi-static regime. Again, here is a short description of SFC2, and more details can be found in a special issue of the *International Journal of Fracture* [2]. SFC2 considered a rate-dependent titanium alloy, Ti-6Al-4V, in sheet form with an unusual set of notches and holes that fostered a competition between tensile- and shear-dominated failure modes. Specimens were tested at two different loading rates, quasi-static and a modest-rate dynamic loading (failure in ~0.1 s). Fourteen teams predicted the fracture path and quantitative far-field metrics including peak load and displacement at crack initiation, and as well as uncertainty bounds on their predictions. The teams were given measurements of the actual SFC2 geometry specimens, not just engineering drawings with tolerances as were provided in SFC1, and calibration data from standard tensile dogbone tests and modified V-notch shear tests, originally designed for testing shear in composites. The SFC2 geometry specimens were tested in three independent laboratories, observing the prevalent failure mode being the shear-dominated crack path and significant differences in the load-displacement behavior for the two different loading rates. In general, the prediction teams had more agreement with the overall far-field load-displacement data than for SFC1, which was attributed to more calibration data and experience gained from SFC1. However, the post-blind assessment revealed several shortcomings in the predictions including inconsistency in the application of appropriate boundary conditions, need for a thermomechanical treatment of the heat generation in the dynamic loading condition, and further difficulties in model calibration based on limited real-world engineering data. Despite being given material and geometric variability data, few teams provided uncertainty bounds on their predictions, showing a lack of experience in robust uncertainty quantification, particularly in limited-time-to-predict scenarios.

6.3 The Third Sandia Fracture Challenge

The third Sandia Fracture Challenge (SFC3), issued in 2016, asked the computational mechanics community to predict ductile fracture in an additively manufactured (AM) structure. AM is a rapidly growing fabrication process that poses many challenges for the engineering community. Many mechanics questions arise from a class of materials with generally more heterogeneity and variability than traditionally formed materials. The SFC3 geometry was an AM 316 L stainless steel tensile bar with through holes and internal cavities that could not have been conventionally machined, as shown in Fig. 6.1, going beyond our previous Challenges that were based on extruded 2D features. The prediction teams were provided extensive materials data from tensile and notched tensile tests of specimens printed on the same build tray to electron backscatter diffraction microstructural maps and micro-computed tomography (micro-CT) scans of the SFC3 geometry specimens (Fig. 6.1c, d). Unlike previous Challenges, SFC3 took advantage of better experimental metrology, namely Digital Image Correlation (DIC), to measure surface field displacements and strains (Fig. 6.1e) for comparison to models. The teams had to predict far-field and local quantities of interest, including predictions of variability in the resulting fracture response.

Two independent laboratories tested nineteen specimens that all cracked beginning at the edge of the central through-hole, emanating out along the angled channels. These specimens had relatively modest bounds in load-displacement behavior (see black lines in Fig. 6.2a for the 20th percentile, average, and 80th percentile responses) with more variability in the surface strain response of the AM structure (see Fig. 6.2b). Twenty-one predictions were submitted from fourteen institutions; the

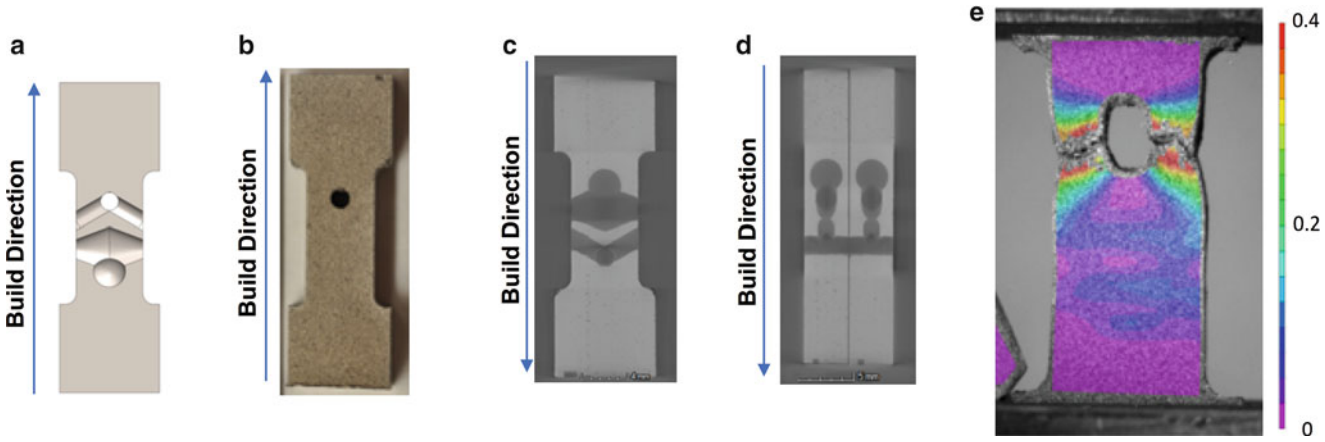

Fig. 6.1 SFC3 Geometry Specimens: (**a**) Schematic of central cross section, revealing the internal cavities; (**b**) image of front surface with AM finish; (**c**) micro-CT scan "thick slab" view of Specimen A32 (front perspective) that essentially sums the data to show all the void and internal feature content (high contrast) through the central section of the specimens; (**d**) micro-CT scan "thick slab" view of Specimens A32 [left] and A15 [right] (side perspective); (**e**) DIC Hencky (logarithmic) vertical tensile strain field immediately after failure of Specimen A23, showing failure along the angled channels and through-hole

load-displacement data (far-field quantity of interest) are in Fig. 6.2a, and one example of a line-scan of the surface vertical strains (a local quantity of interest) is in Fig. 6.2b for all the teams and experiments. The post-blind assessment is currently underway; SFC3 will be fully documented in an upcoming special issue of the *International Journal of Fracture*. Here are some preliminary observations and comments regarding the SFC3 results. Unlike previous Challenges, all the teams predicted the correct crack path. The teams generally fared well when comparing to far-field quantities of interest, with two teams (B and Q) predicting a nominal load-displacement behavior within the bounds of the experimental data. The predictions of local surface strain measures tended to over-predict strains early in the deformation and then under-predict towards failure; also, experimental strain measurements tended to have larger variation than predicted. The teams took vastly different approaches to predict uncertainty bounds in their models, and there was not a straightforward, standard method to quantify those bounds for curve-type measures from the experiments. Surprisingly few teams considered the geometric variation and pore structure characteristics of AM metals, despite considerable data provided to aid that effort. There were examples of clear mis-interpretations of the questions, and the post-blind assessment revealed several clerical errors in the predictions. Both of these types of mistakes are not uncommon in real engineering environments. SFC3 overall showed improved ductile fracture capabilities, particularly from teams with experience in previous Challenges, but also revealed a need for deep conversations on how computationalists should peer-review their work and quantify uncertainties.

6.4 The Future of Blind Assessment of Structural Reliability Mechanics Predictions

The two special issues of the *International Journal of Fracture* for the first two Sandia Fracture Challenges [1, 2] have been the most downloaded articles for that journal, demonstrating the vast impact these challenges have had to raise awareness in the mechanics community about the state-of-the-art in ductile fracture predictions. We anticipate such enthusiasm for SFC3, particularly because of the AM aspect. The three Sandia Fracture Challenges have spurred the formation of the Structural Reliability Partnership (SRP), spearheaded by Sandia National Laboratories, Exxon Mobil, and the University of Texas at Austin. The purpose of the SRP is to coordinate research, share best practices, and leverage investments from multiple institutions on areas of mutual interest in the domain of structural reliability. The SRP will coordinate staggered blind assessment Challenges in many different topics of structural reliability, with shared focus materials that facilitate cross-institution comparisons, knowledge transfer on "best practices", and leveraging of cross-institutional R&D investments to address shortcomings and gaps in structural reliability experiments and predictions.

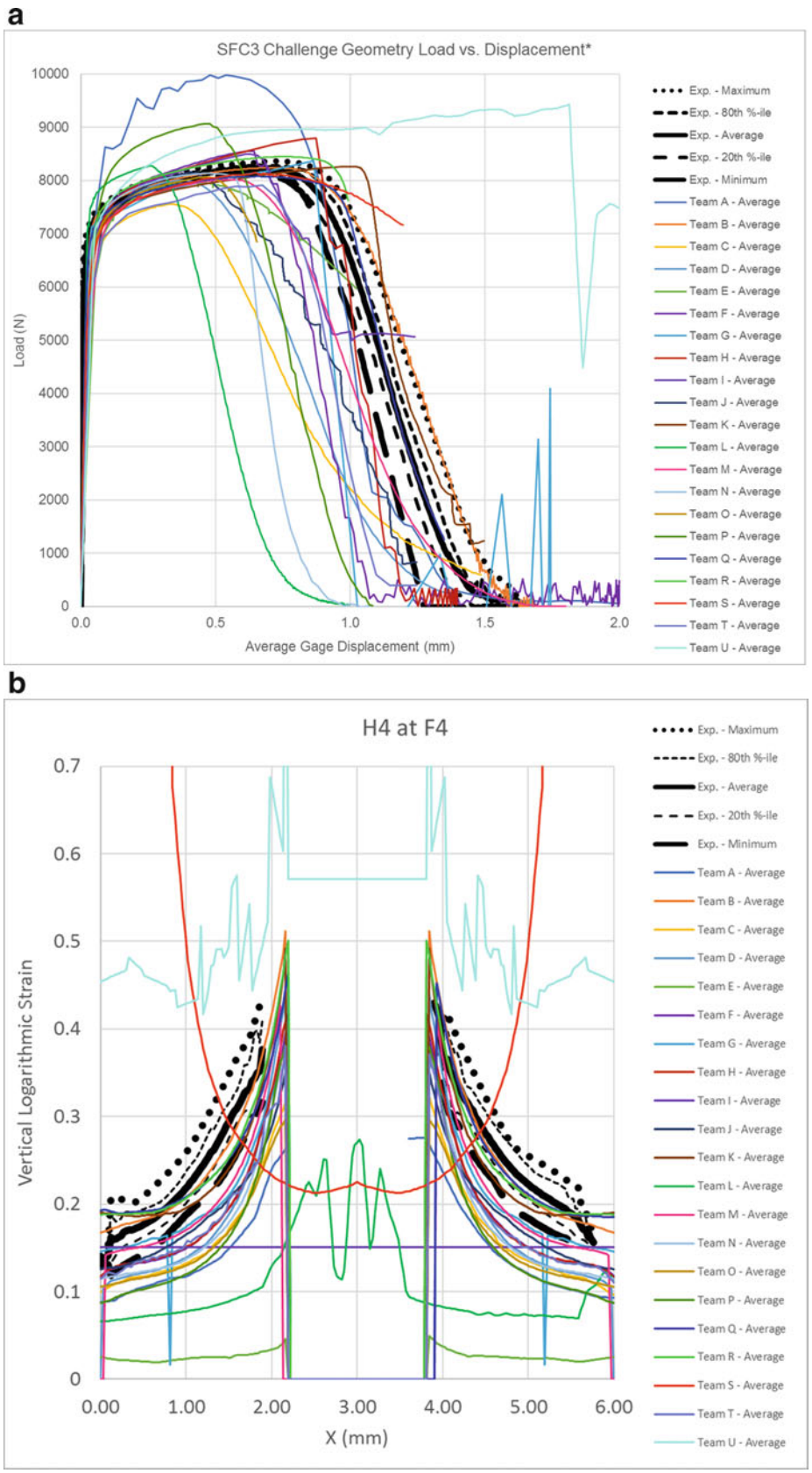

Fig. 6.2 Comparison of Experimental (Black) and Average Computational (Colors) Results with Experimental 20th and 80th percentile Bounds: (**a**) Load-displacement data and (**b**) surface vertical Hencky (logarithmic) strain across the horizontal line intersecting the center of the through-hole (called H4) at the load at 90% of peak load (called F4)

Acknowledgements Sandia National Laboratories is a multi-mission laboratory managed and operated by National Technology and Engineering Solutions of Sandia, LLC., a wholly owned subsidiary of Honeywell International, Inc., for the U.S. Department of Energy's National Nuclear Security Administration under contract DE-NA-0003525.

References

1. Boyce, B.L., Kramer, S.L.B., et al.: The Sandia Fracture Challenge: blind round robin predictions of ductile tearing. Int. J. Fract. **186**, 5–68 (2014)
2. Boyce, B.L., Kramer, S.L.B., et al.: The Second Sandia Fracture Challenge: predictions of ductile failure under quasi-static and moderate-rate dynamic loading. Int. J. Fract. **198**, 5–100 (2016)

Chapter 7
Characterization and Modeling of Low Modulus Composite Patched Aluminum Center Crack Tension Specimen Using DIC Surface Displacements

Daniel C. Hart and Hugh A. Bruck

Abstract Composite patch repairs of aluminum structures used in marine and aerospace industries are designed using closed form solutions assuming thin, plane stress, linear-elastic structures or numerical methods for repairs of thick aluminum. Both methods are based on linear elastic fracture mechanics and compare crack tip predictions to a critical strain energy release rate or stress intensity. Analytical and numerical predictions are reasonable for linear-elastic behavior, but these methods do not account for elastic-plastic behavior at the crack tip that initiates above the linear-elastic limit and continues until the ultimate load. This research used digital image correlation and finite element analysis to study the full field displacement and J-integral ahead of the crack tip for un-patched and patched center crack tension specimens loaded monotonically to failure. Free surface crack tip strain and J-integral behavior remained an intrinsic property of the aluminum directly related to the crack opening displacement (COD) and were independent of one sided composite patch reinforcement. However, the crack tip bending deformations induced by the patch reinforcement increased the COD by 20% over the un-patched behavior after patch failure, most likely due to observed changes in the formation of the plastic zone ahead of the crack. Comparison of test results and analytical predications indicated a significant difference between linear elastic and elastic plastic predictions beyond the linear-elastic limit highlighting the need to utilize elastic plastic fracture mechanics and the J-integral to optimize composite patched center crack tension specimens for ultimate load.

Keywords Composite patch · Aluminum · Digital image correlation · J-integral · Center crack tension

7.1 Introduction

The foundation of bonded joint design started in the late 30's and 40's with the governing differential equations for an explicit adhesive layer [1, 2], and later advanced when Hart-Smith added inelastic behavior of that adhesive layer [3, 4]. In application, the development of aircraft patch repairs continued through a combination of mechanical characterization protocols, development of appropriate design methods based on using the governing equations with mechanical characterization data, and enhancement of analysis efforts [5–9] by incorporating linear elastic fracture mechanics (LEFM) to calculate strain energy release rate (SERR) or stress intensity (K) at the metallic crack tip. When designing composite patch repairs for aluminum, using LEFM results in a conservative design. As the thickness of the repaired plate increases and the loading increases, the failure mechanisms and energies not captured by the existing analyses begin to play significant roles in the ultimate in-plane static tensile load capacity of the repaired region. From the initial research into 2D bonded joints, it was assumed the dominant energy dissipation mechanism was the plastic deformation of the adhesive layer. When extending the design approach for 2D joints to include the crack tip of composite patched aluminum repairs, Wang and Rose utilized a distribution of springs to represent the adhesive and plate theory for the in a linear elastic energy balance for a bending deformation analysis in order to predict crack tip stress intensity using Rose's model [10]. Advancements in computational algorithms, particularly Finite Element Analysis techniques such as Virtual Crack Closure, simplified development of numerical analysis approaches [11–13]. However, neither the analytical or numerical methods incorporated elastic-plastic aluminum behavior at the crack tip in design.

D. C. Hart (✉)
Naval Surface Warfare Center, Carderock Division, West Bethesda, MD, USA
e-mail: daniel.c.hart@navy.mil

H. A. Bruck
University of Maryland Mechanical Engineering Department, College Park, MD, USA

J. Carroll et al. (eds.), *Fracture, Fatigue, Failure and Damage Evolution, Volume 6*, Conference Proceedings of the Society for Experimental Mechanics Series, https://doi.org/10.1007/978-3-319-95879-8_7

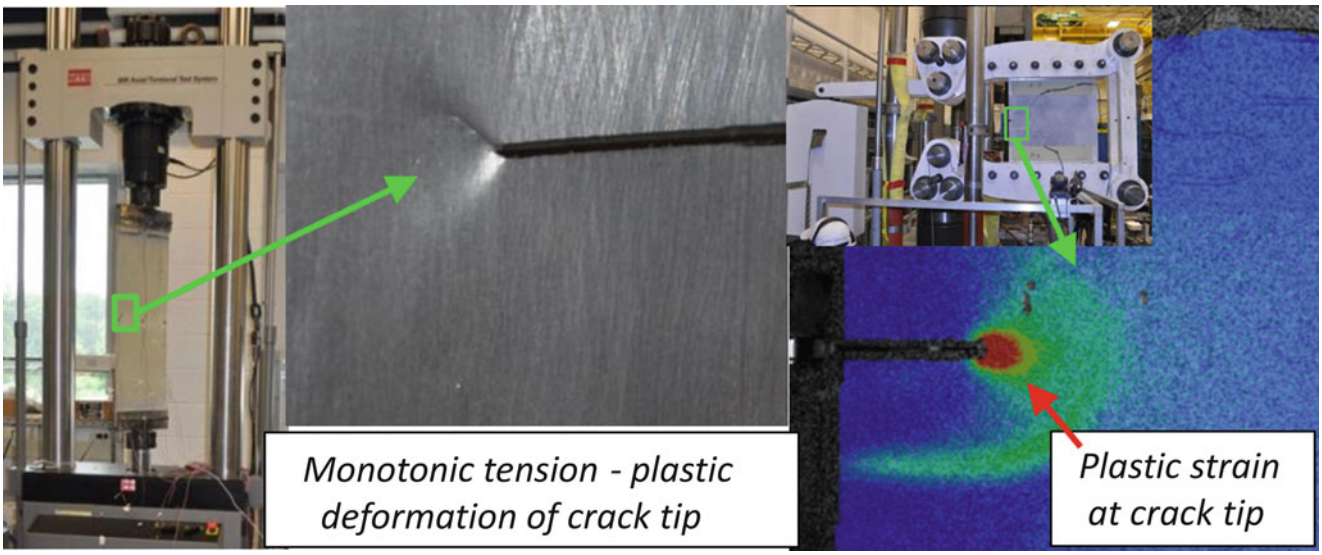

Fig. 7.1 Plastic zone on free surface of large scale patched CCT (L) and ductile tearing (R) specimens

Recent testing of low modulus composite patches on center crack tension (CCT) specimens and a large scale ductile tearing specimen [14–16] have demonstrated significantly more monotonic load capacity of composite patched specimens than un-patched specimens. One of the common failure mechanisms observed which had not been accounted for was significant plastic deformation of the aluminum ahead of the crack tip. Large scale testing of one sided patched aluminum specimens, shown in Fig. 7.1, has shown that the elastic-plastic crack tip behavior occurs before ultimate failure with each patched specimen achieving higher load capacity and greater displacement capacity at failure [11, 14]. The J-integral method developed by Hutchinson, Rice, and Rosengren [17–19] established a measure of the non-linear behavior of the strain energy release rate for ductile metals. To characterize this behavior, Digital Image Correlation (DIC) [20] has been utilized to measure full field surface displacements ahead of the crack tip required to calculate the J-integral value. Initially utilized for linear elastic material behavior [21, 22], inelastic material behavior measured on the surface can be included in the J-integral calculation [23–25]. Research in the plastic zone development under monotonic loading appears to be limited to typical fracture mechanics metallic specimens of a single material [26, 27].

In this paper the focus will be on the effect one sided adhesively bonded low modulus E-Glass/Epoxy composite patch has on development of the crack tip plastic zone and evolution of the J-integral value for cracked aluminum CCT specimens loaded monotonically in tension until failure. Full field 2D DIC data from the un-patched, free, aluminum surface and J-integral calculations will be compared with LEFM and elastic plastic fracture mechanics (LEFM) based J-integral calculations and finite element analysis (FEA) based predictions to improve our understanding of the effect one sided surface reinforcement has on crack tip material behavior. This research looked at the aluminum crack tip behavior and does not currently address non-linear behavior of the adhesive layer or failure of the composite adherend. Low modulus composite patches were selected based on current U.S. Navy use of composite patch repairs to address cracking in sensitized aluminum plate [11, 14, 28, 29].

7.2 J-Integral Using DIC

The foundation of this investigation is the ability to gather full field displacement data ahead of and around the crack tip using 2D DIC. Images of the applied speckle pattern are processed to correlate patterns of gray scale values in specific square subsets between the initial reference image and deformed images [20]. Behavior between the reference frame and each image is approximated by optimizing polynomial coefficients of shape functions such that the squared difference between the pixel subset gray scale values of the image and the assumed values based on the shape functions is minimized. These optimized shape functions can then be used to calculate the displacements and displacement gradients necessary to get the Lagrangian strains. Shape functions are used to get results at the centroid of the subset. Results are stored at each subset offset in the horizontal (U) and vertical (V) directions defined by the step size. For the data reported square subset size was 51 pixels

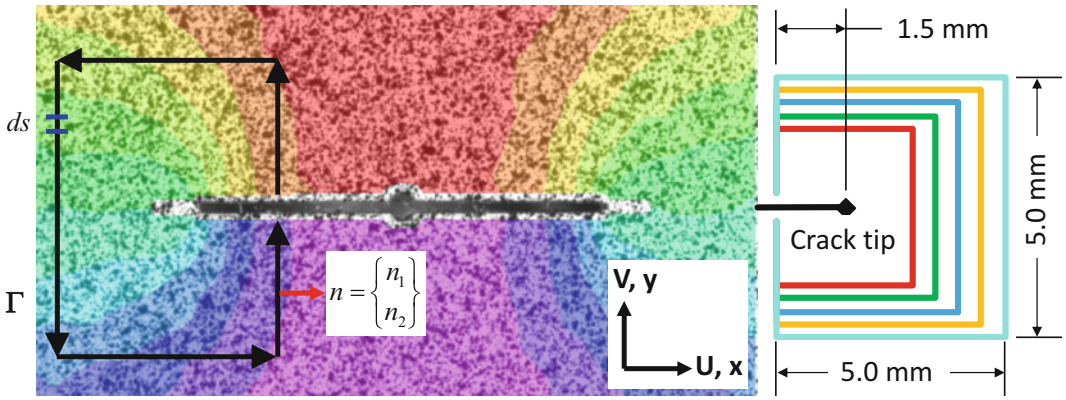

Fig. 7.2 Vertical displacement fields with J-integral path example

(0.35 mm) with results stored every 10 pixels (0.07 mm). Strain results were filtered across 41 data points and then smoothed using the center-weighted Gaussian filter. Processing was performed using the commercially available Correlated Solutions (Irmo, SC) software, Vic2D, and the images taken during the monotonic tensile loading of the CCT specimens. Vic2D output displacements, displacement gradients, and strains. DIC data is limited to one side of the CCT specimen for this test series and can only provide material behavior information directly at the surface. Images were captured with a monochromatic complimentary metal-oxide semiconductor (CMOS) sensor with 4096x2160 pixel resolution.

The J-integral is a path independent contour integral that describes the non-linear strain energy release rate for elastic-plastic materials. The formulation of J assumes a 2D state at the crack tip, in other words plane strain or plane stress. In the case of surface measurements one must assume plane stress for the infinitesimal slice of material at the surface with no ability to infer the stress-strain behavior through the thickness from those measurements. The J-integral developed by Hutchinson, Rice, and Rosengren is shown below:

$$J = \int_{\Gamma} \left(w dy - T_i \frac{\partial u_i}{\partial x} ds \right) = \int_{\Gamma} \left(\int_0^{\varepsilon_{ij}} \sigma_{ij} d\varepsilon_{ij} dy - \sigma_{ij} n_j \frac{\partial u_i}{\partial x} ds \right) \tag{7.1}$$

Here w is the strain energy density, T_i is the traction vector normal (n_j) to the path Γ with infinitesimal segments along that path (ds). Displacements (u_i) and strains (ε_{ij}) along the path and displacement data are located in xy space, such that i is associated with the x-direction and j is associated with the y-direction. From the DIC data processing U and V are in the x and y-directions respectively. Figure 7.2 shows the processed vertical displacement fields (V) with J-integral path variables. Five paths were evaluated about the crack tip. Each square path starts 1.5 mm behind the crack tip and vary from 3 mm to 5 mm.

Assuming, for data processing simplification, that the surface material along the path is outside the crack tip plastic zone and behaves linear elastically the J-integral equation can be derived as a function of material parameters and the displacement gradients along the path Γ measured by DIC. As reported by Bruck [21], the J-integral value for elastic material becomes:

$$J = \frac{G}{2} \int_{\Gamma} \left[\left\{ k_1 \left(\frac{\partial v}{\partial y} - \frac{\partial u}{\partial x} \right) \left(\frac{\partial u}{\partial x} + \frac{\partial v}{\partial y} \right) + \left(\frac{\partial u}{\partial y} + \frac{\partial v}{\partial x} \right) \left(\frac{\partial u}{\partial y} - \frac{\partial v}{\partial x} \right) \right\} dy + \left\{ 2 \left(\frac{\partial u \partial u}{\partial x \partial y} + k_2 \frac{\partial u \partial v}{\partial x \partial x} + k_1 \frac{\partial v \partial v}{\partial x \partial y} \right) \right\} dx \right] \tag{7.2}$$

Here the k_i values are defined, for plane stress, by the Poisson's ratio of the cracked material.

$$plane\ stress: k_1 = \frac{2}{1-\nu}, k_2 = \frac{1+\nu}{1-\nu} \tag{7.3}$$

7.3 Experimental Configuration

The test frame, DIC setup, typical speckle pattern, and specimen configuration are shown in Fig. 7.3. Small scale CCT specimen geometry was selected for manufacturing and testing convenience as well as maintaining a configuration link to the large scale testing performed by Hart et al. [11, 16]. Aluminum selected for the small scale CCT specimens was based on

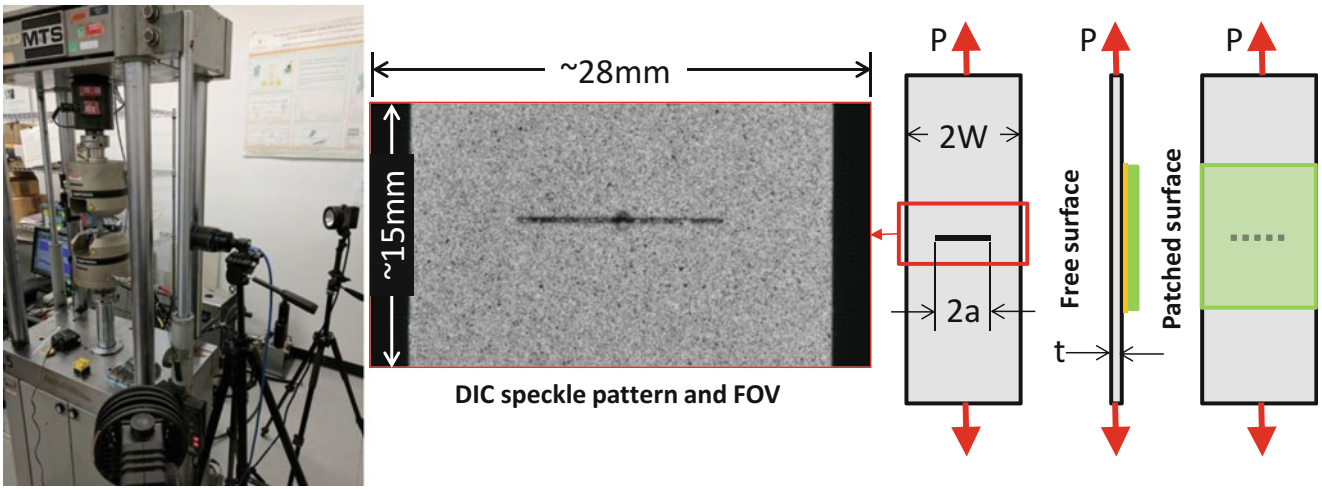

Fig. 7.3 Small scale CCT test frame and DIC configuration (L), FOV (C), and CCT specimen geometry (R)

readily available plate thickness that allowed a nominally 1/third scale from the large scale specimens. A marine grade 5052-H32 aluminum was selected at 2.29 mm (0.090 in. thick, the typical 6.35 mm (0.25in) 5456-H116 was not readily available at that thickness. Small scale CCT specimen blank plates were 24 mm wide (*2 W*) and 114 mm long with electrical discharge machined (EDM) notches nominally 12 mm wide and nominally 0.36 mm high. Cracks were then grown from the notch to develop sharp crack tips using high cycle low load tension-tension fatigue. To grow the cracks the load ratio was 0.1 for a tensile load that varied from 200-2000 N at 10 Hz. The resulting effective ΔK was nominally between 5.6 and 6.7 MPa-$\sqrt{m}$, which resulted in a nominal cycle count of 100 K to achieve crack growth of approximately 1 mm. With sharp crack tips and a crack length (2a) of 14 mm the specimens were paired by crack length and one of each pair received an adhesively bonded composite patch. Surface preparation involved an acetone wipe, light surface abrasion with 80 grit aluminum oxide sandpaper, another acetone wipe, and treatment with 3 M's AC-130-2 bonding agent. A commercially available marine adhesive, West Systems WestSix10, was selected for bonding the pre-fabricated 0/90 E-Glass epoxy laminate. The laminate had an average thickness of 1.27 mm (0.05 in. and was cut to 50 mm long by 24 mm wide. The composite patch was centered on the machined notch and bonded to the cracked aluminum plate with a nominally 0.6 mm thick bondline, which was controlled using 0.024 inch diameter steel welding wire.

Tensile testing was performed on a 20 kip 4-post hydraulic MTS frame with Instron hydraulic wedge grips and controls. Specimens were adapted to the wedge grips with temporarily bonded tabbing; the wedge grips had a minimum grip thickness of 7.8 mm and a 45 mm grip width. Care was taken to install the test specimens such that the edge was vertical to ensure the applied tensile load was perpendicular to the notch. Loading was applied at a rate of 0.18 mm/min until beyond the linear elastic response range when the non-linear load response slope stabilized in the crack blunting region. As crack blunting and plastic deformation began at the crack tip the load rate was doubled.

Images for DIC were taken using a Point Grey Flea FL3-U3-88S2C-C with a Tamron 28-80 mm f/3.5–22 lens resulting in a 28.2 mm $\times$ 14.9 mm overall field of view (FOV). Initial depth of field (DoF) was set such that the initial unloaded surface was at the extreme edge of focus. This provided enough DoF such that the surface remained in focus as load was applied and out of plane deflection decreased the distance between the specimen and the camera. The speckle pattern was achieved using a base of flat white spray paint with light passes of flat black spray paint. To achieve the smallest consistent speckles an improvised paint booth was fogged with black spray, then the specimen was placed in the space for the small floating paint particles to settle on the white surface. This process was repeated until sufficient gray scale information was present in the image. High contrast images were achieved using two evenly spaced 250 watt halogen spot lights; lights were equidistant from the grip bodies, equidistant to the camera body, and level with the camera body and specimen. During the linear elastic response range images were taken at 2 per second, as the response advanced into the crack blunting range the image rate was decreased then increased to the original speed prior to crack growth and failure.

7.4 Test Results

The initial data reported in this paper is limited to 2 un-patched and 2 patched specimens. Load versus crack opening displacement (COD) response due to monotonic tensile loading shown in Fig. 7.4 indicates consistent behavior between like specimens. DIC images were studied to match visual behavior with progression of the crack tip from linear elastic response, crack blunting, then finally crack growth until specimen failure. Load response combined with labels for the crack stage progression are shown in Fig. 7.4 and the DIC measured Von Mises strain ahead of the crack tip versus COD is shown in Fig. 7.5. The data indicates the transition of the fracture behavior on the free surface for both patched and un-patched specimens occurs at the same COD magnitudes. In other words, crack blunting for both un-patched and patched specimens occurs from just beyond the elastic limit until a critical COD limit of approximately 0.6 mm is reached, although the load required to achieve that COD is more than 100% greater for the patched specimen because of the load transfer to the patch that constrains the deformation of the free surface. The patched specimens exhibited visual evidence during crack growth that

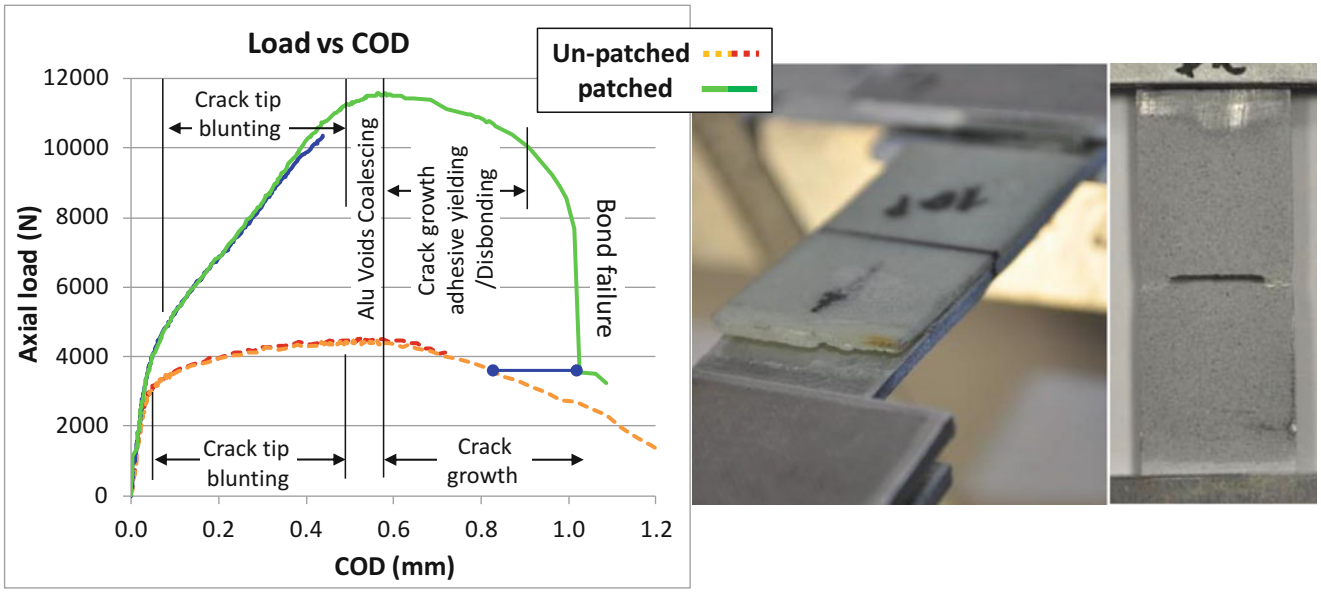

Fig. 7.4 Load versus crack opening displacement and a tested patched (L) and un-patched (R) specimen

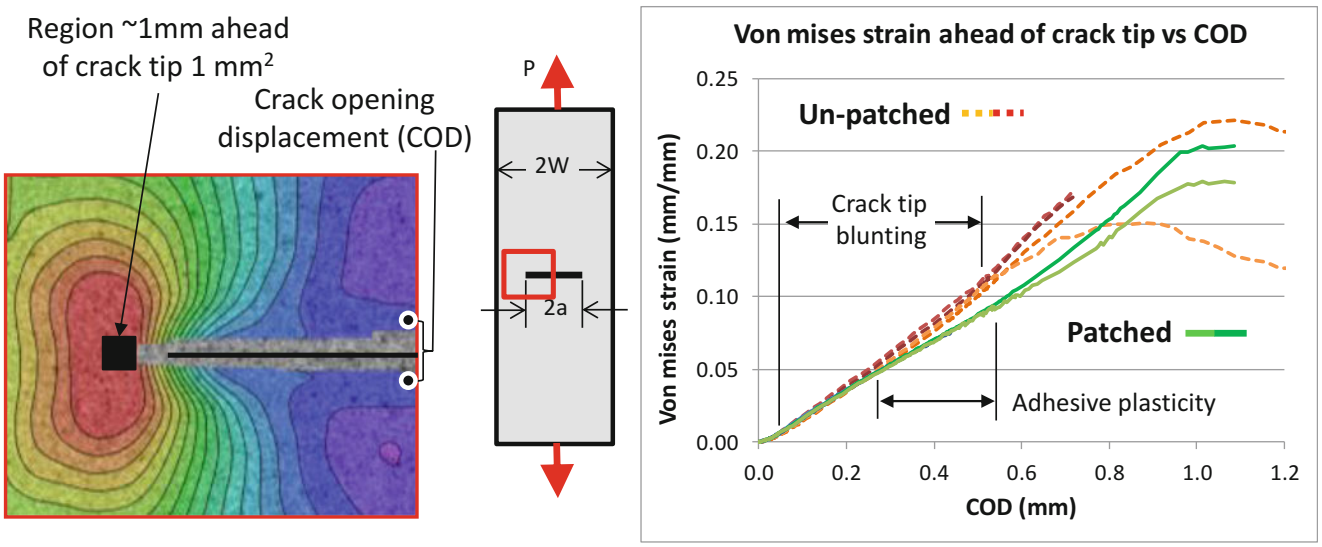

Fig. 7.5 Von Mises strain data ahead of the crack tip

suggests adhesive failure begins to occur after the peak load is achieved, thereby reducing the load transfer to the patch and the overall load-bearing capacity of the specimen. Failure of the adhesive continues until bond failure of half the patch (one side of the notch) where the crack growth behavior is then controlled by the fracture behavior of the aluminum. When comparing aluminum fracture at 3500 N, the load level after patch failure, the COD is 20% greater for the patched specimen shown by the blue line in Fig. 7.4. This additional 0.2 mm of COD on the free surface is related to the increased size and behavior of the plastic zone ahead of the crack tip for the patched specimen.

When comparing free surface behaviors of un-patched and patched specimens as a function of COD, the strain behavior ahead of the crack tip correlate reasonably well to the end of crack tip blunting, meaning the strain response on the free surface of the aluminum is nominally an intrinsic behavior of the material. Though the local crack tip behavior correlates with COD, the load required to achieve the same COD is significantly larger with the addition of the composite patch on the opposite surface, as previously discussed. In Fig. 7.5, the Von Mises strain behavior is plotted as a function of COD. The strain values plotted are averaged over a 1 mm^2 region nominally 1 mm ahead of the crack tip; the distance ahead of the crack varied from 0.8 to 1.2 mm based on the defined area of interest in the DIC software. The area of interest was refined to exclude the crack plane such that failure to correlate image subsets later in the failure progression was minimized. This prevented detailed surface displacement data from being obtained directly at the edge of the crack plane. Average strain magnitude response ahead of the crack tip is the same for both patched and un-patched specimens until approximately 0.25 mm of COD. Here there is a change in the load versus COD as well as strain versus COD responses. This is presumed to be related to increase in the region of peak plastic shear stress in the adhesive allowing higher rate of load increase. As crack blunting transitions to crack growth the aluminum specimens exhibit tearing and a gradual drop in load as COD increases. The composite patched specimens indicate visual evidence of adhesive yielding. As COD is increased, visual evidence indicates bondline failure with large relative displacement between the patch and upper notch edge resulting in a large load drop. Once the composite patch bond fails, failure behavior of the patched specimen matches the load response of the aluminum specimens but with a larger magnitude of COD, as previously discussed.

At low magnitudes of COD, below 0.02 mm, the load versus COD response of the specimen is linear elastic. Von Mises strain contours in Fig. 7.6 are similar with the composite patched specimen showing a higher magnitude and larger region of high strain. This is due to the out-of-plane bending, in the linear elastic region the bending increases until the load passes

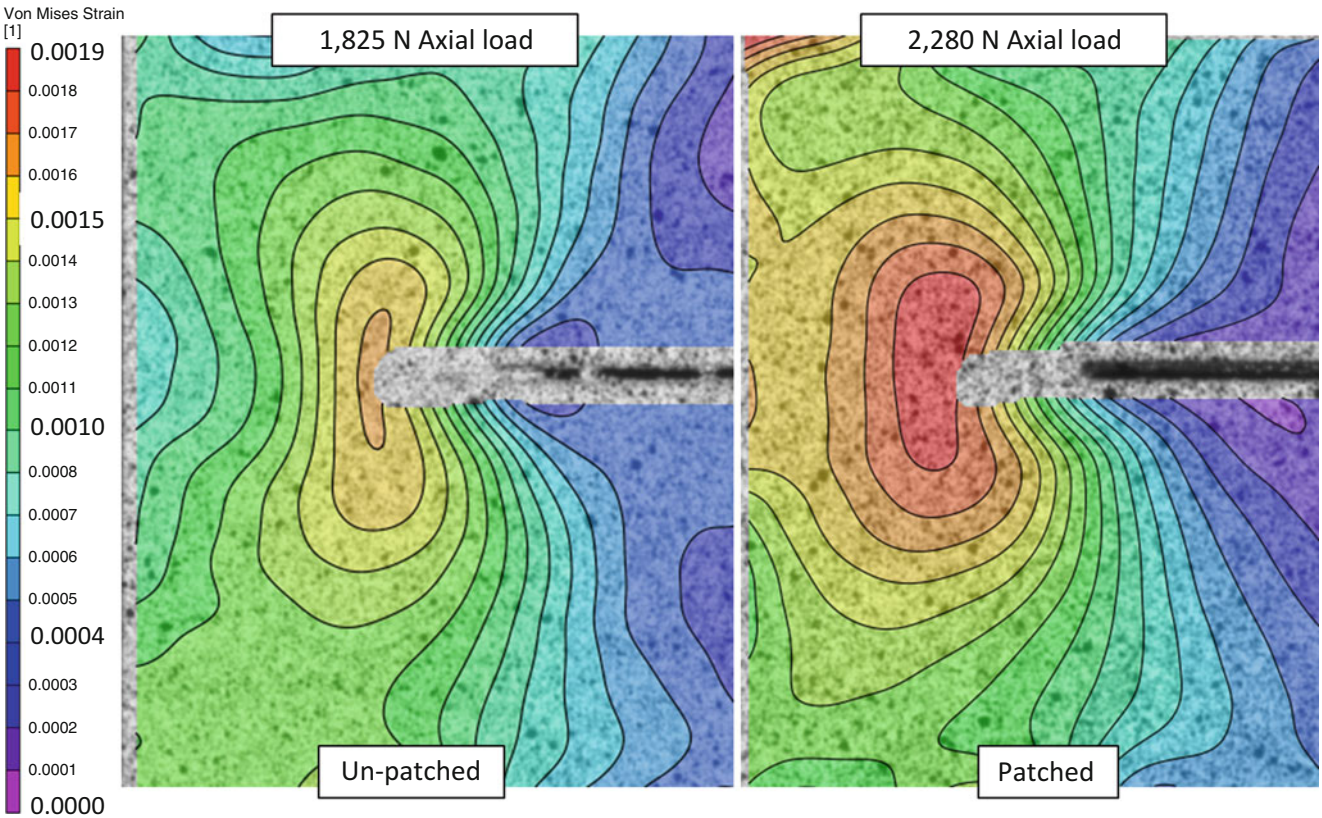

Fig. 7.6 Von Mises strain contour comparison for a COD = 0.02 mm in the linear elastic range

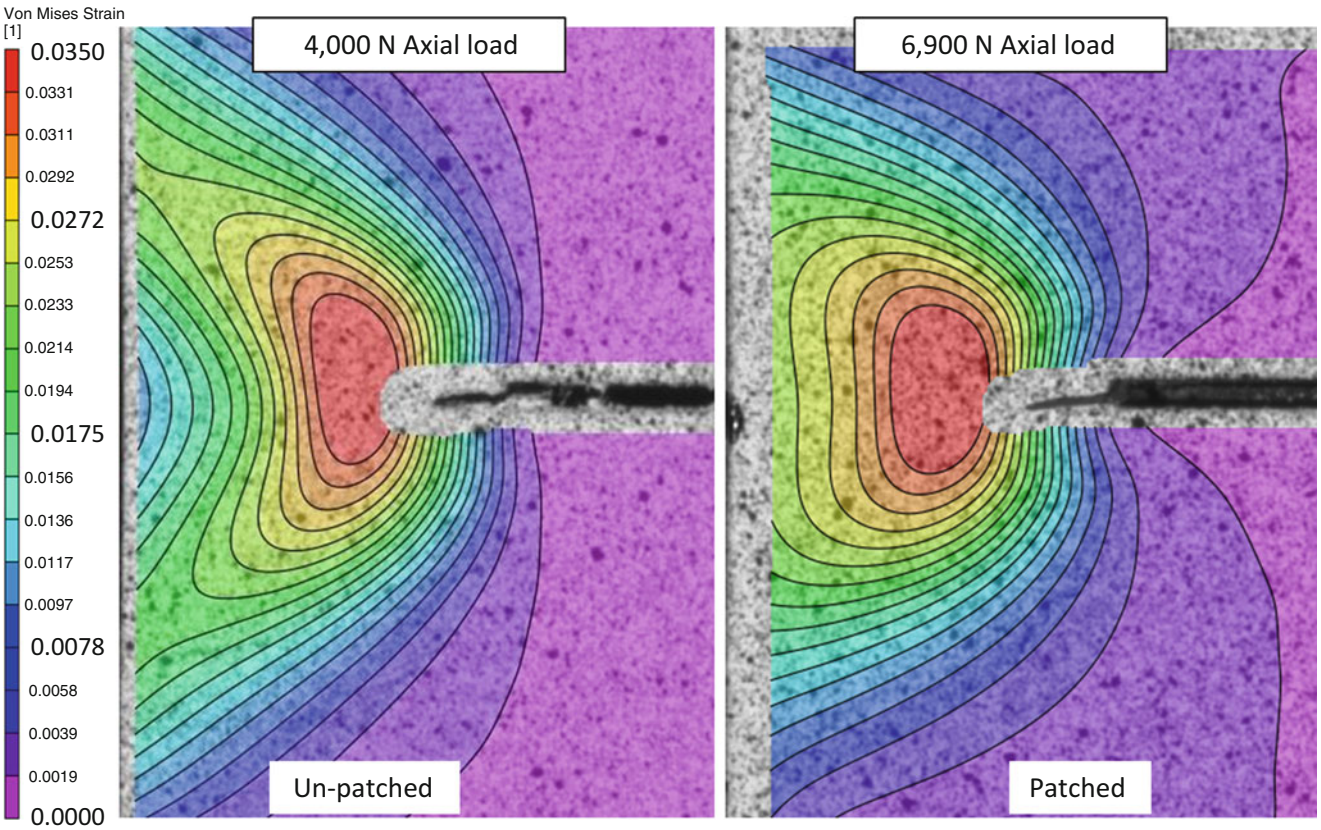

Fig. 7.7 Von Mises strain comparison of un-patched (L) and patched (R) crack tips during the early stage of crack blunting

through the neutral axis of the patch repaired specimen. This causes the surface strain of the composite patched specimen to increase at a greater rate.

Once the load axis aligns with the neutral axis of the specimen both the un-patched and patched strain magnitudes are similar. Strain contours for a COD of 0.2 mm, which is during the early stage of crack blunting, are shown Fig. 7.7. High strain for the un-patched specimen is focused at the crack tip with strains an order of magnitude lower near the specimen edge in line with the initial crack plane. This is due to a significant effect from bending as the region ahead of the crack tip deforms plastically. Strain contours for the patched specimen indicate a measureable effect of the surface reinforcement with a blunted region of high strain ahead of the crack tip and a larger area of aluminum exhibiting high strain ahead of the crack tip. The surface reinforcement in both axial and transverse directions effects the formation of the through thickness strain gradient ahead of the crack tip, which increases the size and shape of the region of aluminum supporting high strains and the area on the surface exhibiting plastic deformation. As previously discussed, this change in the formation of the plastic zone is most likely responsible for the 20% increase in COD when comparing specimen response at matching load levels after the patch fails.

7.5 Finite Element Model

Numerical predictions for the small scale specimen response were performed using a Finite Element Model (FEM) in the commercial software ABAQUS. The extended finite element method (XFEM) was utilized to define the crack and perform calculations of strain energy release rate at the crack tip and the J-integral around element defined paths ahead of the crack tip. Reduced integration linear brick elements (C3D8R) elements were used for all materials and the crack plane was defined by the built-in XFEM method to split the solid elements [30]. The model was loaded in axial tension using nodal displacement control with only the surface nodes in the grip regions being displaced in the Y-direction. Displaced nodes were free to move in the X and Z directions to minimize nodal stress concentrations at the applied boundary conditions. Large displacement formulation was used to account for non-linear geometry due to bending from the asymmetric reinforcement when possible; limitations for J-integral calculation methods will be discussed later. Best practices were followed for the number of elements

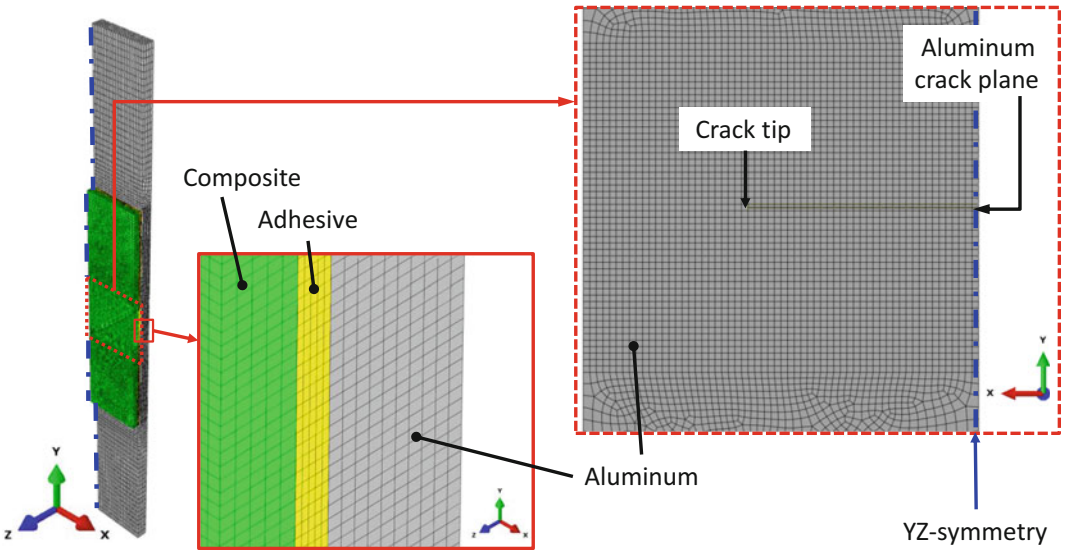

Fig. 7.8 Half symmetric finite element model element configuration details

through the thickness and ahead of the crack tip while maintaining element aspect ratios as close to 1 as possible. A minimum of 5 elements through the thickness is recommended to capture through thickness behavior, and based on previous work to capture the strain gradient necessary to capture fatigue crack growth a minimum of 0.5 mm elements along the crack path was adequate [12]. The resulting finite element model (FEM), shown in Fig. 7.8, had 10 elements through the thickness for the aluminum and 5 elements through the thickness for both the adhesive layer and the composite patch. Elements adjacent to the crack plane are 0.2 mm long (X) and 0.196 mm high (Y). Element thicknesses in the Z-direction vary; Aluminum elements are 0.226 mm thick, adhesive elements are 0.112 mm thick, and composite patch elements are 0.254 mm thick. The resulting element aspect ratios range from 0.56 to 1.30 in the region around the crack.

Two methods were used to calculate the J-integral using built-in XFEM processing methods. The basic method uses the virtual crack closure technique (VCCT), which is based on LEFM, local element based crack geometry, and nodal forces. Output from VCCT is the strain energy release rate (G), which for linear elastic material is equivalent to the J-integral ($G = J$). This method does not capture non-linear behavior of the strain energy release rate as the material deforms plastically ahead of the crack tip. True J-integral behavior must be captured using Eq. 7.1, which when using ABAQUS XFEM is solved using the domain integral method [30]. The limitation with this method is that analysis steps are limited to small-displacement linear steps, which can capture material non-linearity but not geometric non-linearity due bending and limited ability to capture displacement due to elastic-plastic material behavior.

7.6 Material Properties

Constituent properties for each material used to manufacture the CCT specimens were independently verified by mechanical testing. Test data and the material behavior approximation used in the FEA are listed and shown in Fig. 7.9. Aluminum tensile properties were measured following ASTM E8 [31] testing guidelines using an ASTM E466 [32] sheet type specimen and compared against existing data [33]. Aluminum properties were averaged for four specimens with resulting modulus of 70.9 ± 0.9 GPa, 0.2% offset yield strength of 116 ± 1 MPa, and Ramberg-Osgood parameters α and n of 9.9 ± 0.9 and 0.22 ± 0.06 respectively. WestSix10 adhesive tensile dog-bone and thick adhesive shear properties were measured following ASTM D638 and D5656 test standards [34, 35]. A total of six specimens were tested with resulting modulus of 2.4 ± 0.1 GPa and a 0.2% offset yield strength of 23.6 ± 2.7 MPa. Only linear elastic behavior was utilized for the current FEA. A total of six composite dog-bone specimens were tested in tension following ASTM D638. The resulting average modulus was 22.2 ± 1.2 GPa and an average ultimate strength of 300 ± 4 MPa.

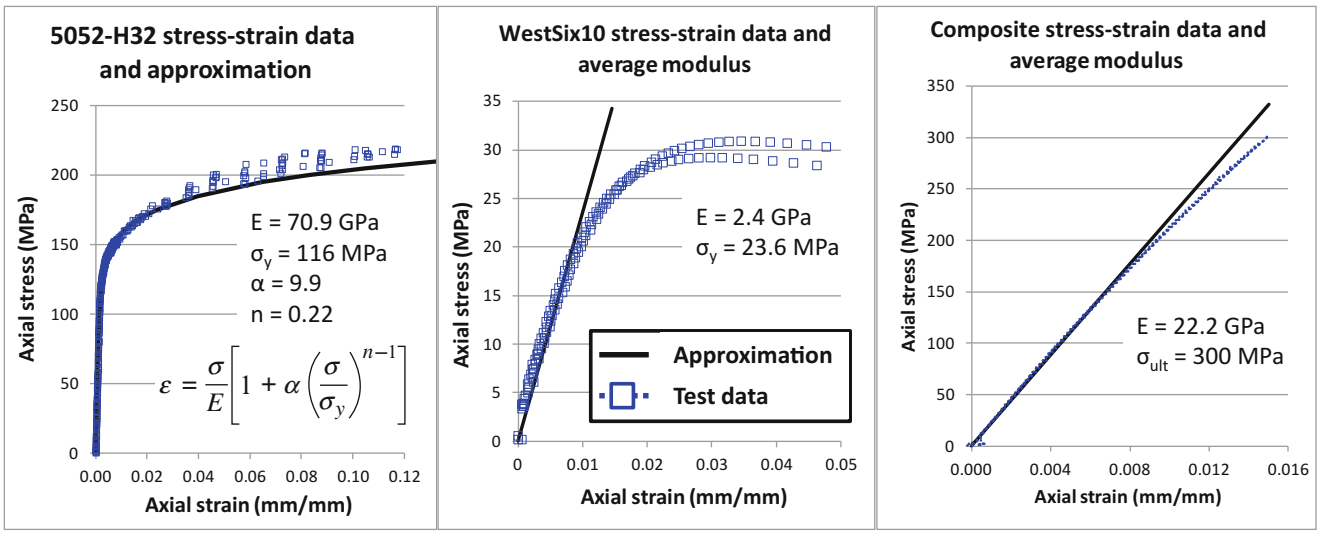

Fig. 7.9 Test data and behavior approximation for aluminum (L), adhesive (M), and composite (R) materials

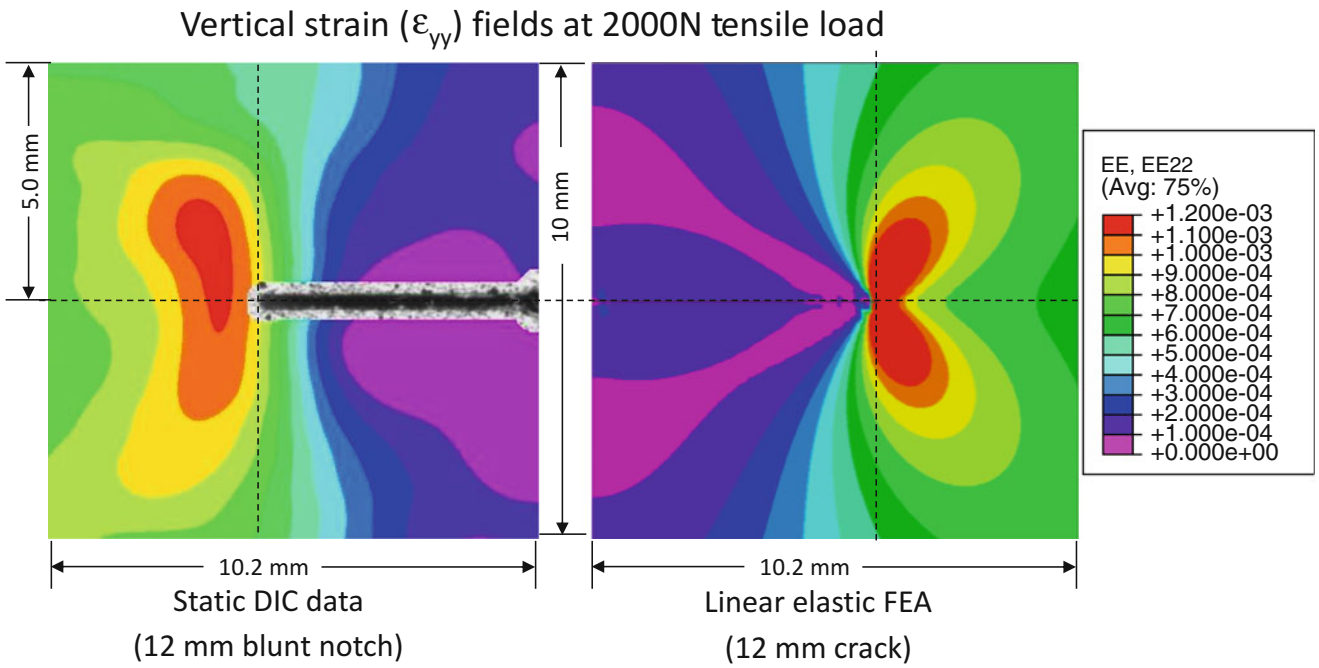

Fig. 7.10 Surface vertical strain: DIC (L) and FEA prediction (R)

7.7 Comparison of Test Results and Predictions

Comparison of the finite element analysis (FEA) predicted surface axial strain (ε_{yy}) and the DIC measured axial strains shown in Fig. 7.10 occurs at a load of 2000 N, which is at the edge of the linear elastic response. Strain magnitude and distribution for the DIC measured (L) and FEA predicted (R) correlate well. Though not shown here the vertical displacements also correlate well in the linear elastic range. The key difference between data and FEA prediction is the crack tip geometry. In the FEM the crack has a sharp tip defined by an infinitesimal plane while in reality the crack is a blunt 12 mm long EDM cut notch (*2a*) prior to fatigue crack growth. Any effect the true notch geometry has on local strain behavior is not captured by the FEM.

Both LEFM and EPFM predictions for the J-integral value are shown in Fig. 7.11. LEFM solutions approximate the relationship between far-field stress and the plane stress crack tip stress intensity (K_I), in Eq. 7.4 where P is the load, B is the aluminum thickness, W is the half width, and a is the half crack length. The finite geometry effect is accounted for using the

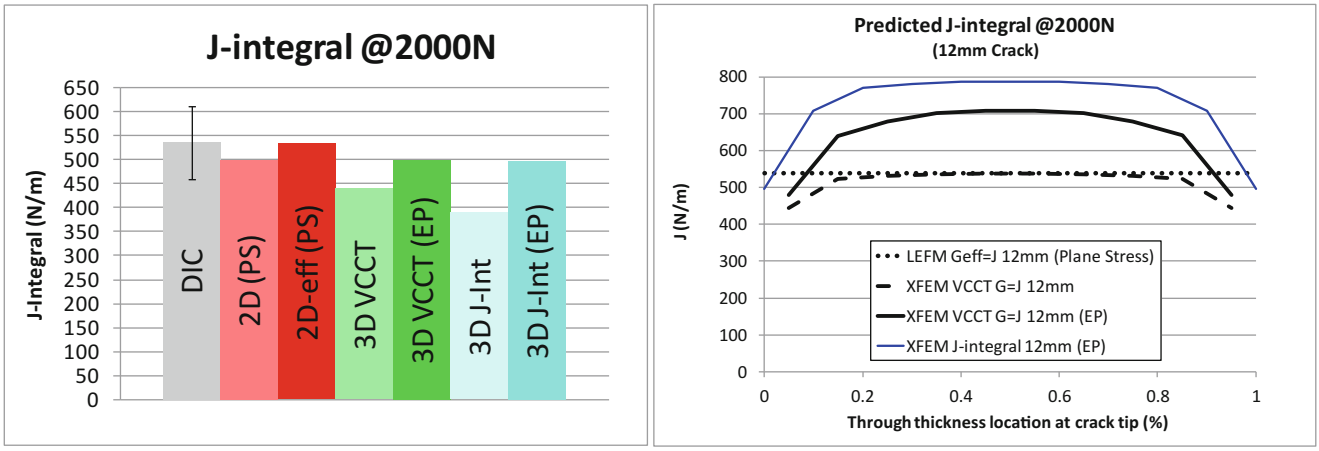

Fig. 7.11 Un-patched specimen DIC data and predictions for 2000 N load on the surface (L) and through the thickness (R)

correction factor in Eq. 7.5 [17] as well as an effective crack length to account for possible small scale first order plasticity at the crack tip in Eq. 7.6. Stress intensity is then converted to plane stress strain energy release rate with the plane stress relationship. Results for the 2D plane stress (2D PS) and effective J-integral (2D-eff PS) are shown in Fig. 7.11.

$$K_I = \frac{P}{B\sqrt{W}} f\left(a/w\right) \tag{7.4}$$

$$f\left(a/w\right) = \sqrt{\frac{\pi a}{4W}} sec\left(\frac{\pi a}{2W}\right)\left[1 - 0.025\left(\frac{a}{W}\right)^2 + 0.06\left(\frac{a}{W}\right)^4\right] \tag{7.5}$$

$$r_y = \frac{1}{2\pi}\left(\frac{K_I}{\sigma_{ys}}\right)^2 \quad a_{eff} = a + r_y \tag{7.6}$$

FEA predictions using VCCT and domain integral calculations are also included for a load of 2000 N. Results show that accounting for small scale plasticity in the J-integral value is necessary, by either using an effective crack length or including elastic-plastic material behavior. When including elastic-plastic behavior the predictions correlate well with DIC calculated J-integral values with predictions within 8% of the data.

Out of plane bending caused by the composite patch changes the through thickness distribution of SERR and strain, as shown in Fig. 7.12. J-integral value predictions, in the linear elastic range, correlate well with the measured value. From ABAQUS, the LEFM VCCT values are elemental values output at the centroid for the reduced integration elements used, while the domain integral is calculated on the element surfaces. Linearly extrapolating the LEFM results, the J-integral value for both prediction methods are within 5% of each other and 10–15% of the mean DIC value. At a load of 2000 N, the end of the linear elastic response, numerical prediction methods start to diverge in both magnitude and through thickness behavior.

The measured and predicted load versus COD behaviors shown in Fig. 7.13 focus on the COD before crack growth and material failure occur; when COD is less than 0.25 mm. For the un-patched specimens physical response is captured when accounting for elastic-plastic behavior of the aluminum. Patched predictions diverge from test data as loading proceeds through the crack blunting stage. Patched FEA is run two ways to get LEFM and EPFM predictions for the J-integral. First, for the LEFM VCCT prediction the model utilizes the non-linear geometry option in ABAQUS for the implicit solution incrementation, meaning equilibrium is solved for between successive analysis increments and accounts for bending that exists due to the asymmetry created by the one sided composite patch. This method over predicts the global stiffness of the non-linear response as COD increases past 0.10 mm; The FEM does not account for the non-linear shear behavior of the explicitly modeled adhesive layer. Then, for the EPFM domain integral method the FEA solution is restricted to linear geometry incrementation, which means that equilibrium is solved for between the initial configuration and the target end displacement or boundary condition for that step. Though both procedures account for non-linear material behavior the nodal displacement as elastic-plastic behavior occurs was over predicted with linear geometry increments. Linear geometry solutions typically result in a stiffer response with higher stress, which with elastic-plastic material behavior results in more strain and displacement per solution increment. Both predictions produce reasonable correlation when COD is less than 0.15 mm.

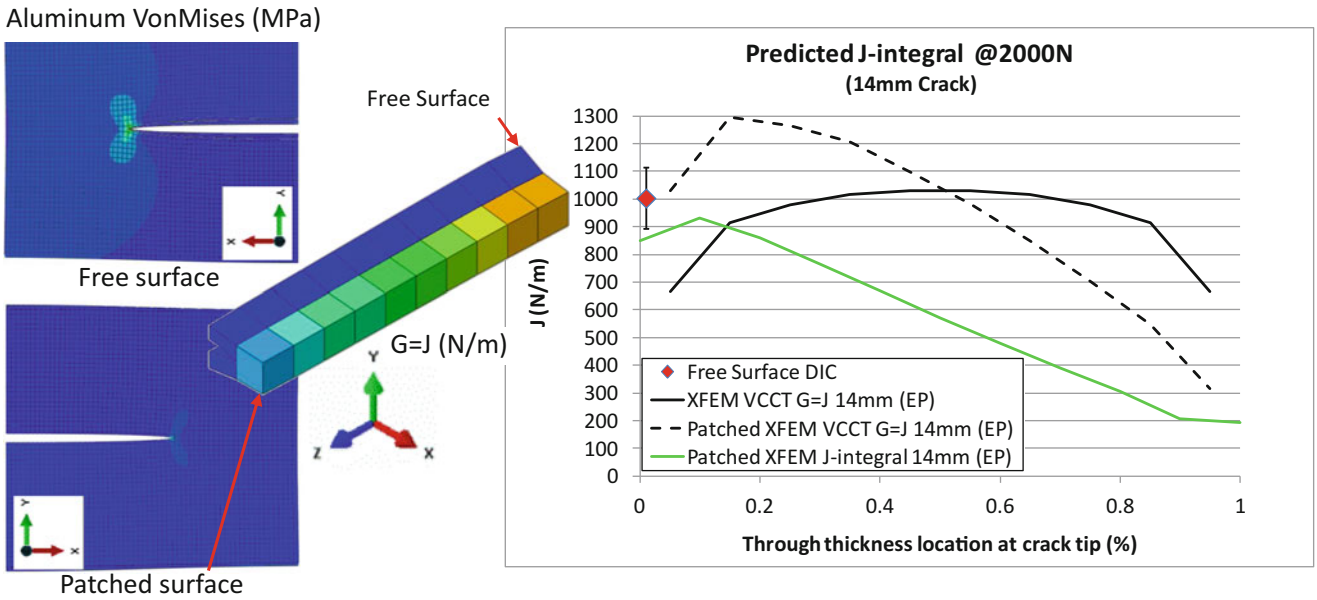

Fig. 7.12 Patched specimen DIC data and predictions of J-integral at 2000 N load

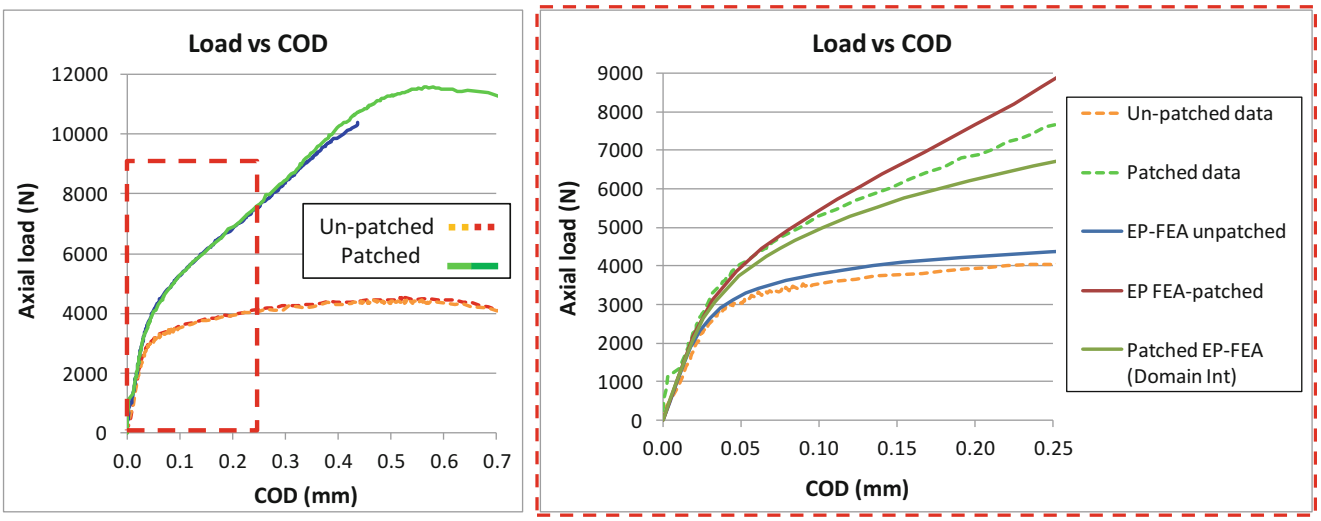

Fig. 7.13 Load versus COD predictions and test data early in the crack blunting stage with COD less than 0.25 mm

With the global specimen response correlating reasonably well, one can compare the J-integral value predictions. The COD response as a function of the J-integral value for COD magnitudes less than 0.25 mm is shown in Fig. 7.14. As shown with the un-patched and patched strain response, the free surface material response is nominally an intrinsic property of the aluminum, that as a function of COD shows negligible variation with surface reinforcement. Though the patched response requires more load to achieve the same COD, similar behavior is observed when the J-integral value on the surface is related to COD. The key finding here is the amount of divergence between LEFM and EPFM J-integral predictions as load and COD increases beyond the linear elastic response. FEA under predicts the COD as a function of the J-integral value, meaning that at a given COD the analytical procedure required to calculate the domain integral predicts a lower load and more strain than measured. Over predicting the strain results in a higher strain energy release rate, or J-integral value, than measured.

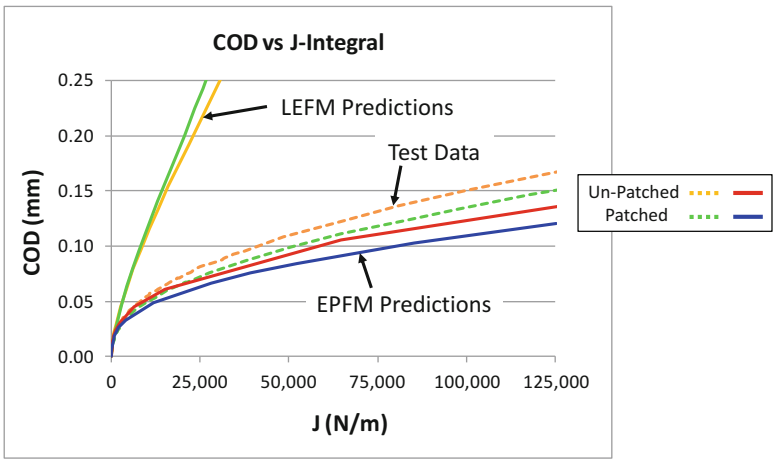

Fig. 7.14 COD versus J-Integral for test data and FEA

7.8 Conclusions

Using full field DIC test data and FEA the influence one sided composite patch reinforcement has on the free surface local crack tip elastic-plastic behavior was studied. Un-patched and patched CCT specimen response to a far field tensile load was both measured and predicted. Monotonic tensile loading until failure demonstrated a greater than 100% increase in ultimate failure load of the patched versus un-patched specimen. Composite patch reinforcement increases the ability of the specimen to carry more tensile load due to the load transfer to the patch, however testing demonstrated behavior on the free-surface ahead of the crack tip appears to remain an intrinsic material property independent of the patch. Both strain and J-integral behavior on the free surface until the end of the crack blunting stage was independent of the specimen configuration, un-patched or patched, when related to the COD. The bending deformations and plastic zone formation ahead of the crack tip induced by the patch did appear to affect crack-tip blunting, which resulted in a 20% increase in COD at a given load level after patch failure.

Both analytical and numerical predictions of load versus COD and J-integral values correlated well with test data in the linear elastic response range. As loading and COD increase beyond the linear elastic response and elastic-plastic material behavior begins to occur, LEFM and EPFM predictions diverge. ABAQUS was used to numerically predict specimen response and J-integral values two ways with different implicit solution methods. The LEFM based VCCT method under predicts the J-integral value beyond the linear elastic response, but accounts for the non-linear response due to bending and elastic-plastic material behavior by solving for equilibrium between each solution increment and automatically sizing the increment. The EPFM predictions are currently limited to finite displacement solution increments that solve for equilibrium between the initial and current state with no automatic step sizing, which results in the over prediction of displacements and strains.

Testing and analysis results will guide future efforts. Comparing test response to the predicted response indicates a few mechanisms still need to be accounted for in the numerical predictions. Un-patched and patched specimen strain response indicates that accounting for the elastic-plastic shear behavior of the adhesive may be required to improve correlation. To fully capture the load response and the J-integral value requires a post processing method to extract surface displacements from an analysis that allows equilibrium solutions between increments. Extracting surface displacements can then be used to perform the J-integral calculation on arbitrary paths about the crack tip. Further improvements in the J-integral correlation can be achieved by including the elastic-plastic stress-strain material behavior at the crack tip as included in methods described by Hickey, Yoneyama et al., and Becker et al. [23–25].

Acknowledgements Work described was performed by the Naval Surface Warfare Center Carderock Division's Survivability, Structures, Materials Department, and University of Maryland College Park's Mechanical and Reliability Engineering department. Financial and technical support was provided by an NSWCCD In-house Laboratory Independent Research (ILIR) program under Dr. Jack Price, and a grant provided to UMD by program officer Dr. Paul Hess of the Office of Naval Research Code 331 under grant number N000141612351.

References

1. Volkersen, O.: Die Niektraft in Zugbeanspruchten mit Kontanten Laschenquerschritten. Luftfahrtforschung. **5**, 41–47 (1938)
2. Goland, M., Reissner, E.: The stress in cemented joints. J. Appl. Mech. **77**, (1944)
3. Hart-Smith, L.J.: Adhesive-Bonded Double-Lap Joints, CR-112235, NASA, (1973)
4. Hart-Smith, L.J.: Adhesive-Bonded Single-Lap Joints, CR-112236, NASA, (1973)
5. Sabelkin, V., Mall, S., Avram, J.B.: Fatigue crack growth analysis of stiffened cracked panel repaired with bonded composite patch. Eng. Fract. Mech. **73**, 1553–1567 (2006)
6. Schubbe, J.J., Mall, S.: Investigation of a cracked thick aluminum panel repaired with a bonded composite patch. Eng. Fract. Mech. **63**, 305–323 (1999)
7. Tsai, G.-C., Shen, S.B.: Fatigue analysis of cracked thick aluminum plate bonded with composite patches. Compos. Struct. **64**, 79–90 (2004)
8. Jones, R., Chiu, W.K.: Composite repairs to cracks in thick metallic components. Compos. Struct. **44**, 17–29 (1999)
9. Duong, C.N.: Design and validation of composite patch repairs to cracked metallic structures. Compos. Part A. **40**, 1320–1330 (2009)
10. Baker, A.A., Rose, L.R.F., Jones, R.: Advances in the Bonded Composite Repair of Metallic Aircraft Structures, vol. 1. Elsevier: Oxford (2002)
11. Noland, J.M., Hart, D.C., Udinski, E.P., Sielski, R.A.: Initiatives in bonded ship structural repairs. In ASNE Fleet Maintenance and Modernization Symposium. San Diego: American Society of Naval Engineers. Conference (2013)
12. Baker, A.A., Rose, L.R.F., Walker, K.E., Wilson, E.S.: Repair substantiation for a bonded composite repair to F111 lower wing skin. Appl. Compos. Mater. **6**, 251–267 (1999)
13. Muller, R., Fredell, R.: Analysis of multiple bonded patch interaction simple design guidelines for multiple bonded repairs in close proximity. Appl. Compos. Mater. **6**, 217–237 (1999)
14. Hart, D.C.: 5xxx Aluminum Sensitization and Application of Laminated Composite Patch Repairs. In: Society for Experimental Mechanics XIII International Congress and Exposition on Experimental Applied Mechanics, Experimental Dynamic Behavior: Integrating Experimental Mechanics. Orlando. Conference (2016)
15. Nahshon, K., Hoffman, W.A., Ullagaddi, C.B.: Characterization of structural scale ductile fracture of aluminum panels using digital image correlation. In: Proceedings of the 2014 Annual Conference on Experimental and Applied Mechanics. Conference (2014)
16. Hart, D.C., Udinski, E.P., Hayden, M.J., Liu, X.: Fatigue performance and analysis of composite patch repaired cracked aluminum plates. In: Sustainability and Stewardship, Vessel Safety and Longevity Through Research. Linthicum Heights: Ship Structures Committee. Conference (2014)
17. Anderson, T.L.: Fracture Mechanics Fundamentals and Applications, 2nd edn. CRC Press LLC: Raton (1995)
18. Hutchinson, J.W.: A Course on Non-Linear Fracture Mechanics. Department of Solid Mechanics, The Technical University of Denmark, Copenhagen (1979)
19. Rice, J.R.: A Path Independent Integral and the Approximate Analysis of Strain Concentration by Notches and Cracks, D.o.D.A.R.P. Agency, Editor (1967)
20. Sutton, M.A., Orteu, J.-J., Schreier, H.W.: Image Correlation for Shape, Motion, and Deformation Measurements. Springer, LLC: New York (2009)
21. Bruck, H.A.: Analysis of 3-D Effects near the Crack Tip on Rice's 2-D J-Integral Using Digital Image Correlation and Smoothing Techniques. In: Department of Mechanical Engineering. University of South Carolina, Columbia (1989)
22. Sutton, M.A., Turner, J.L., Chao, Y.J., Bruck, H.A., Chae, T.L.: Experimental investigations of three dimensional effects near a crack tip using computer vision. Int. J. Fract. **53**, 201–228 (1992)
23. Yoneyama, S., Arikawa, S., Kusayanagi, S., Hazumi, K.: Evaluating J-integral from displacement fields measured by digital image correlation. Strain. **50**, 147–160 (2014)
24. Hickey, W.F.: An investigation into the failure of aluminum alloys. In: Material Science and Engineering. University of Texas at Austin, Austin (2011)
25. Becker, T.H., Mostafavi, M., Tait, R.B., Marrow, T.J.: An approach to calculate the J-integral by digital image correlation displacement field measurement. Fatigue Fract. Eng. Mater. Struct. **35**, 971–984 (2012)
26. Fernandez Zuniga, D., Kalthoff, J.F., Fernandez Canteli A., Grasa, J., Doblare, M.: Three dimensional finite element calculations of crack tip plastic zones and KIC specimen size requirements. In: European Conference on Fracture. Stockholm: Engineering Structural Integrity Society. Conference (2004)
27. Hamam, R., Hild, F., Roux, S.: Stress intensity factor gauging by digital image correlation: application in cyclic fatigue. Strain. **43**, 181–192 (2007)
28. Golumbfskie, W.J.: Aluminum sensitization and the navy. In: The Minerals, Metals, and Materials Society 143rd Annual Meeting and Exhibition. San Diego, Conference (2014)
29. Golumbfskie, W.J., Tran, K.T., Noland, J.M., Park, R., Stiles, D.J., Grogan, G., Wong, C.: Survey of detection, mitigation, and repair technologies to address problems caused by sensitization of Al-Mg alloys on navy ships. Corrosion. **72**(2), 314–328 (2016)
30. V2016, A: Software Users Manuals. Dassault Systemes Simulia Corporation, Providence, RI (2015)
31. ASTM E8M-08: Standard Test Methods for Tension Testing of Metallic Materials. ASTM International, Conshohocken (2008)
32. ASTM E466-07: Standard Practice for Conducting Force Controlled Constant Amplitude Axial Fatigue Tests of Metallic Materials. ASTM International, Conshohocken (2007)
33. Ozturk, F., Toros, S., Kilic, S.: Evaluation of tensile properties of 5052 type aluminum-magnesium alloy at warm temperatures. Arch. Mater. Sci. Eng. **34**(2), 95–98 (2008)
34. ASTM D638: Standard Test Method for Tensile Properties of Plastics. ASTM International, Conshohocken (2003)
35. ASTM D5656: Standard Test Method for Thick-Adherend Metal Lap-Shear Joints for Determination of the Stress-Strain Behavior of Adhesives in Shear by Tension Loading. ASTM International, Conshohocken (2004)

Chapter 8
Influence of the Temperature on Lifetime Reinforcement of a Filled NR

B. Ruellan, J.-B. Le Cam, E. Robin, I. Jeanneau, F. Canévet, and F. Mortier

Abstract Fatigue of crystallizable rubbers has been widely investigated since the pioneer work by Cadwell et al. in 1940 (Cadwell et al., Ind Eng Chem 12:19–23, 1940). This study revealed the significant influence of the mean strain on natural rubber lifetime: for non-relaxing loading conditions (*i.e.* R > 0), strong lifetime reinforcement was observed and attributed strain-induced crystallization (SIC). Better understanding how SIC reinforces fatigue life is therefore a key point to improve the durability of rubbers. Surprisingly, few studies investigated the effect of temperature on the lifetime, while SIC exhibits a high thermo-sensitivity (Lindley, Rubber Chem Technol 47:1253–1264, 1974; Lu Etude du comportement mécanique et des mécanismes d'endommagement des élastomères en fatigue et en fissuration par fatigue. PhD Thesis, Conservatoire National des Arts et Métiers, 1991). The present study aims therefore at investigating how temperature affects the fatigue life reinforcement due to SIC under non-relaxing loading conditions. First of all, fatigue tests are carried out at 23 °C. Damage leading to the end-of-life is investigated at both the macroscopic and the microscopic scales for loading ratios from −0.25 to 0.35. As expected, NR exhibits a reinforcement for positive loading ratios R at 23 °C. Damage, striations due to SIC and number of cycles at crack initiation are mapped using the Haigh diagram. At 90 °C, the fatigue lifetime reinforcement is lower and the signature of SIC on the failure surface disappears. The competition between non-relaxing loading effect and temperature is finally discussed.

Keywords Natural rubber · Fatigue · Strain-induced crystallization · Lifetime reinforcement · Temperature

8.1 Introduction

Literature is very abundant on fatigue of rubbers at ambient temperature.[1] Even though studies differed in the sample geometries tested, in the material formulations and in the loading conditions, general comments can be drawn:

- volumetric samples were generally preferred. Cadwell et al. initially used cylindrical samples [1], then replaced by a diabolo-like geometry introduced by Beatty in 1964 [2]. In the next studies, this type of geometry will be used as the reference one, with a radius of curvature equal to 42 mm [3–16]. Another sample geometries, AE2 and AE5 with lower radius of curvature (2 and 5 mm, respectively), were introduced for investigating multiaxial fatigue of rubber [7–10, 14].
- three end-of-life criteria were used to determine the end-of-life *(i)* the sample failure [1, 15, 17] *(ii)* the occurrence of a crack of a given length at the sample surface. The crack length varies depending on the authors: 1–3 mm [4, 5, 9, 10, 14].

[1]In case of strain prescribed test: $R_\varepsilon = \varepsilon_{min}/\varepsilon_{max}$.

B. Ruellan (✉)
Univ Rennes, CNRS, IPR (Institute de Physique de Rennes) – UMR 6251, Rennes, France

LC-DRIME, Joint Research Laboratory, Cooper Standard – Institut de Physique UMR 6251, Rennes Cedex, France

Cooper Standard France, Rennes, France
e-mail: benoit.ruellan@cooperstandard.com

J.-B. Le Cam · E. Robin
Univ Rennes, CNRS, IPR (Institute de Physique de Rennes) – UMR 6251, Rennes, France

LC-DRIME, Joint Research Laboratory, Cooper Standard – Institut de Physique UMR 6251, Rennes Cedex, France

I. Jeanneau · F. Canévet · F. Mortier
LC-DRIME, Joint Research Laboratory, Cooper Standard – Institut de Physique UMR 6251, Rennes Cedex, France

Cooper Standard France, Rennes, France

J. Carroll et al. (eds.), *Fracture, Fatigue, Failure and Damage Evolution, Volume 6*, Conference Proceedings of the Society for Experimental Mechanics Series, https://doi.org/10.1007/978-3-319-95879-8_8

The choice of a crack length is not physically motivated as discussed in André et al. [7]. Moreover, it is based on an optical detection that is difficult to perform. *(iii)* a critical value of a macroscopic parameter. This criterion applies for initiation of external as well as internal cracks and is therefore easily applicable to fatigue test. Authors link the end-of-life to a drop in the chosen parameter value: 15% of the maximal effort at the 128th cycle [18], 50% of the stabilized shearing effort [5], 20% of the maximal displacement at the 1000th cycle, for tests under prescribed force [16], etc. Other authors correlated the sample end-of-life with the brutal decrease of the maximal reaction force [3]. As the end-of-life criterion differed from one study to another one, comparing the different studies seems complicated.

- as soon as 1940, Cadwell and co-workers showed the influence of the mean stress on fatigue life of NR [1]. Indeed, a strong reinforcement was observed for loading ratios superior to zero. This was corroborated in Refs. [7, 9]. Such reinforcement was not observed for non-crystallizable rubbers [19, 20], which suggested that SIC is responsible for this lifetime reinforcement.
- for static loadings, even though Lindley suggested that NR would behave as a non-crystallizable rubber for sufficiently high temperature [19], this result cannot be directly transposable to fatigue. Treloar estimates the crystallites melting temperature between 75 and 100 °C [21]. Later, authors showed that SIC had almost completely disappeared (i.e. crystallinity measured close to zero) for experiments carried out at 75 °C, 80 °C or at 100 °C and even for large strains. Under fatigue loadings, several studies investigated the effect of temperature [1–3, 16]. Furthermore, in these studies fatigue tests were carried out at constant loading ratios, except in the work by Bathias and co-workers [22] where authors showed that a lifetime reinforcement was still present at 80 °C but occurred for more important mean stress than at 23 °C. Further investigations including a more exhaustive fatigue tests (*i.e.* for $R > 0$ where NR exhibits a strong lifetime reinforcement at 23 °C) could provide additional information on the effect of the temperature on crystallizable rubber durability. In his work, Lu showed that NR end-of-life drops by a decade when the temperature increases from 0 to 100 °C [3]. Duan et al. [23] and Neuhaus et al. [16] highlighted the effect of temperature on the NR fatigue properties. On plane samples, Duan et al. showed that the fatigue resistance of NR was only altered for important maximal strains for test carried out at $R_\varepsilon = 0$ and in the range of temperature from 23 to 90 °C. On diabolo samples, Neuhaus et al. measured a shift of the S-N curves towards the decreasing lifetimes as the temperature increases, independently of the strain applied and for fatigue tests performed at $R_\varepsilon = -1$, for temperatures from 70 to 100 °C. It is worth noting that NR is highly subjected to self-heating, a difference of 50 °C between the bulk and the surface of diabolo tested has been measured [3, 5]. Thus, self-heating has to be taken into account in order to analyse the effect of the temperature on the rubber fatigue behaviour.

As a conclusion, no study investigates the effect of temperature on the lifetime reinforcement due to SIC by characterizing the damage at the microscopic scale. This is the aim of the present study. The next section presents the experimental setup. Then, results are given and discussed. Concluding remark close the paper.

8.2 Experimental Setup

8.2.1 Material and Sample Geometry

The material considered here is a carbon black filled natural rubber (*cis*-1,4 polyisoprene) vulcanised with sulphur. Samples tested are Diabolo samples.

8.2.2 Loading Conditions

The fatigue tests were performed with a uni-axial MTS Landmark equipped with a homemade experimental apparatus presented in Fig. 8.1. This apparatus enables us to test simultaneously and independently eight Diabolo samples, which compensates the fatigue tests duration and the dispersion in the fatigue life.

The tests were performed under prescribed displacement. The corresponding local deformation at the sample surface in the median zone was calculated by FEA. In order to investigate the effect of temperature on and the fatigue properties, a Servathin heating chamber was used. A pyrometer tracked the temperature of a material point located in the diabolo median surface. For that purpose, a second homemade system (not presented in the figure) has been developed to provide the suitable kinematics to the pyrometer. The frequency was chosen in such a way that the global strain rate $\dot{\varepsilon}$ was kept constant, ranging between 1.8 and 2.4 to 2 s^{-1} for one test to another one. In practice, the frequency ranged between 1 and 4 Hz, depending on the strain

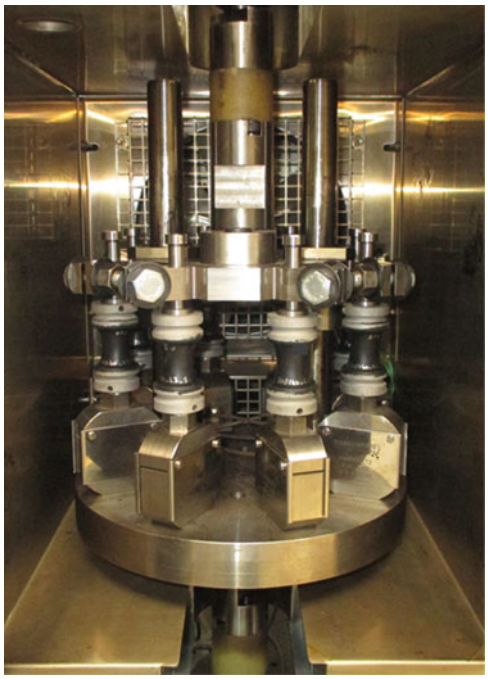

Fig. 8.1 Experimental setup. The homemade apparatus with 8 Diabolo samples tested in an oven

amplitude and self-heating to be limited. Five different loading ratios $R_\varepsilon = \frac{\varepsilon_{min}}{\varepsilon_{max}}$ were used: -0.25; 0; 0.125; 0.25 and 0.35. One can recall that loading ratios inferior, equal and superior to zero correspond to tension- compression, repeated tension and tension-tension, respectively.

8.2.3 End-of-Life Criterion

Considering a crack initiation approach, a physical criterion based on the maximal reaction force evolution was chosen. Three regimes were obtained during the fatigue test: the softening traduced by a slight decrease of the maximal reaction force, its stabilization and its drop (brutal or not, depending on the loading and environmental conditions). The number of cycles at crack initiation is denoted N_i. It corresponds to the number of cycles at the end of the plateau, when the derivative of N_i is no longer constant. In practice, it corresponds to the occurrence of a macroscopic crack which length is maximum 5 mm at the sample surface.

8.2.4 Scanning Electron Microscopy

Second electrons images of diabolo fracture surfaces were stored with a JSM JEOL 7100 F scanning electron microscope (SEM). In addition, the SEM is coupled with an Oxford Instrument X Max Energy Dispersive Spectrometer of X-rays (EDS) and an Aztzec software in order to determine the surface fracture composition, especially in the crack initiation zone. The fracture surfaces to be analysed were previously metallized by vapour deposition of an Au-Pd layer.

8.3 Results and Discussions

Results obtained for tests performed at 23 °C are first described as the reference ones. Then, they are compared to tests carried out at 90 °C in order to evaluate the influence of the temperature on the material reinforcement. For the both temperatures, lifetime as well as damage mechanisms were considered.

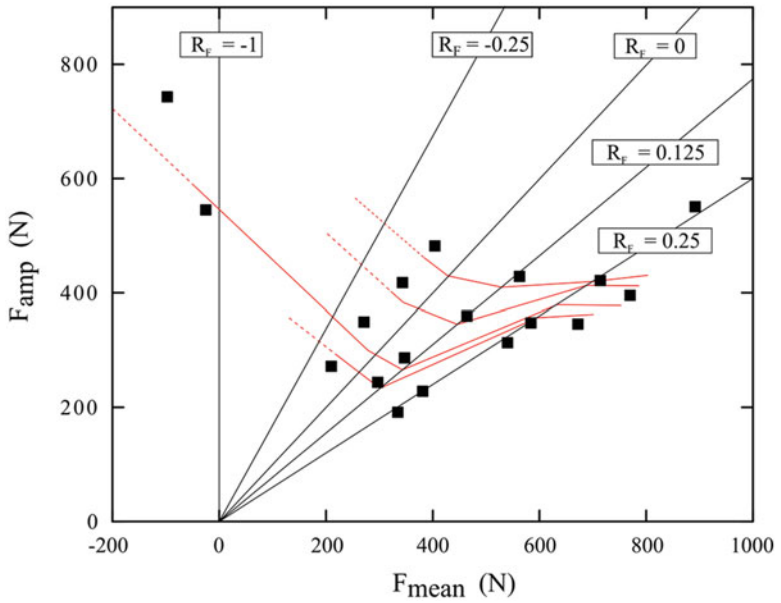

Fig. 8.2 Haigh diagram at 23 °C

Considering tests performed at 23 °C, results are presented in the Haigh diagram plotted in Fig. 8.2. The Haigh diagram provides the iso-lifetime curves in relation to the amplitude and the mean value of the loading. It is classically used to highlight the NR lifetime reinforcement obtained for non-relaxing tension. Here, even though tests were performed under prescribed displacement, the Haigh diagram is plotted in terms of force. Each square in the diagram represents a fatigue test and is linked to a mean lifetime based on eight tests. Considering the loading ratio, three zones can be put into light:

- $-0.25 < R_F < 0$ (tension-compression). The iso-lifetime curves are decreasing monotonously, fatigue damage is driven by F_{max}. In other words, the mean local strain F_{mean} has no influence on the rubber fatigue life.
- $0 < R_F < 0.125$ (tension-tension). For positive loading ratios, F_{mean} has an influence on the rubber durability: the slope of the iso-lifetime curves increases in absolute value.
- $R_F > 0.125$ (tension-tension). The slope of the iso-lifetime curves becomes positive, exhibiting strong lifetime reinforcement.: at a given F_{amp}, the lifetime increases when F_{mean} is increased. For $R_F > 0.25$, the reinforcement is of a less importance.

Post-mortem analyses have been carried out at both the macroscopic and the microscopic scale on damage mechanisms leading to the sample failure. They enabled us to map fatigue damage in relation to the loading applied. This part of the work is not detailed here.

For fatigue tests carried out at 90 °C, results differ in many point compared to fatigue test at 23 °C. Results are presented in Fig. 8.3 and can be summed up as follows:

- $-0.25 < R_F < 0$ (tension-compression). Similarly to tests at 23 °C, the iso-lifetime curves are decreasing, meaning that F_{max} drives fatigue damage for this loading condition. Nevertheless, the fatigue lifetime drops by a factor 2 at $R_F = 0$ when the temperature increases from 23 to 90 °C. This result is in good agreement with the literature [16, 23].
- $0 < R_F < 0.25$ (tension-tension). A slight lifetime reinforcement occurs, it is more significant for the shortest lifetime. For similar value of F_{mean}, the reinforcement at 90 °C is not as important as at 23 °C. Nevertheless, reinforcement is still observed and SIC still plays a role in the fatigue behavior at 90 °C, while crystallites are generally assumed to be melt at this temperature level [24].
- $R_F > 0.25$ (tension-tension). Experiments involving such loading conditions are currently in progress and are therefore not presented here.

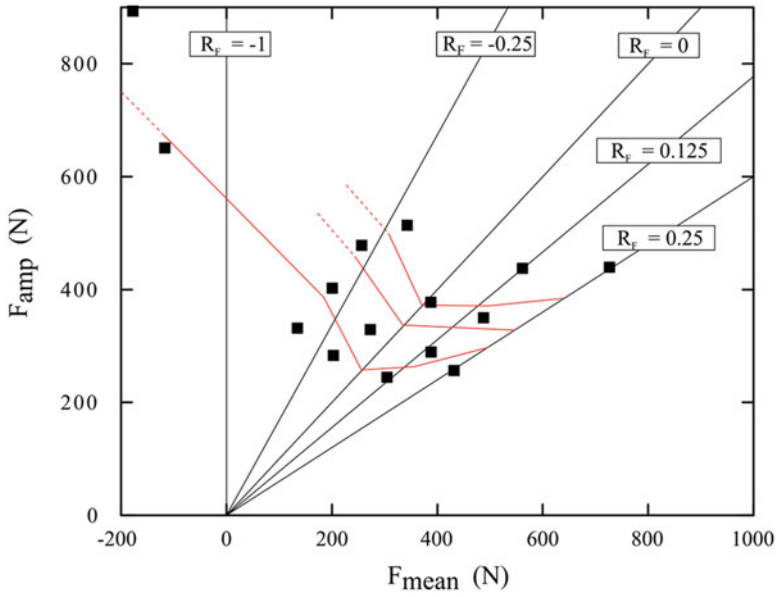

Fig. 8.3 Haigh diagram at 90 °C

8.3.1 Discussion

SIC plays a role of paramount importance in NR fatigue resistance. At 23 °C an important lifetime reinforcement was observed for non-relaxing loading conditions and attributed to SIC. This result was corroborated by the presence of SIC markers on the sample fracture surfaces: wrenchings and fatigue striation. Softer lifetime reinforcement and no SIC signatures were observed at 90 °C, confirming that SIC is strongly altered by the temperature increase. Nevertheless, the reinforcement is still observed. Different conclusions are drawn in comparison to Bathias and co-workers [22] who observed a similar reinforcement at 80 °C and at 23 °C, but for more important mean stress. Even though the crystallinity of filled NR is close to zero for static loading performed at 90 °C, the fatigue loading promote SIC and could be an explanation for the presence of a lifetime reinforcement at 90 °C. It also suggests that only a small value of crystallinity is sufficient to activate the fatigue reinforcement of NR.

8.4 Conclusion

Uni-axial fatigue tests including loading ratios from −0,25 to 0,35 were performed with filled NR at 23 °C and 90 °C. Both lifetime and fracture surface were considered and mapped in Haigh diagrams. Results confirm the high thermosensitivity of NR fatigue properties. Indeed, the material exhibits a strong lifetime reinforcement attributed to SIC at 23 °C. At 90 °C, a softer reinforcement remains for $0 > R_F > 0.25$. This result suggests that during non-relaxing fatigue the crystallinity at 90 °C would not be equal to zero and that only a small value of crystallinity would be sufficient to activate a reinforcement.

Acknowledgements The authors thank the Cooper Standard France company for supporting this work and for fruitful discussions. The authors thank also the National Center for Scientific Research (MRCT-CNRS and MI-CNRS) and Rennes Metropole for supporting this work financially. SEM images were performed at CMEBA facility (ScanMAT, University of Rennes 1) which received a financial support from the European Union (CPER-FEDER 2007-2014).

References

1. Cadwell, S.M., Merril, R.A., Sloman, C.M., Yost, F.L.: Dynamic fatigue life of rubber. Ind. Eng. Chem. (reprinted in Rubber Chem. and Tech. 1940;13:304–315). **12**, 19–23 (1940)
2. Beatty, J.R.: Fatigue of rubber. Rubber Chem. Technol. **37**, 1341–1364 (1964)

3. Lu, C.: Etude du comportement mécanique et des mécanismes d'endommagement des élastomères en fatigue et en fissuration par fatigue. PhD Thesis, Conservatoire National des Arts et Métiers (1991)
4. Svensson, S.: Testing methods for fatigue properties of rubber materials and vibration isolators. Polym. Test. **2**, 161–174 (1981)
5. Xie, J.: Etude de la fatigue et de la rupture des assemblages collés composite-élastomère. PhD Thesis, Ecole Centrale de Paris (1992)
6. Bathias, C., Gorju, K.L., Lu, C., Menabeuf, L.: Fatigue crack growth damage in elastomeric materials. In: ASTM Special Technical Publication, vol. 1296, pp. 505–513 (1997)
7. André, N., Cailletaud, G., Piques, R.: Haigh diagram for fatigue crack initiation prediction of natural rubber components. KGK-Kautschuk Gummi Kunststoffe. **52**, 120–123 (1999)
8. Robisson, A.: Comportement mécanique dÈun élastomère chargé en silice. Etude de lÈinfluence des charges et modélisation par une loi visco-hyperélastique endommageable. PhD Thesis, Ecole Nationale Supérieure des Mines de Paris (2000)
9. Saintier, N.: Prévisions de la durée de vie en fatigue du NR, sous chargement multiaxial. Thèse de doctorat, Ecole Nationale Supérieure des Mines de Paris (2001)
10. Le Cam, J.-B.: Endommagement en fatigue des elastomères. PhD Thesis, Ecole Centrale de Nantes (2005)
11. Le Cam, J.-B., Huneau, B., Verron, E.: Fatigue damage in carbon black filled natural rubber under uni- and multiaxial loading conditions. Int. J. Fatigue. **52**, 82–94 (2013)
12. Le Cam, J.-B., Verron, E., Huneau, B.: Description of fatigue damage in carbon black filled natural rubber. Fatigue Fract. Eng. Mater. Struct. **31**, 1031–1038 (2008)
13. Raoult, I.: Structures élastomères sous chargement cyclique : comportement, fatigue, durée de vie. Thèse de doctorat, Ecole polytechnique (2005)
14. Ostoja-Kuczynski, E.: Comportement en fatigue des élastomères : application aux Structure antivibratoires pour l'automobile. PhD Thesis, Ecole Centrale de Nantes, Université de Nantes (2005)
15. Poisson, J.-L.: Détermination d'un critère de fatigue multiaxial appliqué à un élastomère synthétique. PhD Thesis, Université François Rabelais, Tours (2012)
16. Neuhaus, C., Lion, A., Johlitz, M., Heuler, P., Barkhoff, M., Duisen, F.: Fatigue behaviour of an elastomer under consideration of ageing effects. Int. J. Fatigue. **104**, 72–80 (2017)
17. Roberts, B.J., Benzies, J.B.: The relationship between uniaxial and equibiaxial fatigue in gum and carbon black filled vulcanizates. **2**, 1–13 (1977)
18. Mars, W.V.: Multiaxial fatigue of rubber. PhD thesis, University of Toledo (2001)
19. Lindley, P.B.: Non-relaxing crack growth and fatigue in a non-crystallizing rubber. Rubber Chem. Technol. **47**, 1253–1264 (1974)
20. Fielding, J.H.: Flex life and crystallisation of synthetic rubber. Ind. Eng. Chem. **35**, 1259–1261 (1943)
21. Treloar, L.R.G.: The Physics of Rubber Elasticity. Oxford University Press, Oxford (1975)
22. Bathias, C., Houel, P., Berete, Y.N., Gorju, K.L.: Progress in durability Analysis of Composite Systems, pp. 103–109. Reifsnider & Cardon, Balkema (1998)
23. Duan, X., Shangguan, W.-B., Rakheja, M.L.e.S.: Measurement and modelling of the fatigue life of rubber mounts for an automotive powertrain at high temperatures. Proc. Inst. Mech. Eng. Part D: J. Automob Eng. **230**, 942–954 (2016)
24. Candau, N., Laghmach, R., Chazeau, L., Chenal, J.-M., Gauthier, C., Munch, T.B.e.E.: Temperature dependence of strain-induced crystallization in natural rubber: on the presence of different crystallite populations. Polymer. **60**, 115–124 (2015)

Chapter 9
In-situ Crack Tip Stress Measurement at High Temperature in IN-617 Using Combined Nano-Indentation and Nano-Mechanical Raman Spectroscopy

Yang Zhang, Chandra Prakash, and Vikas Tomar

Abstract In this work, the *in-situ* measurement of crack tip stresses in Inconel 617 at high temperature is presented. The temperature during loading in the current work was varied in the range from room temperature to 1073 K (800 $^{\circ}C$). Three-point bending tests for *in-situ* notch tip stress measurements with increasing load were performed. A Combined Nano indentation and Nano mechanical Raman spectroscopy (NMRS) methods are used to measure notch tip plasticity induced stress distribution. Optical microscopy and SEM imaging is used to analyze the effect of surface finish and oxidation on the Nano indentation measurements. An *in-situ* Nano mechanical Raman spectroscopy is used to obtain the stress distribution at the notch tip during three point bending. The size resolution of measurements of notch-tip stresses was in the range of few microns. Temperature dependent (up to 1073 K) material properties were studied in terms of hardness and elastic modulus variation as a function of temperature. Microstructure dependent local mechanical properties were obtained using Nano indentation and is used in the finite element simulation. A finite element method based formulation to predict microstructure and temperature dependent crack tip stresses is presented and validated using the experimental stress distribution obtained from NMRS.

Keywords Raman spectroscopy · Inconel 617 · Nano indentation · High-temperature

Stress distribution in the vicinity of a crack-tip plays an important role in the analysis of fracture and has received considerable attention in literature [1]. Irwin [2, 3], showed, using theoretical and experimental observations, that the elastic stress field near the tip of a sharp crack play a dominant role in the fracture of the material. Sih [4], proposed an analytical method to calculate stress distribution near internal crack tips. However, theoretical analysis of the crack-tip stress field is limited by the fact that the stress at the crack tip results in a singular stress field. To avoid this singularity in the theoretical analysis, experimental and numerical analysis are needed in order to obtain the crack tip stress field. Several existing experimental methods such as X-ray diffraction (XRD) [5] and cross-sectional transmission electron microscopy (XTEM) [6] are available to measure stress distribution at small scale. Raman spectroscopy is one such method to measure the stress and was first introduced by Anastassakis et al. [7] to measure the mechanical stress inside silicon. This method has been used and developed extensively to investigate stress distribution in materials, especially silicon structures. Compared to the other available methods for stress measurement, Raman spectroscopy method is a non-destructive technique, requires minimal sample preparation, and has spatial resolution of less than one micron that makes it suitable for microscale to nanoscale samples. Most importantly, this method is also suitable for the measurement of temperature [8, 9] and thermal conductivity [10, 11] along with stress.

The material that is being studied in this work is the alloy IN-617 which mainly contains nickel (Ni), chromium (Cr), cobalt (Co) and molybdenum (Mo). IN-617 is widely used in high temperature applications due to its high temperature stability and strength as well as its strong resistance to oxidation and carburization. In very high temperature reactor (VHTR) in nuclear industry, a structural and functional material is needed for the intermediate heat exchanger (IHX) which operates above 850 °C [12]. IN-617 is a candidate material for the IHX. IN-617 has also gained extensive attention for applications in steam generators of ultra-supercritical fossil fuel power plants. Such high temperature application materials requires an extensive studies of their mechanical and fracture properties at high temperatures. In this research, a combined Nano indentation and Nano mechanical Raman spectroscopy (NMRS) methods (developed by Gan and Tomar, [13–15]) is used to measure mechanical properties and crack tip stress distribution at high temperature.

Y. Zhang · C. Prakash · V. Tomar (✉)
School of Aeronautics and Astronautics, Purdue University-IN, West Lafayette, IN, USA
e-mail: tomar@purdue.edu

J. Carroll et al. (eds.), *Fracture, Fatigue, Failure and Damage Evolution, Volume 6*, Conference Proceedings of the Society for Experimental Mechanics Series, https://doi.org/10.1007/978-3-319-95879-8_9

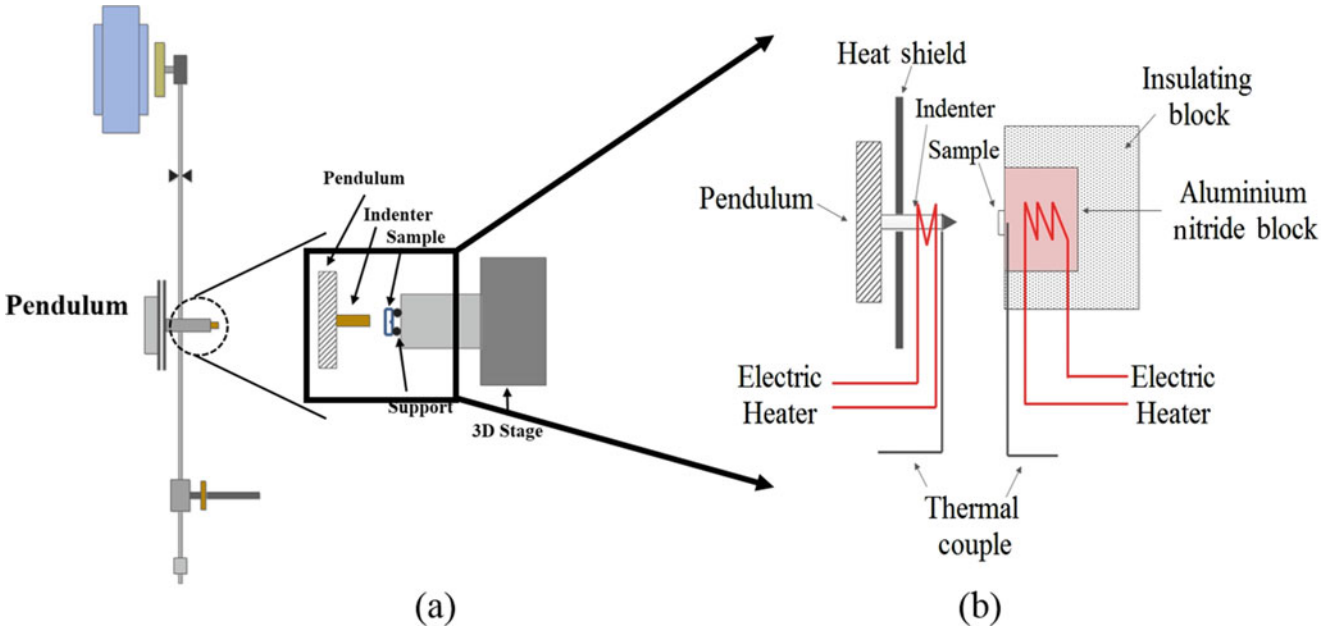

Fig. 9.1 (**a**) Experimental set-up of Nano indentation and (**b**) high temperature apparatus

The overall schedule had three steps for one set of experiments. The first step is to make indentations around the notch tip on the uncoated surface of sample before the bending. These tests are used to determine indentation based stress-train curve in the area before 3-point bending. Thereafter, while applying load to bend the sample, Raman scanning was performed around the notch tip at the coated surface using the NMRS. The Nano indentation experiments were performed under a multi-functional Nano mechanical platform (Micro Materials Ltd., UK) [16, 17], shown in Fig. 9.1. Figure 9.1a is the Nano indentation experimental setup and Fig. 9.1b depicts the setup explaining the approach to perform high temperature indentation. As shown in Fig. 9.1b, at high temperatures, both of the indenter tip and sample were heated to the desired experimental temperature, which was measured and adjusted using thermocouples and its feedback circuit instantaneously. The rest of the parts of the experimental platform were separated by a thermally insulated shield in order to maintain those parts at room temperature.

Indentation tests were performed at room temperature, 400 °C and 800 °C. A Berkovich type indenter made of diamond with tip radius of 20 nm was used for Nano indentation at room temperature and 400 °C, and a CBN (cubic boron nitride) indenter was used at 800 °C. The two indenter tips possess identical geometry. During the experiments, the examined samples were firmly mounted on the hot stage platform using high temperature adhesive to prevent any relative movement during the tests [18]. After both the indenter and the stage reached desired measurement temperature, the setup was kept inactive for one more hour per hundred degree of temperature increase in order to achieve thermal stability. Locations of indented area were chosen in a random way on the surfaces of samples. The elastic modulus and the hardness values of IN-617 samples are plotted in Fig. 9.2 under different maximum loads and temperatures. Poisson's ratio of IN-617 is taken to be 0.3 based on literature [19]. It is observed that the elastic modulus of IN-617 is highly dependent on temperature but not affected by the indentation load and depth. After the high temperature and area calibration, the elastic modulus values under different temperature are very close to the literature values of bulk material.

Next, the stress distribution around a notch is studied using NMRS. The samples used in this research were subjected to 3-point bending based mechanical loading applied by a modified nano-scale loading platform. In order to detect the Raman signal, a 1.0 micrometer thick layer of silicon was deposited on the surface of metals that creates negligible Raman shift phenomenon. The schematic diagram of the experimental setup is shown in Fig. 9.3a. For the 3-point bending tests, the samples were cut into small pieces according to the ASTM D5045 standard with the dimension of 8.8*2.0*0.5 mm, as shown in Fig. 9.3b, with the length of crack equal to 1.0 mm and the width 0.2 mm. After cutting, the samples were mechanically polished, electrolytically polished and etched.

As mechanical load is applied along one axis, the Raman laser is focused onto the side surface using an objective. Back-scattered Raman signal is collected by the same objective and sent to a spectrometer. The temperature as well as stress change affect the position of Raman peak. In this work, both full width half maximum (FWHM) and Raman shift were detected and evaluated at different temperatures. The temperature of sample, which was obtained from FWHM measurement, is used to

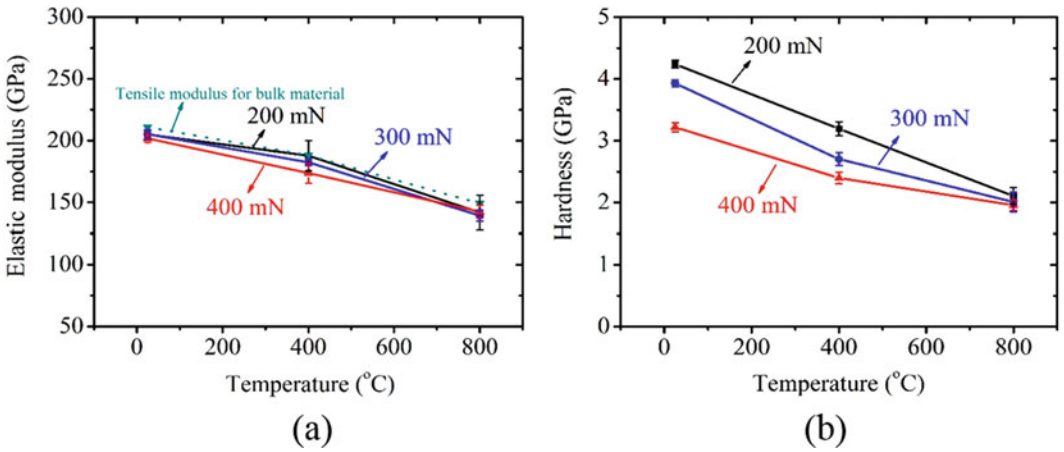

Fig. 9.2 Effect of temperature and peak indentation load on (**a**) elastic modulus (tensile modulus data is taken from Smith and Yates [20]) and (**b**) hardness of Alloy 617

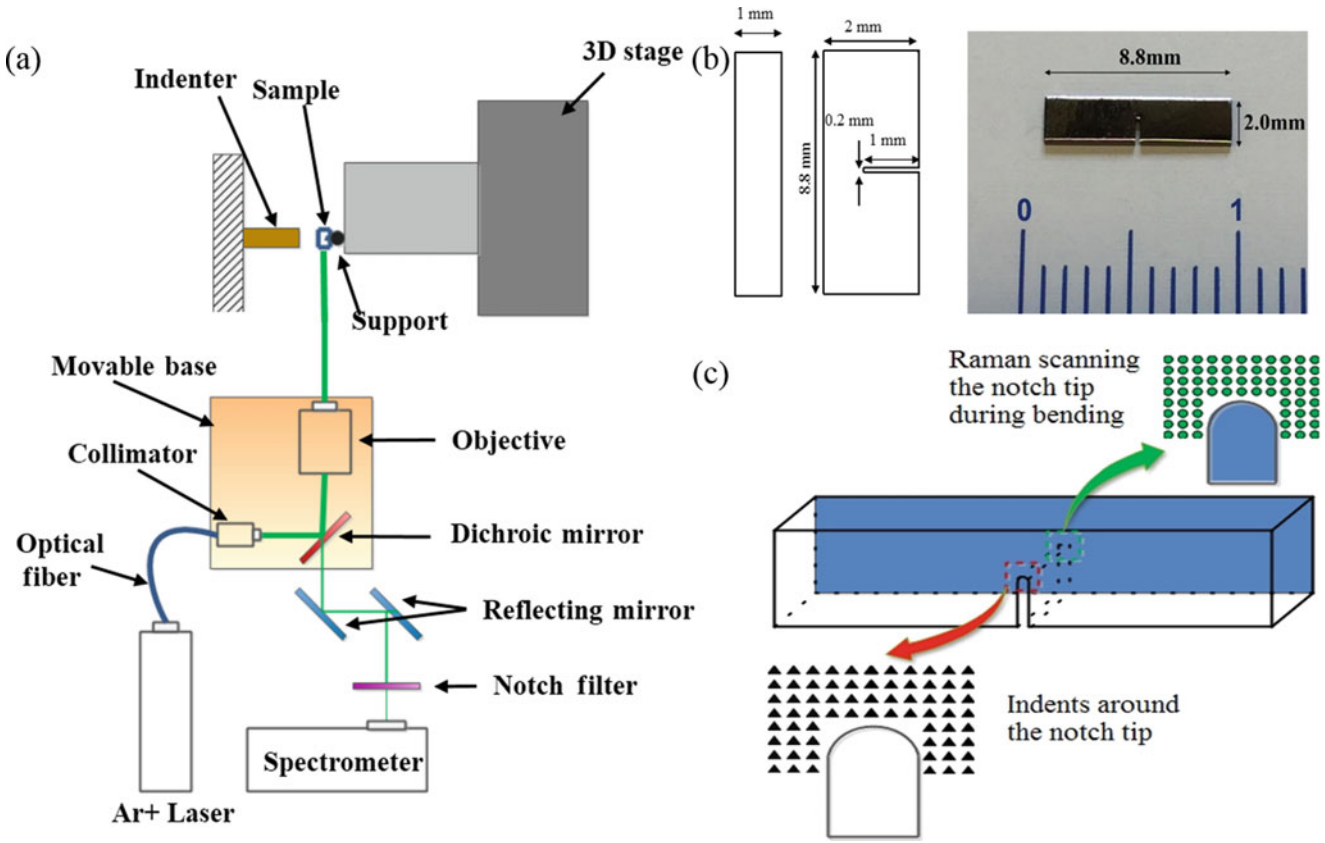

Fig. 9.3 (**a**) Nano-mechanical Raman experimental set-up, (**b**) 3-point bending sample and dimensions, and (c) scan area for Raman and indentation area around the notch

separate the temperature-induced Raman shift from the stress-induced Raman shift [20]. After separating temperature effect on Raman shift and combining the stress information from each measuring point, a contour figure of stress distribution around the notch tip can be plotted. Overall 72 indentations (and corresponding Raman spectrums) were scanned to get the mechanical properties mapping, stress distribution and temperature field. For each spectrum, at least 3 repeated tests were performed to eliminate measurement error. Grain boundary and grain structure play an important role in the mechanical property of polycrystalline material. In this research Orientation Image Microscopy (OIM) [21, 22] which was an automated indexing of electron back-scattered diffraction (EBSD) pattern was used to obtain the characteristic of microstructure.

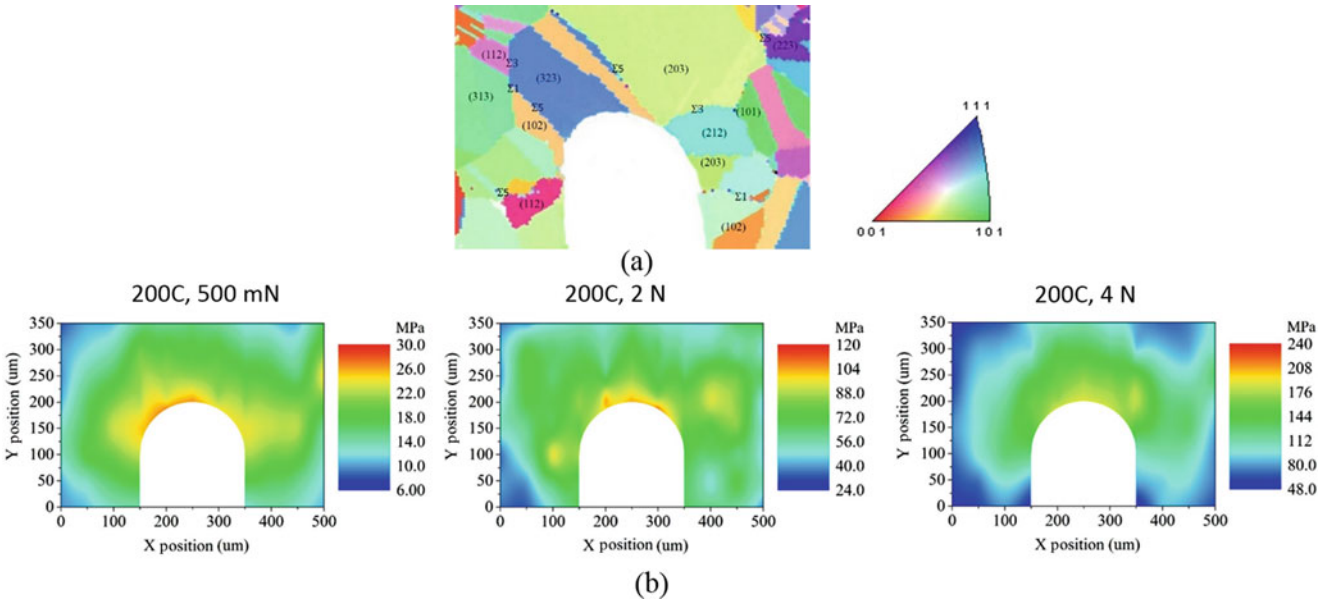

Fig. 9.4 (**a**) EBSD map of the notched sample and (**b**) stress distribution around the notch at 200 °C for increasing load during 3-point bending

The microstructural information obtained from the Raman scanned area using OIM was correlated to the stress distribution data that obtained from Nano mechanical Raman spectroscopy. Through the comparison of stress distribution mapping for different samples under different loads, it is known that the stress is concentrated and higher at the notch tip as expected for any kinds of microstructure. Additionally, notch tip stress increase with the bending load but not proportional to the load due to the plasticity at the notch tip.

The average temperature of the sample during the test was 200 °C, which was monitored by thermocouples. However, the temperature along the notch edge was little lower due to heat convection to the ambient air with obvious lower temperature inside the notch. And the difference of temperature at different area was due to difference of thermal conductivity that was affected by the precipitates on the surface, microstructure of surface and the stress conditions. After subtracting the temperature-induced Raman shift contribution, the remaining Raman shift was used to calculate stress. Stress values at every points around the notch tip was measured. Contour plots that depicted stress distribution of around the notch tip under loads of 500 mN, 2 N and 4 N at the overall temperature of 200 °*C* were also shown in Fig. 9.4b. The temperature field and stress distribution are affected by the microstructure of the notch area and the precipitates.

Due to the combined effect of the grains and grain boundary present in the microstructure, a detailed analysis of stress distribution would require a complex numerical simulation model, which requires grain dependent properties. However, for such complex systems, experimental data, especially at high temperature is very limited. Therefore, an alternate model based on the local mechanical properties obtained from Nano indentation is used in this work. The finite element model with the relevant boundary conditions are shown in Fig. 9.5a. Alloy 617 has a microstructure with an average grain size of approximately 150 microns. For each grain, elastic-plastic stress strain curves were obtained with spacing of 50 microns by converting the load-displacement data obtained from Nano indentation [23]. Instead of considering actual grain structures, different elastic and plastic material properties which were obtained from indentation experiments around the notch area were applied to the same area with 68 small rectangular zones of 50 by 50 microns. Figure 9.5b shows the grid used for such calculations. For each grain average stress-strain behavior was based on spatial average of such curves. These stress-strain curves were fitted to a J2 plasticity model. The validated J2 plasticity model for each grain was taken as a representative for its elastic-plastic deformation behavior. Finite element simulations based on the use of the local experimental data for the grid shown in Fig. 9.5b leads to the incorporation of averaged microstructure effects and plasticity. In the rest of sample, average material properties that were also obtained from the experiments was applied. Stress distribution around the notch tip obtained from NMRS experiment is shown in Fig. 9.5d and that from finite element simulation is shown in Fig. 9.5e. Difference between the experiments and simulations at other points in microstructure away from the notch can be attributed to the residual stresses due to grain boundaries and precipitates. Magnitude-wise, however, stresses are in the same range in the scanned area using NMRS bringing simulations and experiments close in terms of stress prediction.

In the current research, a combined NMRS and Nano indentation experimental procedure was developed to measure crack (notch) tip stresses during in-situ mechanical deformation at high temperature. Based on the Nano indentation stress-strain

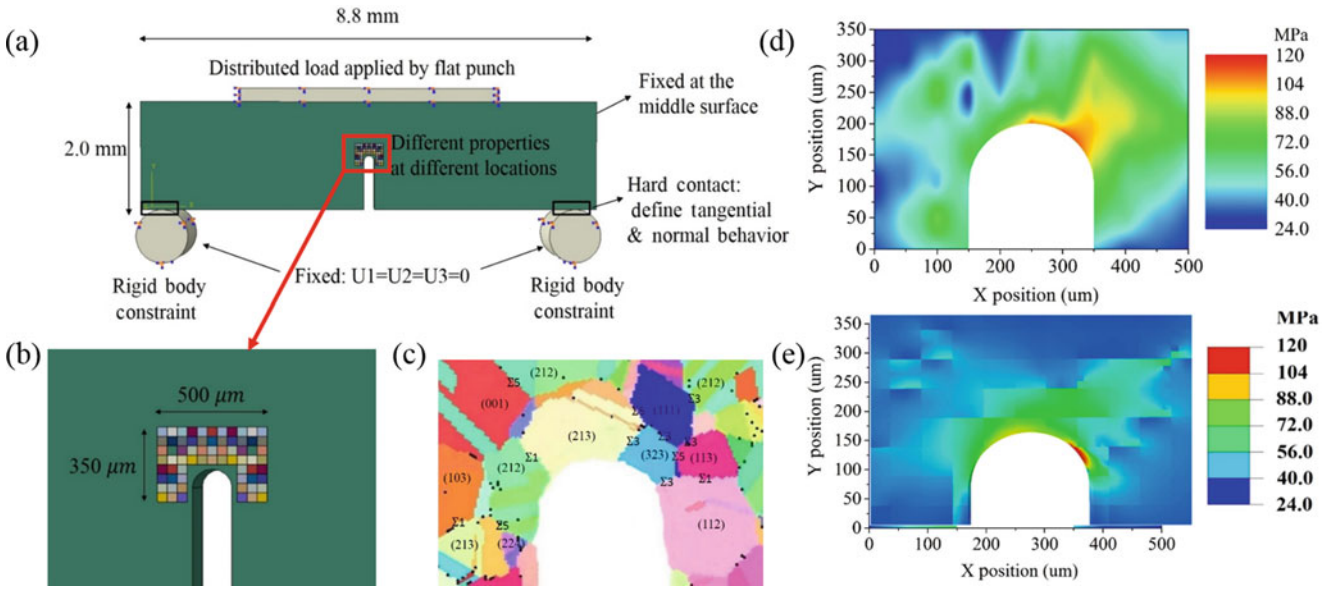

Fig. 9.5 (**a**) Finite element model of the 3-point bending specimen, (**b**) grid used to include experiment based properties, (**c**) EBSD map of the sample being loaded and stress distribution around the notch at room temperature obtained by (**d**) experiment and (**e**) simulation

curve, the Elastic modulus and the hardness at the notch tip was found to decrease with increase in temperature. A small area around notch tip of sample during 3-point bending tests was scanned to obtain Raman spectra at different load. A relation between the stress, temperature and Raman shift was used to obtain temperature field and stress distribution in the notch tip scanned area, by combining Raman peaks at each scan point. A significant effect of temperature change induced residual stress was observed. In order to avoid the complexities in considering actual grain structures with different material properties, a new FE method was adopted to predict stress distribution around the notch area. Predictions from simulations matched closely in stress concentration area near notch with NMRS experimental measurements. However, away from notch area deviation in simulation and experimental predictions due to microstructural effects was observed.

Acknowledgments This work is partially supported by a DoE-NEUP Grant DE-NE0000722 (Yang Zhang and Vikas Tomar) and a US-AFoSR Grant FA9550-15-1-0202 (Program Manager Dr. Martin Schmidt) (Chandra Prakash and Vikas Tomar).

References

1. Savruk, M.P., Kazberuk, A.: Stress Concentration at Notches. Springer, Cham, Switzerland (2017)
2. Irwin, G.R.: Fracture. In: Flugge, S. (ed.) Encyclopedia of Physics, pp. 551–590. Springer, Berlin (1958)
3. Irwin, G.R.: Analysis of stresses and strains near the end of a crack traversing a plate. J. Appl. Mech. **24**, 361–364 (1957)
4. Sih, G.C.: Stress distribution near internal crack tips for longitudinal shear problems. J. Appl. Mech. **32**(1), 51–58 (1965)
5. Flinn, P.A., Waychunas, G.A.: A new x-ray diffractometer design for thin-film texture, strain, and phase characterization. J. Vac. Sci. Technol. B. **6**(6), 1749–1755 (1988)
6. Armigliato, A., et al.: Determination of lattice strain in local isolation structures by electron-diffraction techniques and micro-Raman spectroscopy. In: Microscopy of Semiconducting Materials. CRC Press, Boca Raton (1993)
7. Anastassakis, E., et al.: Effect of static uniaxial stress on the Raman spectrum of silicon. Solid State Commun. **8**(2), 133–138 (1970)
8. Kim, S.H., et al.: Micro-Raman thermometry for measuring the temperature distribution inside the microchannel of a polymerase chain reaction chip. J. Micromech. Microeng. **16**(3), 526–530 (2006)
9. Phinney, L.M., et al.: Raman thermometry measurements and thermal simulations for MEMS bridges at pressures from 0.05 Torr to 625 Torr. J. Heat Transf. **132**(7), 072402 (2010)
10. Abel, M.R., Graham, S.: Thermometry of polycrystalline silicon structures using Raman Spectroscopy. In: Advances in Electronic Packaging, Pts A–C. American Society of Mechanical Engineers, New York (2005)
11. Périchon, S., et al.: Measurement of porous silicon thermal conductivity by micro-Raman scattering. J. Appl. Phys. **86**(8), 4700–4702 (1999)
12. Benz, J.K., et al.: Threshold stress creep behavior of alloy 617 at intermediate temperatures. Metall. Mater. Trans. A. **45**(7), 3010–3022 (2014)
13. Gan, M., Samvedi, V., Tomar, V.: Raman spectroscopy-based investigation of thermal conductivity of stressed silicon microcantilevers. J. Thermophys. Heat Transf. **29**(4), 845–857 (2014)

14. Gan, M., Tomar, V.: An in situ platform for the investigation of Raman shift in micro-scale silicon structures as a function of mechanical stress and temperature increase. Rev. Sci. Instrum. **85**(1), 013902 (2014)
15. Gan, M., Tomar, V.: Surface stress variation as a function of applied compressive stress and temperature in microscale silicon. J. Appl. Phys. **116** (7), 073502 (2014)
16. Prakash, C., et al.: Effect of interface chemistry and strain rate on particle-matrix delamination in an energetic material. Eng. Fract. Mech. **191**, 46–64 (2018)
17. Verma, D., Prakash, C., Tomar, V.: Properties of material interfaces: dynamic local versus nonlocal. In: Voyiadjis, G. (ed.) Handbook of Nonlocal Continuum Mechanics for Materials and Structures, pp. 1–16. Springer, Cham (2017)
18. Gan, M., Tomar, V.: Role of length scale and temperature in indentation induced creep behavior of polymer derived Si–C–O ceramics. Mater. Sci. Eng. A. **527**(29–30), 7615–7623 (2010)
19. Zhang, Y., et al.: High temperature indentation based property measurements of IN-617. Int. J. Plast. **96**, 264–281 (2017)
20. Zhang, Y., Gan, M., Tomar, V.: Raman thermometry based thermal conductivity measurement of bovine cortical bone as a function of compressive stress. J. Nanotechnol. Eng. Med. **5**(2), 021003–021003 (2014)
21. Pathak, S., et al.: Studying grain boundary regions in polycrystalline materials using spherical nano-indentation and orientation imaging microscopy. J. Mater. Sci. **47**(2), 815–823 (2011)
22. Adams, B.L.: Orientation imaging microscopy: emerging and future applications. Ultramicroscopy. **67**, 11–17 (1997)
23. Kalidindi, S.R., Pathak, S.: Determination of the effective zero-point and the extraction of spherical nanoindentation stress–strain curves. Acta Mater. **56**(14), 3523–3532 (2008)

Chapter 10
Modification of Benthem Solution for Mode I Fracture of Cylinder with Spiral Crack Subjected to Torsion

Ali Fahad Fahem and Addis Kidane

Abstract In this paper, a Benthem asymptotic solution is adapted and modified for a linear elastic fracture mechanics of a V-notch spiral crack. A spiral crack on a cylindrical sample is implemented to quantify the mode I fracture toughness of materials subjected to pure quasi-static torsion. The torque corresponding to fracture initiation is measured experimentally and used with a modifying Benthem solution to quantify the fracture parameter. A geometric factor for a cylinder specimen with a spiral crack on the surface is developed by finite element simulation. The proposed solution, along with stress intensity factor data of different materials, is presented here as a benchmark work. The results show that the proposed formula of the stress intensity factor for spiral crack cylinder specimen is in agreement with the other conventional methods, with an average error of less than 5%. The stress distribution and details of the experimental and numerical analysis are discussed.

Keywords Spiral crack · Pure torsion · Benthem solution · Configuration factor · Stress intensity factor

10.1 Introduction

The linear elastic fracture mechanics approach began with Grift [1], and in 1957 [2], Irwin presented the crack tip characterizing parameter of fracture mechanics which is **Stress Intensity Factor** SIF, (K_i) Eq. (10.1). In general, Eq. (10.1), is used with an infinite body that has content flaws. However, to be able to use SIF in engineering applications, a configuration factor (Y) is used to determine the SIF from remote loads and a finite geometry Eq. (10.2).

$$K_k = \sigma^k \sqrt{\pi c} \tag{10.1}$$

$$K_k = \sigma^k \sqrt{\pi c} \times Y^k \tag{10.2}$$

Where:

σ^k far-field stress;
c crack depth;
k loading mode, I, II, and III (no-sum).

Finally, a configuration factor Y which is dimensionless and depending on the geometry and the far field load conditions is as follows:

$$Y = Y(geometry, Far - field - load) \tag{10.3}$$

There are different methods for evaluates the configuration factor Y: The Boundary Collection Method, Boundary Stress Correction Method, Finite Element Methods, Least Square Method, Asymptotic Approximation, Green Function method, Mapping Function Method and more. The handbooks of fracture mechanics give in-depth descriptions of configuration factor Y in a different geometry and load condition [3, 4].

There are few valid experimental methods used to evaluate fracture toughness of materials [5–7]. However, the scientific committee is still working to develop methods to predict the dynamic fracture toughness of materials accurately.

A. F. Fahem (✉) · A. Kidane
University of South Carolina, Columbia, SC, USA
e-mail: afahem@email.sc.edu

J. Carroll et al. (eds.), *Fracture, Fatigue, Failure and Damage Evolution, Volume 6*, Conference Proceedings of the Society for Experimental Mechanics Series, https://doi.org/10.1007/978-3-319-95879-8_10

A cylindrical specimen subjected to pure torsion load results in mode I fracture along a spiral crack on the surface. This condition inspires the researchers to study it and use it in laboratory fracture experimental work. A circumferential crack around the cylindrical bar was used to measure a mode-III of fracture mechanics [8–11].

The fracture toughness of mode-I is larger and more important than mode III as a fracture toughness of material [12]. For this point, Sweeney and Truss used a circular bar with a small crack inclined at 45° with the center of the bar [13, 14]. In this case, they assume the crack is semielliptical under a pure uniform tension load which is physically not valid. More realistic work is done by Wang, the experimental and the numerical simulation of a full spiral crack were used to calculate the fracture toughness of materials in a static case [15, 16]. Recently, the Torsional Spilt Hopkinson Bar and a numerical solution were used to measure the dynamic fracture initiation toughness of material with a full spiral crack model [17, 18].

In general, the cylindrical bar with a spiral crack subjected to pure torsional load is a new successful configuration that is used to find the fracture toughness of material. However, no mathematical setup, up to this article, is available. In this work, a numerical solution and a curve-fitting method were used to develop the novel mode I stress intensity factor K_I equation and novel configuration factor (Y) for cylindrical specimen with spiral cake subjected to torsion loading, and verify the result experimentally.

10.2 SIF and Geometry Factor of Spiral Crack

The finite element analysis of a spiral crack is used to calculate the Mode I stress intensity factor K_I. The model is a solid cylindrical bar with full external spiral crack subjected to pure torsion load as shown in Fig. 10.1a. The commercial package software, ABAQUS, was used to create a three-dimensional model and mesh it with 40,000 C3D20H elements as shown in Fig. 10.1b.

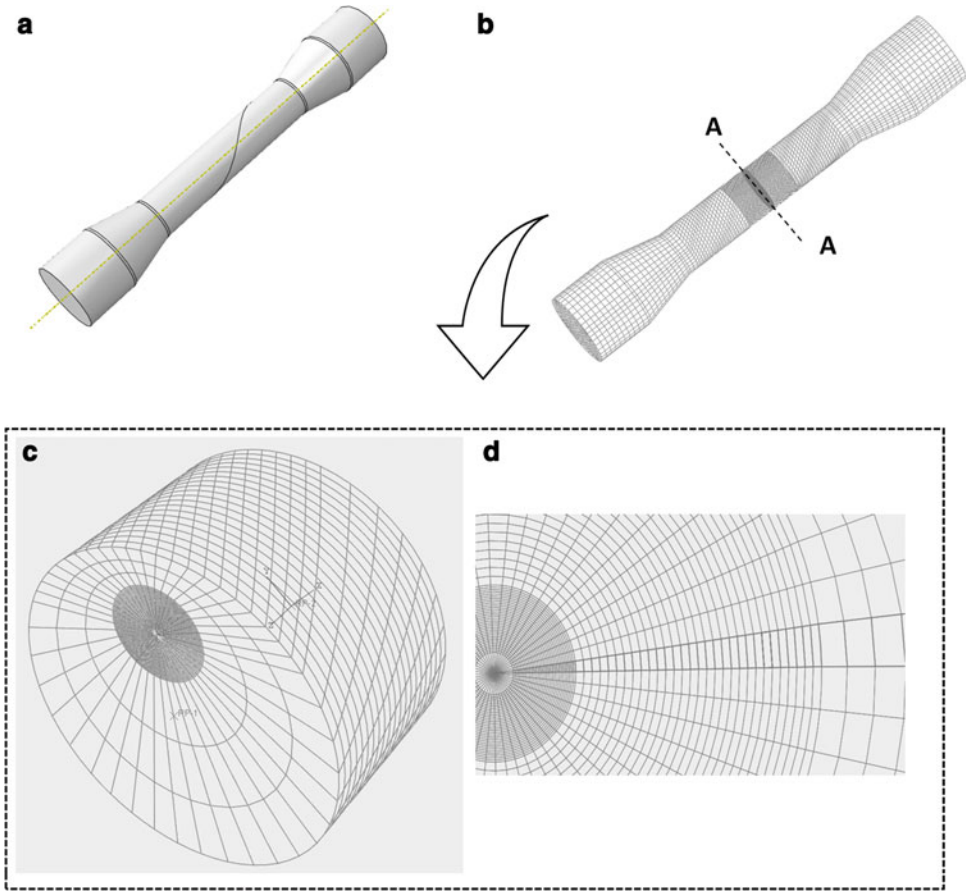

Fig. 10.1 FE Model of a Spiral Crack. (**a**) Solid model. (**b**) Meshing model. (**c**) 3D-concentared mesh at crack tip (A-A). (**d**) 2D-fan meshing around crack tip

Table 10.1 SIF Result of FE model of Spiral Crack

Repeat No.	$\left(\frac{c}{r}\right)$	K_I^s $MPA\sqrt{m}$
1	0.1	1.9107
2	0.15	2.354
3	0.2	2.6454
4	0.31	3.2014
5	0.4	3.5062
6	0.6	4.0454
7	0.8	4.4336
8	0.92	4.5585

To quantify the SIF across the spiral crack tip numerically, the model is idealized as linear isotropic material. The Aluminum model has a gauge diameter of 20.3 mm, the spiral pitch 63.75 mm, Elastic Modulus E = 70GPa and Poisson's ratio $\nu = 0.3$. The spiral crack is generated by a dully revolving shell around the cylinder with 45°. The boundary conditions and the load applied at the ends of the bar as follows. One end, where z = 0, translation and rotation motions are fixed (u = v = w = Rx = Ry = Rz = 0), and at another end, z = L, a uniform torsional load is applied (Tz = T) and all other degree are fixed (u = v = Rx = Ry = 0) [17, 19, 20]. Another boundary conditions are to support the model to avoid any bending or buckling effect, and also to reduce nonlinear error, see [21] for more details. A strong concentric fan mesh around the crack tip was made to achieve the singularity behavior at the crack tip Fig. 10.1c, d [22]. The elements at the singularity dominated zone (crack tip) have the smallest length and the smallest circumference distribution angles [17]. The elements were concentrated in the mid-section of the model to avoid the nonlinearity effect that can come from the boundary condition as shown in Fig. 10.1b. In the static analysis step, the SIF was calculated numerically at each node along the crack tip, a calculation which depends on maximum strain energy release rate theory. The model is repeated sufficient times with a difference crack depth and constant gage diameter. The average's of SIF at each aspect ratio is extracted and documented as shown in Table 10.1.

theoretically, the mode I stress intensity factor of solid bar K_I^s with an external spiral crack that is subject to torsional load can be calculated as following Eq. (10.4):

$$K_I^s = \tau_{\max}\sqrt{\pi c} \times Y(a, c, r_o) \tag{10.4}$$

$$\tau_{\max} = \frac{Tr_o}{J} \quad \text{and} \quad J = \frac{\pi}{2} r_o^4 \tag{10.5}$$

Where r_o is the external radius, a is the crack ligament, c is the crack depth, $\tau_{\max}$ is maximum shear stress at the section far from the crack. Rearrangement Eq. (10.4), the configuration factor is [23]:

$$Y(a, c, r_o) = \frac{K_I^s}{\tau_{\max}\sqrt{\pi c}} \tag{10.6}$$

The result of FE solution was used with Eq. (10.6) to calculate the new configuration factor of spiral crack $Y(a, c, r_o)$. Furthermore, related to the Benthem solution, the configuration factor is composed of two parts Eq. (10.7):

$$Y(a, c, r_o) = f(a, r_o) \times G\left(c, r_o, P_{f/l}\right) \tag{10.7}$$

Where P_{flL} is the ratio of far-field load to local field load.

First, the *f-function* term is a function dependent on the relation between the crack ligament and bar radius. This term does not depend on the load, it is still the same as a circumferential crack, as follow Eq. (10.8).

$$f(a, r_o) = \sqrt{\frac{a}{r_o}} \tag{10.8}$$

Second, the $G - function$ is a function of the crack depth to bar radius and remotely loaded ratio to local load. Substitute Eqs. (10.5, 10.7, 10.8) into Eq. (10.6), then the $G - function$ is:

$$G(c, r_o) = \frac{K_I^s r_o^{(7/2)}}{2T}\sqrt{\frac{\pi}{ac}} \rightarrow (Dimensionless) \tag{10.9}$$

Table 10.2 G-function with a different aspect ratio

Repeat No.	$\left(\frac{c}{r}\right)$	*G-function*
1	0.1	0.948
2	0.15	0.982
3	0.2	0.984
4	0.31	1.025
5	0.4	1.065
6	0.6	1.228
7	0.8	1.65
8	0.92	2.26

The numerical values of SIF, Table 10.1, and the *f-function* at a different aspect ratio (c/r_o) are substituted in Eq. (10.9) to calculate the *G-function*, Table 10.2. Later, the curvetting performances will be used to provide a polynomial equation of the *G-function*, that can cover the range of aspect ratios.

10.3 Experiment Approaches

The Polycarbonate material is used to verify a new formula of SIF of spiral crack, Eq. (10.4). The material was used as received from the McMaster store. Five experimental specimens of a cylindrical bar with spiral crack were prepared. The specimen was manufactured with a different aspect ratio (c/r_o). The dimensions of the specimen are shown in Fig. 10.2. The crack depth is 6, 6.5. 7, 7.5, and 8 mm for each specimen respectively. The test performs with angular displacement controlled. The loading rate is 1 deg./min. The torque, normal load and vertical displacement were developed and recorded through the load cell of Test Resources machine. The crack dimension was measured after the specimen broke by using a VHX-5000 digital microscope.

The typical experimental result of load-twisting is shown in Fig. 10.3. The fracture load, crack depth, and bar radius is measured experimentally and will be used with the Eqs. (10.4, 10.5 and 10.7) to estimate SIF and fracture toughness of polycarbonate materials as shown in the result section.

10.4 Result and Discussion

The curve-fitting performance is used to provide the polynomial equation for the *G-function* to cover whole the range of aspect ratio Eq. (10.11). The final form of new forms of SIF of spiral crack at 45° is shown in Eq. (10.10). The variation of configuration factors of *G-function* with the aspect ratio for pure mode-I of the solid bar is shown in Fig. 10.3. As a measurable element result, the trade of a configuration term (G) in Fig. 10.3 is similar to the solution of Bentham for a circumferential crack under torsion. The difference is the order of values. The geometry factor of a spiral crack is larger than the geometry factor of circumferential crack.

$$KI = \tau_{\max}\sqrt{\pi c} \times Y(a, r_o, c) \tag{10.10}$$

Where:

$$Y(a, r_o, c) = \sqrt{\frac{a}{r_o}} \times G\left(\frac{c}{r_o}\right) \tag{10.11}$$

Equations (10.10 and 10.11) are performed with the five successful spiral cracks experimental test. The experiment was performed at room temperature with polycarbonate material. At each test, the fracture torque was extracted and used with Eq. (10.5) to calculate the maximum shear stress applied. The $f(a, r_o)$ was calculated by using Eq. (10.8) and the G calculated from Fig. 10.3. These values substituted in Eq. (10.10) to calculate the SF. The procedure was repeated for all five specimens. At the fracture torque, the stress intensity factor represents the fracture toughness of the material. The mean value of these five experimental tests is $K_{Ic} = 3.814MPa\sqrt{m}$ with a standard deviation of $\overline{\sigma}_{K_{Ic}} = 0.06MPa\sqrt{m}$ as shown in Table 10.3.

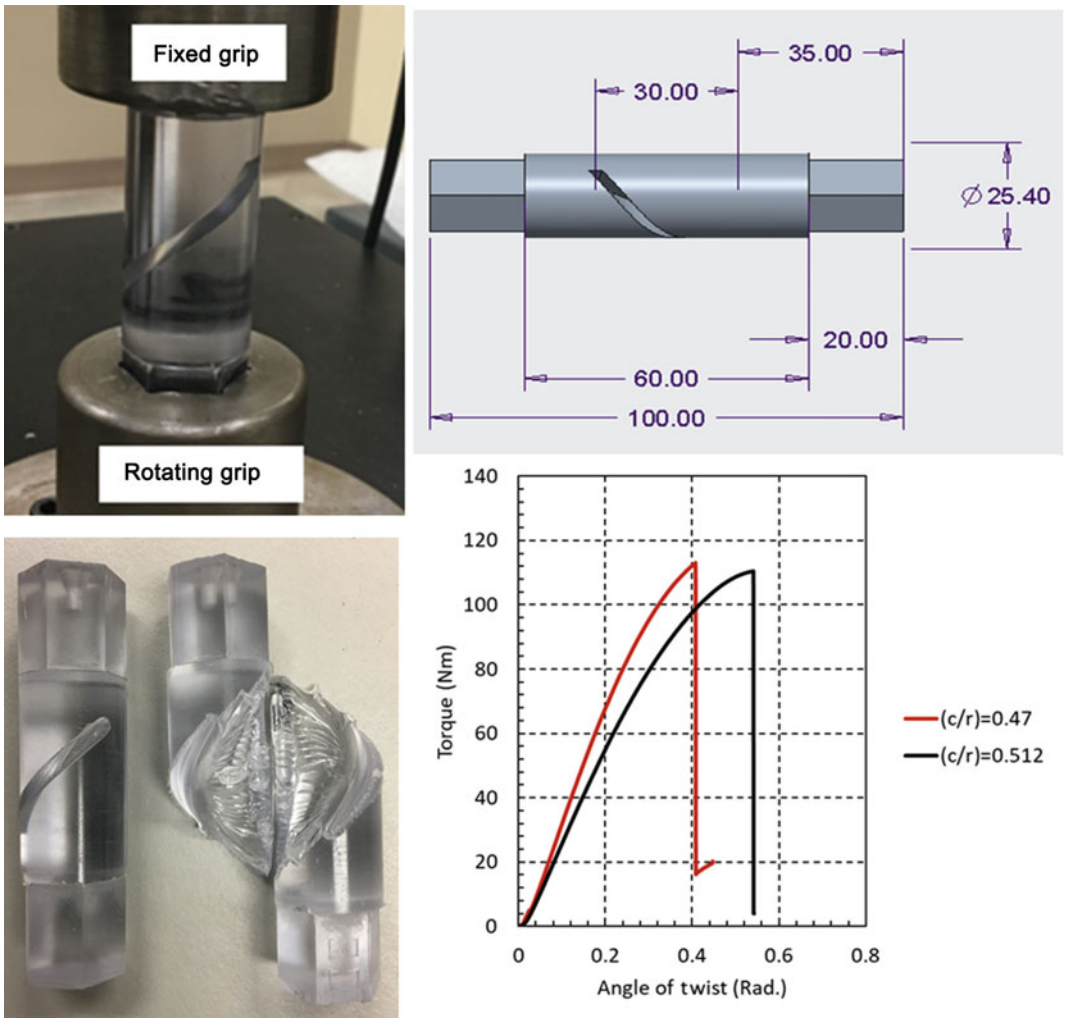

Fig. 10.2 Experimental setup, specimen dimensions, and Typical Load-Twisting data

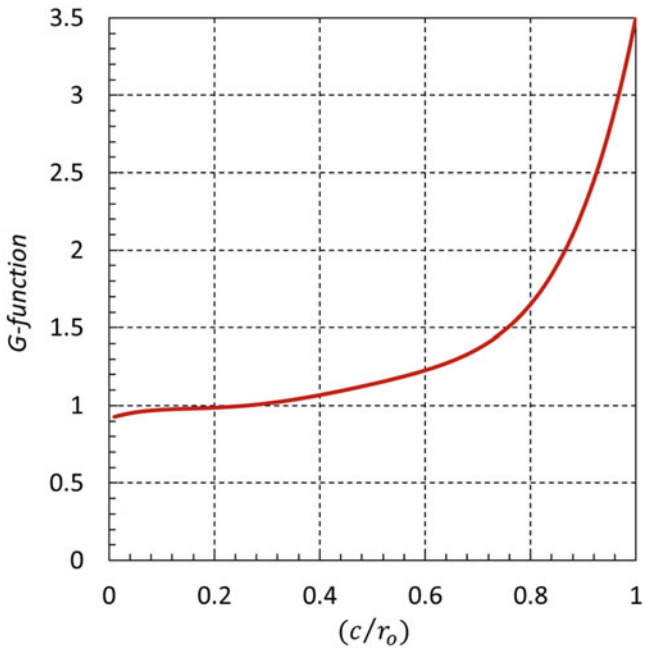

Fig. 10.3 Configuration factor of a solid bar with spiral crack subjected to pure torsion

Table 10.3 Spiral Crack Under Pure Torsion Load

$\left(\frac{c}{r}\right)$	Material	T (Nm)	r (mm)	c (mm)	a (mm)	G (Eq.10.10)	F_1(Eq.10.7)	K_I (Eq.10.9)	K_I Average
0.47	Poly.	113.090	12.7	6.0	6.74	1.117	0.767	3.886	3.814 $(MPa\sqrt{m})$ (SD = 0.06)*
0.51	Poly.	110.609	12.7	6.5	6.2	1.148	0.821	3.914	
0.55	Poly.	104.400	12.7	7.0	5.7	1.181	0.74	3.810	
0.59	Poly.	101.550	12.7	7.5	5.2	1.218	0.768	3.780	
0.64	Poly.	94.662	12.5	8.0	4.5	1.273	0.8	3.741	

*SD is a Standard Deviation

Table 10.4 Benchmark of Spiral Crack and 3 PB Laboratory Work

Material	Torsion Test K_{Ic} Eq. (13)	Ref. [21]	%Error	K_{Ic}
Polycarbonate	**3.814** $MPa\sqrt{m}$	**3.878** $MPa\sqrt{m}$	**1.7**	**Yes**

A comparison between a standard value of SIF with the result of the new formula Eq. (10.10) is shown in Table 10.4. The spiral crack with a new mathematical formula predicted the fracture toughness of material very well, compared with the literature value, with the percentage of error less than 1.7%.

10.5 Conclusion

A novel mathematical solution of spiral crack under pure torsion load was developed by using finite element methods and Bentham equations. The finite element modeling has been used to obtain the SIF of a full spiral crack subjected to remote pure torsion load. The SIF and maximum shear stress are used to extract a geometry factor for different aspect ratios and used to get the geometric factor curve, the formula is validated experimentally. A result of fracture toughness was found from a spiral crack at a fracture load and agrees with literature data. The error between the new formula and a standard formula is less than 1.7%. The result shows that the new formula of spiral crack is geometry independent and it works under plane strain condition. The new formula can be used to calculate SIF and fracture toughness of materials by measuring the torsional fracture load and dimensions of the crack and specimen.

Acknowledgment Mr. Ali Fahem was financially supported by Ministry of Higher Education and Scientific Research, University of Al-Qadisiyah-Iraq and is greatly acknowledged.

References

1. Griffith AA.: The Phenomena of Rupture and Flow in Solids. 163–198 (1920)
2. Irwin, G.R.: Analysis of stresses and strains near the end of a crack traversing a plate. J. Appl. Mech. **24**, 361–364 (1957)
3. Tada H, Paris P.C, Irwin G.: The Stress Analysis of Cracks Handbook, Professional Engineering Publishing, United Kingdom (2000)
4. Rooke, D.P., Cartwright, D.J.: Compendium of Stress Intensity Factors. **80**, 330 (1976). https://doi.org/10.1017/S0001924000033923
5. Anderson, T.L.: Fracture mechanics: fundamentals and applications. Taylor Fr Gr. **58**, 710–734 (2012). https://doi.org/10.1016/j.jmps.2010.02.008
6. Zhu X., Joyce J.A.: Review of fracture toughness (G, K, J, CTOD, CTOA) testing and standardization. **85**:2472 (2012)
7. Fung, Y.C.: Foundations_of_solid_mechanics(BookZZ.pdf)
8. Hunt J.B.: (UNIVERSIT. O KHARTOUM) Fracture Mechanics of Semi-Brittle Steels in Torsion. J. Mech. Phys. Solids **6**:321–326 (1958)
9. Walsh, J.B., Mackenzie, A.C.: Elastic-plastic torsion of a circumferentially notched bar. J Mech physic solid. **7**, 247–257 (1959)
10. Harris, D.O.: Stress intensity factors for hollow circumferentially notched round bars. J. Basic Eng. **89**, 49 (1967). https://doi.org/10.1115/1.3609569
11. Noda, N.A., Takase, Y.: Generalized stress intensity factors of the V-shaped notch in a round bar under torsion, tension, and bending. Eng. Fract. Mech. **70**, 1447–1466 (2003). https://doi.org/10.1016/S0013-7944(02)00115-7
12. SIH G.: Stress Intensity factor Solutions and Formulas (1973)
13. Sweeney, J.: Analysis of a proposed method for toughness measurements using torsion testing. **20**, 1–5 (1985)
14. Truss, R.W., Duckett, R.A., Ward, I.M.: The fracture-toughness of tough Polyethylenes by a novel high-pressure technique. J. Mater. Sci. **19**, 413–422 (1984). https://doi.org/10.1007/Bf00553564

15. Wang, J.A., Liu, K.C.: A new approach to evaluate fracture toughness of structural materials. J. Press. Vessel. Technol. **126**, 534 (2004). https://doi.org/10.1115/1.1804202
16. Wang, J-A., Kenneth, C.: Liu Oak Ridge T (US) Fracture Toughness Determination Using Spiral-Grooved Cylindrical Specimen and Pure Torsional Loading. The United States Pat Application Publ 1–14 (2003)
17. Fahem, A., Kidane, A.: Hybrid computational and experimental approach to identify the dynamic initiation fracture toughness at high loading rate. Dyn. Behav. Mater. **1**(1), 141–146 (2017). https://doi.org/10.1007/978-3-319-00771-7
18. Fahem A.F, Kidane A.: A general approach to evaluating the dynamic fracture toughness of materials. Conf. Proc. Soc. Exp. Mech. Ser. (2017) https://doi.org/10.1007/978-3-319-41132-3_26
19. Kim, H.S.: Finite element analysis of torsional deformation. Mater. Sci. Eng. A. **299**, 305–308 (2001). https://doi.org/10.1016/S0921-5093(00)01416-7
20. Predan, J., Močilnik, V., Gubeljak, N.: Stress intensity factors for circumferential semi-elliptical surface cracks in a hollow cylinder subjected to pure torsion. Eng. Fract. Mech. **105**, 152–168 (2013). https://doi.org/10.1016/j.engfracmech.2013.03.033
21. Fahem, A. F., Kidane, A.: A Progression on the determination of dynamic fracture initiation toughness using spiral crack. In: Fracture, Fatigue, Failure and Damage Evolution. The Proceedings of the SEM Annual Conference & Exposition on Experimental and Applied Mechanics, Vol. 6. Greenville, SC (2019)
22. Fahem, A.F., Fathi, A.A.: A study of the effect of impact loading on DSIFs and crack propagation in plate. Al-Qadisiya J Eng Sci. **2**, 288–303 (2009)
23. Albinmousa, J., Merah, N., Khan, S.M.A.: A model for calculating geometry factors for a mixed-mode I-II single edge notched tension specimen. Eng. Fract. Mech. **78**, 3300–3307 (2011). https://doi.org/10.1016/j.engfracmech.2011.09.005

Chapter 11
An Investigation of Stress Concentration, Crack Nucleation, and Fatigue Life of Thin Low Porosity Metallic Auxetic Structures

L. Francesconi, M. Taylor, and A. Baldi

Abstract This paper investigates, both experimentally and numerically, the mechanical response of low porosity thin metal samples under fatigue loads. The specimens, characterized by an overall porosity of 10%, were designed using selected patterns of voids and then fatigue tested to estimate the influence of both auxetic and non-auxetic tessellations on the mechanical performance. During the loading, detailed deformation maps were recorded by means of bi-dimensional Digital Image Correlation (DIC). The experimental data collected during this study indicate that the use of auxetic patterns could be a strategy to enhance the fatigue life of porous structures. In addition, DIC analysis is shown to be an excellent non-contact experimental method to assess the cumulative damage of the samples and to predict the crack starting points well before they are detectable by the unaided eye.

Keywords Auxetic structures · Fatigue testing · Perforated structures · Digital image correlation · Low-porosity structures

11.1 Introduction

Porous structures play a key role in several industrial sectors, which require materials with, for example, a high strength-to-weight ratio and superior thermal exchange capabilities [1, 2]. Much recent work has focused on designing the void geometry in porous structures to generate novel, and often remarkable, effective material behavior [3]. Such structures are referred to as metamaterials, i.e. those which derive their effective properties from their geometric structure in addition to their constitutive base materials [4, 5]. Of particular recent interest have been auxetic metamaterials, which are those characterized by a negative effective Poisson's ratio. It has been shown that auxetic void patterns can be used to obtain both high and low-porosity structures with tunable mechanical properties aimed at several different applications such as actuators, sensors, tunable optics, filters, smart objects and surfaces and protection devices [6–12].

Negative effective Poisson's ratio behavior has been obtained using a range of different materials as well as a variety of periodic bi-dimensional or tri-dimensional patterns of voids or inclusions [13–15] showing that auxeticity is a scale- and material-independent property, applicable to different classes of solids and scales (from the nanoscale to the macroscale) [14–17]. For this reason, and to fully exploit the auxetic features by accommodating dramatic change in shape and in volume, many numerical and experimental works have focused on high porosity macro-structures using polymers [15–17].

In contrast, Bertoldi et al. [14], Taylor et al. [18], Carta [19] and Mitschke [20], demonstrated that it's possible to induce auxeticity in low-porosity structures through the use high-aspect ratio voids, opening new ways to engineer this class of materials. Francesconi et al. [21] investigated the dynamic behavior of thin metallic low porosity auxetic structures by a numerical-experimental identification of the eigenmodes, characterizing the behavior of these metamaterials and describing in detail the motion of the periodic auxetic cells under static and dynamic loads. Recently, Farhad et al. [22] compared the experimental results obtained by fatigue testing different low-porosity structures (with positive and negative Poisson's ratio) with numerical FEM and X-FEM analyses for different tessellations investigating both the crack propagation behavior and the high-cycle thermo-mechanical performance. The results of this investigation suggest that auxetic samples have a longer fatigue life than similar structure with the same porosity but a positive Poisson's ratio. Despite these advancements, there are still very few data characterizing the behavior of low-porosity metallic auxetic structures under dynamic loading.

L. Francesconi (✉) · M. Taylor
Department of Mechanical Engineering, Santa Clara University, Santa Clara, CA, USA

A. Baldi
Dipartimento di Ingegneria Meccanica, Chimica e dei Materiali, Università degli Studi di Cagliari, Cagliari, Italy

J. Carroll et al. (eds.), *Fracture, Fatigue, Failure and Damage Evolution, Volume 6*, Conference Proceedings of the Society for Experimental Mechanics Series, https://doi.org/10.1007/978-3-319-95879-8_11

The goal of the present study is use some of the methods of the authors' previous investigation [21] to build on the investigation of Farhad et al. [22] to characterize the fatigue behavior of porous materials with both auxetic and non-auxetic structure. The samples in the present study were fabricated, characterized, fatigue tested, and the displacement/damage maps were calculated using digital image correlation (DIC), while numerical simulations have been performed using the commercial finite element software Abaqus/Standard (Simulia Providence, RI).

11.2 Materials and Testing Methods

Rectangular perforated specimens were fabricated by cutting voids of two different shapes into thin laminas of AL-6060 T6 using a CNC machine equipped with a micro end-mills (0.8 mm in diameter). The samples (presented in Fig. 11.1) are characterized by a porosity of 10% and overall dimensions of 260 by 40 by 2 mm. The sample with circular voids (Fig. 11.1a) has positive effective Poisson's ratio, while the other (Fig. 11.1b, hereafter referred to as "stop-hole" based on the voids' shapes) is effectively auxetic. The void centre-to-centre distance is 10 mm in both the vertical and the horizontal directions for both of the investigated samples.

The selection of the specific tessellation geometry was based on general considerations about the stress concentration factors, previous studies by the authors [18, 21], computer simulation, and manufacturing limits. In order to reach low and ultra-low porosities, the planar tessellations require very small features to be cut through the use of state-of-the-art CNC or EDM machines. In this study, we cut out the voids using a CNC machine. To assist in the design of the void geometries, we performed finite element simulations to characterize the effective Poisson's ratios in both infinite periodic geometries (see Fig. 11.2) as well as the finite geometry of the test samples based on the approach of Taylor et al. [18]. Table 11.1 reports the value of the effective Poisson's ratio for these geometries.

Figure 11.3 shows the planar lateral displacement maps (i.e., in the direction perpendicular to the load axis) obtained from the static finite element simulation using Abaqus and applying a tensile traction displacement of 2 mm. The behaviour of the

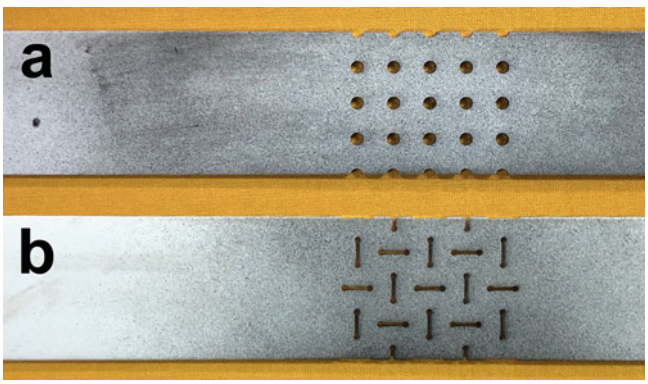

Fig. 11.1 Low porosity (10%) coupons considered in this study: the "Circle" (**a**), and the "Stop-Hole" (**b**)

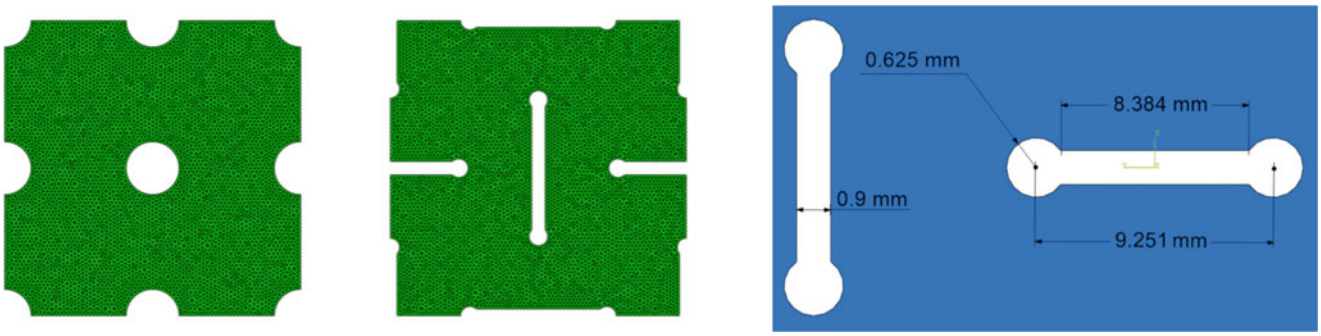

Fig. 11.2 FE meshes used in the periodic finite element analysis (left). Specification of the auxetic tessellation (right)

Table 11.1 Poisson's ratio for the periodic and the full-size structures considered

	Circle	Stop-Hole
Periodic cell (with periodic boundary conditions)	$\nu_{eff} = +0.298$	$\nu_{eff} = -0.310$
Full-size sample (considering the entire perforated area)	$\nu_{eff} = +0.312$	$\nu_{eff} = -0.315$

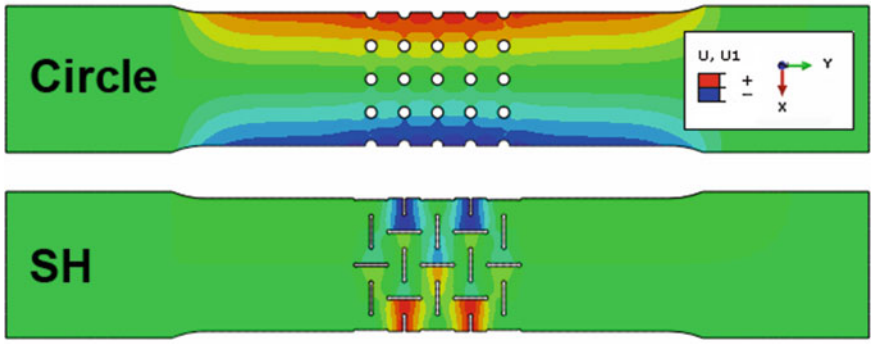

Fig. 11.3 X (direction 1) displacement maps of the low-porosity samples under a tensile load directed along Y

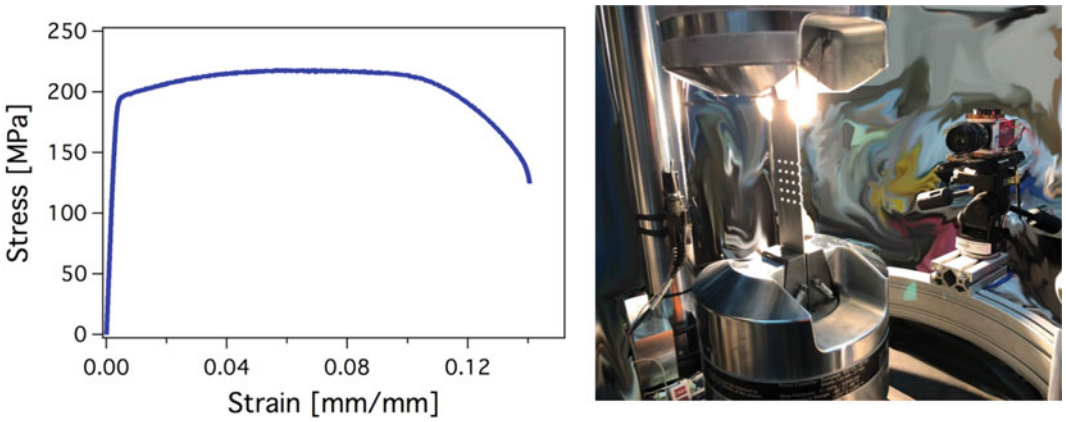

Fig. 11.4 Stress-Strain curve of the material used to fabricate the samples (left) and, on the right, the experimental setup for the fatigue and the DIC tests (the background was blurred for clarity)

two structures is clearly different: while the circular void sample contracts along the entire area where the holes are present, the stop-hole sample, on the other hand, expands in the void region.

The periodic structures were modeled using a single layer of six-node, quadratic two-dimensional solid elements (Abaqus element type CPS6) while the full-size samples were discretized using a single layer of eight-node, quadratic tetrahedral solid elements (Abaqus element type C3D8R). Abaqus' built-in automatic adaptive mesh refinement algorithm was used to optimize the element placement around the complex geometry of the samples, allowing the mesh to become coarser in areas where it will not negatively affect our solution's accuracy near the voids. The mesh was refined based on the strain energy density and von Mises stress error estimators, using the default error targets.

The final meshes resulted in approximately 15,000 elements for the periodic cells and 50,000 elements for the full-size samples. These mesh densities were found to be sufficiently refined for comparison with the corresponding experimental data. The material (aluminum Al-6060 T6) was simulated as linearly elastic and perfectly plastic with a Young's modulus of 65.4 GPa, a Poisson's ratio of 0.32 and a yielding stress (Equivalent Von Mises stress) of 195 MPa in accordance with the data obtained from an initial material characterization (Fig. 11.4a reports the experimental stress-strain law measured in the preliminary tensile quasi-static testing). The static and the dynamic experimental investigation were made using a hydraulic MTS LandMark 370 universal testing machine equipped with a 100 kN load cell.

During the fatigue tests, multiple images were taken at regular intervals by pausing the test and holding the sample at the mean stress used in the sinusoidal cycle. This addition to the normal fatigue test was made in order to monitor the damage progression using DIC analysis. The experimental setup used for DIC, presented in Fig. 11.4, consists in a monochromatic

AlliedVision F421-B Pike high-resolution camera equipped with a Schneider Kreuznach Macro camera lens and in an isotropic spot-free professional illuminator. The camera was mounted on a circular aluminum beam features with a radius of 50 cm (rigidly connected to the columns of the MTS LandMark 370 to allow the changing of the cameras/specimen view angle without focusing problems). The images were all 8 bits and they were taken with a sampling rate of 1 image per 1000 load-cycles.

To evaluate our experimental results, we use the *total life approach* in order to have a common basis for predicting the fatigue life of the samples, which are characterized by very different mechanical responses due to the differences in the tessellations. The fatigue limit σ_f of each sample was calculated (Eq. 11.1) by decreasing the reference stress σ_r obtained from the standard tensile test by multiplying it using a particular set of constants. All of the coefficients K in Eq. 11.1 are used to account for changes in the fatigue limit due to different factors such as: type of load applied (K_1), material used (K_2), geometrical features (K_3), thermo-mechanical and surface treatments (K_4), and the stress concentration factor (K_f). Under the threshold level σ_f, the material/component has effectively infinite life

$$\sigma_f = \sigma_r \cdot K_1 \cdot K_2 \cdot K_3 \cdot K_4 \cdot \frac{1}{K_f} \tag{11.1}$$

where

$$K_f = q \cdot (K_t - 1) + 1$$

We note that the last coefficient (K_f) in Eq. 11.1 is a function of the stress concentration factor K_t, which we estimated using finite element numerical analyses. Once we determined σ_f, we calculated the final fatigue stress applied during the test in order to have a total number of 50,000 reversals to failure. This was done by using the Gerber approach (Eq.11.2) to calculate the applied stress amplitude. We selected this formulation for its better accuracy in describing the mechanical response of aluminium alloys when the load cycles have a non-zero mean stress (a mandatory condition in our tests, since the flat geometries of the specimens do not allow us to fully reverse the cyclical loading due to buckling).

$$\sigma_a = \sigma_a|_{\sigma_m=0} \cdot \left\{ 1 - \left(\frac{\sigma_m}{\sigma_{TS}} \right)^2 \right\} \quad (Gerber) \tag{11.2}$$

11.3 Results

Using the fatigue relations described in Eqs. 11.1 and 11.2, the fatigue test loadings were tuned so that the samples would have a fatigue life of about 50.000 cycles. In each single loading cycle the maximum axial applied load was well below the yielding limit, allowing the damage to gradually accumulate during the experiments. In Table 11.2 the maximum loads and the K_f values are reported for the considered samples together with the number of cycles to failure measured during the fatigue tests:

The tests were performed in load-control mode with a frequency of 20 Hz. For the sake of comparison, we used the sample with the circular void as a benchmark, referencing/normalizing the other data with respect to this one to compare the performance of the different tessellations. Accordingly, we set the normalized fatigue life of the circular void sample equal to 1 in order to have a common base to compare the results obtained from the experimental tests. In addition, the temperature was monitored during through all the tests and no significant changes/increases were found due to the elastic hysteresis.

The first consideration that has to be made in analysing the preliminary data of Table 11.2 is that a significantly longer fatigue life was recorded for the stop-hole sample. The reasons for this could be attributable to the different way that the higher stress zones are distributed along the samples: in particular, these type of structures, under the considered load (sinusoidal traction with a non-zero average stress), do not shrink in the mid-section but they do expand, facilitating a distribution of the stresses/strains that seems to generate a positive effect in the fatigue life of the investigated structures. A better understanding of these phenomena could be obtained by a careful examination of the cracks' patterns and the displacement maps obtained by

Table 11.2 Fatigue test specifications and results for the investigated samples

	Circle	Stop-Hole
Maximum applied tensile load	6050 [*N*]	3505 [*N*]
K_f	+1.415	+5.01
Fatigue life (reversals to failure)	50,000	68,000

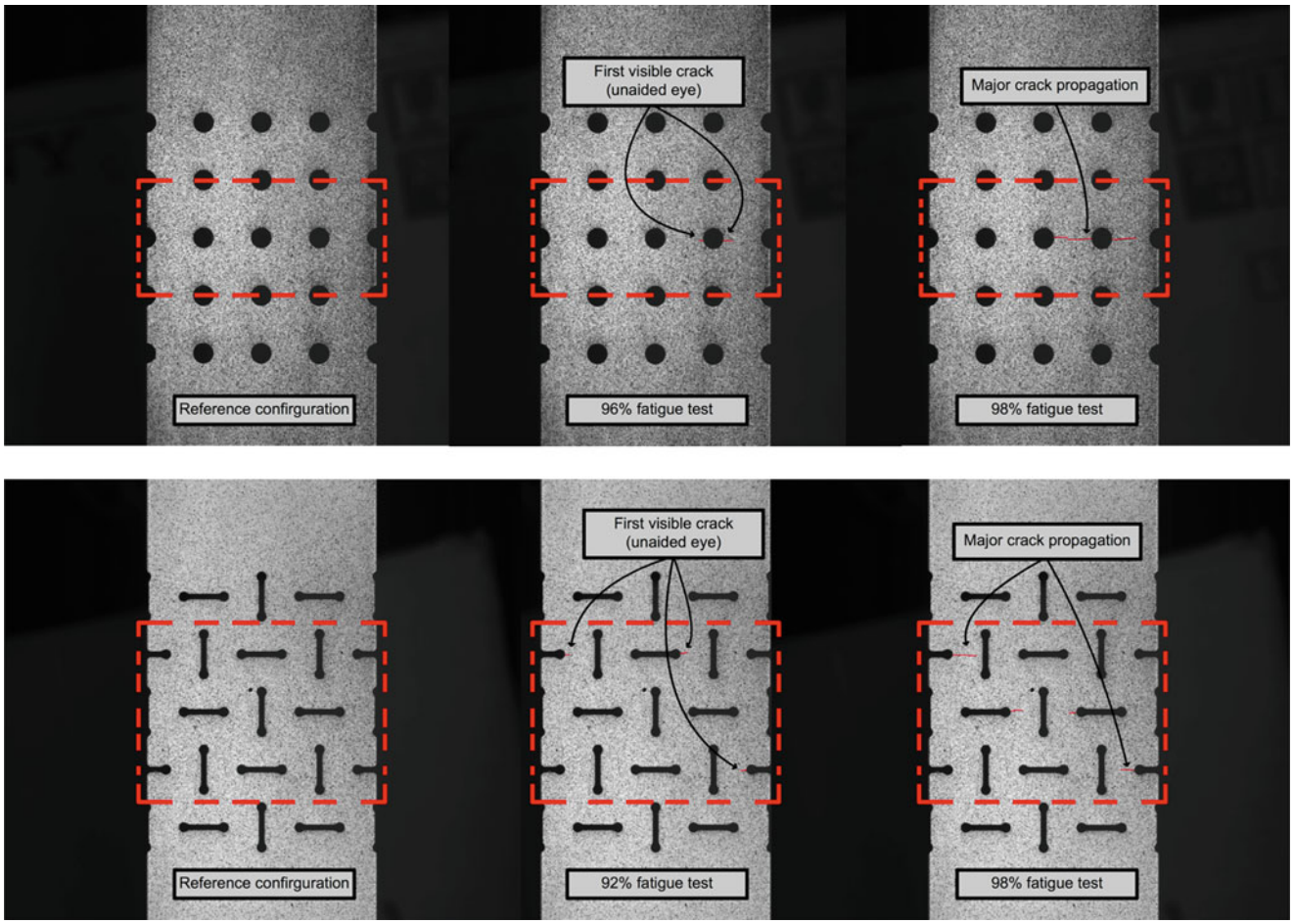

Fig. 11.5 Crack innescation and propagation (highlited with solid red lines) at different stages of the fatigue tests for the Circle sample (top) and the stop hole (bottom). The dashed boxes highilight the fracture/crack propagation area

the digital image correlation analysis. Figure 11.5 shows the crack patterns of the two samples recorded during the fatigue tests.

While the circular void test sample (Fig. 11.5, top) behaves, as expected, with a strong concentration of the damage in the mid-section, the stop-hole test sample (Fig. 11.5, bottom) presents multiple crack tips, with two major cracks right above and below the mid-section due to the different motion of the auxetic cell with respects to the "traditional" one.

The enhancement in the fatigue response of the auxetic samples could also be attributable to the rotational motion of the periodic cells during the loading cycles. This rotation allows for a more homogenised distribution of the stresses/strains along the perforated section of the material also spreading the amount of damage caused by a single loading cycle, even if the auxetic tessellations with respect to the positive Poisson's ratio perforated structures are usually characterized by higher values of the stress-concentration factor.

Through DIC analysis of the perforated section of the material, we were able to estimate the fatigue damage and to track it's accumulation during the fatigue test for both the considered structures well before that the first crack was visible by the unaided eye. The contour plots of Fig. 11.6 show the Lagrangian strain (along the loading axis direction) distribution and clearly highlight the critically loaded regions. These contour maps demonstrate that, by an appropriate selection of the DIC experimental set-up, it is possible to have a very accurate estimation of the cracks' nucleation points at a very early stage of the damage and also that it is possible to describe the fracture and the damage accumulation/propagation of a structure during a fatigue test. The DIC analysis showed a strain/damage concentration from the early stages of both the tested structures (after approximately 25–30% of the total cycles) and, more importantly, DIC was able to unequivocally determine the crack starting points after about the 50% of the fatigue life of the tested samples. In particular, the stop-hole sample (Fig. 11.6, left side) showed a clear concentration of the strain/damage around the 66% of it's total life while the circle one experienced the same for about the 52% of its total life.

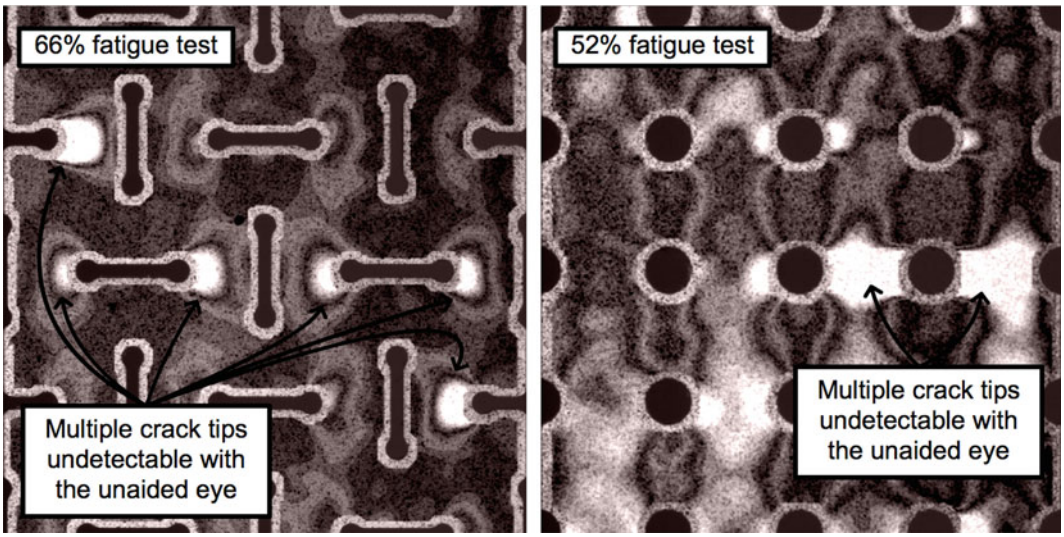

Fig. 11.6 Contour maps of the Lagrangian strains obtained using Digital Image correlation for the auxetic (left) and the circle (right) sample. Lighter colors indicate higher values

11.4 Conclusions

Auxetic and non-auxetic structures were compared and examined in detail to investigate their fatigue performance under the application of cyclic loads. It was found that, for the same porosity (10%), the stop-hole auxetic structure possess a longer fatigue life than the one with the circle void structure, indicating an innovative way to design the fatigue life of low porosity perforated structures. The longer fatigue life of the auxetic pattern is attributable to its rotational deformation behaviour. In auxetic patterns, damage and crack nucleation occurs in multiple (often unconnected) regions, whereas in the circular void pattern, damage concentrates strongly in a single area. The results of this study compare favourably with the investigation of Farhad et al. [22].

Furthermore, the experimental data also suggest that digital image correlation could have tremendous utility in the determination and measurement of the performance of a part under cyclic loads, since it is able to non-invasively track the accumulation of the damage of the ductile samples indicating, with very good accuracy, the crack initiation points before they were detectable by the unaided eye.

From the data presented in this study, it's possible to conclude that the auxetic void patterns could have a remarkable impact in the future design and utilization of low-porosity porous structures in applications where cyclic loading is expected. The findings of this study have to be considered a starting point since a more general analysis needs to be performed in order to better describe the design scenarios and possibilities using these structures. Avenues for further study include testing of additional samples with varying porosity and stress concentrations and more detailed numerical simulation using both finite elements as well as more recent damage- and crack-focused methods such as peridynamics.

References

1. Ashby, M.F., Jones, D.R.H.: Engineering Materials 1: An Introduction to Their Properties and Applications. Butterworth Heinemann, Oxford (1996)
2. Love, A.E.H.: A Treatise on the Mathematical Theory of Elasticity. Dover, New York (1944)
3. Lakes, R.: Advances in negative Poisson's ratio materials. Adv. Mater. **5**, 293–296 (1993)
4. Greaves, G.N., Greer, A.L., Lakes, R.S., Rouxel, T.: Poisson's ratio and modern materials. Nat. Mater. **10**, 823–837 (2011)
5. Prawoto, Y.: Seeing auxetic materials from the mechanics point of view: a structural review on the negative Poisson's ratio. Comput. Mater. Sci. **58**, 140–153 (2012)
6. Grima, J., Gatt, R.: Perforated sheets exhibiting negative poisson's ratios. Adv. Eng. Mater. **12**, 460–464 (2010)
7. Evans, K.E., Alderson, A.: Auxetic materials: functional materials and structures from lateral thinking. Adv. Mater. **12**(9), 617–628 (2000)
8. Sanami, M., Ravirala, N., Alderson, K., Alderson, A.: Auxetic materials for sports applications. Procedia Eng. **72**, 453–458 (2014)
9. Herakovich, C.T.: Composite laminates with negative through-the-thickness Poisson's ratios. J. Compos. Mater. **18**(5), 447–455 (1984)

10. Smith, C.W., Grima, J.N., Evans, K.E.: A novel mechanism for generating auxetic behaviour in reticulated foams: missing rib foam model. Acta Mater. **48**(17), 4349–4356 (2000)
11. Sidorenko, A., Krupenkin, T., Taylor, A., Fratzl, P., Aizenberg, J.: Reversible switching of hydrogel-actuated nanostructures into complex micropatterns. Science. **315**, 487–490 (2007)
12. Bhullar, S.K., Ko, J., Ahmed, F., Jun, M.B.G.: Design and fabrication of stent with negative Poisson's ratio. Int. J. Mech. Aerosp. Ind. Mechatronic Manuf. Eng. **8**(2), 448–454 (2014)
13. Hou, X., Hu, H., Silberschmidt, V.: A novel concept to develop composite structures with isotropic negative Poisson's ratio: effects of random inclusions. Compos. Sci. Technol. **72**, 1848–1854 (2012)
14. Bertoldi, K., Reis, P.M., Willshaw, S., Mullin, T.: Negative Poisson's ratio behavior induced by an elastic instability. Adv. Mater. **22**, 361–366 (2010)
15. Chen, Y., Li, T., Scarpa, F., Wang, L.: Lattice metamaterials with mechanically tunable Poisson's ratio for vibration control. Phys. Rev. Appl. **7** (2), (2017)
16. Larsen, U.D., Sigmund, O., Bouwstra, S.: Design and fabrication of compliant micromechanisms and structures with negative Poisson's ratio. J. Microelectromech. Syst. **6**, 99–106 (1997)
17. Jiang, J.W., Kim, S.Y., Park, H.S.: Auxetic nanomaterials: recent progress and future development. Appl. Phys. Rev. **3**(4), 2016
18. Taylor, M., Francesconi, L., Gerendas, M., Shanian, A., Carson, C., Bertoldi, K.: Low porosity metallic periodic structures with negative Poisson's ratio. Adv. Mater. **26**(15), 2365–2370 (2014)
19. Carta, G., Brun, M., Baldi, A.: Design of a porous material with isotropic negative Poisson's ratio. Mech. Mater. **97**, 67–75 (2016)
20. Mitschke, H., Schwerdtfeger, J., Schury, F., Stingl, M., Körner, C., Singer, R.F., Robins, V., Mecke, K., Schröder-Turk, G.E.: Finding auxetic frameworks in periodic tessellations. Adv. Mater. **23**, 2669–2674 (2011)
21. Francesconi, L., Taylor, M., Bertoldi, K., Baldi, A.: Static and modal analysis of low porosity thin metallic auxetic structures using speckle interferometry and digital image correlation. Exp. Mech. **58**(2), 283–300 (2018)
22. Javid, F., Liu, J., Rafsanjani, A., Schaenzer, M., Pham, M.Q., Backman, D., Yandt, S., Innes, M.C., Booth-Morrison, C., Gerendas, M., Scarinci, T., Shanian, A., Bertoldi, K.: On the design of porous structures with enhanced fatigue life. Extreme Mech. Lett. **16**, 13–17 (2017)

Chapter 12
Cohesive Zone Smoothing of Bending Stiffness Heterogeneities in Tape Peeling Experiments

Louisa Avellar, Tucker Reese, Kaushik Bhattacharya, and Guruswami Ravichandran

Abstract This work studies the interaction between the cohesive zone and elastic stiffness heterogeneity in the peeling of an adhesive tape from a rigid substrate. It is understood that elastic stiffness heterogeneities can greatly enhance the adhesion of a tape without changing the properties of the interface. However, in experiments performed on adhesive tapes with both an elastic stiffness heterogeneity and a substantial cohesive zone, muted adhesion enhancement was observed. It is proposed that the cohesive zone acts to smooth out the effect of the discontinuity at the edge of the elastic stiffness heterogeneities, suppressing their effect on adhesion. This work presents peel tests performed with heterogeneously layered 3 M 810 tape that demonstrate the muted enhancement. Additionally, numerical simulations further investigating the interaction between elastic heterogeneity and cohesive zone are presented.

Keywords Fracture · Cohesive zone · Peeling · Laminates · Heterogeneous materials

12.1 Introduction

In the fracture of 2D- and 3D-materials, it is well understood that elastic contrasts in composite materials affect crack propagation [1, 2]. In laminate peeling, often studied as a one-dimensional approximation to fracture, either an elastic contrast or a difference in thickness can be used to introduce a bending stiffness heterogeneity that has a similar effect in influencing the force required to advance the peel front [3–6]. In order for the peel front to pass through a contrast in bending stiffness, the shape of the peeling profile changes dramatically; the bending energy required to change the peeling profile is what causes variation in the overall peeling force [3]. With numerical studies and experiments, Xia showed that at a step-up in thickness in laminate peeling the amount of peel force increase goes with the thickness cubed, as predicted by Euler-Bernoulli beam theory [4, 6]. Past experiments and theories have been developed assuming brittle peeling; that is, that the cohesive zone at the peel front is negligible. The work presented in this report studies peeling in 3 M 810 tape which has a substantial cohesive zone. Experiments and preliminary simulations indicate that the cohesive zone works to smooth out the bending stiffness heterogeneity introduced by the step up in thickness, thereby smoothing out the toughening inducing discontinuity and reducing the toughening effect of the extra thickness. Additionally, a severe drop in load coinciding with the step down in thickness is present in experiments and simulations that is not present in the brittle case.

12.2 Experiment

Peel experiments using 3 M 810 tape (E = 1.65 GPa [7]) adhered to a glass substrate are performed using the setup shown in Fig. 12.1a. Prior to the adhesion of the tape, the glass is cleaned by wiping with an ethanol wetted Kimwipe followed by a dry Kimwipe. The substrate is then allowed to dry for 1–2 min. The base layer of tape is applied to the substrate and smoothed using a squeegee. The tape is long enough that it can be clamped in the loading grip. Heterogeneities are applied to the base layer by the following process: if the heterogeneity is to be more than one layer, the heterogeneities are laid up by applying the first layer to wax paper and smoothing subsequent layers on top of the first layer until the desired layer count is reached. Strips of the tape 1–5 mm in width, but much longer than the width of tape are cut from the built up tape. The strip is then removed

L. Avellar (✉) · T. Reese · K. Bhattacharya · G. Ravichandran
California Institute of Technology, Mechanical and Civil Engineering, Pasadena, California, USA
e-mail: lavellar@caltech.edu

J. Carroll et al. (eds.), *Fracture, Fatigue, Failure and Damage Evolution, Volume 6*, Conference Proceedings of the Society for Experimental Mechanics Series, https://doi.org/10.1007/978-3-319-95879-8_12

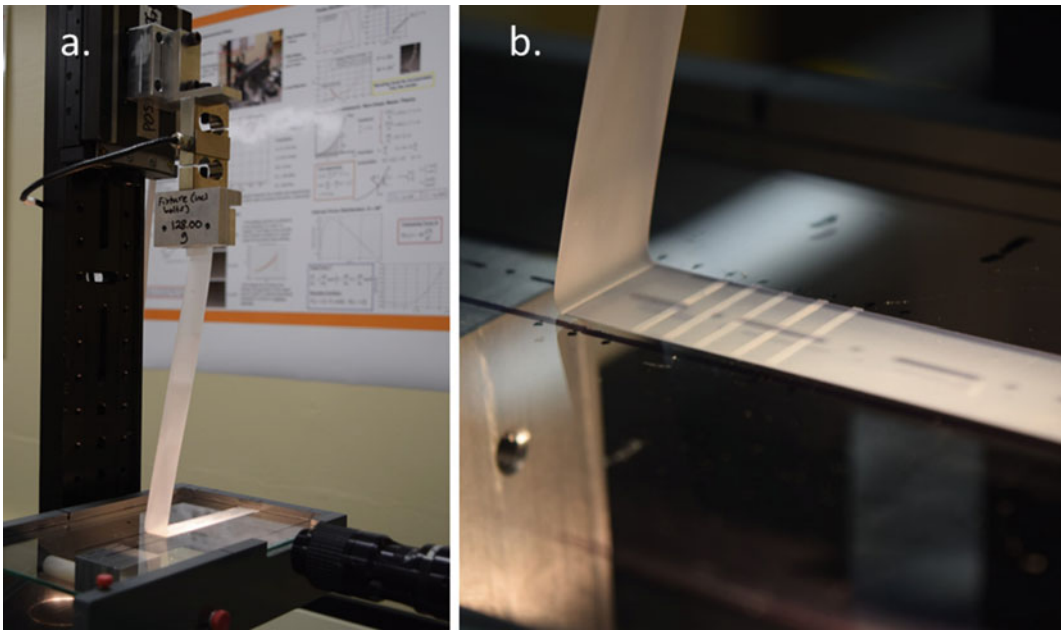

Fig. 12.1 (**a**) Tape peeling experiment configuration (**b**). Close up of heterogeneities

from the wax paper and applied to the base layer spaced 4–5 mm apart. The heterogeneity is trimmed to the width of the tape and smoothed using a squeegee. An image of the tape with heterogeneities is shown in Fig. 12.1b. The tape is left a minimum of 20 min before the beginning of the peel test to ensure consistency of adhesion [7]. The tape is then installed in the loading grip, with a 20 cm peel arm to reduce the effects of the change in peel angle over the course of the test (5 cm). The loading grip is pulled up at the rate of 0.05 mm/s using a PI 410.2S stepper motor and PI Mercury C663 controller. The peel force is measured during the test using an Omega LC101–50 load cell, DP41-BA-C24 strain meter and NI USB-6251 DAQ box. A Navitar microscope lens (1–6010 C-mount coupler, 1–6030 2X Standard Adapter, 1–60,135 6.5X Zoom 12 mm Fine Focus) is attached to a uEye EO-1312 m USB camera and images are taken while the peel front is in the field of view. The images and load cell readings are collected and recorded using a LabVIEW Virtual Instrument.

12.3 Results

The normalized (with respect to the homogeneous single layer peel force) load variation and the evolution of the radius of curvature near the peel front are shown in Fig. 12.2 for a representative experiment. The heterogeneities are two layers thick (for a total thickness of 3 times the base thickness). The normalized peak load is 2.65, which is substantially less than the 27 that would be predicted by Euler-Bernoulli theory. The normalized minimum load is 0.35. The tape starts with a relatively small radius of curvature in the homogeneous zone (A-B). When the tape approaches the heterogeneity, the radius of curvature increases (C-E) before becoming a steady state larger curvature (F-H). At the step down, (I-K), the radius of curvature reduces back to the original radius of curvature (L).

12.4 Summary

The aim of this work is to study peeling in a system with effects from a cohesive zone. Experimental results show that the normalized peak load is suppressed from what would be expected in the brittle case. Preliminary ABAQUS simulations indicate that the normalized peak increases as the size of the cohesive zone is reduced for a constant G_C. Future work includes continuing to refine the ABAQUS simulations to continue to investigate the relationship between the normalized peak load, the normalized minimum load, and the size of the cohesive zone.

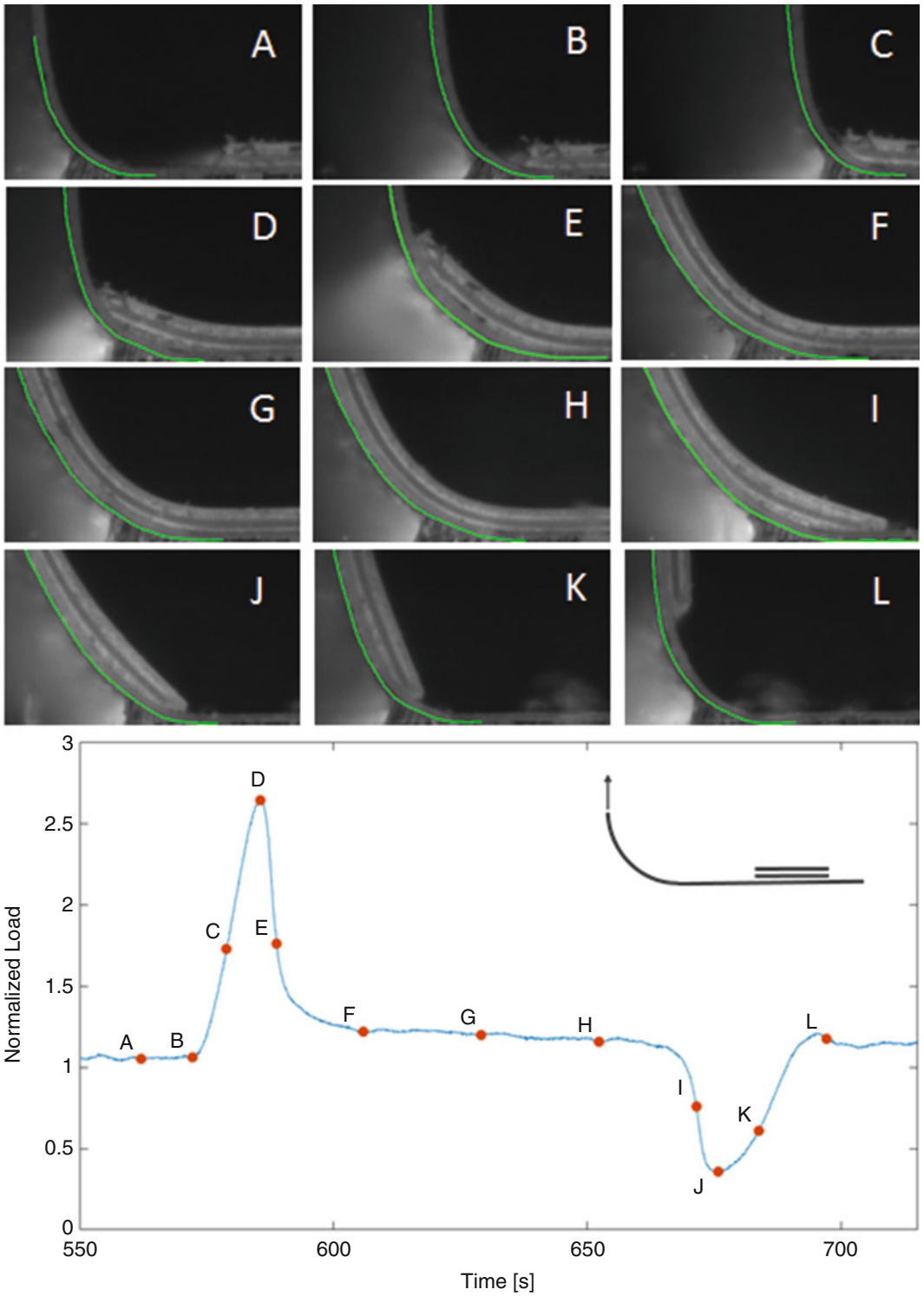

Fig. 12.2 Representative normalized load plot with profile images of the peel front. Plot inset: Heterogeneity configuration is two layers on top of the base layer

Acknowledgements We gratefully acknowledge the support of the National Science Foundation Award No. DMS-1535083 under the Designing Materials to Revolutionize and Engineer our Future (DMREF) program. This material is based upon work supported by the National Science Foundation Graduate Research Fellowship under Grant No. DGE-1144469.

References

1. Zak, A.R., Williams, M.L.: Crack point stress singularities at a bi-material interface. J. Appl. Mech. **30**(1), 142–143 (Mar. 1963)
2. Leguillon, D., Martin, E.: Crack nucleation at stress concentration points in composite materials–application to the crack deflection by an interface. Mathematical Met. Mod. Compos. 401–424 (2013)
3. Kendall, K.: Control of cracks by interfaces in composites. Proc. R. Soc. Lond. Ser. Math. Phys. Sci. **341**(1627), 409–428 (1975)
4. Xia, S., Ponson, L., Ravichandran, G., Bhattacharya, K.: Toughening and asymmetry in peeling of heterogeneous adhesives. Phys. Rev. Lett. **108**(19), 196101
5. Ghatak, A.: Peeling off an adhesive layer with spatially varying modulus. Phys. Rev. E. **81**(2), 021603
6. Xia, S.M., Ponson, L., Ravichandran, G., Bhattacharya, K.: Adhesion of heterogeneous thin films—I: elastic heterogeneity. J. Mech. Phys. Solids. **61**(3), 838–851 (2013)
7. Kovalchick, C.: Mechanics of Peeling: Cohesive Zone Law and Stability. PhD Thesis, California Institute of Technology, Pasedena (2011)

Chapter 13
Experimental Study on Fatigue Performance of Steel-Concrete Composite Girders

Ayman El-Zohairy, Hani Salim, and Aaron Saucier

Abstract Besides the static load, the fatigue load caused by vehicles always exists in the bridge structures. This type of loading may cause failure even when the nominal peak loads are less than the ultimate capacity of the structure. In this paper, an experimental work, consists of two specimens, was introduced to study the fatigue behavior of shear connectors and steel-concrete composite beams. The fatigue tests were conducted under a four-point bending test with two different stress ranges in a constant amplitude. The testing measurements during the fatigue test included deflection, strain in the shear connectors, and slippage between the concrete flange and the steel beam. After completion of the fatigue tests, it was obvious that providing top and bottom longitudinal reinforcement as well as enough transverse reinforcement in the concrete flange can provide adequate confinement to concrete to limit fatigue cracks in the concrete flange. In addition, a growth in the cyclic deflection limits was obtained by increasing the number of cycles due to the damage region that developed in the concrete flange by the shear studs and caused a loss of stiffness in the shear connection.

Keywords Composite · Experimental · Fatigue · Shear connectors · Deflection · Slippage · Strains

13.1 Introduction

Steel-concrete composite beams have been used widely as a statically system for bridge superstructures due to the advantages of combining the benefits of component materials and gaining effective lightweight structural members. In the real life, bridge superstructures are generally subjected to cyclic loads caused by vehicles. The behavior of steel-concrete composite beams under this type of loading differs from the behavior under a static load and such loading conditions may cause a premature failure due to fatigue. Therefore, fatigue tests normally predict the real behavior of steel-concrete composite beams in bridge superstructures more than the common static tests.

There has been a significant research on the fatigue performance of shear connectors using push-out tests. Slutter and Fisher [1] have carried out the first fatigue test on studs, indicating that the fatigue failure of studs occurred in the welding zone between the steel plate and studs. Simplified equations for predicting the fatigue life of studs based on plenty of push-out tests were presented and adopted in the current standards [1, 2]. In addition, semi-empirical analytical methods were developed to determine the reduced static strength and fatigue life of the headed shear studs subjected to unidirectional cyclic loading [3, 4]. Liu and Roeck [5] revealed that the stud spacing has a large influence on the shear force on the stud while the concrete Young's modulus has a relatively small influence. Ovuoba and Prinz [6] presented results from an experimental and analytical study into the fatigue behavior of headed shear studs to address the fatigue limit and to better characterize the effects of fatigue uncertainty on predicted response. Results from composite push-out specimens tested at stress range near the existing AASHTO fatigue limit suggested an increase of the limit to 44.8 MPa rather than 24.1 MPa.

In addition, earlier experimental studies on the fatigue behavior of steel-concrete composite beams confirmed an initiation and a propagation of cracks in the concrete flange which caused failure [7]. As relevant consequences of high cycle loading, the crack propagation through the stud foot and the local damage of concrete surrounding the studs were the fatigue failure mode of full-scale steel-concrete composite beams [8]. In addition, the fatigue performance of the shear connectors and composite beams was significantly affected by the shear stress range and maximum applied load [9, 10]. The maximum applied load had a significant effect on fatigue performance when the difference between it and the load range was large.

A. El-Zohairy (✉) · H. Salim · A. Saucier
Department of Civil and Environmental Engineering, University of Missouri, Columbia, MO, USA
e-mail: aeq76@mail.missouri.edu

J. Carroll et al. (eds.), *Fracture, Fatigue, Failure and Damage Evolution, Volume 6*, Conference Proceedings of the Society for Experimental Mechanics Series, https://doi.org/10.1007/978-3-319-95879-8_13

13.2 Details of the Tested Specimens

In order to explore the fatigue behavior of steel-concrete composite beams subjected to constant fatigue loads, two simply supported steel-concrete composite beams were tested; as summarized in Table 13.1. The overall length was 4572 mm while the clear span between supports was 4419.6 mm as schematically provided in Fig. 13.1. A wide flange steel beam W10X30 (Grade A992) was used for all the specimens. Table 13.2 illustrates the geometric properties of the steel beam section. The width of the steel beam flange was suitable for the arrangement of two rows of the shear connectors, according to AASHTO-LRFD [11]. According to American Society for Testing Materials [12], the yield strength, ultimate strength, and Young's modulus were 345 MPa, 450 MPa, and 204 GPa, respectively.

The thickness and width of the concrete flange were 101.6 mm and 1143 mm, respectively. To obtain the compressive strength of concrete, three concrete cylinders of 100 mm × 200 mm were prepared for each specimen during the concrete casting for compressive strength tests. The cylinders and the concrete flanges were cured in the laboratory under a plastic sheet. The nominal concrete compressive strengths achieved after 28 days was 32.4 MPa. The concrete flanges were reinforced by deformed bars with a diameter of 10 mm in the longitudinal and transverse directions; as detailed in Fig. 13.2. The transverse reinforcement was used as closed ties to provide a confinement to concrete around the studs, prevent concrete from splitting, and avoid the undesired longitudinal shear failures. In order to determine the steel reinforcement's characteristics, tension tests were conducted, according to ASTM A370, to demonstrate the stress-strain

Table 13.1 Summary of the fatigue tests

Specimen	Fatigue load (kN)			Shear stress range (MPa)	No. of cycles
	P_{max}	P_{min}	Range		
B-1	160.1	13.3	146.8	77.0	1,000,000
B-2	177.9	13.3	164.6	87.4	1,000,000

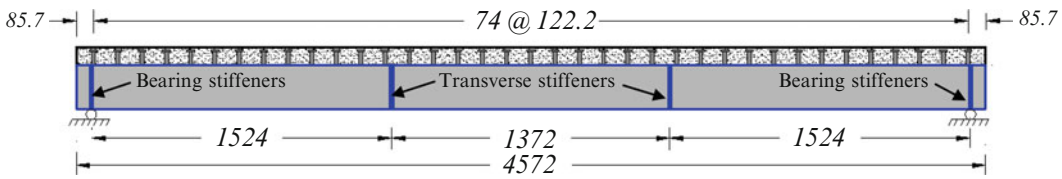

Fig. 13.1 Details of the tested specimens

Table 13.2 Steel section properties

Steel beam section	Total depth (mm)	Flange width (mm)	Flange thickness (mm)	Web thickness (mm)	Area of section (mm^2)	Moment of inertia Ix (mm^4)
W10X30	266	147.6	13	7.6	5703	$7.1x10^7$

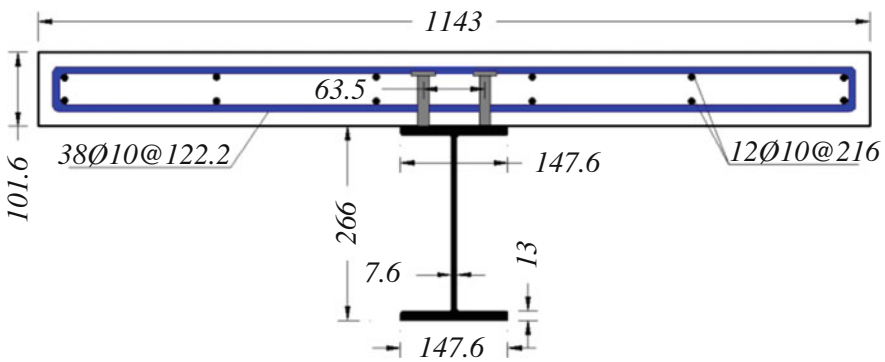

Fig. 13.2 Beam cross-section showing the real rebars details

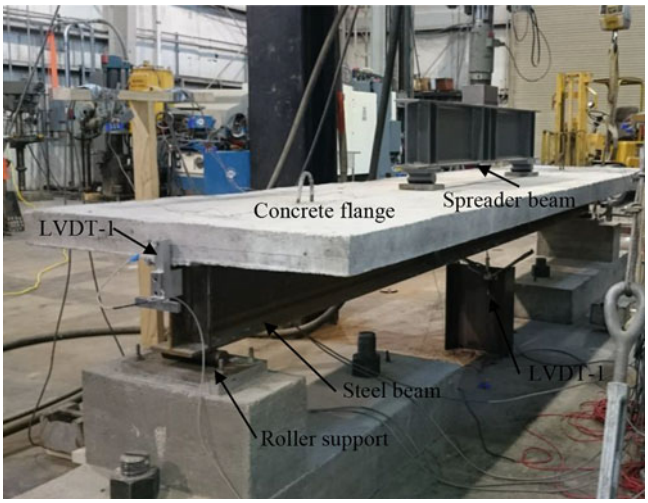

Fig. 13.3 Fatigue test set-up

relationship for the steel rebars. The yield strength, ultimate strength, and Young's modulus were 294.2 MPa, 402.5 MPa, and 207.8 GPa, respectively.

In addition, two rows of 15.875 mm in diameter and 81 mm in height shear connectors were welded to the top flange of the steel beam with a longitudinal and transverse spacing of 122.2 mm and 63.5 mm, respectively. The yield strength, ultimate strength, and Young's modulus; as provided by the manufacturer; were 351.6 MPa, 448.2 MPa, and 206.5 GPa, respectively. To prevent the lateral torsion buckling of the steel web, eight stiffeners with a thickness of half an inch were welded to the steel web as shown in Fig. 13.1. The end bearing stiffeners were at the locations of supports and the transverse stiffeners were welded at locations of the loading points. In addition, a steel plate was added at the support location in order to avoid any stress concentration problems. This provided an even stress distribution over the support area. A roller support was used at one edge and hinged support at the other edge. Other bearing steel plates were used at the loading location to avoid any stress concentration on the concrete flange at the loading points.

13.3 Test Set-Up and Instrumentation

The fatigue tests were carried out under a servo-hydraulic actuator of 890 kN maximum capacity. As illustrated in Fig. 13.3, a spreader beam was used to distribute the applied concentrated load to two loading points spaced 1372 mm apart. The fatigue tests were performed with a loading frequency of 4.0 cycles/sec.

Three LVDTs were used for each specimen to measure the vertical deflection at mid-spans and the slippage between the concrete flange and the steel beam at both ends. Accurate strain measurements were also obtained by using strain gages directly glued to the shear connectors at supports of each specimen. Two strain gages were bonded at the foot of each stud to monitor the tensile and compressive strains on both sides. The uplift forces between the concrete flange and the steel beam at the beam end caused a slight difference in readings between the two sides.

13.4 Fatigue Test Observations and Discussions

Observations of the exterior surfaces of the concrete flanges during fatigue tests showed initiation and propagation of cracks. As the concrete flange was in compression and the neutral axis (NA) of the composite section was designed to stay in-between the steel beam and the concrete flange, no crack should initiate in the top surface of the concrete flange. However, with the increase of load cycles ($N > 50{,}000$), traces of minor cracks were found on the top surface of the concrete flange and on the side faces. Both the number and the size of these cracks were growing with the load cycles; as schematically depicted in Figs. 13.4 and 13.5. The fatigue cracks were observed only in the shear span regions and no cracks were formed around span center section for all specimens. In addition, all cracks were mainly distributed in a direction perpendicular to the longitudinal

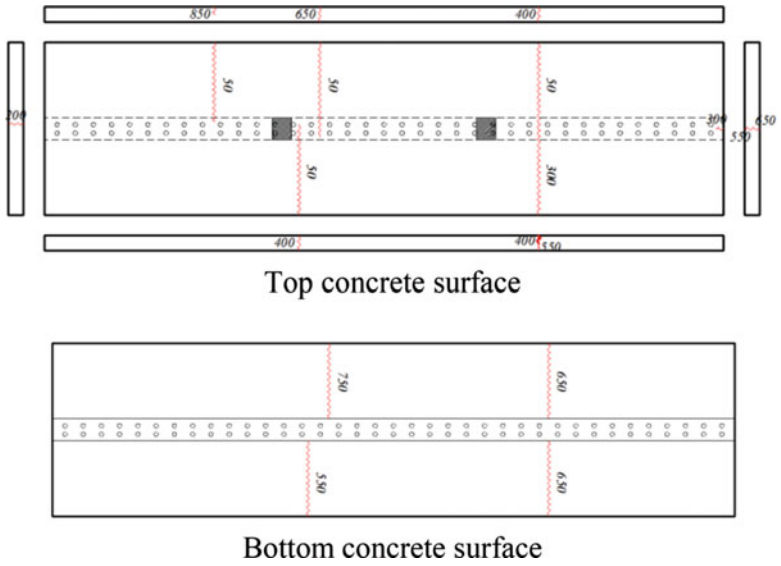

Fig. 13.4 Crack formation and distribution on the concrete flange for specimen B-1 (Number of cycles in thousands)

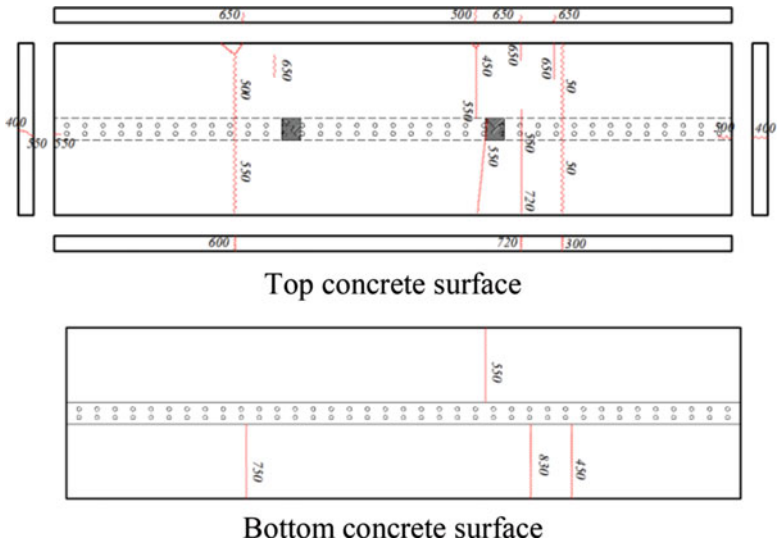

Fig. 13.5 Crack formation and distribution on the concrete flange for specimen B-2 (Number of cycles in thousands)

axis of the specimens. These cracks were considered flexural cracks that mainly initiated due to the fatigue compressive stress of the applied sagging moment. After completion of the fatigue tests, it was obvious that providing top and bottom longitudinal reinforcement as well as enough transverse reinforcement in the concrete flange can provide adequate confinement to concrete to limit fatigue cracks in the concrete flange.

Figure 13.6 showed the cyclic limits of the total mid-span deflection of specimens B-1 and B-2. These limits were slightly increasing linearly with respect to the number of load cycles. A minor propagation of the initial cracks and development of additional cracks were the main reasons for this increase in deflections. A growth in the residual deflection was obtained by increasing the number of cycles due to the damage region that developed in the concrete flange by the shear studs and caused a loss of stiffness in the connection and this growth increased as the fatigue force range increased. Fig. 13.7 showed the cyclic limits of the total strain in the shear connectors at supports. The absence of shear stud fatigue failures was confirmed because the displacements, observed with the LVDTs, did not increase suddenly during the fatigue tests [13]. It was confirmed also by inspecting the conditions of the shear connectors by removing the concrete flanges.

Figure 13.8 illustrated the cyclic limits of the total slippage between the concrete flanges and the steel beams for all fatigue specimens. Based on these results, a plastic slippage occurred and the specimen with higher fatigue load range demonstrated the highest level of such slippage due to more damage in the shear connection between the steel beam and the concrete flange;

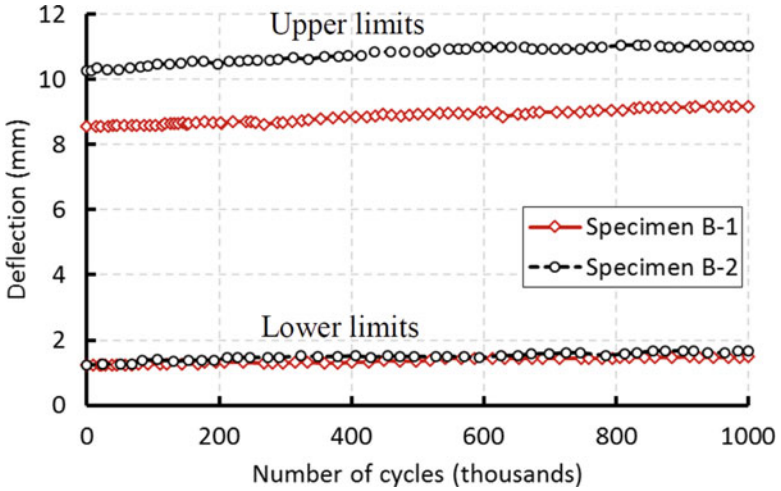

Fig. 13.6 Variation of the total cyclic deflections at mid-spans over fatigue tests

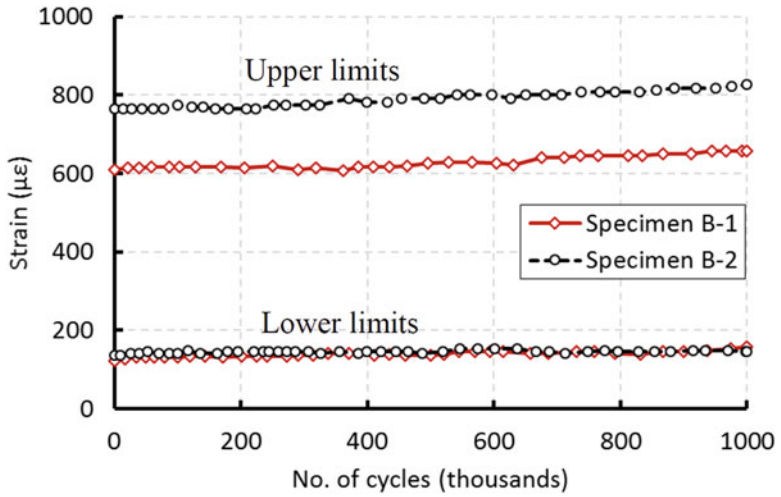

Fig. 13.7 The total cyclic strains in the shear connectors

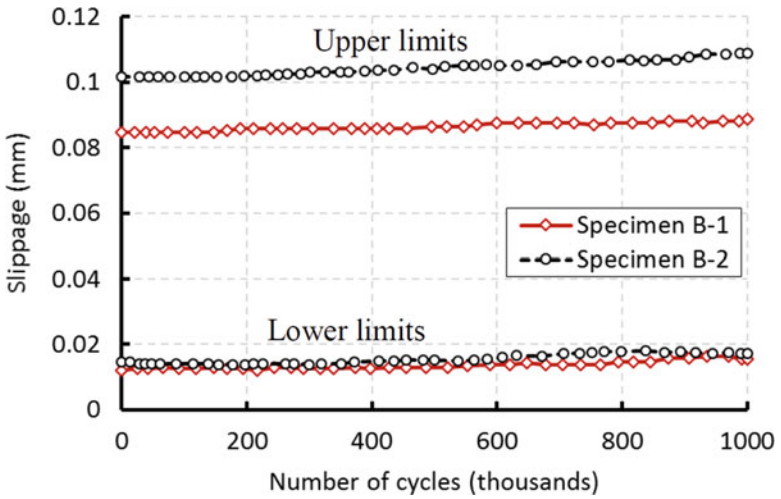

Fig. 13.8 Variation of the total cyclic slippage over fatigue tests

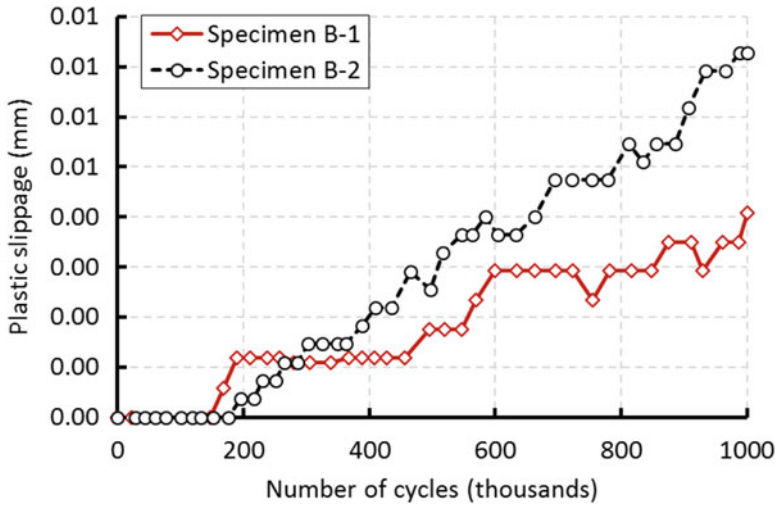

Fig. 13.9 The plastic slippage

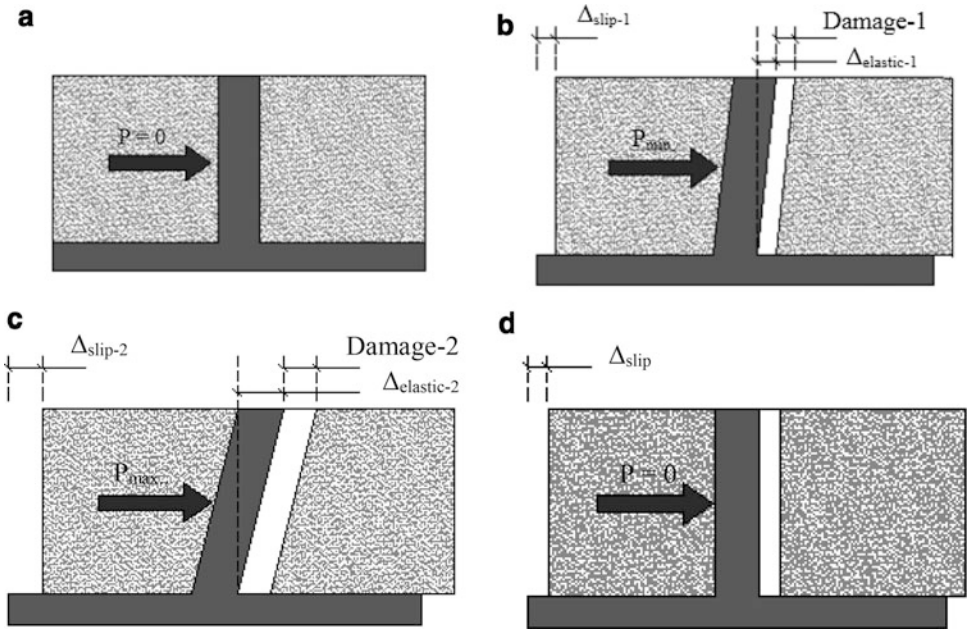

Fig. 13.10 Diagrammatic representation of the shear connection damage under fatigue loads. (**a**) The stud and concrete flange prior to loading ($\Delta_{slip} = 0$). (**b**) The load P_{min} caused a damage in the shear connection (damage-1). ($\Delta_{slip\ -\ 1} = \Delta_{elastic\ -\ 1}$ + damage − 1). (**c**) The load P_{max} aused a damage in the shear connection (damage-2 > damage-1). ($\Delta_{slip\ -\ 2} = \Delta_{elastic\ -\ 2}$ + damage − 2). (**d**) The concrete flange slides through the damage region Δ_{slip}=cumulative of Damage-2

as presented in Fig. 13.9. To demonstrate the reason for such incremental slippage, the inelastic behavior in the local crushing of concrete at the base of the shear connectors caused slip at the stud shear connection to accumulate. To extend our knowledge on the shear connection under fatigue loads, the accumulation of damage in the shear connection during fatigue tests was illustrated in Fig. 13.10. Prior to any loads, there was no slippage between the concrete flange and the steel beam; as demonstrated in Fig. 13.10a. The minimum fatigue load caused an elastic deformation in the shear connector and a damage in the shear connection (damage-1). Therefore, the slippage between the concrete flange and the steel beam became as illustrated in Fig. 13.10b. As the fatigue load increased to the maximum, the elastic deformation in the shear connectors and the damage in the shear connection increased and subsequently the slippage increased; as shown in Fig. 13.10c. An accumulation of damage (summation of damage-2) in the stud shear connection was formed with further repeated load cycles and caused a plastic slippage between the concrete flange and the steel beam; as depicted in Fig. 13.10d.

13.5 Conclusion

In this paper, an experimental work, consists of two specimens, was presented to study the fatigue behavior of shear connectors as well as steel-concrete composite beams. Analysis of the experimental results provided the following conclusions:

1. After completion of the fatigue tests, it was obvious that providing top and bottom longitudinal reinforcement as well as enough transverse reinforcement in the concrete flange can provide adequate confinement to concrete to limit fatigue cracks in the concrete flange.
2. A growth in the cyclic limits of the total deflection was obtained by increasing the number of cycles due to the damage region that developed in the concrete flange by the shear studs and caused a loss of stiffness in the shear connection.
3. The cyclic limits of the total strain in the shear connectors gradually increased over the duration of the fatigue tests.
4. Due to the accumulation of damage in the shear connection, a plastic slippage occurred between the concrete flange and the steel beam.

References

1. Slutter, R.G., Fisher, J.W.: Fatigue strength of shear connectors, Highway Research Record No. 147, pp. 65–88. National Research Council, Washington, DC (1966)
2. Johnson, R.P.: Resistance of stud shear connectors to fatigue. J. Constr. Steel Res. **56**, 101–116 (1997)
3. Hanswille, G., Porsch, M., Ustundag, C.: Resistance of headed studs subjected to fatigue loading part II: analytical study. J. Constr. Steel Res. **63**, 485–493 (2007)
4. Dogan, O., Roberts, T.M.: Fatigue performance and stiffness variation of stud connectors in steel–concrete–steel sandwich systems. J. Constr. Steel Res. **70**(3), 86–92 (2012)
5. Liu, K., De Roeck, G.: Parametric study and fatigue-life-cycle design of shear studs in composite bridges. J. Constr. Steel Res. **65**, 1105–1111 (2009)
6. Ovuoba, B., Prinz, G.S.: Fatigue capacity of headed shear studs in composite bridge girders. J. Bridg. Eng. **21**(12), 04016094 doi.org/10.1061/(ASCE)BE.1943-5592.0000915 (2016)
7. Richard Yen, J.Y., Lin, Y., Lae, M.T.: Composite beams subjected to static and fatigue loads. J. Struct. Eng. **123**(6), 765–771 (1997)
8. Hanswille, G., Porsch, M., Ustundag, C.: The behaviour of steel-concrete composite beams under repeated loading, In: Nordic Steel Construction Conference, NSCC2009, Malmo, (2009)
9. Yu-Hang, W., Jian-Guo, N., Jian-Junb, L.: Study on fatigue property of steel–concrete composite beams and studs. J. Constr. Steel Res. **94**, 1–10 (2014)
10. Dai, X.X., Richard Liew, J.Y.: Fatigue performance of lightweight steel–concrete–steel sandwich systems. J. Constr. Steel Res. **66**(2), 256–276 (2010)
11. AASHTO: AASHTO LRFD bridge design specifications, 6th edn, Washington, DC (2012)
12. ASTM A370, Standard Test Methods and Definitions for Mechanical Testing of Steel Products, West Conshohocken, PA 19428–2959, USA, (2013)
13. Albrecht, P., Lenwari, A.: Fatigue strength of repaired Prestressed composite beams. J. Bridg Eng. **13**(4), 409–417 (2008)

Chapter 14
Numerical Modeling of Charpy Impact Test to Determine the Fracture Characteristics of Aluminium Alloy 6061

Salman Pervaiz, Sathish Kannan, Karthikeyan Ram, and Wael A. Samad

Abstract Impact testing is commonly utilized to determine the fracture characteristics of engineering materials under dynamic loading. Materials have the tendency to behave differently under dynamic high rate loading as compared to their quasi static response. Additionally, impact testing can also reveal information about (i) a material's resisting behavior to high rate loading, as well as (ii) the impact characteristics through measuring the energy consumed during the impact of notched test specimens. The current study incorporates a Johnson-Cook (JC) material constitutive law and failure computational model to simulate the Charpy test for Al-6061. The JC material model is generally employed to simulate the problems related to impact and penetration. The aim of this current study is to provide a numerical assessment tool using ABAQUS for the better and reliable predictions of impact behavior and to facilitate the design process. The numerical results were found in agreement with the experimental validations.

Keywords Charpy · Failure · FEM · Impact · Johnson-cook

14.1 Introduction

Aluminium alloy (AA-6061) is widely used in different industrial sectors such as structural, automotive, transportation and machinery etc. This is the most commonly used 6000 series aluminum alloys, and is famous due to its applications in medium to high strength application [1]. This aluminum alloy is also favoured due to its heat treatability and higher toughness value [2]. Impact testing is generally performed to get the material's response to high rate loading conditions. High rate loading will bring the influence of inertia and rate sensitivity in the material. To incorporate the effects of inertia in finite element (FE) model, dynamic equilibrium equations are used in the explicit mode [3]. Whereas the appropriate selection of material model will capture the influence of rate sensitivity. To accommodate the material behavior, Johnson - Cook (JC) model is majorly employed in the impact or similar problems such as machining, forming processes etc. [4]. Charpy impact test is a low cost but reliable test that breaks a notch specimen under impact loading using a hammer, and evaluates the amount of energy consumed during breakage [5].

Several researchers have focused their work, both experimental and numerical, in the area of impact testing to analyse different materials behavior. Banerjee et al. [6] studied the failure modes under impact loading for the armour steel. The study also incorporated numerical model using ABAQUS. Material behavior for armour steel was developed using Johnson – Cook (JC) material model. The study incorporated tensile testing to establish JC model and JC damage parameters. The study revealed good agreement in between experimental and simulated results. Hufenbach et al. [7] performed an experimental study to figure out the impact resistance of composite material. The experimentation was performed on a specially designed test rig. The study considered three different types of fibre materials (Torayca-T300, Torayca-T700 s and Torayca-T800 s). The study also utilized LSDYNA-3D to develop a finite element model of Charpy test. Both experimental work and simulated results were found in good agreement.

S. Pervaiz · W. A. Samad (✉)
Department of Mechanical and Industrial Engineering, Rochester Institute of Technology, Dubai, United Arab Emirates
e-mail: wascad@rit.edu

S. Kannan
Department of Mechanical Engineering, College of Engineering, American University of Sharjah, Sharjah, United Arab Emirates

K. Ram
Department of Mechanical Engineering, BITS Pilani – Dubai Campus, Dubai, United Arab Emirates

J. Carroll et al. (eds.), *Fracture, Fatigue, Failure and Damage Evolution, Volume 6*, Conference Proceedings of the Society for Experimental Mechanics Series, https://doi.org/10.1007/978-3-319-95879-8_14

The aim of this current study is to provide a numerical assessment tool using ABAQUS for the better and reliable predictions of impact behavior and to facilitate the design process. The numerical results were found in agreement with the experimental validations.

14.2 Experimental Setup

The Charpy impact experiments were conducted on the pendulum impact testing machine. The machine consists of a heavy pendulum of known mass and anvils to support the specimen. The three specimens were prepared using the guidelines as mentioned in ASTM standard and shown in Fig. 14.1. Figure 14.2 shows the experimental setup and a broken sample. Table 14.1 reports the chemical composition and mechanical properties of the raw workpiece material.

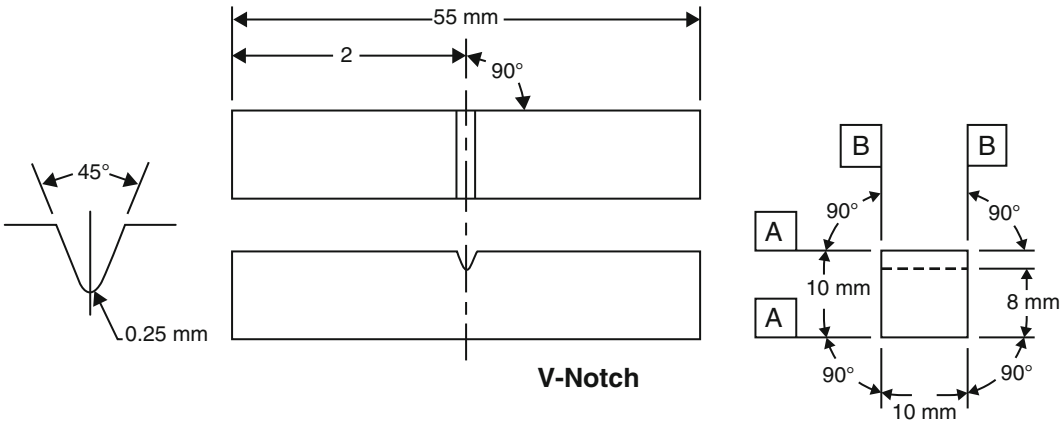

Fig. 14.1 Dimension of the samples prepared for the testing (adopted from ASTM E23 − 16b [8])

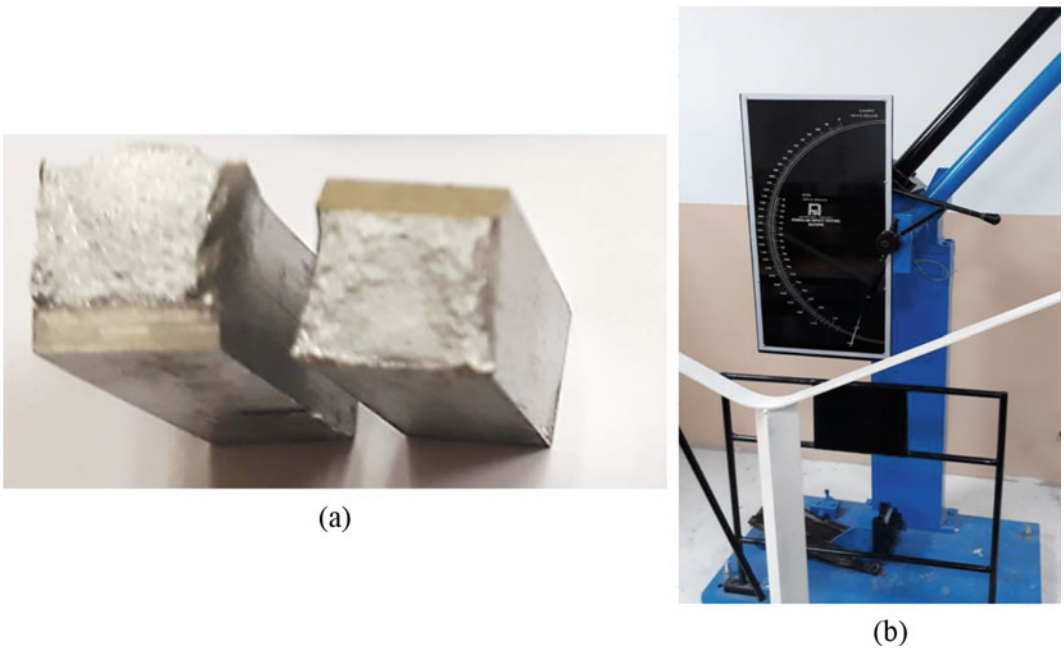

Fig. 14.2 (**a**) Broken sample under Charpy test, (**b**) Pendulum based Charpy impact tester

14.3 Finite Element (FE) Model Setup

The FE model for Charpy test was developed in ABAQUS Explicit. The workpiece materials constitutive behavior was simulated using Johnson – Cook (JC) material model as shown in Eq. 14.1. This constitutive model consists of three terms, mainly used to incorporate the effects of plastic strain hardening, strain rate sensitivity and thermal softening. The damage evolution was controlled using JC damage parameters for Eq. 14.2 (Fig. 14.3, Table 14.2).

Table 14.1 Specifications of workpiece material (6061-O temper)

(A) Chemical Composition							
Element	Wt. %	Element	Wt. %	Element	Wt. %	Element	Wt. %
Si	0.4–0.8	Cu	0.15–0.4	Mg	0.8–1.2	Zi	0.25
Fe	0.7	Mn	0.15	Cr	0.04–0.35	Al	Balance
(B) Mechanical Properties at Room Temperature							
Properties		Values		Properties		Values	
Ultimate tensile strength		110–152 MPa		Elongation		14–16	
0.2% proof stress		65–110 MPa		Brinell hardness number		30–33	

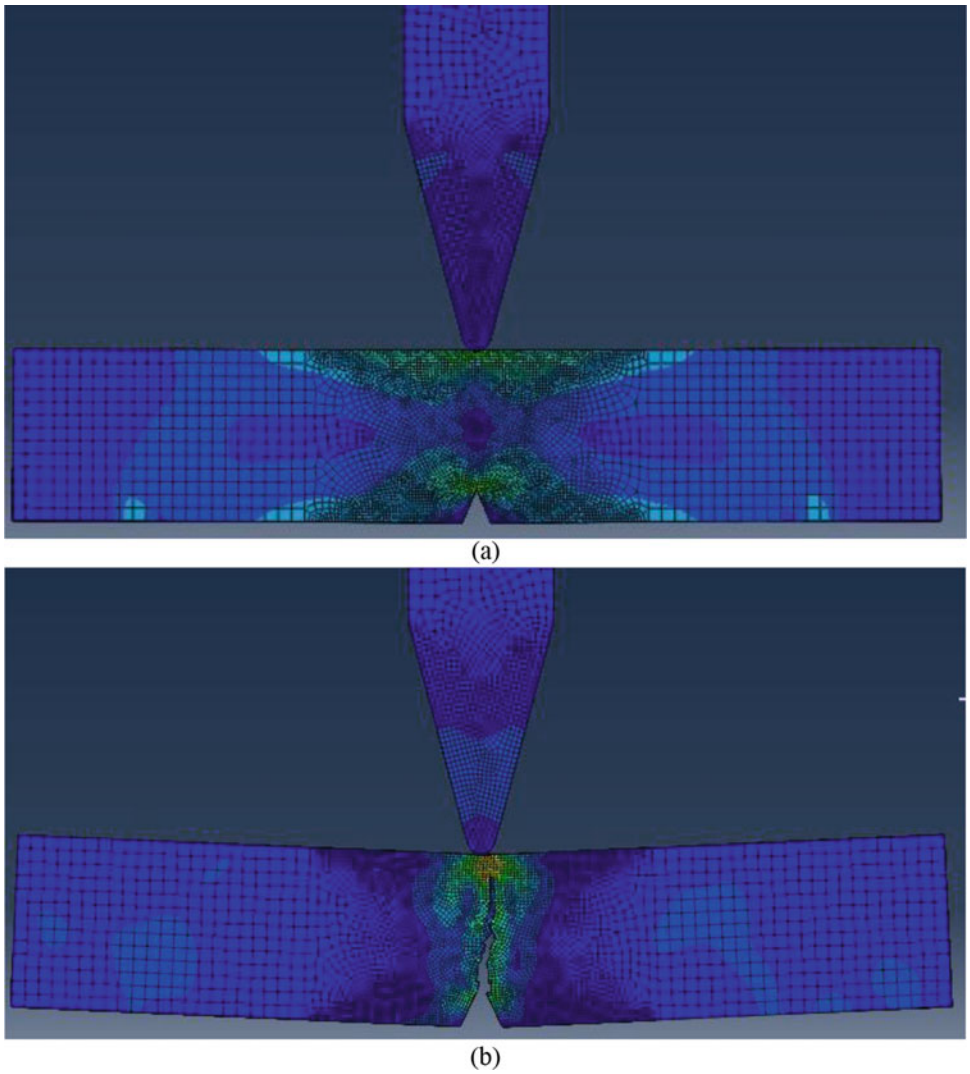

Fig. 14.3 (**a**) Crack initiation at the tip of v- notch, (**b**) Crack propagated

Table 14.2 Johnson – Cook parameters for Al 6061 [9]

A (MPa)	**B(MPa)**	**C**	**n**	**m**
324	114	0.002	0.42	1.34
D_1	**D_2**	**D_3**	**D_4**	**D_5**
−0.77	1.45	0.47	0	1.6

$$\sigma = \left[A + B\left(\varepsilon\right)^n\right]\left[1 + C\ln\left(\frac{\dot{\varepsilon}}{\dot{\varepsilon}_0}\right)\right]\left[1 + \left(\frac{T - T_{room}}{T_{melt} - T_{room}}\right)\right] \tag{14.1}$$

$$\varepsilon_f = [\mathrm{D}_1 + \mathrm{D}_2\exp\left(\mathrm{D}_3\sigma^*\right)]\left[1 + \mathrm{D}_4\ln\left(\varepsilon_p^*\right)\right][1 + \mathrm{D}_5 T^*] \tag{14.2}$$

14.4 Results and Conclusions

- The simulated fracture energy was found to be 23 Joules. However, the average value of experimental fracture energy came to be 28 Joules for three samples.
- The study provided a reliable numerical model to predict the Aluminum 6061 behaviour under high rate impact loading conditions. The simulation-based tool can be used to design any related applications.
- The study utilized Johnson – Cook (JC) material model to incorporate the constitutive behaviour of Al 6061. The selection of JC parameters controls the reliability of the numerical model. These parameters should be incorporated correctly into the model.
- The developed numerical simulation will be used to study the fracture energy at elevated temperatures in future. This can also predict the brittle to ductile transition of the material under observation.

References

1. Cobden, R., Banbury, A.: Aluminium: physical properties, characteristics and alloys. Talal. **1994**(1994), 60 (1994)
2. MacMaster, F.J., Chan, K.S., Bergsma, S.C., Kassner, M.E.: Aluminum alloy 6069 part II: fracture toughness of 6061-T6 and 6069-T6. Mater. Sci. Eng. A. **289**(1–2), 54–59 (2000)
3. Molinari, A., Mercier, S., Jacques, N.: Dynamic failure of ductile materials. Procedia IUTAM. **10**, 201–220 (2013)
4. Johnson, G.R., Cook, W.H.: Fracture characteristics of three metals subjected to various strains, strain rates, temperatures and pressures. Eng. Fract. Mech. **21**(1), 31–48 (1985)
5. ASTM E 23-12c: Standard Test Methods for Notched Bar Impact Testing of Metallic Materials, vol. i, pp. 1–25. Standards, West Conshohocken (2013)
6. Banerjee, A., Dhar, S., Acharyya, S., Datta, D., Nayak, N.: Determination of Johnson cook material and failure model constants and numerical modelling of Charpy impact test of Armour steel. Mater. Sci. Eng. A. **640**, 200–209 (2015)
7. Hufenbach, W., Ibraim, F.M., Langkamp, A., Böhm, R., Hornig, A.: Charpy impact tests on composite structures – an experimental and numerical investigation. Compos. Sci. Technol. **68**(12), 2391–2400 (2008)
8. ASTM Int: Standard Test Methods for Notched Bar Impact Testing of Metallic Materials, vol. i, pp. 1–26. ASTM B. Stand., West Conshohocken (2016)
9. Corbett, B.M.: Numerical simulations of target hole diameters for hypervelocity impacts into elevated and room temperature bumpers. Int. J. Impact Eng. **33**(1–12), 431–440 (2006)

Chapter 15
A Progression on the Determination of Dynamic Fracture Initiation Toughness Using Spiral Crack

Ali F. Fahem and Addis Kidane

Abstract A recent development on identifying the static and dynamic initiation fracture toughness of materials by using a single v-notch spiral crack is presented. A polycarbonate solid cylindrical sample with spiral crack is implemented in this work to demonstrate the method. The quasi-static experiment was conducted by applying a pure torsion on the specimen using an MTS axial-torsion machine. The dynamic fracture experiment was conducted using Torsional Spilt Hopkinson Bar. In both cases, the torque corresponding to fracture initiation is measured experimentally and used as input to the numerical simulation. A new emphasis relation for a cylindrical specimen with spiral crack is also proposed and used with the experimental data to quantify the initiation fracture toughness. The results show that the spiral crack specimen is an effective method to determine the fracture toughness of materials.

Keywords Spiral crack · Dynamic and static SIF · Torsional load · TSHB · Polycarbonate material

15.1 Introduction

The elastic fracture toughness of a material at quasi-static loading has been effectively measured experimentally with different standard methods [1], though these methods have critical requirements to be valid, such as specimen geometry and a plane strain condition [2]. However, there is no standard method available for dynamic fracture toughness K_{Id} [3, 4]. The damage and failure of polymers, Metals and Composites materials under dynamic loading is still something needed to be understtod well [5–7]. The exiting dynamic fracture experimental methods, such as three point bending test in Hokinson pressure bar, have has additional issues related to the inertia load [3]. Novel experimental methods with a spiral crack configuration subjected to pure torsion load has been proposed in 1985 [8]. Letter, a modify of a spiral configuration specimen was used to measure the static fracture toughness of materials K_{Ic} [9]. Very earlier, the spiral crack configuration was used to measure the dynamic fracture toughness of the material K_{Id} by using the numerical method and Torsional Hopkinson Bar [10, 11]. In general, the spiral crack has a couple of advantage, and the most important one is that the spiral crack is geometry independent and the plane strain condition is achieved with different crack depth [12–14]. In this paper, a progression in measuring dynamic fracture toughness is present and a static fracture as well. Experimentally, a Polycarbonate material is used to manufacture the specimens with a spiral crack. Theoretical, the experimental data is using with a new mathematical close form which develops by Kidane [13]. In a static case, the axial-torsion Test Resource machine was used, and in dynamic case, the Torsional Hopkinson Bar was used.

15.2 Experimental Setup

Polycarbonate material (ASTM D3935, Made of UL94HB) is used in this study. Ten different specimen configurations are prepared to perform two types of experiments as discussed below.

A. F. Fahem (✉) · A. Kidane
University of South Carolina, Columbia, SC, USA
e-mail: afahem@email.sc.edu

J. Carroll et al. (eds.), *Fracture, Fatigue, Failure and Damage Evolution, Volume 6*, Conference Proceedings of the Society for Experimental Mechanics Series, https://doi.org/10.1007/978-3-319-95879-8_15

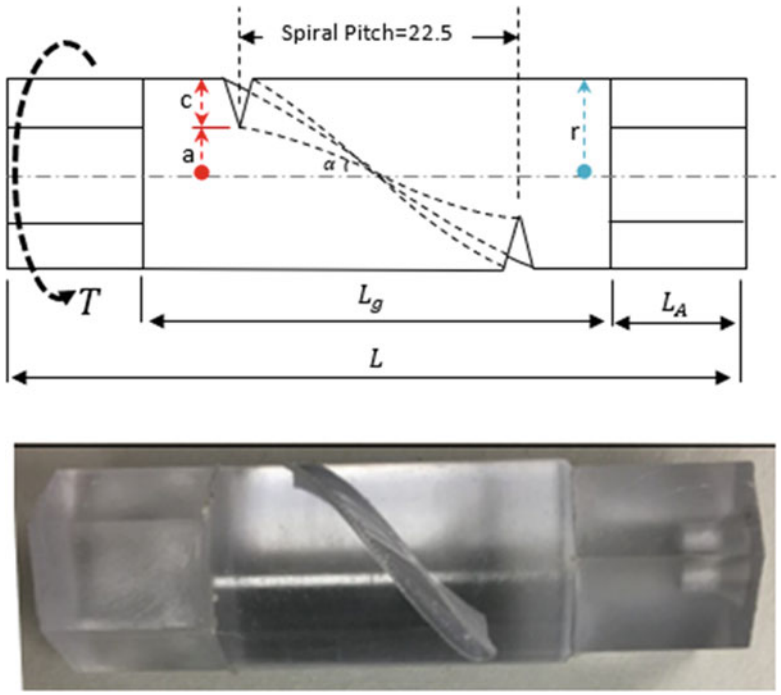

Fig. 15.1 Spiral crack specimen of a static test

15.2.1 Static Experimental Setup

Five specimens of a cylindrical bar with spiral crack were prepared. A Polycarbonate solid bar 25.4 mm diameter, is used to make the specimens. A 4D milling machine was used to generate a v-notch groove on the spiral path around the gauge diameter and along the gauge length. The crack was made by Mico-Engraving V-groove cutter tools (the tip has V-shape with 60°, and a diameter of 0.127 mm). Then stainless-steel razor blade was used to generate the final artificial crack. Specimens were fabricated with a different aspect ratio (c/r), as shown in Fig. 15.1**,** where c is the crack depth and r is the radius of the cylinder. The specimens made with a $\beta_{sp} = 135^{\circ}$, where β_{sp} is the angle of revolution of the spiral pitch. The spiral angle was kept 45° with respect of the axis of the specimen and center of the specimen.

The test was performed under angular displacement control. The angle of twist was varing with the time at a rate of 1Deg./min. The torque developed was recorded through the load cell of the Test Resources machine. The crack dimension was measured after the specimen fractured (Fig. 15.2).

Maximum far-field shear stress develops at the out surface of the specimen is calculated by using Eq. (15.1) [13].

$$\tau_{\max} = \frac{Tr}{J} \quad \text{where } J = \frac{\pi}{32} D^4 \,(\text{at the section far from the crack}) \tag{15.1}$$

Table 15.1, documented the maximum shear stress of the specimens at a fractured moment. These stresses will be used later as a far-field loading to calculate stress intensity factor (Table 15.2).

15.2.2 Dynamic Experimental Setup

Five cylindrical specimens with a spiral v-notch on the surface are used for the dynamic fracture analysis (Fig. 15.3)). Specimens with the same material, Polycarbonate (ASTM D3935, Made of UL94HB), geometry and dimensions used in static experiment are fabricated in the dynamic case following similar method. The outer diameter r, crack deep c, crack ligament a, and crack depth-to-radius ratio (c/t) parameters are shown in Table 15.3.

The Torsional Split Hopkinson Bar (TSHB) is used to generate a torsional impulse wave. The details of the TSHB apparatus and the background are available in the literature [10, 15, 16]. The TSHB used in this work has 2.5 m and 2.2 m long

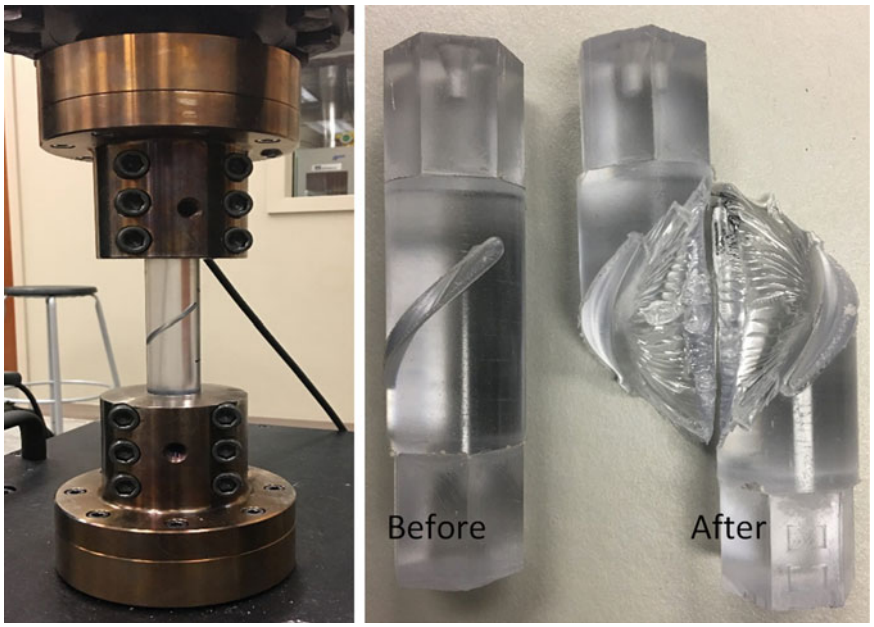

Fig. 15.2 Static Test Setup

Table 15.1 Specimens dimensions of static test

Specimen #	L mm	r mm	L_g mm	L_A mm	c mm	a mm	(c/r)
Specimen#1	92.5	12.7	42.5	25	6.0	6.74	0.47
Specimen#2	92.5	12.7	42.5	25	6.5	6.2	0.51
Specimen#3	92.5	12.7	42.5	25	7.0	5.7	0.55
Specimen#4	92.5	12.7	42.5	25	7.5	5.2	0.59
Specimen#5	92.5	12.7	42.5	25	8.0	4.5	0.64

Table 15.2 Maximum shear stress at a fracture torque

Specimen #	(c/r)	T (Nm)	τ_{max} *MPa.*
Specimen#1	0.47	113.090	35.2
Specimen#2	0.51	110.609	34.4
Specimen#3	0.55	104.400	32.5
Specimen#4	0.59	101.550	31.6
Specimen#5	0.64	94.662	29.4

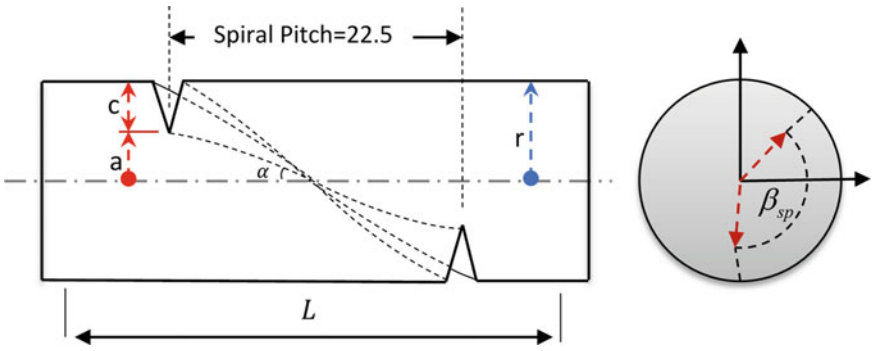

Fig. 15.3 Dynamic specimen configuration

Table 15.3 Dynamic specimen dimensions

Test#	Material	*r* (mm)	*c* (mm)	Spiral angle	*(c/r)*
1	Polycarbonate	12.7	8.0	135	0.63
2	Polycarbonate	12.7	8.0	135	0.63
3	Polycarbonate	12.7	8.0	135	0.63
4	Polycarbonate	12.7	7.0	135	0.55
5	Polycarbonate	12.7	8.5	135	0.67

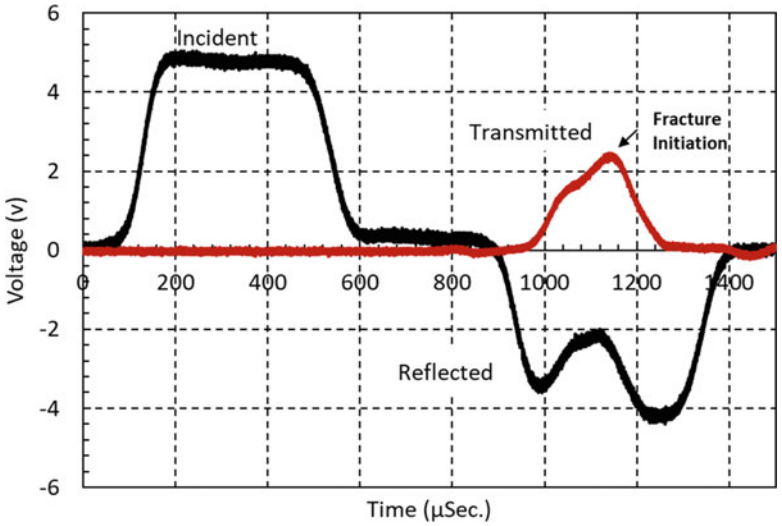

Fig. 15.4 Torsional impulse wave of polycarbonate test

incident and transmitter bars, respectively. These bars made of 25.4 mm diameter Aluminum alloy 7075-T6 (ASTM-B211), and they supported in a horizontal plane. The bars cannot move in the x and y-direction, but they can rotate around their central axis. The specimen is held in place, using a thin layer of JB-Weld epoxy, between the incident and transmitter bars and left for 24 h for full cure.

A hydraulic clamping system with a fracture screw technique is used to generate impulse torsional load as deatiled in the paper [17]. When the incident wave reached the specimen, some of it will transmit into the output bar through the specimen, and the rest will reflect-back to the incident bar. The waves were recorded by using the strain gauges attached to the bars and signal conditions amplifiers and oscilloscope. Typical incident, transmitted and reflected signals are shown in Fig. 15.4.

The classical torsion theory (St. Venant Torsion Theory) and one-dimensional wave analysis are used to calculate the average effective torque in the spiral crack specimens as following. Eq. (15. 2) is the torque at the input-specimen interface $T_1(t)$, Eq. (15.3) is the output-specimen interface $T_2(t)$ and Eq. (15.4) is the average torque on the specimen $T_s(t)$ [15]. The experimental measured effective torque for five diffferent specimens are shown in Fig. 15.5**.**

$$T_1(t) = \frac{GD^3\pi}{16}[\gamma_I(t) + \gamma_R(t)] \tag{15.2}$$

$$T_2(t) = \frac{GD^3\pi}{16}[\gamma_T(t)] \tag{15.3}$$

$$T_S(t) = \frac{T_1(t) + T_2(t)}{2} \tag{15.4}$$

Where G: the shear Modulus of the bar; D: bars diameter; $\gamma_I(t)$, $\gamma_R(t)$, $\gamma_T(t)$: Incident, Reflected and Transmitted shear strains respectively.

The torque measured is used as input for the finite element method and the fracture parameters are extracted Fig. 15.6. More details about the Finite Element model is available in Fahem [11].

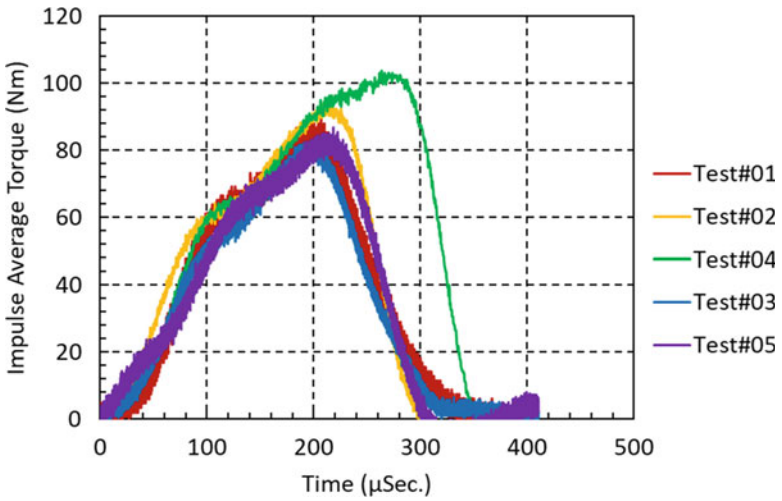

Fig. 15.5 Average effective torque on the specimen

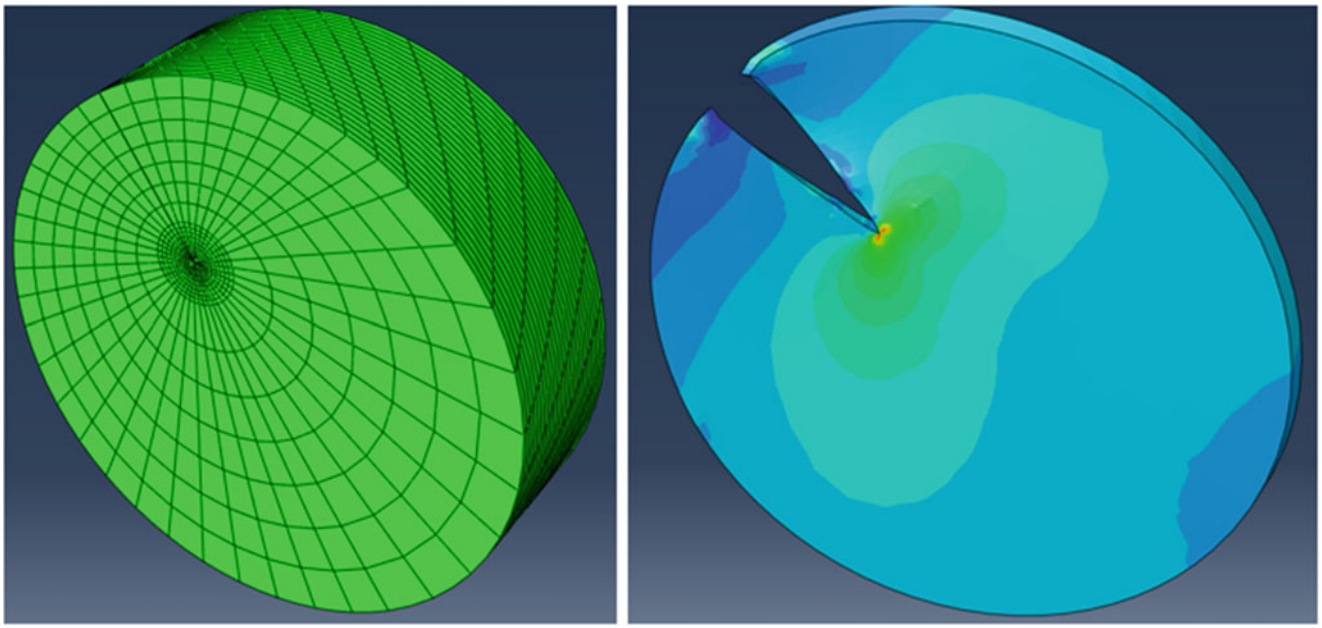

Fig. 15.6 FE model of spiral crack under pure torsion load [10]

15.3 Result and Discussion

The two-experimental methods set up, static and dynamic, are performed at room temperature to identify the fracture toughness of polycarbonate material. Both experimental works are compared throughout the range of aspect ratio.

In a static case, the geometry of the specimen, torque at fracture, and maximum shear stress are used to calculate the stress intensity factor [13]. At each test, the maximum shear stress applied, the configuration factor *Y,* Fig. 15.7**,** are substances in Eq. (15.5) to calculate SIF. The procedure repeated for all specimens. Table 15.4 shows the fracture toughness of polycarbonate material in a quasi-static case.

$$K_I = \tau_{\max.}\sqrt{\pi a} \times Y(a, r, c) \tag{15.5}$$

$$\text{and } Y(a, r, c) = \sqrt{1 - \frac{a}{r}} \times G\left(\frac{c}{r}\right) \tag{15.6}$$

Table 15.4 Spiral crack under pure torsion load (**Test Resource**)

Test#	Material	Radius (*mm*)	Crack Depth (*mm*)	Spiral Revolution	$G\left(\frac{c}{r}\right)$	$K_{Ic}\ MPa\sqrt{m}$
1	Polycarbonate	12.7	4.6	135	1.117	3.886
2	Polycarbonate	12.7	6.0	135	1.148	3.914
3	Polycarbonate	12.7	6.5	135	1.181	3.810
4	Polycarbonate	12.7	7.5	135	1.218	3.780
5	Polycarbonate	12.7	8.0	135	1.273	3.741

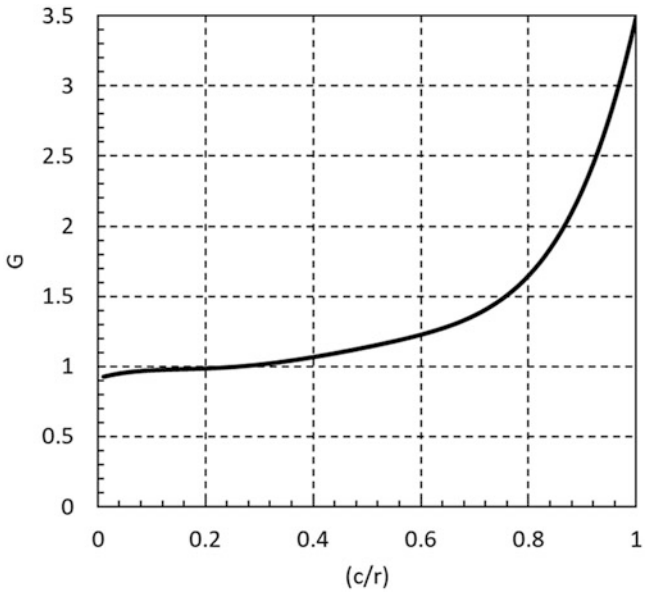

Fig. 15.7 Configuration factor of spiral crack under pure torsion load [13]

Table 15.5 Spiral crack under pure impulse torsion load (**TSHB**)

Test#	Material	Radius (*mm*)	Crack Depth (*mm*)	Spiral Revolution	$K_{Id}(MPa\sqrt{m})$
1	Polycarbonate	12.7	8.0	135	3.37
2	Polycarbonate	12.7	8.1	135	3.28
3	Polycarbonate	12.7	7.9	135	3.12
4	Polycarbonate	12.7	7.0	135	3.78
5	Polycarbonate	12.7	8.5	135	3.59

In a dynamic case, the advantage of torsional Hopkinson Bar is that the inertia load is not affecting the shear stress and it is perpendicular wave propagation direction [12, 18, 19]. Hence the stress intensity factor can be calculated as a function of time by Abaqus Explicitly (Finite Element Simulation). The dynamic fracture initiation toughness K_{Id} of polycarbonate, the stress intensity factor at the initiation of fracture, is calculated and documented in Table 15.5**.**

15.4 Conclusions

The static and dynamic fracture toughness of polycarbonate material has been tested using cylindrical specimen with spiral crack configuration under torsion. In the static case, the specimens have been performing by using a Test-Resource machine with a different low-loading rate. The dynamic test is performed by using a Torsional Hopkinson Bar arrangement. The following remarks can be summarized from the present work.

(a) With a single specimen configuration, cylindrical specimen with spiral crack, under pure torsion load, the static and dynamic performance can be used to get the fracture toughness of materials K_{Ic} and K_{Id}.

(b) At the loading rate $\left(0.4GPa\sqrt{m}/s \leq \dot{K}_I \leq 6.0GPa\sqrt{m}/s\right)$, the fracture toughness of polycarbonate almost the same.

(c) The fracture toughness of polycarbonate at intermidate loading rate $\left(11GPa\sqrt{m}/s \leq \dot{K}_I \leq 16GPa\sqrt{m}/s\right)$ is lower than quasi-static value.

(d) Additional work is needed to further investigate at higher loading rate.

Acknowledgment Mr. Ali Fahem was financially supported by Ministry of Higher Education and Scientific Research, University of Al-Qadisiyah-Iraq and is greatly acknowledged.

References

1. Zhu, X., Joyce, J.A.: Review of fracture toughness (G, K, J, CTOD, CTOA) testing and standardization. Eng. Fract. Mech. **85**, 2472 (2012)
2. ASTM E399-90: Standard Test Method for Plane-Strain Fracture Toughness of Metallic Materials, pp. 487–511. ASTM International, West Conshohocken (1997), https://www.astm.org
3. Ravi-Chandar, K.: Dynamic Fracture. Elsevier, Amsterdam (2004)
4. Meyers, M.A.: Dynamic Behavior of Materials. Wiley, New York (1994)
5. Ravindran, S., Tessema, A., Kidane, A.: Multiscale damage evolution in polymer bonded sugar under dynamic loading. Mech. Mater. **114**, 97–106 (2017). https://doi.org/10.1016/j.mechmat.2017.07.016
6. Fahem, A.F., Fathi, A.A.: A Stusy of the Effect of Impact loading on DSIFs and crack propagation in Plate. Al-Qadisiya J. Eng. Sci. **2**, 288–303 (2009)
7. Anay, R., Soltangharaei, V., Assi, L., et al.: Identification of damage mechanisms in cement paste based on acoustic emission. Constr. Build. Mater. **164**, 286–296 (2018). https://doi.org/10.1016/j.conbuildmat.2017.12.207
8. Sweeney, J.: Analysis of a proposed method for toughness measurements using torsion testing. J. Strain Anal. Eng. Des. **20**, 1–5 (1985)
9. Wang, J.-A., Kenneth, C., Liu Oak Ridge T.:(US): Fracture Toughness Determination Using Spiral-Grooved Cylindrical Specimen and Pure Torsional Loading, pp. 1–24. UT-BATTELLE, LLC, Oak Ridge (2003)
10. Fahem, A.F., Kidane, A.: A general approach to evaluate the dynamic fracture toughness of materials. In: Dynamic Behavior of Materials, Conference Proceedings of the Society for Experimental and Applied Mechanics, pp. 229–236. Florida (2016)
11. Fahem, A., Kidane, A.: Hybrid computational and experimental approach to identify the dynamic initiation fracture toughness at high loading rate. In: Dynamic Behavior of Materials, Conference Proceedings of the Society for Experimental and Applied Mechanics, pp. 141–146, Indianapolis, IN (2017)
12. Wang, J.A., Liu, K., McCABE, D.E., David, S.A.: Using torsional bar testing to determine fracture toughness. Fatigue Fract. Eng. Mater. Struct. **23**, (2000)
13. Fahem, A.F., Kidane, A.: Modification of Benthem solution for mode I fracture of cylinder with spiral crack subjected to Torsion. In: Fracture, Fatigue, Failure and Damage Evolution, vol. 6, the Proceedings of the SEM Annual Conference & Exposition on Experimental and Applied Mechanics, Greenville, SC (2018)
14. Truss, R.W., Duckett, R.A., Ward, I.M.: (the university of leeds).: The fracture toughness of tough polyethylenes by a novel high pressure technique. J. Mater. Sci. **19**, 413–422 (1984)
15. Naik, N.K., Asmelash, A., Kavala, V.R., Ch, V.: Interlaminar Shear Properties of Polymer Matrix Composites : Strain rate effect. Mech. Mater. **39**, 1043–1052 (2007). https://doi.org/10.1016/j.mechmat.2007.05.003
16. Weerasooriya, T.: The MTL Torsional Split-Hopkinson Bar. U.S. Army Materials Technology Laboratory, Watertown (1990)
17. Mallon, S., Koohbor, B., Kidane, A., Reynolds, A.P.: On the Effect of Microstructure on The Torsional Response of AA7050-T7651 at Elevated Strain Rates. Mater. Sci. Eng. A. **639**, 280–287 (2015)
18. Chen, W.W., Bo, S.: Split Hopkinson(Kolsky) Bar Design, Testing and Application. Springer US, Boston (2011)
19. Klepaczko, J.R.: Dynamic crack initiation. Some experimental methods and modelling. Crack Dyn. Met Mater. **310**, 255 (1990)

Chapter 16
Damage Evolution and Local Strain Redistribution in Composite Laminate with Various Fiber Arrangements

Addis Tessema, Suraj Ravindran, and Addis Kidane

Abstract The initiation and gradual development of damage in composites is associated with the degradation of the composite laminate properties. Understanding the characteristics of damage evolution in composite laminates has been one of the major interest in composite studies. There is a lot of progress in this regard, however still there is a lack of clear understanding on how damages are initiated, grown and transformed from one form to another. In this study experiments are conducted to capture the strain localization and cracks formation on the free-edge of composite laminates. Laminates that have a stacking arrangement of $(0/-\Theta/+\Theta/90)_s$ with plies that have different fiber angles ($\Theta = 15^\circ, 30^\circ$ and 45°) are manufactured. Coupon samples are made from these laminates and subjected to a uniaxial tension loading until final fracture. Using digital image correlation technique at high magnification, the local deformation field is determined. From the test, it is observed that the strain/stress response of the composite is influenced by the arrangement of the fiber angle of the off-axis plies. From the strain contours obtained on the free-edge, the gradual initiation and growth of matrix cracks is observed to be localized in the 90° plies. In addition, these matrix cracks grow and lead to cause delamination between the 90° plies and neighboring plies. The local strains in each individual ply are seen to fluctuate along with the emergence of cracks at the vicinity of the damage as a result of stress redistribution.

Keywords Progressive damage · Laminate composite · Matrix cracking · Free-edge · Digital Image Correlation

16.1 Introduction

Fiber reinforced composites has been widely used in various structural and support applications due to their superior stiffness and strength to weight ratio. However, the anisotropic property of the material system has been a big issue in the design and life prediction of laminate structure. The basic mechanics that define the structural response of the composite laminates has been under development for the last six decades. In fact, the earliest Classical laminate plate theory (CLPT) has been used to describe the correlation between the applied load and corresponding deformation [1]. Most failure criteria which are stress or strain based are evaluated from the stress/strain obtained from the CLPT [2, 3]. Nevertheless, this CLPT model considered a 2D plane stress condition for a laminate plate and failed to address the 3D complex stress state formed at the location where geometrical discontinuities within the composite structure are encountered.

Most composite laminate structures have finite size and consisted of different geometrical features (like holes, rectangular cut-outs). These geometrical discontinuities have a stress/traction free surfaces. Note that in composite laminates different layers stacked together in the laminate, and these individual layers have different transverse and shear response/deformation for a given externally applied load. However, since the layers have glued one another, all layers are expected to deform with the same amount transversely and causes interlaminar stresses at the free surfaces. These interlaminar stresses at the free surface makes the stress state much more complex and completely different from the one described in the CLPT.

For this matter, researchers have extended the CLPT formulation to account for force equilibrium and displacement continuity conditions at free-edge, as a result a 3D stress state is acquired at the free-edge and its vicinity [4–9]. These analytical models have incorporated numerous boundary conditions and continuity constraints between plies. In fact, the problem became overly constrained and it is very difficult to find an exact solution. Thus, the approximate solutions are derived using various analytical and numerical approaches [6]. Most of the approximate solutions are based on the theory of elasticity, and developed by using Lekhnitskii's stress potentials [5, 6, 9].

A. Tessema (✉) · S. Ravindran · A. Kidane
Department of Mechanical Engineering, University of South Carolina, Columbia, SC, USA

J. Carroll et al. (eds.), *Fracture, Fatigue, Failure and Damage Evolution, Volume 6*, Conference Proceedings of the Society for Experimental Mechanics Series, https://doi.org/10.1007/978-3-319-95879-8_16

It was discovered that there is stress singularity right at the free-edge. It is presumed that the presence of singular and complex stresses led to the initiation of damage from the free-edges. Earlier microscopic observations have revealed initiation of damage including microcracks, transverse/matrix cracks and lamina delamination at the free-edge [8, 10–14]. It is noticed that these cracks evolved gradually, and the emergence of one form of crack (matrix crack) opens a way to the initiation of the other. The gradual growth and multiplication of the cracks induce degradation in the mechanical property of the laminate system [14–21].

In this work, experimental study is conducted to investigate the strain localizations at micro scale and the associated damage at the free-edge of a laminate. Based on the local strain (axial, transverse and shear) contours obtained by using digital image correlation, the influence of the interlaminar stresses on the free-edge strain localization and progressive damage formation was explored. Moreover, the effect of fiber angle variation on the free-edge strain/stress was investigated by varying the fiber angle of the off-axis plies.

16.2 Sample Preparation

Laminate panels are manufactured by using carbon fiber prepreg obtained from TORAY Composites (America) Inc. with brand name of T-800SC-24 K-10E. First, 8 plies of prepregs are stacked in specific arrangement ((0/−Θ/+Θ/90)s) using an advanced automated fiber placement technique. Following, the stack of prepreg are wrapped with high-temperature plastic bag and the air inside is vacuumed. The bagged stack of plies is placed inside the furnace which is set to cure under a clamping pressure. After completing the curing cycle, the panel is allowed to cool slowly to a room temperature by natural convection.

Rectangular test coupons are cut from the cured laminate using CNC water jet with dimension of 160 mm × 23 mm. The longer side edges of the rectangular coupons are polished using different grades of sandpapers to eliminate debris, notches, or void created during the abrasive water-jet cutting. Further, to protect the fibers from the grip pressure at the time of testing, fiberglass tab (40 × 22 mm^2) are glued at the gripping ends on both sides of the specimen as shown in Fig. 16.1. The tabs are designed to have a wedge tip to reduce the stress concentration and enables a smooth flow of stress from gripping area to the gage area of the laminate.

Two different scales of speckle patterns (black dots over a white background) are made on the two distinct locations of the test coupons (as depicted in Fig. 16.1). Macro size scale (one speckle size is 150–300 μm) speckle pattern are made on the width side of the coupon. Micro scale size (one speckle size is 5–20 μm) speckle are made on the thickness side of the laminate coupons. These speckles are used to obtain the deformation the speckled surface and help to calculate the full-field strain contour.

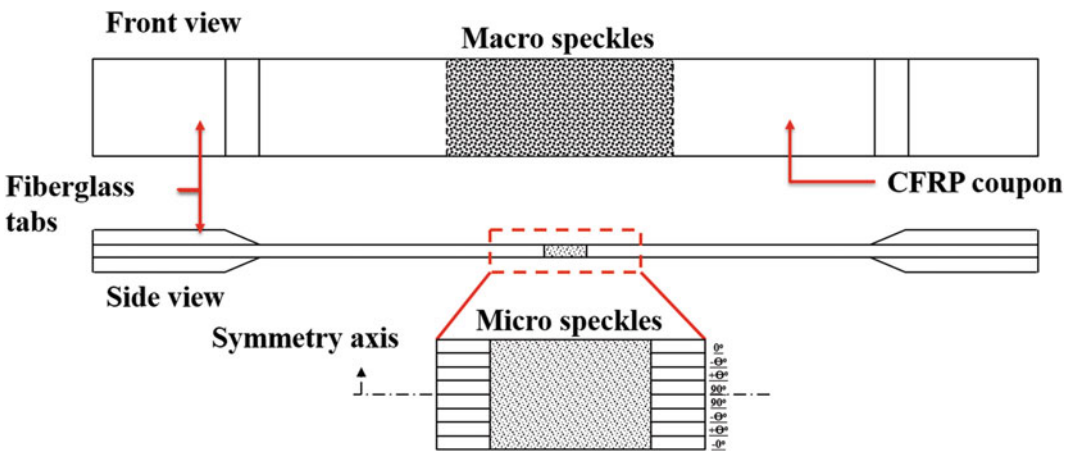

Fig. 16.1 The schematic diagram of coupon specimen with macro and micro speckles

16.3 Experimental Setup

The Material Testing System (MTS 810) is used to perform a displacement controlled quasi-static tensile tests on the coupons specimens. The coupon specimen was gripped at the top and bottom tabs by the two hydraulic grips. A monotonic uniaxial tensile load is applied at the displacement rate of 0.2 mm/min until the coupon failed completely. Two distinct 2D-DIC system are used for the corresponding speckled regions as shown in Fig. 16.2.

For this matter, a 5 MPixels CCD (Grasshopper) camera and 60 mm Nikon lens is used for the macroscale measurement on the width surface of the sample. For measuring the local deformation on the edge of the sample, a 9 MPixels CCD (Grasshopper) camera is paired with 3X magnification Navitar lens directed at the speckled region. The meso-scale 2D-DIC setup has an approximate field of view of 4.15 × 3.32 mm^2 and every image has an approximate resolution of 0.9 μm/pixel. A LED lamp is used for the macro speckles and a halogen light source is used for the micro speckle region. For both 2D-DIC setups, the images are acquired simultaneously and recorded at a rate of 2 frames per second.

Once the experiment is concluded, the images obtained from each setup are post-processed by using ©VIC-2D commercial software (Correlated Solution Inc.). The image correlation was performed independently for each speckled region using correlation parameters with subset size of 37 pixels (34 μm) for micro speckle and 45 pixels(1 mm) for the macro speckle, and step size of 5 pixels (4.5 μm) for micro speckle and 5 pixels (0.12 mm) for the macro speckle. Here, it should be noted that the strains over the field of the macro and micro speckle regions extracted independently.

16.4 Results and Discussion

16.4.1 Comparison Between the Angle Plies

Typical stress-strain plots for the three laminates conducted in this study is depicted in Fig. 16.3. From this plot, higher failure strength is observed for the laminate with 15° angle laminas. In contrast, the smallest strength and highest failure strain is recorded for the 45° laminate, while the 30° laminate has shown strength in between the two laminates. A nearly linear relation is noted between the stress and strain for all groups with elastic modulus (E) of 80 GPa, 75 GPa and 58 GPa for 15°, 30° and 45° laminates respectively. This can give a hint on the direct association of the laminas fiber angle with the macroscale response of the laminate. In fact, from the uni-directional tests, it is observed that the laminates with higher fiber angle experienced a higher failure strain and lower strength, and the reverse is true for the lower fiber angle laminates.

By comparing the local response of these angled laminas, the role of the fiber orientation on the over response of the laminate is explored in detail. From the axial strain plot shown in Fig. 16.3b, linear increment in strain along the applied stress is featured for all off-axis laminas. Relatively higher axial strain is attained in the 45° lamina and lower strain is captured in the 30° lamina as depicted in Fig. 16.3b. On the other hand, for the transverse strain, the 15° lamina showed dominance while the 30° lamina had the lowest strain. The transverse strain result seems to oppose what is expected as a response to the Poisson's

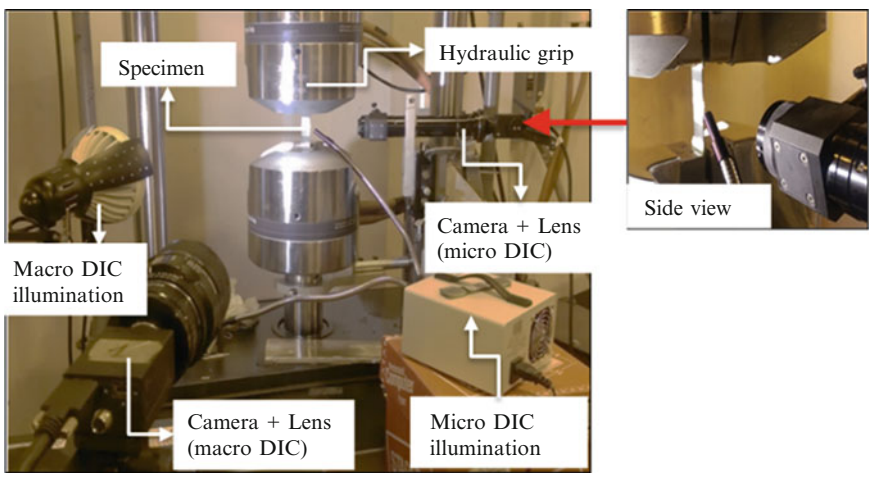

Fig. 16.2 The actual image of the experimental setup

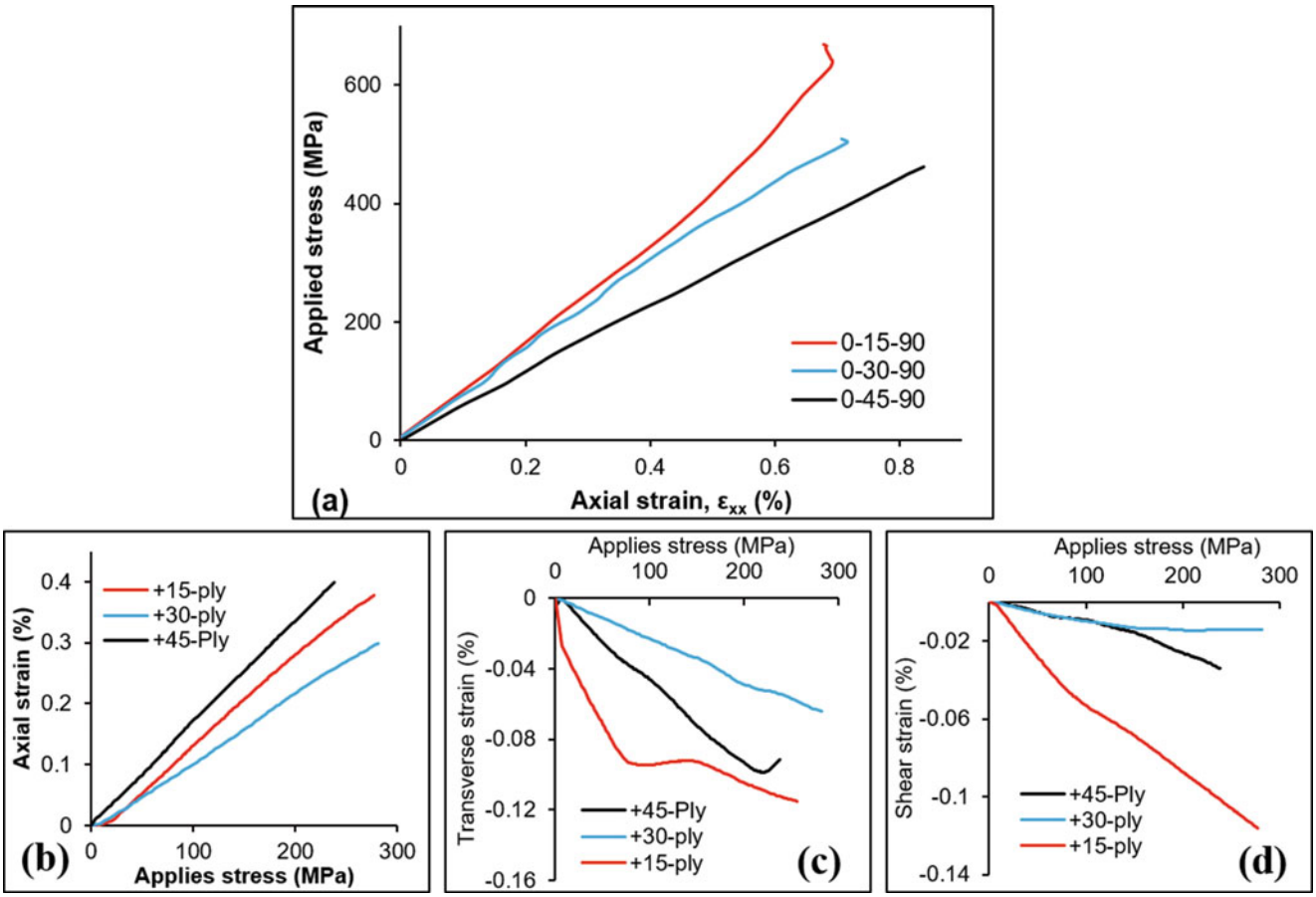

Fig. 16.3 (**a**) The global axial stress-strain, (**b**) Local axial strain-stress (**c**) Local transverse strain-stress and (**d**) Local shear strain-stress, for +45, +30 and 15 laminas

ratio effect. It is known that out of the off-axis laminas the lowest Poisson's ratio is obtained for the 15° fiber angle lamina, and hence the smallest transverse strain was expected in this lamina. Nevertheless, the reverse is observed as shown in Fig. 16.3c. This might indicate that the whole transverse deformation is not only induced by the axial deformation, rather due to highly complex loading situation.

Despite the few irregularities in the transverse strain, more of the complexity is seen on the shear response curves shown in Fig. 16.3d. The interlaminar shear strain on the 15° lamina is much higher than the 30° and 45°. This observation is highly related to the variation of the in-plane shear deformation of the individual laminas. As expected, the main cause of the shear stress/strain variation over the free-edge is the relative in-plane shear deformation of the different laminas in a given laminate. However, it is unexpected that the shear strain is almost the same for the 30° and 45° laminas at the lower stage of loading.

16.4.2 Comparison of the Interlaminar Interfaces

Beyond comparison of the individual plies, a close-up observation on the interfaces is required to deal with the interlaminar strain profiles and to determine the influence of fiber angle on the interface stresses. Perhaps, the delamination of laminas at the free-edge is recognized as the crucial form of damage. For this purpose, the strains of the interface between the two adjacent angled laminas (+Θ/−Θ) are extracted and depicted in Fig. 16.4.

In the transverse strain plots shown in Fig. 16.4a, all the interfaces showed a compressive (negative) strain. The −30/+30 interface has the highest strain and the −15/+15 interface has the lowest. It is logical to presume higher positive transverse strain at the interface where the laminas have higher shrinking strain. In fact, the interface made from laminas with the highest negative transverse strain has the lowest negative transverse strain and vice versa.

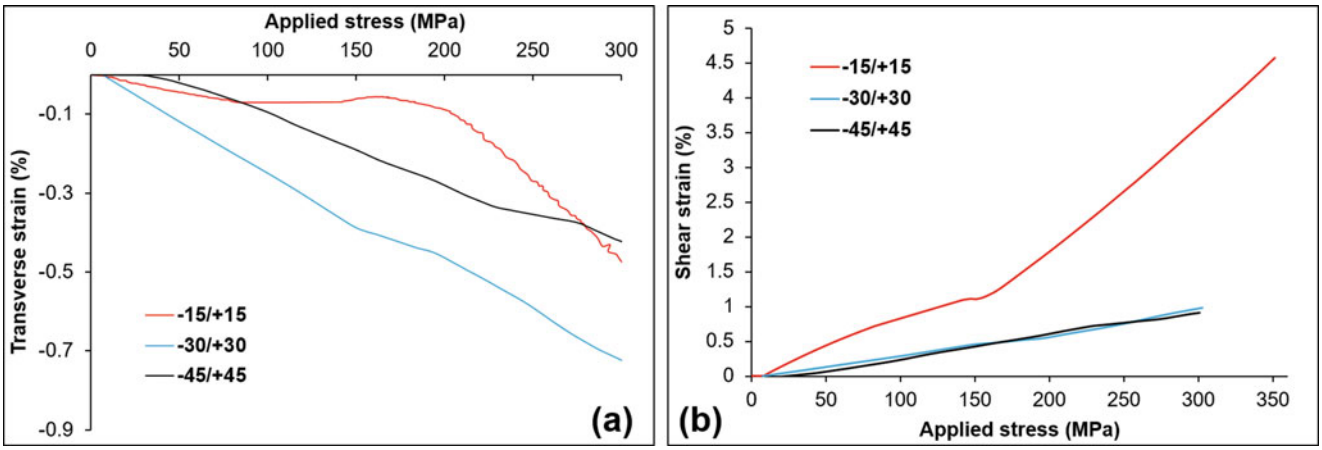

Fig. 16.4 (**a**) Transverse strain-stress and (**b**) Shear strain-stress, for −15/+15, −30/+30 and − 45/+45 interfaces

In the shear strain case, the two interfaces, the −30/+30 and − 45/+45 interfaces, have almost the same magnitude and followed a similar trend of strains. The shear strain in the −15/+15 interface is observed to deviate from the group. The interfaces of −30/+30 and − 45/+45 laminas have singular linear trend, whereas the interface of −15/+15 laminas is far much higher and has a bilinear trend. The shear response of the interfaces is similar to that of the individual laminas depicted in Fig. 16.4d.

16.5 Summary

Damage evolution in multi-directional laminates subjected to uni-axial tensile loading is investigated. It is found that the 90° lamina has a positive transverse strain (ε_{zz}) under the applied tensile axial strain (ε_{xx}). Among the different fiber angle laminas, the 15° lamina showed the largest transverse and shear strain. A compressive transverse strain localizations are observed in all of the interfaces. A high shear strain localization is sited at the interface between off-axis laminas (−Θ/+Θ), nevertheless, small shear localizations are observed at the rest interfaces. At early stage of loading, transverse/matrix cracking is observed to dominate in the 90° laminas. Later, these cracks are grown delaminating the 90/+Θ interface.

References

1. Nettles, A.T.: Basic Mechanics of Laminated Composite Plates, p. 107. NASA Ref Pulication, Huntsville (1994)
2. Kaddour, A.S., Hinton, M.J., Smith, P.A., Li, S.: A comparison between the predictive capability of matrix cracking, damage and failure criteria for fibre reinforced composite laminates: Part A of the third world-wide failure exercise. J. Compos. Mater. **47**, 2749–2779 (2013). https://doi.org/10.1177/0021998313499476
3. Talreja, R.: Assessment of the fundamentals of failure theories for composite materials. Compos. Sci. Technol. **105**, 190–201 (2014). https://doi.org/10.1016/j.compscitech.2014.10.014
4. Tahani, M., Nosier, A.: Free edge stress analysis of general cross-ply composite laminates under extension and thermal loading. Compos. Struct. **60**, 91–103 (2003). https://doi.org/10.1016/S0263-8223(02)00290-8
5. Kassapoglou, C., Lagace, P.A.: An Efficient Method for the Calculation of Interlaminar Stresses in Composite Materials. J. Appl. Mech. **53**, 744 (1986). https://doi.org/10.1115/1.3171853
6. Mittelstedt, C., Becker, W.: Free-Edge Effects in Composite Laminates. Appl. Mech. Rev. **60**, 217 (2007). https://doi.org/10.1115/1.2777169
7. Murthy, P., Chamis, C.: Free-edge delamination: laminate width and loading condition effects. Nasa_Tm-100238 (1987)
8. Nailadi, C.L., Adams, D.F., Adams, D.O.: An Experimental and Numerical Investigation of the Free Edge Problem in Composite Laminates. J. Reinf. Plast. Compos. **21**, 3–39 (2002). https://doi.org/10.1106/073168402024280
9. Pagano, N.J., Pipes, R.B.: The Influence of Stacking Sequence on Laminate Strength. J. Compos. Mater. **5**, 50–57 (1971). https://doi.org/10.1177/002199837100500105
10. Berthelot, J.-M.: Transverse cracking and delamination in cross-ply glass-fiber and carbon-fiber reinforced plastic laminates: Static and fatigue loading. Appl. Mech. Rev. **56**, 111–147 (2003). https://doi.org/10.1115/1.1519557
11. Mortell, D.J., Tanner, D.A., McCarthy, C.T.: An experimental investigation into multi-scale damage progression in laminated composites in bending. Compos. Struct. **149**, 33–40 (2016). https://doi.org/10.1016/j.compstruct.2016.03.054

12. París, F., Blázquez, A., McCartney, L.N., Barroso, A.: Characterization and evolution of matrix and interface related damage in [0/90]S laminates under tension. Part II: Experimental evidence. Compos. Sci. Technol. **70**, 1176–1183 (2010). https://doi.org/10.1016/j.compscitech.2010.03.006
13. Tong, J., Guild, F.J., Ogin, S.L., Smith, P.A.: On matrix crack growth in quasi-isotropic laminates-I. Experimental investigation. Compos. Sci. Technol. Elsevier Sci Ltd. **57**, 1527–1535 (1997). https://doi.org/10.1016/S0266-3538(97)00080-8
14. Tessema A, Mymers N, Patel R, Ravindran S, Kidane A. Experimental investigation on the Correlation between Damage and Thermal Conductivity of CFRP. Proc. Am. Soc. Compos. Thirty-First Tech. Conf., (2016)
15. Fahem, A.F., Kidane, A.: Hybrid computational and experimental approach to identify the dynamic initiation fracture toughness at high loading rate. In: Dynamic Behavior of Materials, vol. 1, pp. 141–146. Springer, Cham (2018). https://doi.org/10.1007/978-3-319-62956-8_24
16. Fahem, A.F., Kidane, A.: A General Approach to Evaluate the Dynamic Fracture Toughness of Materials. In: Casem, D., Lamberson, L., Kimberley, J. (eds.) Dynamic Behavior of Materials, vol. 1, pp. 185–194. Springer, Cham (2017). https://doi.org/10.1007/978-3-319-41132-3_26
17. Tessema, A., Kidane, A.: Cross-property interaction between stiffness, damage and thermal conductivity in particulate nanocomposite. Polym. Test. **64**, 127–135 (2017). https://doi.org/10.1016/j.polymertesting.2017.09.032
18. Tessema, A., Ravindran, S., Kidane, A.: Gradual damage evolution and propagation in quasi-isotropic CFRC under quasi-static loading. Compos. Struct. **185**, 186–192 (2017). https://doi.org/10.1016/j.compstruct.2017.11.013
19. Tessema, A., Ravindran, S., Kidane, A.: Experimental study of residual plastic strain and damages development in carbon fiber composite. In: Fracture, Fatigue, Failure and Damage Evolution, vol. 8, pp. 31–36. Springer, Cham (2017)
20. Tessema, A., Ravindran, S., Wohlford, A., Kidane, A.: In-Situ Observation of Damage Evolution in Quasi-Isotropic CFRP Laminates. In: Fracture, Fatigue, Failure and Damage Evolution, vol. 7, pp. 67–72. Springer, Cham (2018)
21. Tessema, A., Zhao, D., Kidane, A., Kumar, S.K.: Effect of micro-cracks on the thermal conductivity of particulate nanocomposite. In: Fracture, Fatigue, Failure and Damage Evolution, vol. 8, pp. 89–94. Springer, Cham (2016)

Chapter 17
Combined Modeling and Experimental Approach to Improve Mechanical Impact Survivability of GaN Power FET

John B. Ferguson, Sangwook Sihn, Albert M. Hilton, Curtis M. McKinion, Steven R. Dooley, Ajit K. Roy, Amanda M. Schrand, and Eric R. Heller

Abstract An alternative approach was taken to improve the high-g shock tolerance of electronic devices. Rather than stiffening electronic devices with potting, the electronic device mass was reduced by an appropriate amount to match the compliance of the device to the circuit board. The devices studied were field effect transistors (FET) in bare die form factor and allowed a wafer thinning process to be utilized. A global-local finite element model was utilized to determine the ideal die thickness for matching the compliance. Test boards were populated with optimal thinned devices and stock devices for comparison on the same board. A three step thinning process was utilized in an effort to minimize the induced defects from the thinning process. The circuit boards with mounted FET's were dropped from a shock drop tower to successively higher g-shocks up to 60,000-g. The electrical performance of each device was tested and verified after each level of mechanical shock. In general, most devices (both stock and thin) fail electrically before visual evidence of mechanical failure was present. The highest peak acceleration a device survived without failure is used as a figure of merit (e.g. the device failed on the next higher drop). The average of the "peak survived accelerations" for thinned devices is found to be about 25% higher for thin devices than for stock devices. However there was a wide variability in the results, which appears to be the greatest challenge to improving stock tolerance predictability and high confidence reliability of electronic devices.

Keywords High-g · Mechanical shock · Electronics reliability · Finite element modeling · Solder failure

17.1 Introduction

Electronic devices are pervasive in many environments which is being further expanded by consumers taking sophisticated electronics into numerous and challenging mobile environments. This trend is driving the demand for electronics that can survive in rugged shock, vibration, high impact and high acceleration (high-g) mobile environments. This involves not only dropped electronics (cell phones, portable equipment, etc.) but also shock survivability in vehicle collisions, aircraft crashes, as well as many military specific extreme environments. Making mobile electronics more survivable requires advances in almost all engineering aspects including wafer processing, component and substrate mechanical compliance, solder and solder contact design, and overall packaging. Also, several potting materials have been applied to provide rigidity and strength. Limited research has been conducted on shock and impact of electronics and included investigating the solder joint holding the electronic devices to the circuit board [1–3]. Many factors such as type of solder, voids in the solder, shape, size and

J. B. Ferguson (✉) · A. K. Roy · E. R. Heller
Air Force Research Laboratory, Materials and Manufacturing Directorate, Wright-Patterson Air Force Base, OH, USA
e-mail: john.ferguson.5@us.af.mil

S. Sihn
Air Force Research Laboratory, Materials and Manufacturing Directorate, Wright-Patterson Air Force Base, OH, USA

University of Dayton Research Institute, Nonstructural Materials Division, Dayton, OH, USA

A. M. Hilton
Air Force Research Laboratory, Materials and Manufacturing Directorate, Wright-Patterson Air Force Base, OH, USA

Wyle Laboratories, Dayton, OH, USA

C. M. McKinion · A. M. Schrand
Air Force Research Laboratory, Munitions Directorate, Eglin Air Force Base, FL, USA

S. R. Dooley
Air Force Research Laboratory, Sensors Directorate, Wright-Patterson AFB, OH, USA

J. Carroll et al. (eds.), *Fracture, Fatigue, Failure and Damage Evolution, Volume 6*, Conference Proceedings of the Society for Experimental Mechanics Series, https://doi.org/10.1007/978-3-319-95879-8_17

orientation of the contact with respect to the acceleration direction affect the resultant survivability. In addition the circuit board construction, layout and circuit board materials also affect survivability.

These approaches can be broadly categorized as ways to increase rigidity and strength of the electronics and packaging. Although they increase the ultimate breaking strength of the electronics, continuation down this route leads to bulkier and heavier modules which is counter to the desire to make them more mobile. Also, adding to the packaging increases the mass and the inherent inertial forces (i.e. $F = ma$) when velocity and acceleration changes occur at impact. The increase in mass can be counter to the goal of increasing shock and impact survivability. Alternative research has taken the opposite route towards increasing the impact and shock tolerance by constructing electronics using flexible and compliant polymers which are electrically conductive [4–6]. Also, recent efforts to produce thin silicon membrane have the goal of producing "wearable electronics" in the form of adhesive patches for health and performance monitoring [7, 8]. However, these devices are not necessarily high power devices. Improving the shock tolerance of power electronics is necessary to provide sufficient power for many mobile electronic applications.

In order to investigate flexible power electronic devices we have chosen to investigate an interesting and novel idea of using commercially available transistor dies with a lateral rather than a vertical structure. The lateral structure has all device structures on the top of the die which allows thinning the substrate from the back side to allow the device become more flexible and compliant. High electron mobility transistors (HEMT) utilizing GaN/AlGaN interface to create the 2-dimensional electron gas (2DEG) are an emerging technology for power electronics. They offer benefits such as higher operating temperature, smaller size than silicon or silicon carbide for the same power, and faster switching speeds. They operate in enhancement mode similar to many other standard power FET's.

Wafer thinning is an established technique to provide increased thermal energy conduction, provide a small form factor, and allow 3D integration for example. One of the findings of prior work on thinning electronics is identifying complex failure mechanisms due to stress interaction with the surface roughness, sub-surface defects and modified stress field due to the thinning processes [9–11]. Several approaches have been developed to reduce or eliminate the sub-surface defects during wafer thinning. The greatest contributor to the defects is rapid removal of material to thin the wafer or device, although this is the most economical method to remove material. Slow material removal with a very fine polishing grit creates very little subsurface defects. A balance between the fast and slow material removal is to perform the coarse grind on the initial and largest portion of the depth removal but stop before reaching the desired thickness. The next process is then either a fine grit polishing or a chemical-mechanical polishing to remove most of the sub-surface defects induced by the rapid coarse grind. A final reactive ion etch (RIE) is used to remove the final material layer and is considered to be the least damaging process. The result is a thin substrate and surface which is nearly stress free and defect free.

Although there has been prior research performed with respect to solder and other mechanical failure, less emphasis has been placed on monitoring the survivability of the internal device structures, such as the gate, drain and source within field effect transistors for electrical performance. Improving the survivability of semiconductor structures to high shock, vibration, impact and acceleration will provide improvements for use of electronics in rugged environment. Taking into account the mechanical compliance of the complete package including the circuit board, electronic devices, and location of the solder contacts on the circuit board and the device will allow optimizing the design to reduce stresses on the components leading to better survivability.

Finite element modeling of the package mechanical response can be utilized to adjust available parameters to reduce the stresses on the electronic device, solder contacts and circuit board. In the present study, the location of the contacts are dictated by the manufacturer. However, the thickness of the device and the methods used to thin the stock device are adjustable. An integrated approach with finite element modeling has been pursued to analyze the effect of wafer thinning on the stress field and then to improve the shock survivability of the electronics. The modeling predicted an optimal die thickness of the devices for minimum stress during impact.

17.2 Experimental

High performance 2DEG GaN/AlGaN field effect transistors from Energy Power Conversion (EPC), part number EPC2012b, were utilized for this study. In addition to the benefits mentioned, the smaller size and mass result in lower inertial mass forces during impact and shock. The construction of the devices is a very thin epitaxial deposited aluminum nitride buffer on top of a silicon wafer. Then a GaN/AlGaN (less than 100 μm) field effect transistor is constructed on top of the buffer layer. The total stock device thickness is approximately 700 μm and includes a top passivation. The contacts are pre-soldered but the solder is not included in these thickness values. The silicon substrate can be thinned (from the backside) to match the mechanical response to the circuit board and reduce stresses.

A global finite element (FE) model was developed to predict dynamic responses of the FR4 circuit board and the FET devices mounted on the board. A local FE model using a cohesive zone model was also developed to predict interfacial damage behaviors between the board and the FET device. This global-local FEM model simulation indicated that the interfacial stresses built-up during shock/impact could be significantly reduced when the die of the GaN FET device is thinned so that the flexibility of the GaN FET device matches that of the circuit board. Parametric study was conducted by varying the die thickness to determine the optimal thickness of approximately150 μm for minimal stresses during shock/impact.

A three step process was utilized to thin the devices for comparison shock testing. The first step was an aggressive coarse grind removing approximately 450 um from the silicon backside, resulting in a thickness of about 250 um. The second process was fine mechanical wet polishing stepping down the particle size of the polishing paper (10 um–0.5 um particle size). The thickness of the dies after fine polishing was in the range of 140–200 um. Multiple FET dies were adhered to a rigid substrate with Crystalbond adhesive and simultaneously thinned for both the coarse grind and the fine polish. A final reactive ion etch was performed to remove approximately 15 more um. The final optimally thinned devices were between 120 and 180 um thick. In addition several devices were thinned to between 130 and 170 um using only the coarse grinding process. This allowed comparison of the 3 step process to the coarse grind only process. If the 3 step process does not offer substantial improvement over the coarse only method the extra cost of the 3 step process may not be justified. The thicknesses of the devices was determined by measuring 3 locations across the length with a microscope and averaging.

The circuit boards utilized are standard FR4 (fire retardant 4). A ball grid array placement tool (ATCO model AT-GDP-3) was used to flux and position the FET's on the circuit board prior to solder re-flow. A solder reflow oven (ATCO model PRO 1600 SMT) was utilized to solder the devices and programmed to follow a reflow schedule close to that recommended by EPC. The layout of the circuit board with 3 EPC2012 FET's solder in place is shown in Fig. 17.1. Three FET's were mounted on each board. They are mounted symmetrically with respect to the caul clamps (convex surface) giving close to similar mechanical response for all three FET's. The terms shock and impact are sometimes used interchangeably. The scenario we are investigating is when the test sample undergoes the change in velocity with the highest peak acceleration (e.g. the sample is dropped). This is usually referred to as shock testing. Impact testing usually describes the situation where the test sample is immovable, being supported and anchored to the ground. A "mass impactor" is dropped from the proper height to give a desired kinetic energy at impact, striking the sample and imparting a mechanical wave into the test sample.

A shock drop tower (MTS) was utilized for shock testing. The load shuttle is raised to various heights against elastic cords for additional downward accelerating force. Felt "programmers" are used at the base to vary the shock duration versus peak acceleration. In the context of this paper 1 g = 9.8 m/s^2, the acceleration due to gravity at the earth's surface. An accelerometer was mounted on the drop shuttle to measure the peak acceleration and duration of each drop. The populated circuit boards were mounted on the MTS drop tower shuttle for shock testing one at a time. A sequence of tests from low to high shock acceleration was performed on each circuit board. This was a sequence of successively higher drop heights from 0.305 m to 1.83 m in steps of 0.3 m (12–72 in., 12 in steps). Electrical properties were measured before testing as a baseline. The electrical properties were re-measured after each successively higher height drop for each device. The electrical properties measured are listed in Table 17.1.

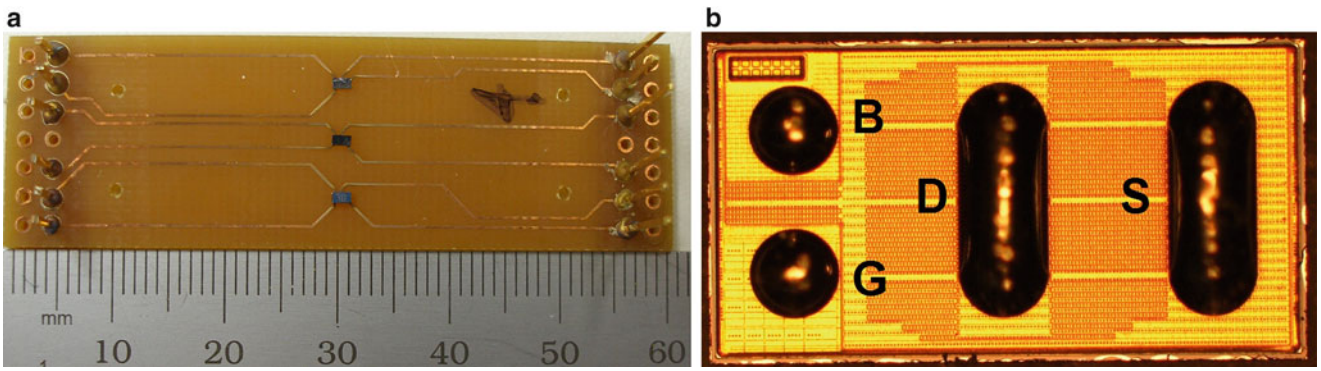

Fig. 17.1 (**a**) FR4 circuit board with 3 GaN/AlGaN HEMT devices soldered; The circuit board is clamped in the drop tower shuttle by 2 caul clamps parallel to the headers at the board edges; The top device is 161 μm thick, middle 144 μm thick, bottom stock (700 μm thick); (**b**) Solder (and device) side of the EPC2012 die with the solder balls (dark) for the gate (G), body/substrate (B), drain (D) and source (S)

Table 17.1 Electrical properties measured

IGSS	Gate leakage current vs. gate-source voltage, VGS = 0 V – 5 V, VDS = 0 V
IDon	Drain-source current vs gate-source voltage, VGS = 0 V – 5 V, VDS = 1 mV
IDSS	Drain leakage current vs drain-source voltage, VDS = 0 V – 200 V, VGS = 0 V

Table 17.2 Test results

Optimal			Coarse			Stock		
Thickness, μm	Peak survived Accel., g	Elec. Fail	Thickness, μm	Peak survived Accel., g	Elec. Fail	Thickness, μm	Peak survived Accel., g	Elec. Fail
136.7	41,125	D-S*	132.3	3459	SF	700	51,578	NF
119.3	61,514	NF	136	23,256	D-G*	700	34,783	D-O
185.7	51,578	NF	170.3	41,235	D-S	700	63,960	NF*
161.3	63,960	NF*				700	22,598	G-S
158.3	22,598	D-S				700	29,727	G-O
						700	36,519	NF
						700	26,575	D-S
152.3	48,155		146.2	22,650			37,963	Avg.
22.6	15,117		17.1	15,428			13,664	St. Dev.

Abbreviations for fail are as follows, *NF* no failure, *D-S* drain to source short, *D-G* drain to gate short, *G-S* gate to source fail, *D-O* drain open, *G-O* gate open, *SF* solder failure, * indicates crack

Although it is desirable to have the FET's electrically biased during the impact, the instrumentation setup was only able to provide bias and measurement under static conditions. Two source-measure units (Keithley models 2410, 2425) were utilized to bias the drain, gate and source with the source as a common ground. Keithley ACS-Basic was used to automate the current-voltage (I-V) measurement process (source voltage, measure current).

17.3 Results

A total of 6 circuit boards comprising 16 FET devices were utilized for this study (2 FET's failed the electrical pre-test and were presumably damaged during the mounting and/or solder reflow process). The FET's tested comprised 5 "optimally thinned" devices (between 120 μm and 180 μm thick and 3 step thinning process), 3 devices coarse grind only thinned, 7 stock FET's, and one device under thinned (95 μm). After each drop the electrical properties of the FET's were measured (static, resting condition). Many of the devices failed electrically before reaching the highest drop (1.83 m). However 6 of the devices survived to 1.83 m (72 in.) height and presumably might have survived an even higher g-force. Generally, a device which was considered as passing the shock load had leakage currents that grouped together within a factor of 2 of the pretest curve and still within the manufacturer's acceptable tolerance for the parameter (IGSS, IDon, IDSS). However, failure of a device electrically was catastrophic and changed orders of magnitude. The g-force dependence on height does vary from drop to drop. A height of 1.83 m generally resulted in a maximum g-force of between 50,000 g and 64,000 g. Each circuit board was dropped from successively greater heights unless all three devices had failed on the board. Four of the six circuit boards were tested to the full 1.83 m drop, one to 1.52 m drop and one to 1.22 m drop. Out of all 18 FET devices drop tested only one had failure of the solder and separated from the circuit board (the two which failed the electrical pretest were still attached to their circuit boards). The data with the peak acceleration to which each device survived electrically is in Table 17.2.

Microscopy was conducted before and after the testing to identify any mechanical failures (Fig. 17.2). This revealed two of the optimally thinned devices had a crack during testing due to the shock environment. However, one of the cracked devices still performed satisfactorily. Moreover, one of the coarse only thinned device had a crack as well as one stock device. One additional mounted device was only 95 μm thick or thinner than optimal. Although this device only survived to approximately 14,000 g, a sample of one is not enough to draw any conclusions.

17.4 Discussion

The emphasis of this study was to use electrical performance and the requirement to have devices functioning electrically as a criteria for a "passing" determination rather than a purely mechanical criteria. It was also obvious for the small FET dies utilized, that electrical failure occurs before mechanical failure in the die was observed.

The bottom 2 rows of Table 17.2 have the average and standard deviation values (thickness and peak survived acceleration) for the three categories of specimens drop tested (optimal 3 step thinned, coarse only thinned, and stock devices). The average maximum acceleration (sometimes referred to as g-force) survived by 3-step (optimal) thinned devices (48,000 g) is 10,000 g higher than stock devices (38,000 g) which is a 25% improvement. The standard deviation is still slightly larger than the difference between averages. Also, having more devices tested would improve the confidence in the statistics. However the results are encouraging. As mentioned in the introduction, adding potting and other packaging approaches to increase stiffness actually adds mass to the device. When the mobile electronics are the moving object, the overall vehicle velocity and collision environment determine the change in velocity the inherent peak acceleration. The ultimate attachment region is the solder pad which is a fixed surface area. Thus the mass of the device and the peak acceleration will determine the peak force ($F = ma$) at the attachment point which is spread to the rest of the device. By reducing the mass the experimental approach is reducing the peak forces acting on the die.

There is no correlation between the maximum survived g force and the FET thickness in the range 120 –180 μm thickness. This is evident from the data plotted in Fig. 17.3, peak survived acceleration versus thickness of the optimally thinned devices. Also, consider that all 7 of the stock devices are the same thickness but they have a standard deviation in peak acceleration which is comparable to the optimal thinned device data standard deviation. Reducing the large variation in breaking point appears to be the greater challenge. The standard deviation is approximately 1/3 the average maximum peak survived acceleration. Many applications will want a statistically high confidence survival level so the worst performing sample will set the requirement for this level. A take away of the current study is perhaps the thinning process performed for this study could be suboptimal. Our thinning process utilized SEM preparation equipment and is not optimized semiconductor equipment for thinning semiconductor materials. Utilizing thinning process equipment optimized to reduce the induced

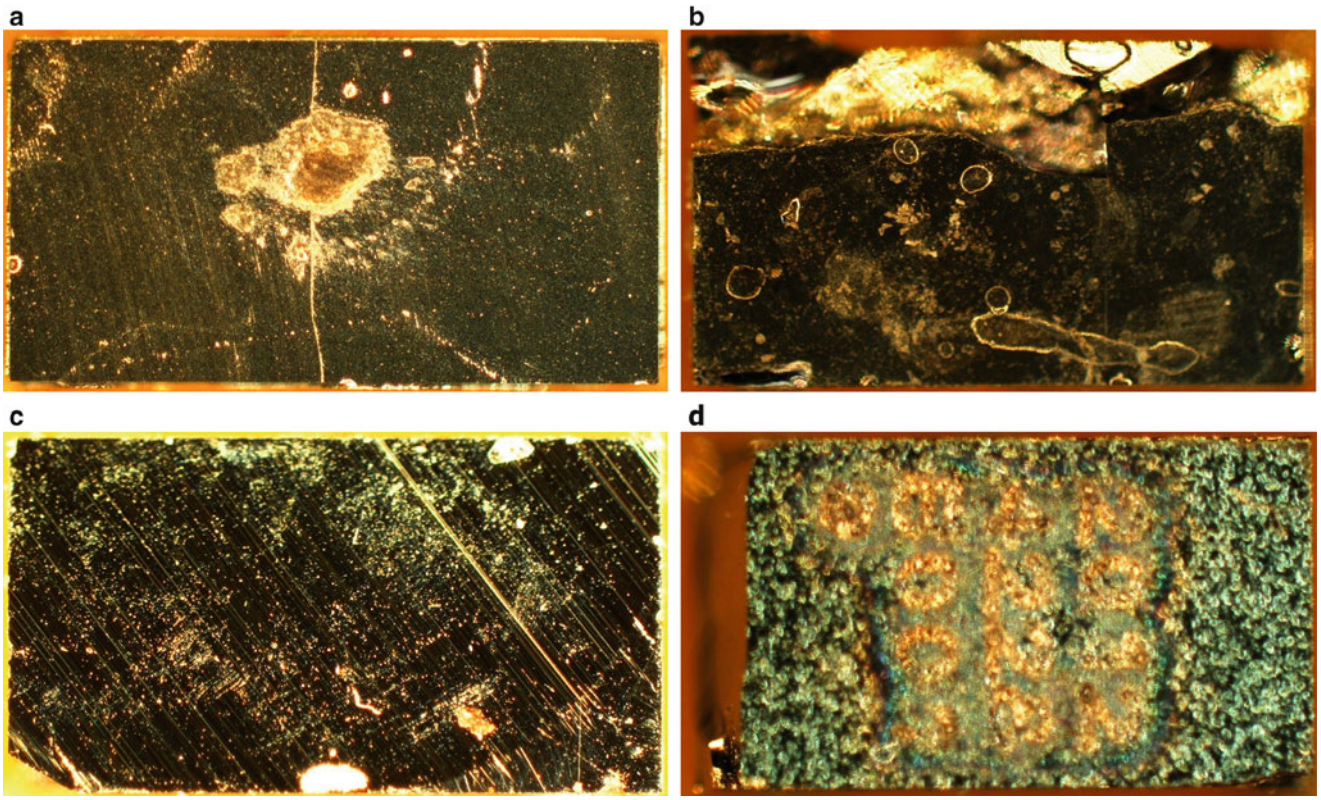

Fig. 17.2 Microscopy images of devices with cracks. (**a**) Optimal process device 136.7 μm thickness crack in middle (drain); (**b**) Optimal process device 161.3 μm thickness crack along top; (**c**) Course only process device 136 μm thickness "arc" crack at bottom; (**d**) Stock device crack at left (survived to highest acceleration)

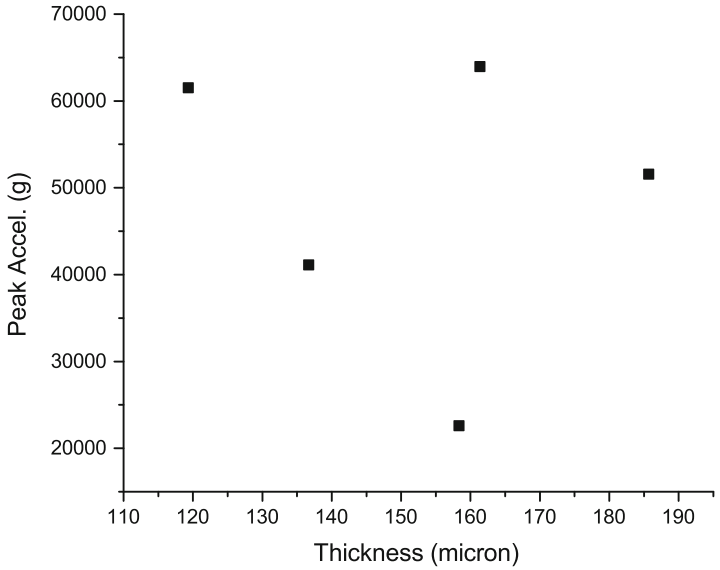

Fig. 17.3 Plot of Peak Acceleration vs Thickness for the optimally thinned devices

subsurface damage could lead to better stock survivability. It is noteworthy that two of the three devices exhibiting a cracks occurred at below average peak accelerations. If those devices had higher than average internal defects, they could become crack initiation sites, leading to early fracture of the die. Also noteworthy is that 6 of the electrical failures involve the FET drain while 2 involve the gate. The drain is located at the center of the device and could experience a higher internal stress than the ends.

17.5 Conclusion

The increasing mobilization of electronics is driving a need for electronics with better mechanical shock and impact tolerance. This is true not only for commercial applications but military as well. The results of this study indicate it is possible to improve mechanical shock survivability by designing the electronics die compliance to match that of the circuit board on which it is mounted. However, the standard deviation in peak acceleration survived values significantly reduces the "safe threshold" to ensure desired confidence levels to ensure a high percentage of devices survive a shock event or even repeated events. Reducing the standard deviation is necessary to allow the matched compliance method of shock tolerance to be adopted. Identifying methods to reduce the variation is a next step and one possibility is further improvements in the thinning processes. Further investigations into the failure mechanisms of the electrical performance would also be beneficial.

References

1. Lall, P., Dornala, K., Lowe, R., Foley, J.: Survivability assessment of electronics subjected to mechanical shocks up to 25,000 g. 15th IEEE ITHERM Conference, 507 (2016)
2. Lall, P., Patel, K., Lowe, R., Strickland, M., Blanche, J., Geist, D., Montgomery, R.: Modeling and reliability characterization of area-array electronics subjected to High-G mechanical shock up to 50,000G. IEEE 62nd ECTC Conference, 1194 (2012)
3. Lall, P., Patel, K., Lowe, R.: High-G shock reliability of ceramic area-array packages. 13th IEEE ITHERM Conference, 1028 (2012)
4. Ahn, B.Y., Duoss, E.B., Motala, M.J., Guo, X., Park, S.-I., Xiong, Y., Yoon, J., Nuzzo, R.G., Rogers, J.A., Lewis, J.A.: Omnidirectional Printing of Flexible, Stretchable, and Spanning Silver Microelectrodes. Science. **323**, 1590, 5921 (2009)
5. Patton, S.T., Frasca, A.J., Hu, J., Varshney, V., Phillips, B.S., Roy, A.K., Voevodin, A.A.: Multiphysics characterization of multi-walled carbon nanotube thermoplastic polyurethane polymer nanocomposites during compression. Carbon. **98**, 638 (2016)
6. Ilyas, N., Cook, A., Tabor, C.E.: Designing Liquid Metal Interfaces to Enable Next Generation Flexible and Reconfigurable Electronics. Adv. Mater. Interfaces. **4**(15), 1700141 (2017)

7. Ahn, J.-H., Kim, H.-S., Menard, E., Lee, K.J., Zhu, Z., Kim, D.-H., Nuzzo, R.G., Rogers, J.A., Amlani, I., Kushner, V., Thomas, S.G., Duenas, T.: Bendable Integrated Circuits on Plastic Substrates by Use of Printed Ribbons of Single-Crystalline Silicon. Appl. Phys. Lett. **90**, 213501 (2007)
8. Kim, D.-H., Ahn, J.-H., Choi, W.M., Kim, H.-S., Kim, T.-H., Song, J., Huang, Y.Y., Liu, Z., Lu, C., Rogers, J.A.: Stretchable and Foldable Silicon Integrated Circuits. Science. **320**(5875), 507–511 (2008)
9. Jiun, H.H., Ahmad, I., Jalar, A., Omar, G.: Effect of wafer thinning methods towards fracture strength and topography of silicon die. Microelectron. Reliab. **46**(5–6), 836 (2006)
10. Sullivan, S.M.: Current Evolution of Wafer Thinning and Dicing. Electro. Chem. Soc. Trans. **18**(1), 745 (2009)
11. Miyazaki, C., Shimamoto, H., Uematsu, T., Abe, Y.: Development of wafer thinning and dicing technology for thin wafer. IEEE International Conference on 3D Systems Integration. 1 (2009)

Chapter 18
Mechanics of Materials and Fracture for High School Students

Louisa Avellar and Kimberley Mac Donald

Abstract We developed a nine session after-school curriculum to introduce high school students to fracture mechanics through interactive and hands-on experimental exploration of mechanics of materials and structures. Each session begins with a discussion of the week's core concept in the context of a real world example of its application or importance. The remaining time is devoted to small group hands-on activities that reinforce and further explore the concept. The program revolves around the use of a custom designed portable load frame to perform material testing of 3D printed materials and structures. Students are introduced to the load frame during the second session where they determine material properties using a cantilever beam experiment. In the following sessions students focus on individual concepts in the experiment such as the source of the cantilever beam equation or dimensional analysis to determine the units of their results. The final three sessions involve bringing together all the concepts from the previous sessions to try to design the stiffest beam within a constrained cross-sectional area. Students go through the engineering design process from defining the problem to designing and testing prototypes to choosing a final design, 3D printing it, and testing it. Throughout the tests, they collect load and displacement data to calculate the achieved beam stiffness. Additionally, all beams are tested to failure to observe fracture mechanisms and ultimate strength. The primary goals for this program are to reinforce students' prior knowledge from their science classes, demonstrate potential applications of additive manufacturing, and inspire interest in mechanics of materials.

Keywords Education · Outreach · Mechanics of materials · Fracture mechanics · 3D printing

18.1 Introduction

Many schools are readily embracing new technologies in the classroom. From SMART Boards to student laptop computers to 3D printers, today's students are able to learn using a variety of technologies. These schools are also supporting and starting more clubs and programs related to engineering including rocketry and robotics clubs. There are, however, many less such programs that explore ideas in solid and structural mechanics at the high school level. Exposing students to a variety of different aspects of engineering helps give them an opportunity to find a passion and to practice both recalling and applying what they already know. Practicing recall, especially in new contexts, has been shown to promote retention and enhance learning across disciplines [1]. The hands-on and active learning nature of these types of programs has also been shown to offer a wide variety of benefits in many student's learning [2]. Engineering programs teach valuable problem-solving skills applicable in many other classes as well as in daily life. They also allow students to see real world applications of their basic science and mathematics courses.

For this program, we used 3D printing, which is already available in our local schools, as a starting point for designing a curriculum that teaches the basics of mechanics of materials and fracture mechanics. Throughout each session, we employ a variety of active learning techniques including providing context through stories, and hands-on demonstrations and experiments.

L. Avellar · K. Mac Donald (✉)
California Institute of Technology, Pasadena, CA, USA
e-mail: kmacdonald@caltech.edu

J. Carroll et al. (eds.), *Fracture, Fatigue, Failure and Damage Evolution, Volume 6*, Conference Proceedings of the Society for Experimental Mechanics Series, https://doi.org/10.1007/978-3-319-95879-8_18

18.2 Materials

Many of the materials used in this program are readily available in most classrooms or can be purchased at a grocery, office supply, or hardware store. However, there are two pieces of special equipment that are needed to complete some of the modules: a mini portable load frame (or the materials to build one) and a 3D printer with appropriate modelling and slicing software.

The portable load frame shown in Fig. 18.1 is designed such that only a few parts need special machining. The majority of the parts can be cut with a saw and a laser cutter. The frame itself is made of 80/20 T-slot aluminum framing and fasteners with laser-cut acrylic brackets. A large threaded rod is used to apply displacement controlled loading and requires a custom machined aluminum block attachment. The specimen grips are also custom machined from aluminum blocks. A slide potentiometer and disk load cell are used to measure displacement and load respectively via an Arduino with an LCD screen.

A wide variety of low cost and easy to use 3D printers are available on the market. For this program, we used a Deezmaker Bukito 3D printer in the Caltech Library TechLab 3D Printing Facility to print specimens before each session and a Stratsys uPrint SE available at the school to print student designs. Any 3D modeling software capable of saving STL files can be used to model specimens including free web aps and student versions of industry softwares. We used SolidWorks to model example specimens and students used AutoDesk Inventor which was available on their school's computers.

18.3 Modules

The primary educational concept used throughout this program is active learning. Each module is built up from a "story" about a major engineering failure providing not only a practical application of the concepts they are learning but also a platform to inspire questions and critical thinking about the topics. Every session also includes some kind of hands-on activity or experiment, reinforcing the concepts discussed.

The first session or module begins with the story of the Titanic including what we know about how and why it sank, and how this and other failures inspired changes in how we design modern ships. It also serves as an introduction to the program and re-introduces students to foundational concepts used in mechanics of materials that they learned in their previous science classes. Additionally, it introduces the concept of fracture mechanics. This is achieved through a series of mini experiments using everyday objects such as paper cups, paperclips, rubber bands, and chalk to demonstrate stress, strain, elastic, plastic, ductile, and brittle.

In the second session, the load frame is introduced and used to measure the stiffness of a cantilever beam specimen and thus the material's Young's modulus. Concepts such as yielding, stiffness, Young's modulus, and margin of safety for engineering

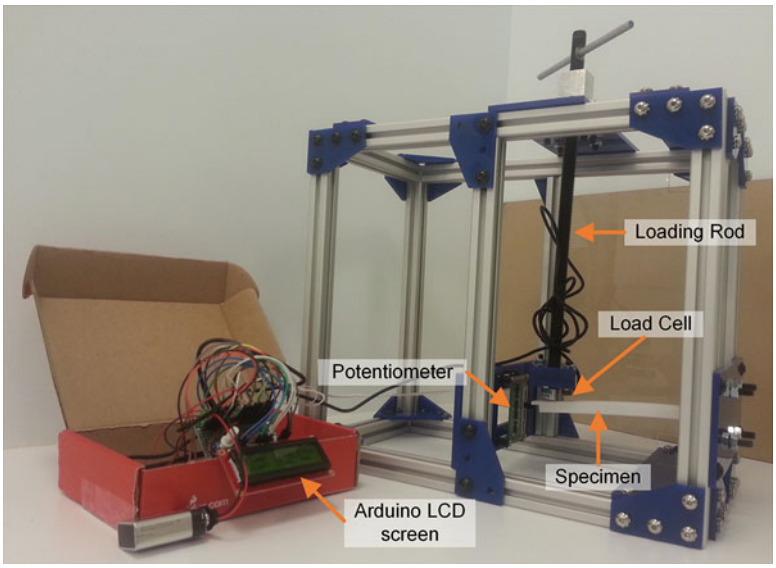

Fig. 18.1 Portable load frame with cantilever beam specimen undergoing displacement controlled loading and with potentiometer and load cell readings on an Arduino LCD screen

design are also introduced. These concepts were first introduced through a discussion on why the Brooklyn Bridge has so many suspension cables. Students then conduct a cantilever beam loading test and calculate Young's modulus from load and displacement data they collect during the experiment. Groups not conducting an experiment or analyzing their data practice 3D modeling and CAD skills by drawing an example beam that could be tested on the load frame once printed.

The third and fourth sessions focus on dimensional analysis, sanity checks, and estimation techniques, which were particularly important in failure of the Mars Climate Orbiter. Students continue to run their beam experiments and use dimensional analysis to check their experimental results and better understand the equations they use. They also apply significant digits conventions and appropriate measurement units to a variety of measurements. Fermi problems are used to practice estimation techniques. We also discuss problem solving techniques and how to use estimation and dimensional analysis as a sanity check for their work.

Sessions five and six focus on geometry and engineering drawing. Students analyze different geometries using ratios and learn how different geometries can affect engineering designs. They also learn to draw and dimension an engineering drawing using hidden lines, center lines, and scale. Fracture mechanics concepts such as stress concentrations are also discussed through learning about the de Havilland Comet failures and why airplane windows do not have sharp corners like those on our homes and other buildings.

The remaining three sessions allow students to apply all the knowledge they have gained to design the stiffest beam they can with a limited cross-sectional area. Students begin by choosing a cross-sectional shape and then calculate the theoretical stiffness based on a cantilever beam configuration. They try several designs and then model, print, and test the one they think will be the stiffest. On the final day, they choose their final design, print it, and test it to show that their beam really is as stiff as they predict.

18.4 Outcomes and Conclusions

In this nine session after-school curriculum we introduced high school students to fracture mechanics and mechanics of materials through a variety exploratory hands-on experiments. The use of stories about real world applications of each week's concepts helped engage students early in the session and kept them thinking throughout the activities. Students were able to use our simple portable load frame to determine material properties and test their specimens to failure, such as the specimen shown in Fig. 18.2 which failed in tensile fracture near the grip. We observed students applying prior knowledge from their science and math classes while actively participating in activities and experiments as well as gaining confidence in their understanding of physics, 3D printing, and mechanics.

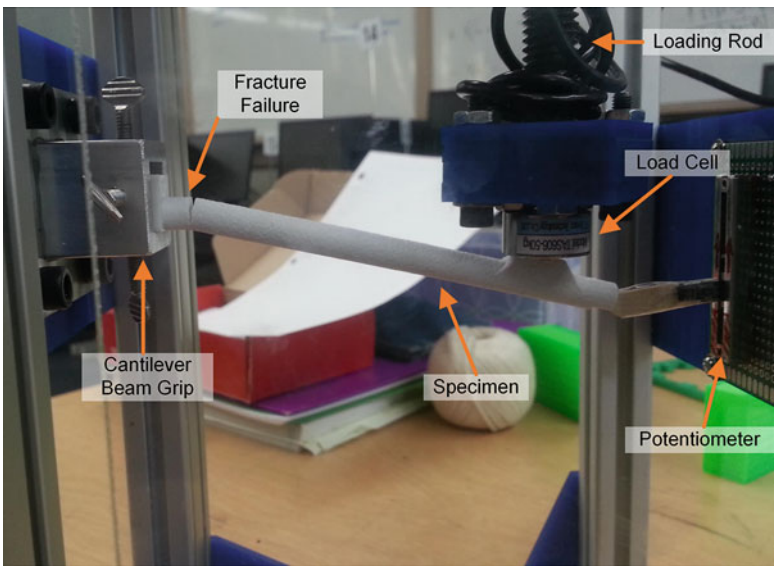

Fig. 18.2 Cantilever specimen tested to failure by tensile fracture near grip in upper portion of beam

Acknowledgements The authors wish to thank Neal Brodnik for his role in implementing this program, Mitch Aiken of the Caltech Center for Teaching Learning and Outreach (CTLO) for his support and assistance in arranging for this program to be taught at a local high school, and the teachers who allowed us to use their classrooms and promoted this program. This material is based upon work supported by the National Science Foundation Graduate Research Fellowship Grant No. DGE-1144469 and Designing Materials to Revolutionize and Engineer our Future (DMREF) Award No. DMS-1535083. Parts were fabricated at the Caltech Library TechLab 3D Printing Facility, which was created and is sustained by funding from both the Caltech Moore-Hufstedler Fund and the Caltech Library.

References

1. Ambrose, S., et al.: How does the way students organize knowledge affect their learning? In: How Learning Works: Seven Research Based Principles for Smart Teaching, 1st edn, pp. 40–64. Jossey-Bass, San Francisco (2010)
2. Prince, M.: Does active learning work? A review of the research. J. Eng. Educ. **93**(3), 223–231 (2004)